Dipl.-Ing. Florian Maislinger, BSc.

Non-Equilibrium Approaches to Strongly Interacting Many Body Systems

DOCTORAL THESIS

to achieve the university degree of

Doktor der technischen Wissenschaften

submitted to

Graz University of Technology

Supervisor:
Ao.Univ.-Prof. Dipl.-Phys. Dr.rer.nat. Hans Gerd Evertz

Institute of Theoretical and Computational Physics

Graz, April 2021

EIDESSTATTLICHE ERKLÄRUNG

AFFIDAVIT

Ich erkläre an Eides statt, dass ich die vorliegende Arbeit selbstständig verfasst, andere als die angegebenen Quellen/Hilfsmittel nicht benutzt, und die den benutzten Quellen wörtlich und inhaltlich entnommenen Stellen als solche kenntlich gemacht habe. Das in TUGRAZonline hochgeladene Textdokument ist mit der vorliegenden Doktorarbeit identisch.

I declare that I have authored this thesis independently, that I have not used other than the declared sources/resources, and that I have explicitly indicated all material which has been quoted either literally or by content from the sources used. The text document uploaded to TUGRAZonline is identical to the present doctoral thesis.

Datum/Date	Unterschrift/Signature

Für Adenike
hob di gern!

So, five-card stud, nothing wild.
And the sky's the limit.

Abstract

The intriguing nonequilibrium physics of strongly interacting many body systems has become increasingly accessible to theoretical studies in recent years, fueled to a large extent by new and improved theoretical methods. A non-equilibrium setup is for example the shining of a short laser pulse onto a material, or a sudden change of one or more Hamiltonian parameters of a theoretical model like the Hubbard model. The present thesis contains three parts, introducing a new non-equilibrium Dynamical Mean Field Theory (DMFT) solver and expanding the range of accessible problems, studying non-equilibrium physics of light absorption in a small Hubbard system, and studying front dynamics in spin systems.

In the first part of the present thesis a new so-called impurity solver for non-equilibrium DMFT is introduced. DMFT is one of the most promising avenues for describing, predicting, and understanding strongly correlated materials. One of the crucial elements of every DMFT simulation is the impurity solver. In equilibrium, several solvers are available which satisfy important criteria like the usage of a controlled approximation, flexibility of parameter regions, and the ability to solve the impurity problem at low temperatures. In non-equilibrium setups, currently available solvers cannot satisfy all of the aforementioned properties. Examples of existing non-equilibrium solvers are the Non-Crossing Approximation (NCA), which does not have a fine-grained control parameter and is severely restricted to certain parameter regions, and Continuous-Time Quantum Monte Carlo (CTQMC), which has a dynamic sign problem or phase problem. In the present thesis, we develop a new impurity solver for non-equilibrium DMFT at zero temperature, modifying the Hamiltonian formalism at finite temperatures developed by Gramsch et al. The new solver employs Matrix Product States (MPS), which have been used successfully as solvers in equilibrium setups and also in non-equilibrium setups with trivial initial states in recent years. The MPS ansatz brings in all the desired properties mentioned above. It is a controlled approximation, in the sense that one can increase the matrix dimensions involved and get a more accurate result. As long as the required matrix dimensions stay low, one can freely change the parameters of the Hamiltonian. The solver is formulated directly at zero temperature. While large matrix dimensions may pose a problem in certain simulations, there is no sign problem.

An important non-equilibrium effect, with potential applications in solar cells, is impact ionization, where one photon can excite more than one electron by means of electron-electron scattering processes. In the second part of the thesis we investigate the 4×3 Hubbard model under the influence of a short laser pulse. Impact ionization has been observed for the Hubbard model, but only with the help of DMFT or similar methods, which all neglect spatial correlations. On a small lattice, it is possible to fully account for spatial correlations. We indeed observe impact ionization for suitably high photon energies, and Auger recombination for lower photon energies. We are also able to show that there is multiple photon absorption at high light intensity and we introduce a technique to study the individual time-evolution for different multiphoton contributions.

In the third part we simulate front dynamics of the one dimensional XY spin-model. The dynamics of spin chains have gained a recent surge in popularity as they can be experimentally realized with laser traps and have several other interesting properties, such as integrability of theoretical models. We investigate the behavior of a chain for several different initial states, such as a Jordan-Wigner excitation or a double domain wall. For the Jordan-Wigner excitation of the symmetry broken ground state we find what we call a hydrodynamical phase transition. The magnetization profile of the steady state and the entanglement entropy show a qualitatively different behavior above and below a certain critical magnetic field strength. For the double domain wall we find that the magnetization profile factorizes and can be related to a single domain wall.

Zusammenfassung

Durch die Entwicklung von neuen und verbesserten Methoden wurde die Erforschung von korrelierten Vielteilchensystemen im Nichtgleichgewicht in den letzten Jahren stark vorangetrieben. Ein Beispiel für ein solches System im Nichtgleichgewicht ist etwa ein Material unter Einfluss eines kurzen Laserpulses, oder eine plötzliche Veränderung von einem oder mehreren Parametern des Hubbard-Modells. Die vorliegende Arbeit besteht aus drei Teilen, erstens der Entwicklung eines neuen Nichtgleichgewichts Dynamical Mean Field Theory (DMFT, dynamische Molekularfeldtheorie) Solvers, der die Menge an untersuchbaren Problemen vergrößert, zweitens der Untersuchung von Lichtabsorptionen in einem kleinen Hubbardsystem, und drittens der Untersuchung der Frontdynamik eines Spin-Modells.

Im ersten Teil dieser Arbeit wird ein neuer sogenannter Impuritysolver (impurity = Störstelle) für Nichtgleichgewichts-DMFT eingeführt, welche eine der vielversprechendsten Ansätze ist, um die Materialeigenschaften von stark korrelierten Materialien zu beschreiben, zu verstehen und vorherzusagen. Der Impuritysolver ist einer der wichtigsten Bestandteile von DMFT, wobei für den Gleichtsgewichtsfall mehrere Solver verfügbar sind. Diese erfüllen mehrere wichtige Qualitätskriterien, wie die Nutzung einer kontrollierten Approximation, eine große Reichweite an untersuchbaren Paramtererbereichen, und die Möglichkeit, das Impurityproblem bei niedrigen Temperaturen zu lösen. Im Nichtgleichgewicht ist die Situation derzeit so, dass es keinen Solver gibt, der alle oben genannten Kriterien erfüllt. Als Beispiele für Nichtgleichgewichtssolver seien die Non-Crossing Approximation (NCA) und Continuous-Time Quantum Monte Carlo (CTQMC) genannt. Dabei hat NCA das Problem, dass es keinen guten Kontrollparameter für die Approximation besitzt, während CTQMC durch das dynamische Vorzeichenproblem geplagt wird. In der vorliegende Arbeit entwickeln wir einen Solver für Nichtgleichgewichts-DMFT und bauen dabei auf den Hamiltonschen Formalismus für endliche Temperaturen auf, der von Gramsch et al. vorgestellt wurde. Dieser neue Solver funktioniert mithilfe von Matrixproduktzuständen (MPS), die schon erfolgreich als Solver für Gleichgewichts-DMFT und Nichtgleichgewichts-DMFT mit trivialen Anfangszuständen in den letzen Jahren verwendet wurden. Die Methode der MPS liefert alle oben erwähnten gewünschten Qualitätskriterien eines Solvers. Es ist eine kontrollierte Approximation, in dem Sinne, dass die benutzten Matrixdimensionen vergrößert werden können um die Genauigkeit zu

erhöhen, und so lange diese klein genug bleiben, können die Parameter des Hamiltonoperators nach Belieben angepasst werden. Außerdem ist der Solver direkt für die Temperatur des absoluten Nullpunkts formuliert. Wenn man MPS verwendet, gibt es in der Simulation kein Vorzeichenproblem, jedoch könnten die benötigten Matrixdimensionen ein Problem darstellen, wenn diese zu groß werden und damit die benötigte Rechenleistung zu stark ansteigt.

Ein wichtiger Nichtgleichgewichtseffekt, der für Solarzellen relevant ist, ist Stoßionisation (impact ionization), bei der ein Photon mehr als ein Elektron anregen kann. Dies geschieht mithilfe von Elektron-Elektron Streuprozessen. Im zweiten Teil dieser Arbeit untersuchen wir ein 4×3 Hubbard-Model, das sich unter dem Einfluss eines kurzen Laserpulses befindet. Mithilfe von DMFT und ähnlichen Methoden wurde der Nachweis von Stoßionisation im Hubbard-Modell bereits erbracht. Ein Nachteil dieser Methoden ist, dass sie örtliche Korrelationen vernachlässigen. Dieser Nachteil kann umgangen werden, indem man nur ein kleines System simuliert, wo es möglich ist, alle Korrelationen in die Rechnung miteinzubeziehen. Wir können tatsächlich die Existenz von Stoßionisation auf dem kleinen Gitter nachweisen, wenn die Photonenenergie ausreichend groß ist. Bei niedrigen Photonenenergien beobachten wir den verwandten Effekt der Auger-Rekombination. Bei hohen Lichtintensitäten tritt die Absorption von mehreren Photonen auf. Außerdem führen wir eine Methode ein, die es ermöglicht, die Beträge und Zeitentwicklungen der verschieden Multiphotonenabsorptionen einzeln zu untersuchen.

Im dritten Teil der vorliegenden Arbeit analysieren wir die Frontdynamik des eindimensionalen XY-Spin-Modells. Durch die Tatsache, dass Spinketten mittels Laserfallen realisiert werden können und mehrere weitere interessanter theoretische Eigenschaften, wie zum Beispiel die Integrabilität dieser Modelle, wurden sie in den letzten Jahren ein immer populäreres Ziel von wissenschaftlichen Arbeiten. Für die vorliegende Arbeit untersuchen wir das Verhalten der XY-Kette bei verschiedenen Anfangszuständen, wie der Jordan-Wigner-Anregung oder der einer doppelten Domänenwand. Für den Fall einer Jordan-Wigner-Anregung des symmetriegebrochenen Grundzustandes entdecken wir einen Effekt, den wir als hydrodynamischen Phasenübergang bezeichnen. Bei diesem zeigen das Magnetisierungsprofil und die Von-Neumann-Entropie des sich einstellenden stationären Zustandes ein qualitativ unterschiedliches Verhalten, je nachdem ob die magnetische Feldstärke unter- oder oberhalb einer kritischen Feldstärke liegt. Bei der doppelten Domänenwand zeigt sich, dass das Magnetisierungsprofil faktorisiert und in das Profil einer einfachen Domänenwand übergeführt werden kann.

Contents

Preface

1 Introduction

This thesis is separated into three main parts. The first part is about a new non-equilibrium Dynamical Mean Field solver based on Matrix Product States, formulated to work directly at zero temperature, without the need of an analytic continuation, and without any sign problem. In the second part we analyze a small Hubbard model under the influence of a short laser pulse, taking spatial correlations fully into account. The third part is about front dynamics of the XY model.

One of the main goals of theoretical solid state physics is to do *ab initio* calculations. This means we want to start from the full Hamiltonian and correctly understand material properties of elements and material compounds without the use of parameters obtained from experiments. The Hamiltonian of the electrons in a many body system is given by:

$$H = -\sum_i \frac{\hbar^2 \nabla_i^2}{2m_e} + \sum_{i \neq j} \frac{e^2}{8\pi\epsilon_0 \left|x_i - x_j\right|} + V(x_1, x_2, \dots) \tag{1}$$

From here on, we will use atomic units ($\hbar = e = m_e = (4\pi\epsilon_0)^{-1} = 1$). An important area of research here is Density Functional Theory[1] (DFT), which has been successfully used to predict material properties in many cases. With DFT one maps the Hamiltonian to a set of non-interacting particles in so-called Kohn-Sham orbitals, which are easier to self-consistently solve than the full many body Hamiltonian. This mapping is in principle exact, though the knowledge of the exact potential in the Kohn-Sham orbitals would involve solving the full many body Hamiltonian, thus there is a need of approximations here. Further improvements are possible by extracting a Hubbard-type model[2–4] from the DFT results, the simplest case of which is described below. From there, there are several routes one can take. One possibility is to solve the Hubbard-type model with with Dynamical Mean Field Theory[5–8] (DMFT). Note that these steps are not isolated and need to be solved in a self-consistent manner in a realistic material calculation, meaning that one uses the results from DMFT and plugs them back into DFT and so on, until convergence is reached. This long self-consistent loop is the state of the art for modern ab initio material calculations. Another approach is to reduce the Hubbard-type model until one reaches a model where a solution or approximate solution can be found. In the simplest case, only a hopping term (kinetic energy) and an on-site repulsion (potential energy) remain. The Hubbard model has become the basic model to understand the interplay of kinetic and potential energy terms in many-body systems, with applications for example in understanding ferromagnetism[9], superconductivity[10], and metal-insulator transitions[11]. After over half a century, the Hubbard model is still a hot topic of research.

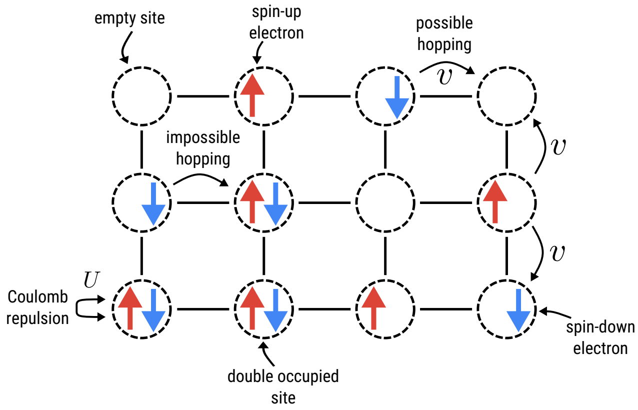

Figure 1. The Hubbard model with nearest-neighbor hopping.

> **Definition 1: Hubbard model**
>
> $$H = -v \sum_{\langle i,j\rangle,s} c^\dagger_{i,s} c_{j,s} + c^\dagger_{j,s} c_{j,s} + U \sum_i \left(n_{i,\uparrow} - \frac{1}{2}\right)\left(n_{i,\downarrow} - \frac{1}{2}\right) - \mu \sum_{i,s} n_{i,s} \qquad (2)$$

The Hubbard model is defined in Def. (1) Usually the hopping amplitude is denoted by t. We will use v here because t is used for time, and will call U the Coulomb repulsion or interaction, μ is the chemical potential, and s is the spin, $s \in \{\uparrow, \downarrow\}$. The c_i and $c_i^\dagger$ are the electron annihilation and creation operators with the anticommutating relationship:

$$\{c_{i,s}, c_{j,s'}\} = c_{i,s}\, c_{j,s'} + c_{j,s'}\, c_{i,s} = 0 \tag{3}$$

$$\{c^{\dagger}_{i,s}, c^{\dagger}_{j,s'}\} = 0 \tag{4}$$

$$\{c_{i,s}, c^{\dagger}_{j,s'}\} = \delta_{i,j}\, \delta_{s,s'} \tag{5}$$

$$n_{i,s} = c^{\dagger}_{i,s}\, c_{i,s} \tag{6}$$

Even though the Hubbard model is a very simplified version of the full many body Hamiltonian, an analytic solution for the thermodynamic limit is yet to be found, except in one dimension, where the Hubbard model has been solved by the Bethe ansatz[12,13]. With *solution*, we mean the computation of the eigenstates of the system or at least the quasi-particle spectrum, where quasi-particles are one-particle excited states of the ground state[14]. The spectrum can be calculated from the retarded Green function:

$$G_k(t) = -i\, \theta(t)\, \left(\left\langle c_k(t)\, c^{\dagger}_k \right\rangle + \left\langle c^{\dagger}_k\, c_k(t) \right\rangle\right) \tag{7}$$

The Green function in itself is an interesting quantity because it is closely connected to experiment via Photo Emission Spectroscopy (PES)[15,16] and X-ray Absorption Spectroscopy (XAS)[17]. Unfortunately, without any simplifications or clever tricks that are only possible in certain situations, the Green function is mostly as hard to compute exactly as the diagonalization of the Hamiltonian. Probably the simplest workaround to solve this problem is to neglect the electron-electron interaction in the full many-body Hamiltonian, amounting to setting the Coulomb repulsion U to zero in the Hubbard model. This approximation is called free electron approximation and works surprisingly well for some materials[18]. A better approximation can be obtained by perturbation theory[19–22], where one does an expansion of the Green function (or other desired quantities) with respect to one of the Hamiltonian parameters and can often obtain good results, depending on the investigated parameter values. However, there is a class of materials called strongly correlated where these approaches predict qualitatively wrong material properties, e.g. telling us that a material should be a metal while experiments show it to be insulator. This remains a problem for a number of approaches including the free electron approximation, static mean field calculations, perturbation theory in the Coulomb repulsion U or the hopping amplitude v, or Density Functional Theory[23]. To correctly predict and understand material properties of strongly correlated materials one simply needs to account for both the Coulomb repulsion and the hopping amplitude.

For small system sizes it is possible to calculate the properties of the Hubbard model with Exact Diagonalization (ED) or Lanczos-based methods[24]. Although these methods are exact and can fully account for spatial correlations, at the time of this thesis this fails at about 15-20+ lattice sites at half filling, depending on the employed computer architecture, because of exponential growth of the Hilbert space. Another important method to gain information from the many body Hamiltonian is Quantum Monte Carlo[25] (QMC). The static[26] and dynamic[27–29] properties of large one-dimensional systems are accessible[30] with Matrix Product State (MPS) based methods, even in the one-dimensional thermodynamic limit[31].

With DMFT it is possible to approximately solve the Hubbard model, neglecting spatial correlations but keeping temporal correlations, by mapping the Hubbard model to the Anderson Impurity Model[32,33], for which the simplest case is shown below. The mapping from the Hubbard model is exact in the limits of $U = 0$, $U = \infty$, and infinite dimension. Although the mapping is only exact in these cases, the combination of DFT and DMFT can be used to reliably predict and understand properties of strongly correlated materials[6,7,34,35].

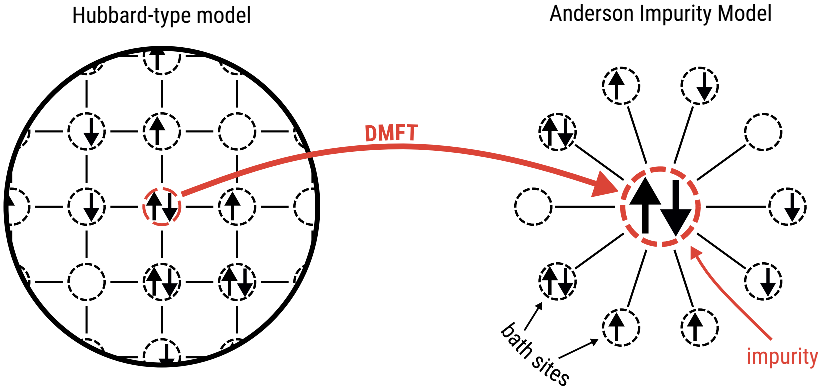

Figure 2. With DMFT the Hubbard model gets mapped to the Anderson impurity model.

Definition 2: Anderson Impurity Model (AIM)

$$H = H_{imp} + H_{bath} + H_{hyb} \tag{8}$$

$$H_{imp} = U\left(n_{0,\uparrow} - \frac{1}{2}\right)\left(n_{0,\downarrow} - \frac{1}{2}\right) - \mu\, n_{0,s} \tag{9}$$

$$H_{bath} = \sum_{p,s} \left(\epsilon_{p,s} - \mu\right) n_{p,s} \tag{10}$$

$$H_{hyb} = \sum_{p,s} V_{p,s}(t)\, c^{\dagger}_{0,s} c_{p,s} \, + \, V^{*}_{p,s}(t)\, c^{\dagger}_{p,s} c_{0,s} \tag{11}$$

0 *is the lattice site of the impurity.*

If one is interested only in static properties, the hopping amplitudes to the bath sites $V_{p,s}$ are time-independent. So, instead of solving the Hubbard model, one must solve the Anderson Impurity model, which is still not an easy task. In the context of DMFT, solving means computing the one-particle impurity Green function $G(t)$. With the approximation of a local self-energy one can use DMFT to predict properties of real three-dimensional materials and it is possible to qualitatively and quantitatively predict properties of strongly correlated materials (see e.g. Refs. 6, 36–38). To solve the impurity problem there are a number of readily available solvers, including Continuous-Time Quantum Monte Carlo (CTQMC)[39], Numerical Renormalization Group (NRG)[40], and recently developed multi-orbital MPS-based methods[41].

DMFT is mostly employed to answer questions about the static properties of materials with a constant Hamiltonian. However, it is also possible to predict the behavior of systems under a time-dependent Hamiltonian, by using a non-equilibrium version of DMFT[42]. This is relevant for example for computing the absorbed energy of a strongly correlated material when it is hit by a short laser pulse, where the pulse is approximated with a Peierls phase[43], amounting to multiplying the hopping amplitude by a time-dependent complex phase. The most important component of the DMFT framework is the impurity solver which computes the Green function of the Anderson Impurity Model. In equilibrium, the most used solver is CTQMC which can be extended to non-equilibrium setups[42] but has the disadvantage of being hindered by a sign problem, related to to the complex nature of e^{-itH}. It is known that there probably will never be a general solution to the sign problem[44], though in equilibrium one can do basis transformations to reduce it. In non-equilibrium there is no workaround for the so-called dynamic sign problem, although it can be alleviated[45]. To circumvent the dynamic sign problem, the Non-Crossing Approximation (NCA) or its generalizations[46] have been used to solve the non-equilibrium impurity problem. Although NCA can reach long simulation times, it has the problem that it is not a controlled approximation and it takes a great deal of experience to interpret the validity of the results. Therefore, a new impurity solver for non-equilibrium DMFT would be helpful. Other relevant methods that should be mentioned are the Configuration Interaction[47] (CI) method, the inchworm method[45], and the Auxiliary Master Equation Approach[48] (AMEA).

For the present thesis we solve the non-equilibrium impurity problem with a non-trivial initial state at zero temperature. To this end, we modify the usually used L-shaped Kadanoff-Baym contour[42] into a two-dimensional real time contour and show that it is possible to do non-equilibrium DMFT at zero temperature with correlated initial states. The new solver is Hamiltonian based and we extend the mapping method developed in Ref. 49 and Ref. 50 for its use. The method developed in Ref. 49 has already beed used with the MPS ansatz as an non-equilibrium impurity solver[51], but so far only trivial initial states and small bath sizes were simulated with this method. To test the new solver we replicate the simulations done in Ref. 52 and the subsequent Ref. 53 and furthermore extend the results by simulating initial states that have not been accessible before at zero temperature. Similar simulations have been performed in Ref. 46 at non-zero temperature as a proof of concept for the Non-Crossing Approximation and its generalizations.

As mentioned above, instead of trying to obtain quantitative ab initio results with DFT+DMFT (or other methods), one can simplify the full body Hamiltonian to a manageable model and find good qualitative results. In the second part of the present thesis we do this by investigating photoexcitations of strongly correlated systems. We compute the double occupancy as a function of time of the ground state of a 4×3 Hubbard model under the influence of a Peierls laser pulse[43,54–58]. The double occupancy is an important quantity here, because it is a measure for the number of free charge carriers, which in turn is an important quantity for many fields including solar power generation. Here, an important effect is impact ionization, where an excited electron with sufficient energy creates further excitations by electron-electron scattering, potentially allowing the production of solar cells with greater efficiency than the Shockley–Queisser limit[59,60]. Relevant studies were already performed with DMFT[55,61,62] and a Boltzmann approach[63] where spatial correlations are neglected[64]. To study whether such correlations suppress impact ionization[65] and the inverse process Auger recombination[65] we simulate this small system by exact diagonalization where the spatial correlations can be accounted for. A study, performed in parallel, that focuses on different lattice geometries and disorder, was done by Kauch et al.[58].

An ongoing area of non-equilibrium research concerns the behavior and properties of spin-models, which are connected to the Hubbard model in the limit of high interaction parameters U. The general class of integrable spin-models is interesting, because of the high number of conservations laws and the fact that they can be experimentally realized by ultra-cold atoms in laser traps[66]. In the course of this thesis the one dimensional XY-model with Jordan-Wigner, domain wall and spin flip initial states was investigated with the tool of Matrix Product States.

$$H = -\sum_{i=1}^{n-1} \frac{1+\gamma}{4}\,\sigma_i^x\,\sigma_{i+1}^x + \frac{1-\gamma}{4}\,\sigma_i^y\,\sigma_{i+1}^y - \frac{h}{2}\sum_i \sigma_i^z \tag{12}$$

Matrix Product States proved to be a viable and flexible tool to simulate such systems and to compare the results to other methods. The reason is that Matrix Product States are a general description of the underlying model and as long as the required matrix dimensions stay low, one can e.g. freely change the initial state of the investigated system and compute the observables and entanglement entropy as a function of time.

The structure of the thesis is as follows. In Subpart I.A, we review the currently used framework for non-equilibrium DMFT. There, in Sec. I.A.1 we provide some historic background on the development of non-equilibrium DMFT and how it relates to the present work, and we briefly review equilibrium DMFT in Sec. I.A.2. A review of the framework of non-equilibrium Green functions can be found in Sec. I.A.3. These are extensively used for non-equilibrium DMFT itself, which is presented in Sec. I.A.4.

In Subpart I.B we present the our adaptations of the formalism necessary to solve the problem of mapping to the Hamiltonian parameters of the Anderson Impurity Problem and for our approach to non-equilibrium DMFT at zero temperature. There, we introduce a new contour with two real time axes in Sec. I.B.1 and an effective contour, used to do the computation of the Green function, in Sec. I.B.2. The mapping to the Hamiltonian parameters of the Anderson Impurity Model from the hybridization function, which is based on the work of Ref. 49, is described in Sec. I.B.3. The computation of the momentum resolved Green function on the new contour is covered in Sec. I.B.2. After reviewing existing non-equilibrium solvers in Sec. I.B.5, we review MPS in Sec. I.B.6 and swap gates, used for time-evolution, in Sec. I.B.7. Section I.B.8 contains a summary of the new solver.

In Subpart I.C, we test the new solver by replicating the results of Ref. 52 and the subsequent Ref. 53, where quenches to the Hubbard model on the Bethe lattice have been simulated. We also extend these results by simulating interacting initial states, which was not possible at zero temperature before.

Part II contains a submitted publication regarding the Hubbard under the influence of a short laser pulse as mentioned above. In Part III we present two publications regarding the front dynamics of one dimensional spin systems.

2 List of Special Symbols and Abbreviations

Description	**Symbol**	**Introduced in/at**
equilibrium time	t_E	Def. (I.A.1)
non-equilibrium time	t_N	Def. (I.A.1)
imaginary time	τ	Def. (I.A.1)
time on contour	$\mathbf{t}$	Def. (I.A.1)
operator A in Schrödinger picture	$A_{\mathbf{t}}$	Def. (I.A.2)
L-shaped contour		Fig. I.A.1
contour with two real time axes		Fig. I.B.2
contour greater	$>_{\mathcal{C}}$	Def. (I.A.2)
contour Heaviside function	$\theta_{\mathcal{C}}$	Def. (I.A.2)
contour Dirac delta	$\delta_{\mathcal{C}}$	Def. (I.A.3)
contour ordering operator	$\mathcal{T}_{\mathcal{C}}$	Def. (I.A.2)
integral over contour	$\int_{\mathcal{C}}$	Def. (I.A.3)
convolution over contour	$*$	Def. (I.A.3)
inverse of F, so that $F * F^{-1} = F^{-1} * F = \delta_{\mathcal{C}}$	$F^{-1}(\mathbf{t}, \mathbf{t}')$	Def. (I.A.3)
greater non-equilibrium component	$> N$	Def. (I.A.5), Def. (I.B.9)
greater equilibrium component	$> E$	Def. (I.B.9)
lesser non-equilibrium component	$< N$	Def. (I.A.5), Def. (I.B.9)

lesser equilibrium component	$< E$	Def. (I.B.9)
right-mixing component	$\ulcorner$	Def. (I.A.5), Def. (I.B.9)
pre-right-mixing component	$\llcorner$	Def. (I.B.9)
left-mixing component	$\urcorner$	Def. (I.A.5), Def. (I.B.9)
pre-left-mixing component	$\lrcorner$	Def. (I.B.9)
Matsubara component	M	Def. (I.A.5)
retarded non-equilibrium component	RN	Def. (I.A.5), Def. (I.B.9)
retarded equilibrium component	RE	Def. (I.B.9)
advanced non-equilibrium component	AN	Def. (I.A.5), Def. (I.B.9)
advanced equilibrium component	AE	Def. (I.B.9)

Sign convention used for the Fourier transform and inverse Fourier transform:

$$\mathcal{F}[f](\omega) = f(\omega) = \int_{-\infty}^{\infty} e^{i\omega t_E} f(t_E)\ \mathrm{d}t_E$$

$$\mathcal{F}^{-1}[f](t_E) = f(t_E) = \frac{1}{2\,\pi}\int_{-\infty}^{\infty} e^{-i\omega t_E} f(\omega)\ \mathrm{d}\omega$$

We will generally use the same symbol for a function in ω-space and t_E-space but with different arguments ω and t_E.

There is no unique notation in various publications with respect to the different parts of the Hamiltonian of the Anderson Impurity Model. If not stated otherwise, we will use H_{imp}, H_{bath}, and H_{hyb} in the present thesis. For example, what we call H_{imp} here, is called H_{loc} or H_{int} in some publications. We will however use H_{loc} in some parts of the thesis, were it refers to the local part of some Hubbard-type Hamiltonian, which coincides with H_{imp} of the Anderson Impurity Model.

Part I

Non-Equilibrium Dynamical Mean Field Theory

I.1 Overview

In the first part of the thesis a new non-equilibrium Dynamical Mean Field Theory (DMFT) solver is introduced and tested on quenches in the Hubbard model on the Bethe lattice. The new solver works directly at zero temperature, does not need an analytic continuation, and can incorporate any parameter regime, including quenches from interacting ground states. As discussed in the introduction, the combination of Density Functional Theory (DFT) and DMFT is the state of the art for modern ab initio material calculations. In Sec. I.A.1 we provide some historic background on the development of non-equilibrium DMFT and how it relates to the present work. It is easier to understand non-equilibrium DMFT if one has an understanding of equilibrium DMFT first. There is a short review of equilibrium DMFT in Sec. I.A.2. In Sec. I.A.3, we present the framework of non-equilibrium Green functions, which are the basis for non-equilibrium DMFT introduced in Sec. I.A.4. The ansatz of non-equilibrium Green functions is modified in Sec. I.B.1 for the new solver. The main reason to modify this formalism is to provide a mapping from the hybridization function to the Hamiltonian parameters that works directly at zero temperature, which is presented in Sec. I.B.3 and extends the formalism introduced in Ref. 49 and Ref. 50. In Sec. I.B.1 a new contour is introduced which contains time-evolutions of time from $-\infty$ and ∞. In practice these time-evolutions cannot be performed to infinity and for the computation of the impurity Green functions it suffices to use an effective contour which is presented in Sec. I.B.2. For DMFT we need to be able to compute the momentum resolved Green function from the impurity Green function. While in equilibrium this is a simple computation in ω-space, in non-equilibrium one needs to solve an integral equation on the contour. We present a way to solve this equation in Sec. I.B.4. In Sec. I.B.5, there is an overview over the existing non-equilibrium solvers, before we shortly review Matrix Product States in Sec. I.B.6 and swap gates in Sec. I.B.7. The new solver is tested in Subpart I.C by replicating and extending the results of Ref. 52 and the following Ref. 53.

Subpart I.A

State of the Art

I.A.1 Development of Non-Equilibrium DMFT

This section serves as an short overview over the history of DMFT and non-equilibrium DMFT and how the first two parts of the present thesis are related to the field. An extensive history of DMFT can be found in Ref. 64. After the work in the early 1990s of Metzner et al.[32], Ohkawa[67], and Georges et al.[33] it was clear it is possible to self-consistently map the infinite dimensional Hubbard model to the Anderson Impurity Model, subject to the condition that the hopping amplitude is correctly scaled down as the dimensionality of the Hubbard model goes to infinity. A key insight was that in the limit of infinite dimensions the self-energy of the Hubbard model becomes local[64], i.e. is independent of the lattice sites and is only a function of ω in ω-space. An important feature of this mapping is, while the Anderson Impurity Model is still an interacting many body problem its local Green function is generally much easier to compute than its pendant of the Hubbard model. Further relevant insights with respect to the present thesis were provided in the early 2010s[68–70] where it was shown that it is possible to compute the spectral function of the Anderson Impurity Model using Matrix Product States and the Chebyshev expansion for up to two orbitals[70], or alternatively compute the Green function directly in the time-domain with Matrix Product States for up to two orbitals[69]. Later, it was shown that it is possible to directly compute the Green function with a modified MPS ansatz for three and more orbitals by Bauernfeind et al.[41,71], where so-called Fork Tensor Product States were introduced. There, instead of matrices tensors are arranged in a tree structure, better fitting the geometry of the Anderson Impurity Model, and swap gates[30,72], in combination with the Suzuki-Trotter decomposition[73] of the time-evolution operator, were used to efficiently compute the Green function. One of the main advantages of the Matrix Product and Fork Product approaches is that they allow the solution of the Impurity problem at zero temperature where the performed approximations are in a controlled manner, i.e. the errors stemming from their approximations (finite bond dimension, time step) can in principal be made arbitrary small in exchange for higher computational cost. This stands in contrast to e.g. perturbation theory where the error depends discontinuously on the included order of the Taylor expansion.

Meanwhile, in 2006, Freericks et al.[74,75] showed that it is possible to generalize the DMFT formalism to non-equilibrium setups, i.e. situations where the Hamiltonian of the lattice system is time-dependent. In the early stages of non-equilibrium DMFT primarily the Falicov-Kimball was investigated[76] as its Green function can be computed exactly[77–79]. Important results include the derivation of the momentum sum rules[80] and the theoretical connection of non-equilibrium DMFT to pump-probe experiments and photoemission spectroscopy by[81,82]. One of the most critical parts of every DMFT simulation is the Impurity solver and there the the weak[83] and strong[84] coupling expansion of CTQMC were translated to non-equilibrium, as well as the Non-Crossing Approximation (NCA) and its generalizations[46]. The latter, though being confined to high U parameter regions, have the advantage of reaching very long simulation times without the sign problem. A defining feature of CTQMC and NCA is that they do not need an explicit Hamiltonian of the Anderson Impurity model, because they are based on the effective action. A mapping from the action to time-dependent Anderson Impurity model Hamiltonian parameters was achieved in the in the early 2010s by Gramsch et al.[49], paving the way to use Hamiltonian based solvers. This mapping was subsequently used by Wolf et al. to solve non-equilibrium DMFT with Matrix Product States[51], for relatively small bath sites and a product-like initial state of the lattice system[85].

Other methods that are not related to this work but are relevant to the field include the Configuration Interaction[47] (CI) method, which can be used as a solver for DMFT[86], the inchworm method[45], a sampling method alleviating the dynamical sign problem, and the Auxiliary Master Equation Approach[48] (AMEA), where the impurity problem is mapped to an auxiliary open quantum system and steady states can be investigated. A relevant package for non-equilibrium computations named NESSi has also recently been published[87].

In the present thesis we build on and extend the work of Gramsch et al.[49] to derive a mapping for the Hamiltonian parameters at $T = 0$ and use swap gates in combination with the time-evolution operator as introduced by Bauernfeind et al.[41] to build an Impurity solver for non-equilibrium DMFT that works with correlated initial states at $T = 0$. As a work of reference we use Refs. 52 and 53 by Eckstein et al., where a quench in the interaction parameter U and $T = 0$ was simulated. In Refs. 52 and 53 the simulation of the system at $T = 0$ was possible as the authors used the ground state of $U = 0$ where the self-energy vanishes and this simplifies the computation.

I.A.2 Equilibrium Dynamical Mean Field Theory

The Hubbard model has only been solved exactly in one dimension[12,13]. As we would like to model a real material, one must use approximations to get the properties of the Hubbard model in two or three dimensions. One of the more successful methods is Dynamical Mean Field Theory (DMFT)[5,6,32,33,64]. With DMFT the Hubbard model gets approximately mapped to an Anderson Impurity Model (AIM), which is in general still a fully interacting model but easier to solve than the full Hubbard model. In general, this mapping is not exact, because it assumes a local self-energy of the Hubbard model. Despite this approximation, DMFT (in combination with Density Functional Theory) is one of the most successful methods, when it comes to predicting and understanding the properties of strongly correlated materials[6,34,88].

The central quantity of DMFT is the retarded single particle Green function. In the literature, equilibrium DMFT is usually derived on the imaginary axis[64]. We will stay on the real axis here, where the concepts stay the same and treat the case of zero temperature, for future reference later in this thesis.

$$G_k(t) = -i\,\theta(t)\,\left(\left\langle\psi\,\middle|\,c_k(t)c_k^\dagger\,\middle|\,\psi\right\rangle + \left\langle\psi\,\middle|\,c_k^\dagger c_k(t)\,\middle|\,\psi\right\rangle\right) \tag{I.A.1}$$

Here k numbers the eigenstate of the free ($U = 0$) Hamiltonian, and $|\psi\rangle$ is its ground state (assumed to be unique). Usually, the retarded Green function is marked with a superscript R. For the sake of brevity, we will omit this in this section. The Green function is interesting because several important properties like the density of states or the optical conductivity can be derived from it. Thus, computing $G_k(t)$ is one of the most important tasks in many body physics, albeit not an easy one. In the context of DMFT, the Green function is the central quantity because the mapping to the AIM is done so that the Hubbard model and the AIM have the same Green function. Equation (I.A.1) treats the case $T = 0$. When the task is to predict properties of real material compounds, one can formulate this for finite temperatures with the density matrix formalism. This is discussed in later chapters. To examine the inner workings of DMFT we start by taking a look at the Green function of the non-interacting

Hamiltonian ($U = 0$), $G_{0,k}(t)$.

$$G_{0,k}(t) = -i\,\theta(t)\,\Big(\Big\langle\psi_0\,\Big|\,c_k(t)c_k^\dagger\,\Big|\,\psi_0\Big\rangle + \Big\langle\psi_0\,\Big|\,c_k^\dagger c_k(t)\,\Big|\,\psi_0\Big\rangle\Big) \tag{I.A.2}$$

In contrast to $U \neq 0$, this Green function is easy obtained, and after a Fourier transform we get:

$$G_{0,k}(\omega) = \int_{-\infty}^{\infty} e^{i\omega t}\,G_{0,k}(t)\;\mathrm{d}t = \frac{1}{\omega - \epsilon_k + \mu + i0^+} \tag{I.A.3}$$

0^+ is an infinitesimal small number introduced to solve the integral of the Fourier transform[89]. The ansatz for the interacting case is to introduce the self-energy $\Sigma(\omega, k)$ (see Ref. 64).

$$G_k(\omega) = \frac{1}{\omega - \epsilon_k + \mu - \Sigma(\omega,k) + i0^+} \tag{I.A.4}$$

$$\Rightarrow\;\; G_k(\omega)^{-1} = G_{0,k}(\omega)^{-1} - \Sigma(\omega,k) \tag{I.A.5}$$

$$\Rightarrow\;\; G_k(\omega) = G_{0,k}(\omega) + G_{0,k}(\omega)\,\Sigma(\omega,k)\,G_k(\omega) = G_{0,k}(\omega) + G_k(\omega)\,\Sigma(\omega,k)\,G_{0,k}(\omega) \tag{I.A.6}$$

The last line is known as the Dyson equation. Note that this is only a definition and transforms the problem of computing $G_k(\omega)$ to computing $\Sigma(\omega, k)$.

On the other hand, it can be shown that the Green function of the Anderson Impurity model at the impurity G_{IMP} can be written as follows[5,64]:

$$-i\,\omega\,G_{\mathrm{IMP}}(\omega) = i\,\mu\,G_{\mathrm{IMP}}(\omega) - i\,\Sigma_{\mathrm{IMP}}(\omega)\,G_{\mathrm{IMP}}(\omega) - i\,\Delta(\omega)\,G_{\mathrm{IMP}}(\omega) - i \tag{I.A.7}$$

$$\Rightarrow\quad G_{\mathrm{IMP}}(\omega) = \frac{1}{\omega + \mu - \Delta(\omega) - \Sigma_{\mathrm{IMP}}(\omega)} \tag{I.A.8}$$

$$\Delta(\omega) = \sum_p \frac{|V_p|^2}{\omega - \epsilon_p + \mu + i0^+} \tag{I.A.9}$$

Where Δ is the so-called hybridization function, and the self-energy of the impurity $\Sigma_{\mathrm{IMP}}(\omega)$ is defined similarly to $\Sigma(\omega, k)$, meaning that it is zero if $U = 0$. The DMFT approximation is that $\Sigma(\omega, k) \approx \Sigma_{\mathrm{IMP}}(\omega)$. As this expression is independent of k, it amounts to assuming a local self-energy of the lattice model $\Sigma_{ij}(\omega) = \Sigma_{\mathrm{IMP}}(\omega)\,\delta_{ij}$.

It can be shown that the self-energy can be computed from the lattice Green function[5,64]:

$$G(\omega)^{-1} = \omega + \mu - \Sigma(\omega) - \Delta(\omega) \tag{I.A.10}$$

$$\mathcal{G}_0(\omega)^{-1} = \omega + \mu - \Delta(\omega) \tag{I.A.11}$$

$$\Sigma(\omega) = \mathcal{G}_0(\omega)^{-1} - G_{\text{loc}}(\omega)^{-1} \tag{I.A.12}$$

$$G_{\text{loc}}(\omega) = \frac{1}{N_k} \sum_k G_k(\omega) \underbrace{e^{-ik0}}_{=1} \qquad \left(\tfrac{1}{N_k} \textstyle\sum_k = 1\right) \tag{I.A.13}$$

Equation (I.A.12) follows directly from Eqs. (I.A.10) and (I.A.11). $\mathcal{G}_0(\omega)$ is called Weiss effective field and plays the same role as the effective magnetic field plays in classical mean field theory. $G_{\text{loc}}(\omega)$ is the inverse spatial Fourier transformation of G_k for equal lattice sites of the creation and annihilation operators and called local Green function. Because we investigate translational invariant systems, this quantity is equal to the lattice Green function. All of the equations above form a set of coupled non-linear equations that need to be solved simultaneously. As this is not possible in general, the ansatz is to solve them iteratively and self-consistently. The resulting solution scheme is depicted in Alg. (I.A.1).

As mentioned above, the only approximation is a k-independent self-energy. This means DMFT is exact in the limits $U = 0$, $U \to \infty$, and in the case of infinite dimensions[64]. This gives an intuitive explanation why DMFT works so well for real materials.

Algorithm I.A.1: Equilibrium Dynamical Mean Field Theory

The superscript (n) *denotes the iteration number.*

0. *Start with initial guess for* $\Delta^{(0)}(\omega)$*. Set* $(n) \longrightarrow (0)$*.*
   Most of the time, if no good guess is available and the solution is suspected to be metallic one can start from the semicircular density of states.

1. *From* $\Delta^{(n)}(\omega)$ *compute the bath parameters* $V_l^{(n)}, \epsilon_l^{(n)}$*.*

2. *Solve impurity problem, i.e. compute impurity Green function* $G_{IMP}^{(n)}(\omega)$*.*
   If $\left|G_{IMP}^{(n)}(\omega) - G_{IMP}^{(n-1)}(\omega)\right|$ *is sufficiently small the algorithm is converged.*

3. *Compute* $\Sigma_{IMP}^{(n)}(\omega) = G_{0,IMP}^{(n)}(\omega)^{-1} - G_{IMP}^{(n)}(\omega)^{-1}$*.*
   Now, the DMFT approximation is $\Sigma^{(n)}(\omega) = \Sigma_{IMP}^{(n)}(\omega)$*.*

4. *Compute the local Green function* $G^{(n)}_{loc}(\omega) = \frac{1}{N_k}\sum_k G^{(n)}_k(\omega) = \frac{1}{N_k}\sum_k \left(G^{(n)}_{0,k}(\omega)^{-1} - \Sigma^{(n)}(\omega)\right)^{-1}$.
5. *Compute the Weiss effective field* $\mathcal{G}^{(n)}_0(\omega) = \left(G^{(n)}_{loc}(\omega)^{-1} + \Sigma^{(n)}(\omega)\right)^{-1}$.
6. *Compute the hybridization function of the next iteration* $\Delta^{(n+1)}(\omega) = \omega + \mu - \mathcal{G}^{(n)}_0(\omega)^{-1}$.
7. *Go to step 1 and start a new iteration* $(n) \longrightarrow (n+1)$.

If the algorithm is done on the Bethe lattice one can skip steps $3-6$ *and instead do:* $\Delta^{(n+1)}(\omega) = \left|v^2\right| G^{(n)}_{IMP}(\omega)$.

I.A.3 Non-Equilibrium Green Functions

The DMFT algorithm as described above (Alg. (I.A.1)) only works for situations where the Hamiltonian of the lattice system is constant with respect to time. This is sufficient to predict the properties of real world materials in equilibrium[64]. On the other hand, it is desirable to analyze setups where a time-dependent Hamiltonian is needed, e.g. when simulating the effect of a laser pulse on a material[55]. A laser pulse can be simulated by introducing a time-dependent hopping amplitude $v(t)$ in the lattice model (Peierls phase[43]). To this end, a modification of the equilibrium DMFT formalism is necessary. As equilibrium DMFT heavily relies on the use of ω-space of the Green functions we also need to extend the definition of the Green function, because the Fourier space is of limited use in a time-dependent setting. In this section we take a look at the framework of non-equilibrium Green functions and follow Ref. 42. First, we will review the usual formalism used for $T \neq 0$ and then will introduce the extensions used to simulate systems at $T = 0$ in another section. From here on, when we talk about ”time” we will have to distinguish between three different concepts of time.

Definition I.A.1: Equilibrium time, imaginary time, and non-equilibrium time

Let $H(t)$ be the time-dependent Hamiltonian of our system. The Hamiltonian is assumed to be constant for $t \leq 0$. The equilibrium time will be denoted as t_E, the non-equilibrium time as t_N, and the imaginary time as τ. They are defined over different time-evolutions, as can be seen in the Heisenberg picture of a generic operator O.

$$\begin{aligned} &\textit{equilibrium time} && O(t_E) = e^{i\,H(0)\,t_E}\, O\, e^{-i\,H(0)\,t_E} && \text{(I.A.14)} \\ &\textit{imaginary time} && O(\tau) = e^{H(0)\,\tau}\, O\, e^{-H(0)\,\tau} && \text{(I.A.15)} \\ &\textit{non-equilibrium time} && O(t_N) = \left(\mathcal{T}\, e^{i\int_0^{t_N} H(\bar{t})\,\mathrm{d}\bar{t}}\right)\, O\, \left(\mathcal{T}\, e^{-i\int_0^{t_N} H(\bar{t})\,\mathrm{d}\bar{t}}\right) && \text{(I.A.16)} \end{aligned}$$

where $\mathcal{T}$ is the time-ordering operator. If not stated otherwise, the bare letter t denotes a time, that is either one of those three time concepts. The boldfaced time $\mathbf{t}$ is defined as the tuple containing positional information and a numerical value:

$$\mathbf{t} = (\mathcal{C}_i, t) \tag{I.A.17}$$

where $\mathcal{C}_i$ is the i-th element of the contour $\mathcal{C}$ we integrate over (as defined below).

I.A.3.1 Finite Temperature

This subsection of the finite temperature Green functions follows Ref. 42, with adapted notation. In the context of non-equilibrium DMFT we are interested in expectation values of the form

$$\langle A(t_N)\, B(t'_N)\rangle = \mathrm{tr}\left(\rho\, A(t_N)\, B(t'_N)\right) \tag{I.A.18}$$

$$= \frac{\mathrm{tr}\left(e^{-\beta\, H(0)} A(t_N)\, B(t'_N)\right)}{\mathrm{tr}\left(e^{-\beta\, H(0)}\right)} \tag{I.A.19}$$

Here, $A(t_N)$ and $B(t'_N)$ are in the Heisenberg picture:

$$A(t_N) = \left(\mathcal{T} e^{i\int_0^{t_N} H(\bar{t})\,\mathrm{d}\bar{t}}\right)\, A\, \left(\mathcal{T} e^{-i\int_0^{t_N} H(\bar{t})\,\mathrm{d}\bar{t}}\right) \tag{I.A.20}$$

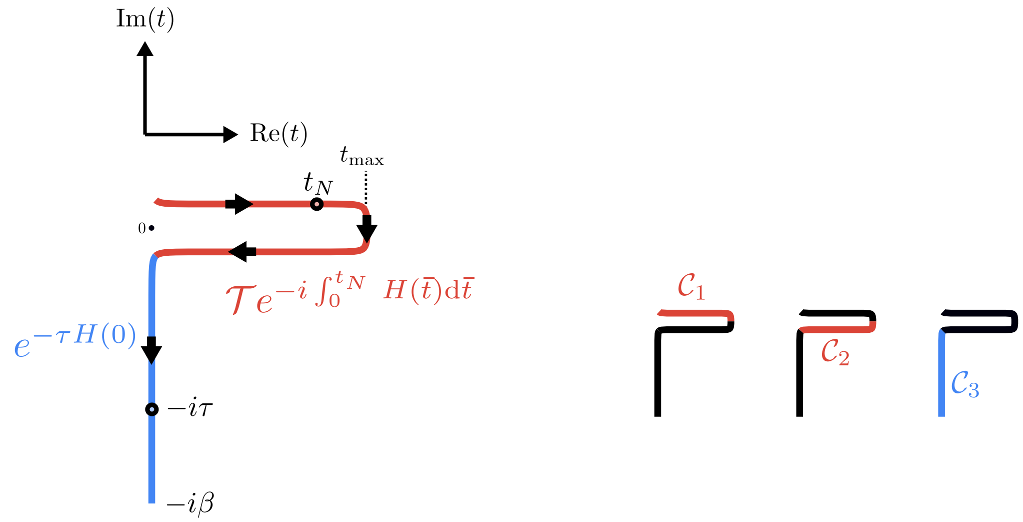

Figure I.A.1. The L-shaped contour of the Kadanoff-Baym formalism.

$H(0)$ is the Hamiltonian at time $t_N \leq 0$. The idea is to rewrite Eq. (I.A.19), so we can define a non-equilibrium Green function that lets us derive a non-equilibrium DMFT formalism that is formally equivalent to equilibrium DMFT. To this end, we need some further definitions.

Definition I.A.2: Contour notation

$$A_{\mathbf{t}} = \textit{Operator } A \textit{ in the Schrödinger picture.} \tag{I.A.21}$$

Is still subject to contour ordering $\mathcal{T}_{\mathcal{C}}$ as defined below.

$$\mathbf{t} >_{\mathcal{C}} \mathbf{t}' = \begin{cases} \textit{true} & \textit{if } \mathbf{t} \textit{ comes after } \mathbf{t}' \textit{ on the contour (Fig. I.A.1)} \\ \textit{false} & \textit{otherwise} \end{cases} \tag{I.A.22}$$

$$\theta_{\mathcal{C}}(\mathbf{t}, \mathbf{t}') = \begin{cases} 1 & \textit{if } \mathbf{t} >_{\mathcal{C}} \mathbf{t}' \\ 0 & \textit{otherwise} \end{cases} \tag{I.A.23}$$

$$\mathcal{T}_{\mathcal{C}}\, A_{\mathbf{t}}\, B_{\mathbf{t}'} = \begin{cases} A_{\mathbf{t}}\, B_{\mathbf{t}'} & \textit{if } \mathbf{t} >_{\mathcal{C}} \mathbf{t}' \\ \pm\, B_{\mathbf{t}'}\, A_{\mathbf{t}} & \textit{if } \mathbf{t}' >_{\mathcal{C}} \mathbf{t} \end{cases} \tag{I.A.24}$$

$$\overline{\mathcal{T}}_{\mathcal{C}}\, A_{\mathbf{t}}\, B_{\mathbf{t}'} = \begin{cases} \pm\, B_{\mathbf{t}'}\, A_{\mathbf{t}} & \textit{if } \mathbf{t} >_{\mathcal{C}} \mathbf{t}' \\ A_{\mathbf{t}}\, B_{\mathbf{t}'} & \textit{if } \mathbf{t}' >_{\mathcal{C}} \mathbf{t} \end{cases} \tag{I.A.25}$$

$$\tag{I.A.26}$$

where we take the minus sign if A and B are fermionic.

Definition I.A.3: Contour calculus notation

$$\int_{\mathcal{C}} F(\bar{\mathbf{t}})\ \mathrm{d}\bar{\mathbf{t}} = \overbrace{\int_0^{t_{max}} F(\bar{t}_N)\ \mathrm{d}\bar{t}_N}^{\bar{t}_N \in \mathcal{C}_1} + \overbrace{\int_{t_{max}}^{0} F(\bar{t}_N)\ \mathrm{d}\bar{t}_N}^{\bar{t}_N \in \mathcal{C}_2} - i \overbrace{\int_0^{\beta} F(\bar{\tau})\ \mathrm{d}\bar{\tau}}^{\bar{\tau} \in \mathcal{C}_3} \tag{I.A.27}$$

$$(F * G)(\mathbf{t}, \mathbf{t}') = \int_{\mathcal{C}} F(\mathbf{t}, \bar{\mathbf{t}})\, G(\bar{\mathbf{t}}, \mathbf{t}')\ \mathrm{d}\bar{\mathbf{t}}\,,\ \textit{convolution} \tag{I.A.28}$$

$$\frac{\partial F(\mathbf{t})}{\partial \mathbf{t}} = \lim_{h \to 0} \frac{F(\mathbf{t} + h) - F(\mathbf{t} - h)}{2h} \tag{I.A.29}$$

$$\delta_{\mathcal{C}}(\mathbf{t}, \mathbf{t}') = \frac{\partial \theta_{\mathcal{C}}(\mathbf{t}, \mathbf{t}')}{\partial \mathbf{t}} = -\frac{\partial \theta_{\mathcal{C}}(\mathbf{t}, \mathbf{t}')}{\partial \mathbf{t}'} \tag{I.A.30}$$

$$(\delta_{\mathcal{C}} * F)(\mathbf{t}, \mathbf{t}') = (F * \delta_{\mathcal{C}})(\mathbf{t}, \mathbf{t}') = F(\mathbf{t}, \mathbf{t}') \tag{I.A.31}$$

$$(F^{-1} * F)(\mathbf{t}, \mathbf{t}') = (F * F^{-1})(\mathbf{t}, \mathbf{t}') = \delta_{\mathcal{C}}(\mathbf{t}, \mathbf{t}') \tag{I.A.32}$$

> *In Eq.* (I.A.29) *the sum* $\mathbf{t} + h$ *is not an ordinary sum and to be interpreted as move* h *forward on the contour from position* $\mathbf{t}$*. In the same manner* $\mathbf{t} - h$ *is to be interpreted as move* h *backwards on the contour from position* $\mathbf{t}$*.*

With these tools it is possible to generalize Eq. (I.A.19) into the contour-ordered expectation value. This generalization is indicated by the action S in the subscript.

$$\langle A(\mathbf{t})\, B(\mathbf{t}')\rangle_S = \frac{\mathrm{tr}\,(\mathcal{T}_{\mathcal{C}}\, e^{S}\, A_{\mathbf{t}}\, B_{\mathbf{t}'})}{\mathrm{tr}\,(\mathcal{T}_{\mathcal{C}}\, e^{S})} \qquad S = -i \int_{\mathcal{C}} H(\bar{\mathbf{t}})\ \mathrm{d}\bar{\mathbf{t}} \tag{I.A.33}$$

With the ordinary time-evolution operator

$$\mathcal{U}(t,t') = \begin{cases} \mathcal{T} e^{-i\int_{t'}^{t} H(\bar{t})\,\mathrm{d}\bar{t}} & \text{if } t > t' \\ \overline{\mathcal{T}} e^{i\int_{t}^{t'} H(\bar{t})\,\mathrm{d}\bar{t}} & \text{otherwise} \end{cases} \tag{I.A.34}$$

it is possible to sketch a proof, that all information of Eq. (I.A.19) is contained in Eq. (I.A.33). To this end, we investigate the special case when A_{t_N} is located on part $\mathcal{C}_2$ of the contour and $B_{t'_N}$ is located on part $\mathcal{C}_1$ of the contour.

$$\mathcal{T}_{\mathcal{C}}\, e^{-i\int_{\mathcal{C}} H(\bar{t})\,\mathrm{d}\bar{t}}\ \overbrace{A_{t_N}}^{\mathcal{C}_2}\ \overbrace{B_{t'_N}}^{\mathcal{C}_1} = \mathcal{T}_{\mathcal{C}}\ \overbrace{\mathcal{U}(-i\beta,0)}^{\mathcal{C}_3}\ \overbrace{\mathcal{U}(0,t_{\max})}^{\mathcal{C}_2}\ \overbrace{\mathcal{U}(t_{\max},0)}^{\mathcal{C}_1}\ \overbrace{A_{t_N}}^{\mathcal{C}_2}\ \overbrace{B_{t'_N}}^{\mathcal{C}_1} \tag{I.A.35}$$

$$= U(-i\beta,0)\,\mathcal{U}(0,t_N)\, A\,\mathcal{U}(t_N,t'_N)\, B\,\mathcal{U}(t'_N,0) \tag{I.A.36}$$

$$= U(-i\beta,0)\,\mathcal{U}(0,t_N)\, A\,\mathcal{U}(t_N,0)\, U(0,t'_N)\, B\,\mathcal{U}(t'_N,0) \tag{I.A.37}$$

$$= e^{-\beta H(0)}\, A(t_N)\, B(t'_N) \tag{I.A.38}$$

In the last line, $A(t_N)$ and $B(t'_N)$ are in the Heisenberg picture again. In addition to Eq. (I.A.19), the contour ordered version of the expectation value also contains the expectation value $\langle B(t'_N)\, A(t_N)\rangle$, because the operators can switch places if we place them on the contour accordingly (Fig. I.A.2). Now we have all the necessary basics to define the central quantity of non-equilibrium DMFT.

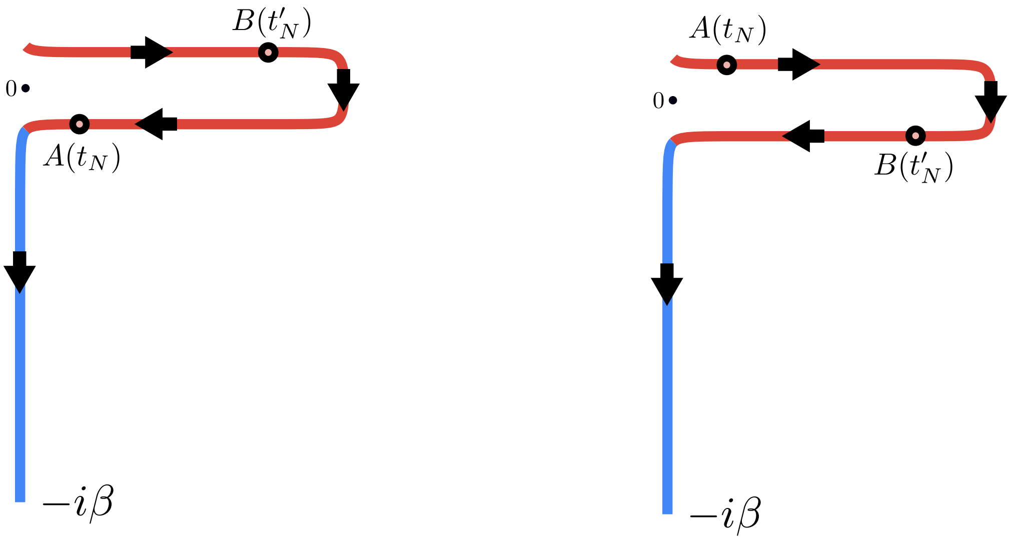

Figure I.A.2. Sketch of the difference between $\langle \overbrace{A(t_N)}^{\mathcal{C}_2}\ \overbrace{B(t'_N)}^{\mathcal{C}_1} \rangle_S$ (left) and $\langle \overbrace{A(t_N)}^{\mathcal{C}_1}\ \overbrace{B(t'_N)}^{\mathcal{C}_2} \rangle_S$ (right). The numerical values of t_N and t'_N may be the same on the left and right hand side, but the expectation values are different, because of the contour-ordering.

Definition I.A.4: Contour-ordered Green function of the L-shaped contour

$$G(\mathbf{t}, \mathbf{t}') = -i \, \frac{\operatorname{tr}\left(\mathcal{T}_{\mathcal{C}}\, e^{S}\, c_{\mathbf{t}}\, c^{\dagger}_{\mathbf{t}'}\right)}{\operatorname{tr}\left(\mathcal{T}_{\mathcal{C}}\, e^{S}\right)} = -i \, \left\langle c(\mathbf{t})\, c^{\dagger}(\mathbf{t}')\right\rangle_S \tag{I.A.39}$$

where $S = -i \int_{\mathcal{C}} H(\bar{\mathbf{t}})\, \mathrm{d}\bar{\mathbf{t}}$.

As mentioned above the exact order of operators c and $c^\dagger$ depends on the position of their time arguments on the contour. Let $G_{ij}(\mathbf{t}, \mathbf{t}')$ be the Green function where $\mathbf{t} \in \mathcal{C}_i$ and $\mathbf{t}' \in \mathcal{C}_j$, and $i, j \in \{1, 2, 3\}$. It can be seen that the Green function has nine different components that are not totally independent of each other. Namely there are only four independent components.

$$G_{11}(t_N, t'_N) = \begin{cases} G_{12}(t_N, t'_N) & \text{if } t_N \leq t'_N \\ G_{21}(t_N, t'_N) & \text{otherwise} \end{cases} \qquad G_{22}(t_N, t'_N) = \begin{cases} G_{21}(t_N, t'_N) & \text{if } t_N < t'_N \\ G_{12}(t_N, t'_N) & \text{otherwise} \end{cases} \tag{I.A.40}$$

$$G_{23}(t_N, \tau) = G_{13}(t_N, \tau) \qquad G_{32}(\tau, t_N) = G_{31}(\tau, t_N) \tag{I.A.41}$$

$$G_{33}(\tau, \tau') = \begin{cases} G_{31}(\tau - \tau', 0) & \text{if } \tau \geq \tau' \\ G_{13}(0, \tau' - \tau) & \text{if } \tau < \tau' \end{cases} \tag{I.A.42}$$

The two cases in Eq. (I.A.42) are equal to G_{33}, because the backwards time-evolution along the contour cancels if there is no operator placed there and this can be shown in the eigenbasis of $H(0)$. To store the Green function in memory and to examine it analytically, we will give its components names and will use the same convention as in existing literature[42].

> **Definition I.A.5: Components of the Green function of the L-shaped contour**
>
> *Let* $G_{ij}(\mathbf{t}, \mathbf{t}') = G(\mathbf{t}, \mathbf{t}')$ *where* t *and* t' *live on the L-shaped contour (Fig. I.A.1), and* $t \in \mathcal{C}_i$ *and* $t \in \mathcal{C}_j$*. The components of the contour-ordered Green function are defined as follows.*

greater non-eq.
$$G_L^{>N}(t_N, t'_N) = G_{21}(t_N, t'_N) = -i\, \langle c(t_N)\, c^\dagger(t'_N) \rangle \tag{I.A.43}$$

lesser non-eq.
$$G_L^{<N}(t_N, t'_N) = G_{12}(t_N, t'_N) = i\, \langle c^\dagger(t'_N)\, c(t_N) \rangle \tag{I.A.44}$$

right-mixing[90]
$$G_L^{\lceil}(\tau, t_N) = G_{31}(\tau, t_N) = -i\, \langle c(\tau)\, c^\dagger(t_N) \rangle \tag{I.A.45}$$

left-mixing
$$G_L^{\rceil}(t_N, \tau) = G_{13}(t_N, \tau) = i\, \langle c^\dagger(\tau)\, c(t_N) \rangle \tag{I.A.46}$$

Matsubara
$$G_L^{M}(\tau, \tau') = -iG_{33}(\tau, \tau') = \begin{cases} -\langle c(\tau)\, c^\dagger(\tau') \rangle & \textit{if } \tau \geq \tau' \\ \langle c^\dagger(\tau')\, c(\tau) \rangle & \textit{if } \tau < \tau' \end{cases} \tag{I.A.47}$$

retarded non-eq.
$$G_L^{RN}(t_N, t'_N) = \theta(t_N - t'_N)\, \left(G_L^{>N}(t_N, t'_N) - G_L^{<N}(t_N, t'_N) \right) \tag{I.A.48}$$

advanced non-eq.
$$G_L^{AN}(t_N, t'_N) = \theta(t'_N - t_N)\, \left(G_L^{<N}(t_N, t'_N) - G_L^{>N}(t_N, t'_N) \right) \tag{I.A.49}$$

The subscript L was added in this thesis to distinguish the notation from the zero temperature formalism described below. It will always be used from here on, when we talk about the Green function of the L-shaped contour.

These are the same definitions as in Ref. 42. In this thesis, the extra superscript N is used to distinguish the non-equilibrium components from the equilibrium counter parts that will be introduced later.

Definition I.A.6: Components of generic functions on the contour

For generic functions on the contour we define the same components as in Def. (I.A.5). For example: $A_L^{>N}(t_N, t'_N) = A_{21}(t_N, t'_N)$. *All generic functions on the contour convolute as described below.*

I.A.3.2 Convolution

The exact rules how to write the convolutions of two functions $A_L(\mathbf{t}, \mathbf{t}')$ and $B_L(\mathbf{t}, \mathbf{t}')$ over the contour are called Langreth rules[91]. We will look at an example here and how it can be written in terms of the components defined in Def. (I.A.5). Note that the definition of the components in Def. (I.A.5) slightly vary in literature and the corresponding convolution may differ. For example, Ref. 91 uses $G^M(\tau,\tau') = G_{33}(\tau,\tau')$ instead of the more commonly used $G^M(\tau,\tau') = -iG_{33}(\tau,\tau')$. We will take a look at the right-mixing component of the convolution.

$$\begin{aligned}
(A_L * B_L)^{\ulcorner}(\tau, t_N) &\equiv (A_L * B_L)_{31}(\tau, t_N) && \text{(I.A.50)}\\
&= \sum_{j=1}^{3} \int A_{L,3j}(\tau, \bar{\mathbf{t}})\, B_{L,j1}(\bar{\mathbf{t}}, t_N)\ \mathrm{d}\bar{\mathbf{t}} && \text{(I.A.51)}\\
&= \int_0^{t_N} A_{L,31}(\tau, \bar{t}_N)\, B_{L,11}(\bar{t}_N, t_N)\ \mathrm{d}\bar{t}_N && \text{(I.A.52)}\\
&\quad + \int_{t_N}^{0} A_{L,32}(\tau, \bar{t}_N)\, B_{L,21}(\bar{t}_N, t_N)\ \mathrm{d}\bar{t}_N\\
&\quad - i \int_0^{\beta} A_{L,33}(\tau, \bar{\tau})\, B_{L,31}(\bar{\tau}, t_N)\ \mathrm{d}\bar{\tau}
\end{aligned}$$

In the second line, j marks the region where $\bar{\mathbf{t}}$ lies on the contour. $A_{L,3j}$ is to be read as: The $3j$ component of A on the L-shaped contour. First, we plug in the definitions of the components:

$$\begin{aligned}
(A_L * B_L)^{\ulcorner}(\tau, t_N) &= \int_0^{t_N} A_L^{\ulcorner}(\tau, \bar{t}_N)\, B_L^{<N}(\bar{t}_N, t_N)\ \mathrm{d}\bar{t}_N && \text{(I.A.53)}\\
&\quad + \int_{t_N}^{0} A_L^{\ulcorner}(\tau, \bar{t}_N)\, B_L^{>N}(\bar{t}_N, t_N)\ \mathrm{d}\bar{t}_N\\
&\quad - i \int_0^{\beta} iA_L^{M}(\tau, \bar{\tau})\, B_L^{\ulcorner}(\bar{\tau}, t_N)\ \mathrm{d}\bar{\tau}
\end{aligned}$$

It is possible to combine the first and second line into one single expression.

$$\begin{aligned}
(A_L * B_L)^{\ulcorner}(\tau, t_N) &= \int_0^{\infty} A_L^{\ulcorner}(\tau, \bar{t}_N)\, B_L^{AN}(\bar{t}_N, t_N)\ \mathrm{d}\bar{t}_N && \text{(I.A.54)}\\
&\quad + \int_0^{\beta} A_L^{M}(\tau, \bar{\tau})\, B_L^{\ulcorner}(\bar{\tau}, t_N)\ \mathrm{d}\bar{\tau}
\end{aligned}$$

Below, we will take the limit $\beta \to \infty$. To stay consistent, we write:

$$
\begin{aligned}
(A_L * B_L)^{\ulcorner}(\tau, t_N) = &\int_0^{\infty} A_L^{\ulcorner}(\tau, \bar{t}_N)\, B_L^{AN}(\bar{t}_N, t_N)\, \mathrm{d}\bar{t}_N \\
&+ \int_0^{\frac{\beta}{2}} A_L^{M}(\tau, \bar{\tau})\, B_L^{\ulcorner}(\bar{\tau}, t_N)\, \mathrm{d}\bar{\tau} \\
&+ \int_{\frac{\beta}{2}}^{\beta} (-A_L^{M}(\tau, \beta - \tilde{\tau}))\, (-B_L^{\ulcorner}(\beta - \tilde{\tau}, t_N))\, \mathrm{d}\tilde{\tau}
\end{aligned}
\tag{I.A.55}
$$

In the last line we used the periodicity[42] of fermionic Green functions $f(-\tau) = -f(\beta - \tau)$. Now, substitute $\bar{\tau} = \beta - \tilde{\tau}$:

$$
\begin{aligned}
(A_L * B_L)^{\ulcorner}(\tau, t_N) = &\int_0^{\infty} A_L^{\ulcorner}(\tau, \bar{t}_N)\, B_L^{AN}(\bar{t}_N, t_N)\, \mathrm{d}\bar{t}_N \\
&+ \int_0^{\frac{\beta}{2}} A_L^{M}(\tau, \bar{\tau})\, B_L^{\ulcorner}(\bar{\tau}, t_N)\, \mathrm{d}\bar{\tau} \\
&+ \int_{-\frac{\beta}{2}}^{0} A_L^{M}(\tau, \bar{\tau})\, B_L^{\ulcorner}(\bar{\tau}, t_N)\, \mathrm{d}\bar{\tau}
\end{aligned}
\tag{I.A.56}
$$

In the limit $\beta \to \infty$ we get:

$$
\begin{aligned}
(A_L * B_L)^{\ulcorner}(\tau, t_N) = &\int_0^{\infty} A_L^{\ulcorner}(\tau, \bar{t}_N)\, B_L^{AN}(\bar{t}_N, t_N)\, \mathrm{d}\bar{t}_N \\
&+ \int_{-\infty}^{\infty} A_L^{M}(\tau, \bar{\tau})\, B_L^{\ulcorner}(\bar{\tau}, t_N)\, \mathrm{d}\bar{\tau}
\end{aligned}
\tag{I.A.57}
$$

The last equation is a compact representation of the right-mixing component of the convolution in the limit of zero temperature.

I.A.4 Non-Equilibrium Dynamical Mean Field Theory

In this section we derive the formalism of non-equilibrium Dynamical Mean Field Theory (DMFT). First, we will derive the Dyson equation, which connects the Green function and the self-energy. Like in equilibrium DMFT, we assume the self-energy to be k-independent. In the next subsection we will show that computation of the Green function can be formulated with an effective action instead of the full lattice Hamiltonian. The effective action of the

Anderson impurity model and the Hubbard model in infinite dimensions (where the self-energy is indeed local) will have the same form. Eventually, we will derive the non-equilibrium DMFT equations. In this whole section we will use the concept of contour-ordered Green functions as introduced above. Note, that we will use that there is some kind of contour, but will not use the specific shape of the contour. This means that the derivation is valid for every contour.

I.A.4.1 Derivation of the Non-Equilibrium Dyson Equation

For the derivation of the non-equilibrium Dyson equation there is a myriad of sources, e.g. Refs. 50, 91–93, though many use slightly different formalisms or approaches. We will loosely follow Ref. 50. We shortly review the derivation process here with the equations of motion of the Green function.

In this section, we assume that there is some contour $\mathcal{C}$ over which we integrate to compute the Green function but make no restriction about the specific form or shape. The only assumption is that we integrate from the initial position $\mathbf{t_i}$ to the final position $\mathbf{t_f}$. The Hamiltonian of the Hubbard model can be split into non-interacting (H_0) and interacting (H_1) part. Note that we use here a generalized version of Def. (1) and allow time-dependent Hamiltonian parameters and a bond-dependent hopping.

$$H = H_0 + H_1 \tag{I.A.58}$$

$$H_0 = \sum_{i,j,s} v_{ij}(t)\, c^{\dagger}_{i,s}\, c_{j,s} - \mu(t) \sum_{i,s} n_{i,s} \tag{I.A.59}$$

$$H_1 = U(t) \sum_{i} \left(n_{i,\uparrow} - \frac{1}{2}\right) \left(n_{j,\downarrow} - \frac{1}{2}\right) \tag{I.A.60}$$

We work in the basis of the diagonalized non-interacting Hamiltonian:

$$H_0 = \sum_{k,s} \left(\epsilon_k(t) - \mu(t)\right) n_{k,s} \tag{I.A.61}$$

It is possible to write a generalization of the time-evolution operator $\mathcal{U}_{\mathcal{C}}(\mathbf{t}, \mathbf{t}')$ on the contour. It has almost the same definition as the normal time-evolution operator, the only difference being the integration in the exponential function, where we integrate over the contour:

$$\mathcal{U}_{\mathcal{C}}(\mathbf{t},\mathbf{t}') = \begin{cases} \mathcal{T} e^{-i\int_{\mathcal{C},\mathbf{t}'}^{\mathbf{t}} H(\bar{\mathbf{t}})\,\mathrm{d}\bar{\mathbf{t}}} & \text{if } \mathbf{t} > \mathbf{t}' \\ \overline{\mathcal{T}} e^{i\int_{\mathcal{C},\mathbf{t}}^{\mathbf{t}'} H(\bar{\mathbf{t}})\,\mathrm{d}\bar{\mathbf{t}}} & \text{otherwise} \end{cases} \tag{I.A.62}$$

For this time-evolution operator it is relatively straight forward to calculate the derivative.

$$\frac{\partial \mathcal{U}_{\mathcal{C}}(\mathbf{t},\mathbf{t}')}{\partial \mathbf{t}} = -i\, H_{\mathbf{t}}\, \mathcal{U}_{\mathcal{C}}(\mathbf{t},\mathbf{t}') \tag{I.A.63}$$

$$\frac{\partial \mathcal{U}_{\mathcal{C}}(\mathbf{t},\mathbf{t}')}{\partial \mathbf{t}'} = -i\, \mathcal{U}_{\mathcal{C}}(\mathbf{t},\mathbf{t}')\, H_{\mathbf{t}'} \tag{I.A.64}$$

Furthermore, we can define the contour Heisenberg representation of an operator $O(\mathbf{t})$ and compute its derivative. Like the contour time-evolution operator, it has a very similar definition to its real time counter part.

$$O(\mathbf{t}) = \mathcal{U}_{\mathcal{C}}(\mathbf{t_i},\mathbf{t})\, O_{\mathbf{t}}\, \mathcal{U}_{\mathcal{C}}(\mathbf{t},\mathbf{t_i}) \tag{I.A.65}$$

$$\frac{\partial O(\mathbf{t})}{\partial \mathbf{t}} = i\,\mathcal{U}_{\mathcal{C}}(\mathbf{t_i},\mathbf{t})\,[H_{\mathbf{t}}, O_{\mathbf{t}}]\,\mathcal{U}_{\mathcal{C}}(\mathbf{t},\mathbf{t_i}) + \mathcal{U}_{\mathcal{C}}(\mathbf{t_i},\mathbf{t})\left(\frac{\partial O_{\mathbf{t}}}{\partial \mathbf{t}}\right)\mathcal{U}_{\mathcal{C}}(\mathbf{t},\mathbf{t_i}) \tag{I.A.66}$$

A general contour ordered expectation value with two time arguments can now be represented as a sum of the two different orderings multiplied by the Heaviside function on the contour $\theta_{\mathcal{C}}$ (see Def. (I.A.2)).

$$\langle A(\mathbf{t})\, B(\mathbf{t}')\rangle_S = \begin{cases} \langle A(\mathbf{t})\, B(\mathbf{t}')\rangle_{\mathcal{U}_{\mathcal{C}}} & \text{if } \mathbf{t} >_{\mathcal{C}} \mathbf{t}' \\ \pm\langle B(\mathbf{t}')\, A(\mathbf{t})\rangle_{\mathcal{U}_{\mathcal{C}}} & \text{otherwise} \end{cases} \tag{I.A.67}$$

$$= \langle A(\mathbf{t})\, B(\mathbf{t}')\rangle_{\mathcal{U}_{\mathcal{C}}}\ \theta_{\mathcal{C}}(\mathbf{t},\mathbf{t}') \pm \langle B(\mathbf{t}')\, A(\mathbf{t})\rangle_{\mathcal{U}_{\mathcal{C}}}\ \theta_{\mathcal{C}}(\mathbf{t}',\mathbf{t}) \tag{I.A.68}$$

$$\langle ... \rangle_{\mathcal{U}_{\mathcal{C}}} = \frac{\mathrm{tr}\,(\mathcal{U}_{\mathcal{C}}(\mathbf{t_f},\mathbf{t_i})\ ...\ )}{\mathrm{tr}\,(\mathcal{U}_{\mathcal{C}}(\mathbf{t_f},\mathbf{t_i}))} \tag{I.A.69}$$

Where one takes the $+$ sign if A and B commute with each other, and the $-$ sign if they anticommute with each other. The Green function can now be represented as:

$$G_k(\mathbf{t},\mathbf{t}') = -i\left(\left\langle c_k(\mathbf{t})\, c_k^\dagger(\mathbf{t}')\right\rangle_{\mathcal{U}_\mathcal{C}}\ \theta_\mathcal{C}(\mathbf{t},\mathbf{t}') - \left\langle c_k^\dagger(\mathbf{t}')\, c_k(\mathbf{t})\right\rangle_{\mathcal{U}_\mathcal{C}}\ \theta_\mathcal{C}(\mathbf{t}',\mathbf{t})\right) \tag{I.A.70}$$

$$\langle\ldots\rangle_{\mathcal{U}_\mathcal{C}} = \frac{\mathrm{tr}\left(\mathcal{U}_\mathcal{C}(\mathbf{t_f},\mathbf{t_i})\ \ldots\right)}{\mathrm{tr}\left(\mathcal{U}_\mathcal{C}(\mathbf{t_f},\mathbf{t_i})\right)} \tag{I.A.71}$$

Here we explicitly write down the k that are the eigenstates of the non-interacting Hamiltonian. The equation above may look cumbersome in comparison to the compact notation in Def. (I.A.4) we used above. The advantage is, and the reason we introduced the definitions above, it is now easy to compute the derivative of the Green function:

$$\frac{\partial}{\partial \mathbf{t}} G_k(\mathbf{t},\mathbf{t}') = \left\langle [H,c_k](\mathbf{t})\, c_k^\dagger(\mathbf{t}')\right\rangle_{\mathcal{U}_\mathcal{C}}\ \theta_\mathcal{C}(\mathbf{t},\mathbf{t}') - \left\langle c_k^\dagger(\mathbf{t}')\, [H,c_k](\mathbf{t})\right\rangle_{\mathcal{U}_\mathcal{C}}\ \theta_\mathcal{C}(\mathbf{t}',\mathbf{t}) - i\delta_\mathcal{C}(\mathbf{t},\mathbf{t}') \tag{I.A.72}$$

Now we use the fact that we split the Hamiltonian into interacting and non-interacting part and compute the commutator.

$$[H,c_k] = -\left(\epsilon_k(t) - \mu(t)\right) c_k + [H_1, c_k] \tag{I.A.73}$$

The first term of the right hand side reduces to the Green function, when inserted into Eq. (I.A.72). The second term introduces higher order terms to the derivative which are in general harder to calculate than the Green function itself. The only exception is $U = 0$ where $H_1 = 0$.

These higher order terms will be eliminated by introducing the non-equilibrium self-energy, which is implicitly defined as the solution of the following equation[50]:

$$\left(\Sigma_k * G_k\right)(\mathbf{t},\mathbf{t}') = i\ \left\langle [H_1,c_k](\mathbf{t})\, c_k^\dagger(\mathbf{t}')\right\rangle_{\mathcal{U}_\mathcal{C}}\ \theta_\mathcal{C}(\mathbf{t},\mathbf{t}') - i\ \left\langle c_k^\dagger(\mathbf{t}')\, [H_1,c_k](\mathbf{t})\right\rangle_{\mathcal{U}_\mathcal{C}}\ \theta_\mathcal{C}(\mathbf{t}',\mathbf{t}) \tag{I.A.74}$$

At first glance, the definition of the non-equilibrium self-energy may seem odd, but this definition allows us to get a Dyson equation that is form equivalent to the equilibrium case.

With the self-energy the derivative of the Green function breaks down to:

$$\frac{\partial}{\partial \mathbf{t}} G_k(\mathbf{t}, \mathbf{t}') = -i\,(\epsilon_k(\mathbf{t}) - \mu(\mathbf{t}))\, G_k(\mathbf{t}, \mathbf{t}') - i\,(\Sigma_k * G_k)(\mathbf{t}, \mathbf{t}') - i\delta_{\mathcal{C}}(\mathbf{t}, \mathbf{t}') \tag{I.A.75}$$

After we bring every instance of G_k that is not in a contour convolution to the left hand side, we get the following important intermediate result:

$$\left(i\frac{\partial}{\partial \mathbf{t}} - (\epsilon_k(\mathbf{t}) - \mu(\mathbf{t}))\right) G_k(\mathbf{t}, \mathbf{t}') = (\Sigma_k * G_k)(\mathbf{t}, \mathbf{t}') + \delta_{\mathcal{C}}(\mathbf{t}, \mathbf{t}') \tag{I.A.76}$$

In the non-interacting case ($U = 0$) the self-energy vanishes

$$\left(i\frac{\partial}{\partial \mathbf{t}} - (\epsilon_k(\mathbf{t}) - \mu(\mathbf{t}))\right) G_{0,k}(\mathbf{t}, \mathbf{t}') = \delta_{\mathcal{C}}(\mathbf{t}, \mathbf{t}') \tag{I.A.77}$$

and it is possible to find an explicit formula for $G_{0,k}^{-1}(\mathbf{t}, \mathbf{t}')$ by convoluting both sides of the equation above with $G_{0,k}^{-1}(\mathbf{t}, \mathbf{t}')$ from the right (by definition $G * G^{-1} = \delta_{\mathcal{C}}$):

$$G_{0,k}^{-1}(\mathbf{t}, \mathbf{t}') = \left(i\frac{\partial}{\partial \mathbf{t}} - (\epsilon_k(\mathbf{t}) - \mu(\mathbf{t}))\right) \delta_{\mathcal{C}}(\mathbf{t}, \mathbf{t}') \tag{I.A.78}$$

With this explicit form of $G_{0,k}^{-1}$ we can compute the convolution $G_{0,k}^{-1} * G_k$:

$$\begin{aligned}
\left(G_{0,k}^{-1} * G_k\right)(\mathbf{t}, \mathbf{t}') &= \int_{\mathcal{C}} \left(i\frac{\partial}{\partial \mathbf{t}} - (\epsilon_k(\mathbf{t}) - \mu(\mathbf{t}))\right) \delta_{\mathcal{C}}(\mathbf{t}, \bar{\mathbf{t}})\, G_k(\bar{\mathbf{t}}, \mathbf{t})\, \mathrm{d}\bar{\mathbf{t}} && \text{(I.A.79)}\\
&= \left(i\frac{\partial}{\partial \mathbf{t}} - (\epsilon_k(\mathbf{t}) - \mu(\mathbf{t}))\right) G_k(\mathbf{t}, \mathbf{t}) && \text{(I.A.80)}\\
&= (\Sigma_k * G_k)(\mathbf{t}, \mathbf{t}') + \delta_{\mathcal{C}}(\mathbf{t}, \mathbf{t}') && \text{(I.A.81)}
\end{aligned}$$

From the second last to last line we used Eq. (I.A.76). Thus we find:

$$G_{0,k}^{-1} * G_k = \delta_{\mathcal{C}} + \Sigma_k * G_k \tag{I.A.82}$$

After convolution of both sides with $G_{0,k}$ from the left we get the non-equilibrium Dyson equation:

> **Definition I.A.7: Dyson equation**
>
> $$G_k = G_{0,k} + G_{0,k} * \Sigma_k * G_k \tag{I.A.83}$$

This equation looks like the equilibrium Dyson equation (Eq. (I.A.6)) in ω-space. The difference is the use of the contour convolution instead of a simple product in ω-space. In fact, if the Hamiltonian is constant and the C-shaped Keldysh contour is used, then this Dyson equation reduces to the equilibrium case. It should be emphasized again, that we did not specify the exact form of the contour $\mathcal{C}$. The Green function, the self-energy, and the contour convolution may change with a different contour, but the Dyson equation stays the same. On a further note, it is possible to do the calculation in this chapter not in k-space but in the space of the lattice sites, where the Green function is:

$$G_{(i,j)}(\mathbf{t}, \mathbf{t}') = -i \, \frac{\operatorname{tr}\left(\mathcal{T}_{\mathcal{C}} \, e^{S} \, c_{i,\mathbf{t}} \, c^{\dagger}_{j,\mathbf{t}'}\right)}{\operatorname{tr}\left(\mathcal{T}_{\mathcal{C}} \, e^{S}\right)} \tag{I.A.84}$$

In that case the Dyson equation emerges again[50]:

$$G = G_0 + G_0 \circledast \Sigma \circledast G \tag{I.A.85}$$

The difference here is that the Green function and self-energy are now matrices with lattice site indices and the convolution is a matrix product and contour convolution:

$$\left(F \circledast G\right)_{ij}(\mathbf{t}, \mathbf{t}') = \sum_{m} \left(F_{im} * G_{mj}\right)(\mathbf{t}, \mathbf{t}') \tag{I.A.86}$$

This formalism is not needed for the present thesis and we will stay in k-space.

I.A.4.2 Effective Action

This subsection summarizes the results of section III of Ref. 49. One way to rewrite Hubbard-like Hamiltonians is to single out one site 0 and split the Hamiltonian in terms that act only on site 0, on sites other than 0, and terms that connect site 0 with the rest[49]. With

Hubbard-like we mean a general Hamiltonian with arbitrary geometry. This includes the Anderson impurity model. To avoid a symbol collision with the non-interacting Hamiltonian, we will use $H_{(0)}$ instead of H_0 for the Hamiltonian of the isolated site which is used in Ref. 49. Note that the Hamiltonian parameters are implicitly time-dependent and we furthermore let the hopping amplitude be spin-dependent.

$$H = H_{(0)} + H^{(0)} + \Delta H = \sum_{ijs} v_{ijs}\, c^\dagger_{i,s}\, c_{j,s} + v_{jis}\, c^\dagger_{j,s}\, c_{j,s} + \sum_i U_i\, n_{i,\uparrow}\, n_{i,\downarrow} \tag{I.A.87}$$

$$H_{(0)} = \sum_s 2\, v_{00s}\, c^\dagger_{0,s}\, c_{0,s} + U_0\, n_{0,\uparrow}\, n_{0,\downarrow} \tag{I.A.88}$$

$$\Delta H = \sum_{is} v_{i0s}\, c^\dagger_{i,s}\, c_{0,s} + v_{0is}\, c^\dagger_{0,s}\, c_{j,s} \tag{I.A.89}$$

$$H^{(0)} = \sum_{\substack{ijs\\ i,j\neq 0}} v_{ijs}\, c^\dagger_{i,s}\, c_{j,s} + v_{jis}\, c^\dagger_{j,s}\, c_{j,s} + \sum_{\substack{i\\ i\neq 0}} U_i\, n_{i,\uparrow}\, n_{j,\downarrow} \tag{I.A.90}$$

The parameters U and v are implicitly time-dependent. The action also splits into three parts, $S = S_{(0)} + S^{(0)} + \Delta S$, where $S_{(0)} = -i \int_{\mathcal{C}} H_{(0)}(\mathbf{t})\ \mathrm{d}\mathbf{t}$ and accordingly for the other two parts of the Hamiltonian. It is possible to split the total trace into the two subspaces formed by the occupation bases of site 0 and the rest.

$$\operatorname{tr} O = \sum_{\{n_i\}=0,1} \langle n_0, n_1, ... \,|\, O \,|\, n_0, n_1, ...\rangle \tag{I.A.91}$$

$$\operatorname{tr}_0 O = \sum_{\{n_0\}=0,1} \langle n_0 \,|\, O \,|\, n_0\rangle \tag{I.A.92}$$

$$\operatorname{tr}_R O = \sum_{\{n_i\}=0,1; i\neq 0} \langle n_1, n_2, ... \,|\, O \,|\, n_1, n_2, ...\rangle \tag{I.A.93}$$

$$O_0 = \operatorname{tr}_R O \tag{I.A.94}$$

$$\operatorname{tr} O = \operatorname{tr}_0 \operatorname{tr}_R O = \operatorname{tr}_0 O_0 \tag{I.A.95}$$

Here the n_i are the occupation numbers in the occupation basis. As shown in Ref. 49, one can trace out the rest of the system and derive an effective action S_{eff}. Then the expectation value of an operator O that acts only on site 0 can be written in terms of the effective action.

$$\langle O\rangle_S = \langle O\rangle_{S_{\text{eff}}} = \frac{1}{Z_{eff}} \operatorname{tr}_0 \left(\mathcal{T}_{\mathcal{C}}\, e^{S_{\text{eff}}}\, O\right) \tag{I.A.96}$$

The effective action is expressed in terms of general $2n$-time hybridization functions Δ.

$$S_{\text{eff}} = S_{(0)} - i \sum_{n=1}^{\infty} \sum_{\substack{s_1,\dots,s_n\\ s'_1,\dots,s'_n}} \overbrace{\int_{\mathcal{C}} \dots \int_{\mathcal{C}}}^{2n \text{ integrals}} \Delta_{s_1,\dots,s_n,s'_1,\dots,s'_n}(\mathbf{t_1},\dots,\mathbf{t_n},\mathbf{t'_1},\dots,\mathbf{t'_n}) \\ c^{\dagger}_{0,s_1,\mathbf{t_1}} \dots c^{\dagger}_{0,s_n,\mathbf{t_n}} c_{0,s_1,\mathbf{t'_1}} \dots c_{0,s_n,\mathbf{t'_n}} \, \mathrm{d}\mathbf{t_1} \dots \mathrm{d}\mathbf{t_n} \, \mathrm{d}\mathbf{t'_1} \dots \mathrm{d}\mathbf{t'_n} \tag{I.A.97}$$

The $2n$-time hybridization functions Δ can be expressed in terms of connected Green functions.

$$\Delta_{s_1,\dots,s'_n}(\mathbf{t_1},\dots,\mathbf{t'_n}) = \frac{(-i)^{n-1}}{n!^2} \sum_{\substack{i_1,\dots,i_n,j_1,\dots,j_n\\ s_1,\dots,s_n,s'_1,\dots,s'_n}} v_{0,i_1,s_1} \dots v_{j_n,0,s'_n} \, G^{(0),c}_{(i_1,s_1),\dots,(j_n,s'_n)}(\mathbf{t_1},\dots,\mathbf{t'_n}) \tag{I.A.98}$$

The connected Green functions indicate that the sum over the lattice site indices $i_1 \dots j_n$ includes only terms where the lattice sites are connected by the Hamiltonian $H^{(0)}$. This is going to be important for the Anderson Impurity Model and the Hubbard model on the Bethe lattice.

$$G^{(0),c}_{(i_1,s_1),\dots,(j_n,s'_n)}(\mathbf{t_1},\dots,\mathbf{t'_n}) = (-i)^n \left\langle c_{i_1,s_1,\mathbf{t_1}} \dots c_{i_n,s_n,\mathbf{t_n}} \, c^{\dagger}_{j_1,s'_1,\mathbf{t'_1}} \dots c^{\dagger}_{j_n,s'_n,\mathbf{t'_n}} \right\rangle_{S^{(0)}} \tag{I.A.99}$$

To summarize this lengthy result so far: It is possible to reduce the computation of the Green function of a general Hamiltonian to the Hilbert space of only one lattice site without loss of generality. The problem is, in order to do so, one needs to know the higher order Green functions $G^{(0),c}$ which are harder to compute than just the Green function. However, there are three important cases, where the computation vastly simplifies[49,64]. The conceptually simplest one is the Anderson Impurity Model, where isolated lattice site 0 is the impurity. When the impurity is removed and it is the only site connecting the bath sites, all higher order connected Green functions vanish.

$$S_{\text{eff}} = S_{(0)} - i \sum_{s,s'} \int_{\mathcal{C}} \Delta_{s,s'}(\mathbf{t},\mathbf{t}') \, c^{\dagger}_{0,s,\mathbf{t}} \, c_{0,s',\mathbf{t}'} \, \mathrm{d}\mathbf{t} \, \mathrm{d}\mathbf{t}' \tag{I.A.100}$$

The same effective action can be derived very similarly for the Bethe lattice because the removal of site 0 splits the lattice into $\mathcal{Z}$ separated sublattices, where $\mathcal{Z}$ is the connectivity.

The third case is the limit to infinite dimensions $d = 2\mathcal{Z} \rightarrow \infty$ on the hypercubic lattice. If the hopping is scaled like $v = \frac{v_0}{\sqrt{\mathcal{Z}}}$, one finds that all higher order terms vanish in Eq. (I.A.98) and the same effective action as in Eq. (I.A.100) is recovered.

On the Bethe lattice with infinite connectivity it is also relatively simple to connect the Green function with the hybridization function[42,49,64] and to get a self-consistency condition for DMFT. In the limit of infinite connectivity, the effect of the removal of one lattice site can be neglected for the Green function (here, $i \neq 0$).

$$\lim_{\mathcal{Z}\rightarrow\infty} G^{(0),c}_{(i,s),(i,s')}(\mathbf{t},\mathbf{t'}) = \lim_{\mathcal{Z}\rightarrow\infty} G_{(i,s),(i,s')}(\mathbf{t},\mathbf{t'}) \tag{I.A.101}$$

To this end, one needs to do the same scaling of the hopping as above, so that the kinetic energy stays finite. Then, there is a very simple connection between the Green function and the hybridization function.

$$\Delta(\mathbf{t},\mathbf{t'}) = v(\mathbf{t})\, G(\mathbf{t},\mathbf{t'})\, v(\mathbf{t'})^* \tag{I.A.102}$$

To summarize this subsection, it can be shown that the computation of the local Green function (or any operator that acts only on one site) of the Hubbard model can be substituted by the computation of the Green function on the Anderson Impurity Model, provided that the right hybridization function is used.

I.A.4.3 Self-Consistency Scheme

In this subsection we will closely follow Refs. 42 and 50. The idea behind the derivation of non-equilibrium DMFT is the same as for equilibrium DMFT (see Sec. I.A.2). We will show that there is again a simple set of coupled equations that include the Green function G, the self-energy Σ, and the hybridization function Δ, under the assumption that the self-energy is local (k-independent).

As just discussed in Sec. I.A.4.2, the Hubbard model in infinite dimensions and the Anderson impurity model can be modeled with an effective action S_{eff} that contains the hybridization function $\Delta(\bar{\mathbf{t}},\bar{\bar{\mathbf{t}}})$.

$$S_{(0)} = -i \int_{\mathcal{C}} U(\bar{\mathbf{t}}) \left(n_{0,\uparrow} - \frac{1}{2}\right) \left(n_{0,\downarrow} - \frac{1}{2}\right) - \mu(\bar{\mathbf{t}}) \sum_s n_{0,s} \, \mathrm{d}\bar{\mathbf{t}} \tag{I.A.103}$$

$$S_{\text{eff}} = S_{(0)} - i \iint_{\mathcal{C}} c^\dagger_{\bar{\mathbf{t}}} \, \Delta(\bar{\mathbf{t}},\bar{\bar{\mathbf{t}}}) \, c_{\bar{\bar{\mathbf{t}}}} \, \mathrm{d}\bar{\mathbf{t}} \, \mathrm{d}\bar{\bar{\mathbf{t}}} \tag{I.A.104}$$

$$G(\mathbf{t},\mathbf{t}') = -i \, \frac{\operatorname{tr}\left(\mathcal{T}_{\mathcal{C}} \, e^{S_{\text{eff}}} \, c_{0,\mathbf{t}} \, c^\dagger_{0,\mathbf{t}'}\right)}{\operatorname{tr}\left(\mathcal{T}_{\mathcal{C}} \, e^{S_{\text{eff}}}\right)} \tag{I.A.105}$$

Depending on what model is exactly described with Eq. (I.A.104), the meaning of the Green function in Eq. (I.A.105) changes. If the model is the Anderson Impurity Model, then $G = G_{\text{IMP}}$. On the other hand, if the model is the investigated lattice model, then G is the Green function of the lattice, where the modelling with a hybridization function $\Delta(\bar{\mathbf{t}},\bar{\bar{\mathbf{t}}})$, with only two time arguments, is in general only an approximation.

In the same way as above (Sec. I.A.4.1) we can compute the equation of motion, though one cannot define a simple contour Heisenberg picture of the time-evolution operator because of the presence of $\Delta(\bar{\mathbf{t}},\bar{\bar{\mathbf{t}}})$. Note that the Green function is not defined with a Hamiltonian here, but with an effective action. The next steps[50] correspond to Eqs. (I.A.72) and (I.A.76), where the Green function is defined with a Hamiltonian.

$$\frac{\partial}{\partial \mathbf{t}} G(\mathbf{t},\mathbf{t}') = \left\langle [H_{\text{loc},\mathbf{t}}, c_{\mathbf{t}}], c^\dagger_{\mathbf{t}'} \right\rangle_S - i(\Delta * G)(\mathbf{t},\mathbf{t}') - i\delta_{\mathcal{C}}(\mathbf{t},\mathbf{t}') \tag{I.A.106}$$

Similar to Sec. I.A.4.1, we have again split the local Hamiltonian into interacting and non-interacting part, $H_{\text{loc}} = \underbrace{-\mu \sum_s c^\dagger_{0,s} c_{0,s}}_{H_0} + \underbrace{U\left(n_{0,\uparrow} - \tfrac{1}{2}\right)\left(n_{0,\downarrow} - \tfrac{1}{2}\right)}_{H_1}$ and pull all higher order terms of the commutator into the self-energy.

$$\frac{\partial}{\partial \mathbf{t}} G(\mathbf{t},\mathbf{t}') = i\mu(\mathbf{t}) \, G(\mathbf{t},\mathbf{t}') - i \left(\Sigma * G\right)(\mathbf{t},\mathbf{t}') - i(\Delta * G)(\mathbf{t},\mathbf{t}') - i\delta_{\mathcal{C}}(\mathbf{t},\mathbf{t}') \tag{I.A.107}$$

This equation corresponds to Eq. (I.A.7) in the equilibrium case. Following from that we get again explicit results for the inverse of the Green function G^{-1} and the inverse of the non-interacting Green function G_0^{-1}. Note that, in contrast to ω-space, in the time domain the inverse $G^{-1}(\mathbf{t},\mathbf{t}') \neq \frac{1}{G(\mathbf{t},\mathbf{t}')}$ (see Def. (I.A.3)), but is defined via Eq. (I.A.32)

$$G^{-1} * G = G * G^{-1} = \delta_{\mathcal{C}}. \tag{I.A.108}$$

After replicating the steps corresponding to Eqs. (I.A.77) to (I.A.79), the Dyson equation emerges again:

$$G^{-1}(\mathbf{t},\mathbf{t}') = \left(i\,\frac{\partial}{\partial \mathbf{t}} + \mu(\mathbf{t})\right)\,\delta_{\mathcal{C}}(\mathbf{t},\mathbf{t}') - \Sigma(\mathbf{t},\mathbf{t}') - \Delta(\mathbf{t},\mathbf{t}') \tag{I.A.109}$$

$$G_0^{-1}(\mathbf{t},\mathbf{t}') = \left(i\,\frac{\partial}{\partial \mathbf{t}} + \mu(\mathbf{t})\right)\,\delta_{\mathcal{C}}(\mathbf{t},\mathbf{t}') - \Delta(\mathbf{t},\mathbf{t}') \tag{I.A.110}$$

$$G = G_0 + G_0 * \Sigma * G = G_0 + G * \Sigma * G_0 \tag{I.A.111}$$

Equations (I.A.109) and (I.A.110) correspond to Eqs. (I.A.10) and (I.A.11) in the equilibrium case. Here we explicitly assumed a k-independent self-energy. This holds true for the infinite dimensional system, but not for a general Hamiltonian (e.g. the three-dimensional Hubbard model). On the other hand, the explicit knowledge of the lattice geometry allows us to compute the k-dependent Green function from the Dyson equation (Eq. (I.A.83)), with the approximation of a k-independent self-energy.

$$G_k = G_{0,k} + G_{0,k} * \Sigma * G_k \tag{I.A.112}$$

$$G(\mathbf{t},\mathbf{t}') = G_{\text{loc}}(\mathbf{t},\mathbf{t}') = \frac{1}{N_k}\sum_k G_k(\mathbf{t},\mathbf{t}') \qquad \left(\tfrac{1}{N_k}\textstyle\sum_k{=}1\right) \tag{I.A.113}$$

Analogous to the equilibrium case, Eq. (I.A.105) and Eq. (I.A.109) to Eq. (I.A.113) form a set of coupled equations that need to be solved. Like in the equilibrium case, it is generally not possible to solve these equations simultaneously and the remedy is to solve them iteratively and self-consistently (Alg. (I.A.2)). A closer inspection of the equations shows that they are formally equivalent to the equilibrium case (see Sec. I.A.2). The difference is that instead of multiplication in ω-space a convolution on the contour is done and that we cannot get the inverse of a function on the contour by a simple division in ω-space but need to find the inverse of the contour convolution. In fact, in equilibrium and under a suitable contour (e.g. the C-shaped contour) the equations above simplify to the equilibrium equations of Sec. I.A.2 after a Fourier transform to ω-space.

Algorithm I.A.2: Unstable Non-Equilibrium Dynamical Mean Field Theory[42]

The superscript (n) *denotes the iteration number.*

0. *Start with initial guess for* $\Delta^{(0)}(\mathbf{t},\mathbf{t}')$*. Set* $(n) \longrightarrow 0$.
   When no good guess is available and the solution is suspected to be metallic, one can usually start from the semicircular density of states.
1. *From* $\Delta^{(n)}(\mathbf{t},\mathbf{t}')$ *compute the bath parameters* $V_l^{(n)}, \epsilon_l^{(n)}$ *(see Sec. I.B.3).*
2. *Solve impurity problem, i.e. compute impurity Green function* $G_{IMP}^{(n)}(\mathbf{t},\mathbf{t}')$.
   If $\left|G_{IMP}^{(n)}(\mathbf{t},\mathbf{t}') - G_{IMP}^{(n-1)}(\mathbf{t},\mathbf{t}')\right|$ *is sufficiently small for all* $\mathbf{t}$ *and* $\mathbf{t}'$*, the algorithm is converged.*
3. *Compute* $\Sigma_{IMP}^{(n)}(\mathbf{t},\mathbf{t}') = G_{0,IMP}^{(n)}(\mathbf{t},\mathbf{t}')^{-1} - G_{IMP}^{(n)}(\mathbf{t},\mathbf{t}')^{-1}$*, where* $G_{0,IMP}^{(n)}(\mathbf{t},\mathbf{t}')$ *is the non-interacting Green function of the impurity system.*
   Now, the DMFT approximation is $\Sigma^{(n)}(\mathbf{t},\mathbf{t}') = \Sigma_{IMP}^{(n)}(\mathbf{t},\mathbf{t}')$.
4. *Compute the local Green function*
   $G_{loc}^{(n)}(\mathbf{t},\mathbf{t}') = \frac{1}{N_k}\sum_k G_k^{(n)}(\mathbf{t},\mathbf{t}') = \frac{1}{N_k}\sum_k \left(G_{0,k}^{(n)}(\mathbf{t},\mathbf{t}')^{-1} - \Sigma^{(n)}(\mathbf{t},\mathbf{t}')\right)^{-1}$.
5. *Compute the Weiss effective field* $\mathcal{G}_0^{(n)}(\mathbf{t},\mathbf{t}') = \left(G_{loc}^{(n)}(\mathbf{t},\mathbf{t}')^{-1} + \Sigma^{(n)}(\mathbf{t},\mathbf{t}')\right)^{-1}$.
6. *Compute the hybridization function of the next iteration*
   $\Delta^{(n+1)}(\mathbf{t},\mathbf{t}') = \left(i\,\frac{\partial}{\partial \mathbf{t}} + \mu(\mathbf{t})\right)\,\delta_{\mathcal{C}}(\mathbf{t},\mathbf{t}') - \mathcal{G}_0^{(n)}(\mathbf{t},\mathbf{t}')^{-1}$.
7. *Go to step 1 and start a new iteration* $(n \longrightarrow n+1)$

If the algorithm is done on the Bethe lattice one can skip steps $3-6$ *and instead do:*
$\Delta^{(n+1)}(\mathbf{t},\mathbf{t}') = v(\mathbf{t})\,G_{IMP}^{(n)}(\mathbf{t},\mathbf{t}')\,v(\mathbf{t}')^*$.

The problem of Alg. (I.A.2) is that the necessary contour inversions in steps 3, 4, 5, and 6 are not stable[42]. With contour inversion we mean the computation of F^{-1} from F. One example is in step 3, which is the Dyson equation (Eq. (I.A.111)) rearranged. Convoluting the right hand side of Eq. (I.A.111) with $G_{0,\mathrm{IMP}}^{-1}$ from the right and bringing the resulting $\delta_{\mathcal{C}}$

to the left, we obtain:

$$G_{\mathrm{IMP}} * G_{0,\mathrm{IMP}}^{-1} - \delta_{\mathcal{C}} = G_{\mathrm{IMP}} * \Sigma \tag{I.A.114}$$

Solving this equation for Σ amounts to solving an equation of the following form for X:

$$\text{Solve for } X\text{:} \quad F * X = Q \tag{I.A.115}$$

Here, $Q = G_{\mathrm{IMP}} * G_{0,\mathrm{IMP}}^{-1} - \delta_{\mathcal{C}}$, $F = G_{\mathrm{IMP}}$, and $X = \Sigma_{\mathrm{IMP}}$. This process is numerically not stable[42].

A way around this is to use the impurity Green function g of an isolated impurity[42].

$$g^{-1}(\mathbf{t}, \mathbf{t}') = \left(i \frac{\partial}{\partial \mathbf{t}} + \mu(\mathbf{t})\right) \delta_{\mathcal{C}}(\mathbf{t}, \mathbf{t}') - \Sigma(\mathbf{t}, \mathbf{t}') \tag{I.A.116}$$

$$\Rightarrow \; g^{-1} = G^{-1} + \Delta \tag{I.A.117}$$

Convoluting Eq. (I.A.117) with G from the right and g from the left (or G from left and g from right) yields an equation similar to the Dyson equation:

$$G = g + g * \Delta * G \tag{I.A.118}$$

$$= g + G * \Delta * g \tag{I.A.119}$$

The lattice geometry gets included from the k-dependent Dyson equation (with k-independent self-energy) and one can show that the following holds true[42]:

$$G_k = g + g * \varepsilon_k * G_k \tag{I.A.120}$$

$$= g + G_k * \varepsilon_k * g \tag{I.A.121}$$

where $\varepsilon_k(\mathbf{t}, \mathbf{t}') = \epsilon_k(\mathbf{t})\, \delta_{\mathcal{C}}(\mathbf{t}, \mathbf{t}')$.

Performing the k-sum on both sides of Eq. (I.A.120) allows us to extract Δ again.

$$\frac{1}{N_k}\sum_k G_k = \frac{1}{N_k}\sum_k g + \frac{1}{N_k}\sum_k g * \varepsilon_k * G_k \tag{I.A.122}$$

$$G = g + \frac{1}{N_k} g * \sum_k \varepsilon_k * G_k \tag{I.A.123}$$

From the first to the second line we were able to pull g out of the k-sum as this quantity is independent of k. A comparison to Eq. (I.A.118) shows:

$$\Delta * G = \frac{1}{N_k}\sum_k \varepsilon_k * G_k \tag{I.A.124}$$

A further insertion shows:

$$\Delta * \overbrace{G}^{\text{Eq. (I.A.119)}} = \frac{1}{N_k}\sum_k \varepsilon_k * \overbrace{G_k}^{\text{Eq. (I.A.121)}} \tag{I.A.125}$$

$$\Delta * (g + G * \Delta * g) = \frac{1}{N_k}\sum_k \varepsilon_k * (g + G_k * \varepsilon_k * g) \tag{I.A.126}$$

$$\Delta * g + \Delta * G * \Delta * g = \frac{1}{N_k}\sum_k \varepsilon_k * g + \varepsilon_k * G_k * \varepsilon_k * g \tag{I.A.127}$$

After convolution with g^{-1} from the right we get:

$$\Delta + \overbrace{\Delta * G}^{\text{Eq. (I.A.124)}} * \Delta = \frac{1}{N_k}\sum_k \varepsilon_k + \varepsilon_k * G_k * \varepsilon_k \tag{I.A.128}$$

$$\Delta + \left(\frac{1}{N_k}\sum_k \varepsilon_k * G_k\right) * \Delta = \frac{1}{N_k}\sum_k \varepsilon_k + \varepsilon_k * G_k * \varepsilon_k \tag{I.A.129}$$

This means Δ can be extracted from the equation:

$$\Delta + G_1 * \Delta = G_2 \tag{I.A.130}$$

$$G_1 = \frac{1}{N_k}\sum_k \varepsilon_k * G_k \tag{I.A.131}$$

$$G_2 = \frac{1}{N_k}\sum_k \varepsilon_k + \varepsilon_k * G_k * \varepsilon_k \tag{I.A.132}$$

The equations above form again a set coupled equations that can be solved iteratively and self-consistently (Alg. (I.A.3)). The difference to Alg. (I.A.2) (and the reason for all these transformations) is that all contour inversions are now of the form:

$$\text{Solve for } X: \quad X + F * X = Q \tag{I.A.133}$$

This contour inversion is numerically much more stable[42] than Eq. (I.A.115).

Algorithm I.A.3: Stable Non-Equilibrium Dynamical Mean Field Theory[42]

The superscript n denotes the iteration number.

0. *Start with initial guess for $\Delta^{(0)}(\mathbf{t},\mathbf{t}')$. Set $(n) \longrightarrow 0$.*
   When no good guess is available and the solution is suspected to be metallic, one can usually start from the semicircular density of states.
1. *From $\Delta^{(n)}(\mathbf{t},\mathbf{t}')$ compute the bath parameters $V_l^{(n)}, \epsilon_l^{(n)}$ (see Sec. I.B.3).*
2. *Solve impurity problem, i.e. compute impurity Green function $G^{(n)}_{IMP}(\mathbf{t},\mathbf{t}')$.*
   If $\left|G^{(n)}_{IMP}(\mathbf{t},\mathbf{t}') - G^{(n-1)}_{IMP}(\mathbf{t},\mathbf{t}')\right|$ is sufficiently small for all $\mathbf{t}$ and $\mathbf{t}'$ the algorithm is converged.
3. *Solve for $g^{(n)}$:*

$$G^{(n)}_{IMP} = g^{(n)} + g^{(n)} * \Delta^{(n)} * G^{(n)}_{IMP} \tag{I.A.134}$$

4. *Solve $\forall\, k$:*

$$G^{(n)}_{k} = g^{(n)} + g^{(n)} * \varepsilon_k * G^{(n)}_{k} \tag{I.A.135}$$

   where $\varepsilon_k(\mathbf{t},\mathbf{t}') = \epsilon_k(\mathbf{t})\,\delta_{\mathcal{C}}(\mathbf{t},\mathbf{t}')$

5. *Compute k-sum:*

$$G^{(n)}_{loc} = g^{(n)} + \frac{1}{N_k} g^{(n)} * \left(\sum_k \varepsilon_k * G^{(n)}_{k}\right) \tag{I.A.136}$$

6. *Solve for* $\Delta^{(n+1)}$*:*

$$G_2^{(n)} = \Delta^{(n+1)} + G_1^{(n)} * \Delta^{(n+1)} \tag{I.A.137}$$

where

$$G_1^{(n)} = \frac{1}{N_k} \sum_k \varepsilon_k * G_k^{(n)} \tag{I.A.138}$$

$$G_2^{(n)} = \frac{1}{N_k} \sum_k \varepsilon_k + \varepsilon_k * G_k^{(n)} * \varepsilon_k \tag{I.A.139}$$

7. *Go to step 1 and start a new iteration* ($n \longrightarrow n+1$)

If the algorithm is done on the Bethe lattice one can skip steps $3-6$ *and instead do:* $\Delta^{(n+1)}(\mathbf{t},\mathbf{t}') = v(\mathbf{t})\, G_{IMP}^{(n)}(\mathbf{t},\mathbf{t}')\, v(\mathbf{t}')^*$.

Progressive Propagation Scheme

Because the equations used in non-equilibrium DMFT are causal[42], it is possible to do Alg. (I.A.3) in a modified manner[49]. With causal we mean that e.g. the convolution $(A * B)^{>N}(t_N, t'_N)$ does not depend on $A^{>N}(\bar{t}_N, \bar{t}'_N)$ (or other components) if at least one of its arguments is greater than either one of the arguments of the convolution:

$$\max(\bar{t}_N, \bar{t}'_N) > \min(t_N, t'_N) \tag{I.A.140}$$

Assuming that one discretizes the time in slices of distance Δt, one can first converge the DMFT loop at $t_N = 0$, then at $t_N = \Delta t$, then at $t_N = 2\,\Delta t$, and so on. This iteration scheme is illustrated in the top right of Fig. I.A.3, and requires a mapping method from the hybridization function to the Anderson Impurity Model Hamiltonian parameters that is also causal, i.e. computing $V(t_N)$ does not change $V(t'_N)$, when $t'_N < t_N$. We present such a mapping in Sec. I.B.3.

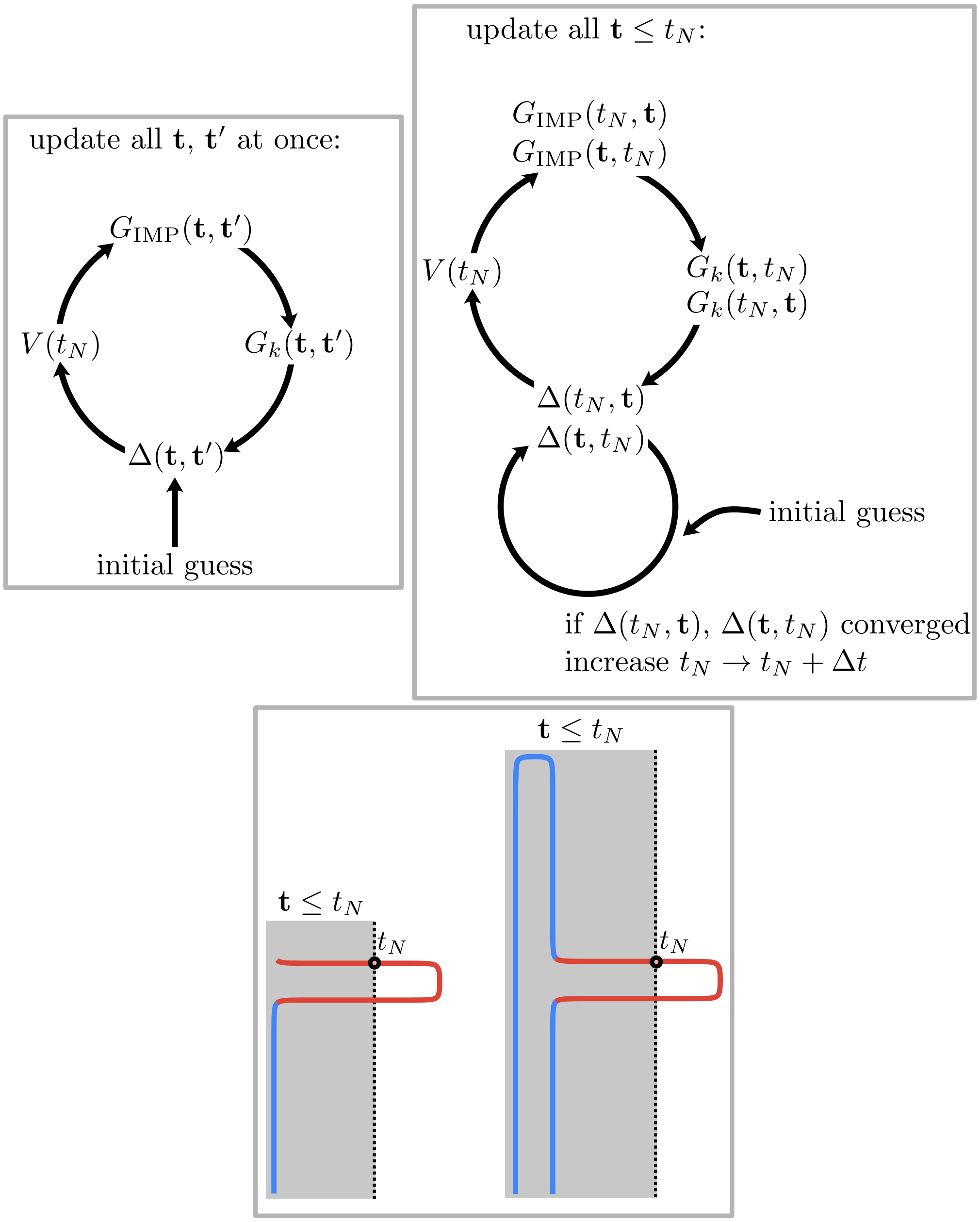

Figure I.A.3. Two possible iteration schemes for the DMFT loop. Top left: All quantities are updated for all time steps at once. Top right: t_N is fixed and the Green function, hybridization function, and the hoppings of the Anderson Impurity Model are updated only if one the time arguments is equal to t_N. After the DMFT loop is converged for t_N, t_N is increased by Δt. Bottom: Meaning of $\mathbf{t} \leq t_N$ in this context on the L-shaped contour and on the contour with two real axis which is introduced in Sec. I.B.1. Figure adapted from Ref. 49.

Subpart I.B

New Approach to Non-Equilibrium Green function at $T = 0$

I.B.1 Non-Equilibrium Green Functions at $T = 0$

In some situations, it is preferable to do non-equilibrium DMFT directly at $T = 0$ with only real time arguments instead of taking the limit $\beta \to \infty$. The motivation to use only real time arguments is the ill-posed analytic continuation which is needed to compute the Hamiltonian parameters of the Anderson impurity model[49,95], and to extract physical quantities (e.g. the spectrum) from the Green function. Measurements in experiments are always done on the real axis. The analytic continuation can drastically reduce energy resolution[96]. In the case of multi-orbital equilibrium DMFT at zero temperature, recent progress has been made regarding the computation of pure real time Green functions with new Matrix Product State based methods[41,69,71]. For the present thesis this ansatz is carried on to the non-equilibrium DMFT framework. To this end, the non-equilibrium Green function formalism needs to be modified. For equilibrium DMFT, the imaginary time-evolution used by CTQMC or similar methods can be replaced by a real time-evolution[71] at zero temperature.

For non-equilibrium DMFT at zero temperature, we extend the C-shaped contour used in the Keldysh formalism, as illustrated in Fig. I.B.1. We consider the case where the Hamiltonian is constant at negative times and may be time-dependent at positive times. The initial state at time $t = 0$ is taken to be the ground state of the constant Hamiltonian $H(t \leq 0)$. Now, we first draw the Keldysh contour in a different shape, bent down vertically for times $t \leq 0$. For the DMFT mapping from the hybridization function to Hamiltonian parameters of the Anderson Impurity model in non-equilibrium (Sec. I.B.3), we will need Green functions involving the initial (equilibrium) Hamiltonian at both negative and positive times. We therefore extend the contour as shown in Fig. I.B.1 (bottom), giving us the full axis for the "equilibrium time" $-\infty < t_E < \infty$, on which the constant Hamiltonian acts, and an axis for the "non-equilibrium" time $t_N \geq 0$, where the Hamiltonian can be time-dependent. Corresponding time-evolutions were defined in Def. (I.A.1). The extended contour with two real time axes is depicted in Fig. I.B.2. We note that the additional part of the contour by itself, when no creation or annihilation operators are applied there, integrates to unity for the time-evolution operator. The inclusion of positive equilibrium times will allow us to perform a well defined Fourier transform over the equilibrium axis for the DMFT mapping (Sec. I.B.3).

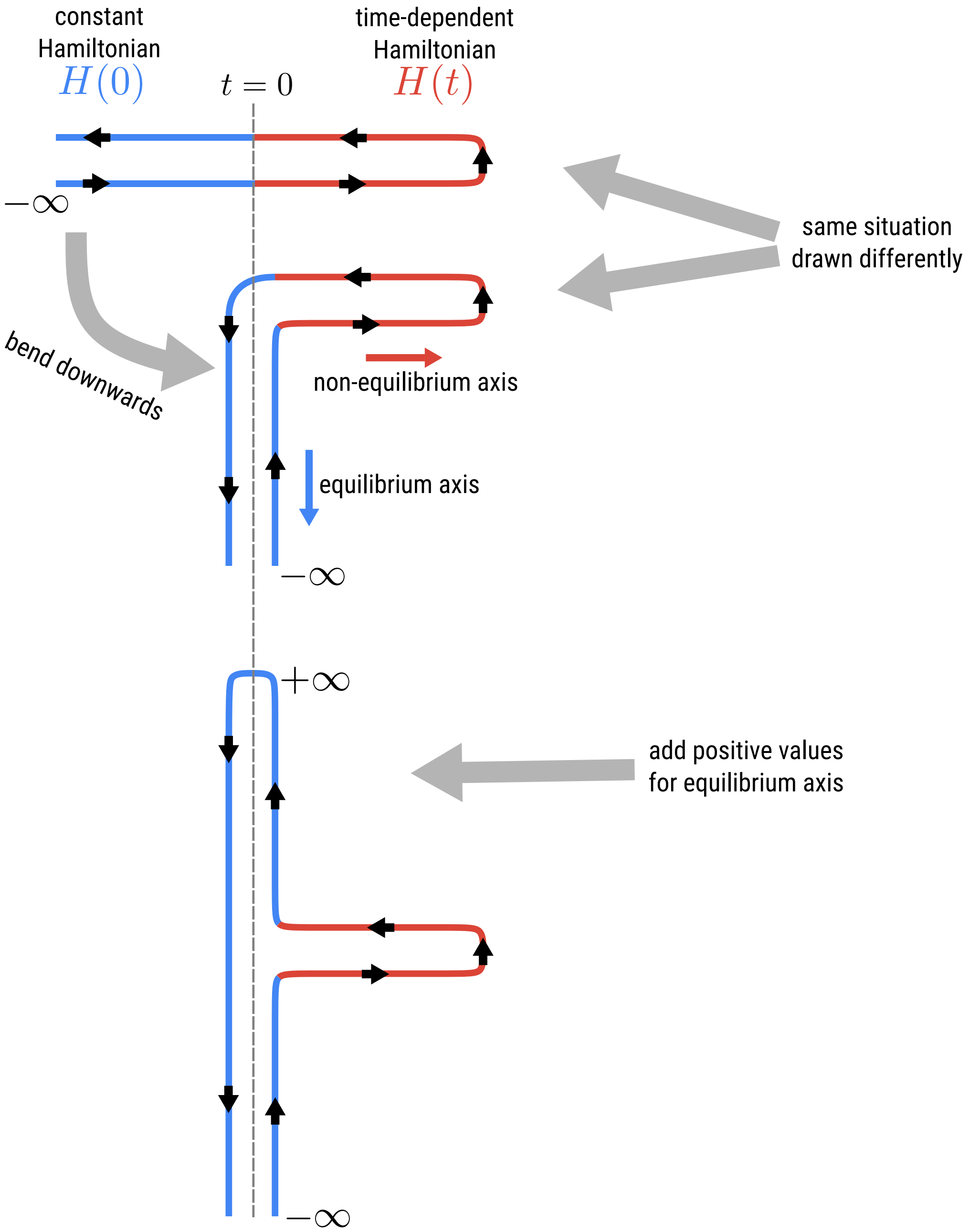

Figure I.B.1. Top contour: C-shaped contour used in the Keldysh formalism[94]. The Hamiltonian for $t \leq 0$ is constant (blue part), while the Hamiltonian for $t > 0$ may be time-dependent (red part). Center contour: The same situation is shown as in the top contour, where the negative times have been bent downwards. We can identify the vertical axis with the equilibrium time and the horizontal axis with the non-equilibrium time (Def. (I.A.1)). Bottom contour: Extended contour which allows for the computation of the Green function with times $t_E > 0$. This is necessary to perform the mapping, from the hybridization function to Hamiltonian parameters, like described in Sec. I.B.3. Note that the added part of the contour by itself, when no creation or annihilation operators are applied there, integrates to unity for the time-evolution operator.

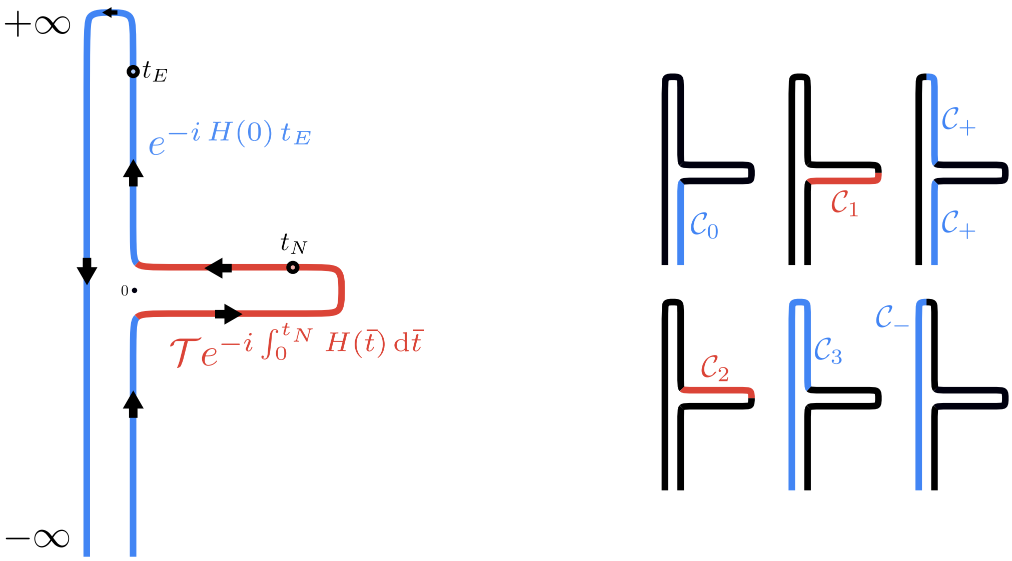

Figure I.B.2. The contour $\mathcal{C}$ with two real time axes. Note that the arrows of time are chosen differently from Fig. I.A.1. Thus $\mathcal{C}_1$ here corresponds to $\mathcal{C}_1$ in Fig. I.A.1. The same holds true for $\mathcal{C}_2$.

The contour with two real time axes has a similar structure as the L-shaped contour (Fig. I.A.1). With the equilibrium time, we can obtain correlations from and within the initial state of the system, whereas the non-equilibrium time deals with correlations that build up after a quench in the parameters of the Hamiltonian. In Sec. I.B.1.2 we will show the equality of the Green functions on the contour with two real axes, with the ground state of the equilibrium Hamiltonian as the initial state, and the finite temperature formulation (Sec. I.A.3) in the limit of $T \to 0$. We note that a large variety of initial states can be implemented, by choosing a corresponding equilibrium Hamiltonian for which the desired initial state is the ground state. Ideas related to the contour with two real time axes were presented in Ref. 53. There, the authors used real-frequency representations of the right- and left-mixing components of the Green function to simplify the computations necessary for non-equilibrium DMFT at zero temperature on the L-shaped contour with a non-interacting initial state.

The exact shape of the contour guarantees that the equilibrium components of a convolution of two Green functions is a function of the time difference of the two time arguments. The tools for the calculus on the new contour are formally the same as Def. (I.A.2) and (I.A.3), the only difference being the shape of the contour. The same holds true for the definition of the Green function:

Definition I.B.8: Contour-ordered Green function

$$G(\mathbf{t}, \mathbf{t}') = -i \left\langle \psi \middle| \mathcal{T}_{\mathcal{C}}\, e^{-i \int_{\mathcal{C}} H(\bar{\mathbf{t}})\, \mathrm{d}\bar{\mathbf{t}}}\, c_{\mathbf{t}}\, c^{\dagger}_{\mathbf{t}'} \middle| \psi \right\rangle \tag{I.B.1}$$

Here $|\psi\rangle$ is the ground state of $H(0)$.

This is the same definition as in the usual non-equilibrium setting (Def. (I.A.4)) in the limit of $\beta \to \infty$, only that the Green function now lives on contour $\mathcal{C}$ (Fig. I.B.2) and not on the L-shaped contour in the Kadanoff-Baym formalism. For the formalism with two real time axes we have similar convolution rules as for the L-shaped contour. We will show in Secs. I.B.1.2 and I.B.1.3 that we can use methods developed for the L-shaped contour also for the new contour, as long as they only depend on addition and contour convolution.

Now, we have the same situation as in the finite temperature case, because there are several components of the Green function depending on where on the contour the time arguments lie. Again, all these components are not independent of each other. Based on the finite temperature formalism, we will give the components names:

Definition I.B.9: Components of Green function

Let $G_{ij}(\mathbf{t},\mathbf{t}') = G(\mathbf{t},\mathbf{t}')$ *where* $\mathbf{t} \in \mathcal{C}_i$ *and* $\mathbf{t}' \in \mathcal{C}_j$ *(Fig. I.B.2). The components of the contour-ordered Green function are defined as follows.*

greater eq.
$$G^{>E}(t_E, t'_E) = G_{-+}(t_E, t'_E) = -i\,\langle \psi \,|\, c(t_E)\, c^\dagger(t'_E) \,|\, \psi \rangle \tag{I.B.2}$$

lesser eq.
$$G^{<E}(t_E, t'_E) = G_{+-}(t_E, t'_E) = i\,\langle \psi \,|\, c^\dagger(t'_E)\, c(t_E) \,|\, \psi \rangle \tag{I.B.3}$$

greater non-eq.
$$G^{>N}(t_N, t'_N) = G_{21}(t_N, t'_N) = -i\,\langle \psi \,|\, c(t_N)\, c^\dagger(t'_N) \,|\, \psi \rangle \tag{I.B.4}$$

lesser non-eq.
$$G^{<N}(t_N, t'_N) = G_{12}(t_N, t'_N) = i\,\langle \psi \,|\, c^\dagger(t'_N)\, c(t_N) \,|\, \psi \rangle \tag{I.B.5}$$

right-mixing
$$G^{\ulcorner}(t_E, t_N) = G_{31}(t_E, t_N) = -i\,\langle \psi \,|\, c(t_E)\, c^\dagger(t_N) \,|\, \psi \rangle \tag{I.B.6}$$

left-mixing
$$G^{\urcorner}(t_N, t_E) = G_{13}(t_N, t_E) = i\,\langle \psi \,|\, c^\dagger(t_E)\, c(t_N) \,|\, \psi \rangle \tag{I.B.7}$$

pre-right-mixing
$$G^{\llcorner}(t_E, t_N) = G_{01}(t_E, t_N) = i\,\langle \psi \,|\, c^\dagger(t_N)\, c(t_E) \,|\, \psi \rangle \tag{I.B.8}$$

pre-left-mixing
$$G^{\lrcorner}(t_N, t_E) = G_{10}(t_N, t_E) = -i\,\langle \psi \,|\, c(t_N)\, c^\dagger(t_E) \,|\, \psi \rangle \tag{I.B.9}$$

retarded non-eq.
$$G^{RN}(t_N, t'_N) = \theta(t_N - t'_N)\ \left(G^{>N}(t_N, t'_N) - G^{<N}(t_N, t'_N)\right) \tag{I.B.10}$$

advanced non-eq.
$$G^{AN}(t_N, t'_N) = \theta(t'_N - t_N)\ \left(G^{<N}(t_N, t'_N) - G^{>N}(t_N, t'_N)\right) \tag{I.B.11}$$

retarded eq.
$$G^{RE}(t_E, t'_E) = \theta(t_E - t'_E)\ \left(G^{>E}(t_E, t'_E) - G^{<E}(t_E, t'_E)\right) \tag{I.B.12}$$

advanced eq.
$$G^{AE}(t_E, t'_E) = \theta(t'_E - t_E)\ \left(G^{<E}(t_E, t'_E) - G^{>E}(t_E, t'_E)\right) \tag{I.B.13}$$

Keldysh eq.
$$G^{KE}(t_E, t'_E) = G^{>E}(t_E, t'_E) + G^{<E}(t_E, t'_E) \tag{I.B.14}$$

where $|\psi\rangle$ *is the ground state of* $H(0)$*. Note that the pre-mixing components* $G^{\llcorner}(t_E, t_N)$ *and* $G^{\lrcorner}(t_N, t_E)$ *are strictly speaking only defined for* $t_E \leq 0$*, but one can easily modify the contour to integrate to positive* t_E *and back to* 0*, before switching to* $\mathcal{C}_1$*.*

We chose the names and symbols in Def. (I.B.9) so that there is correspondence to the notation used in Def. (I.A.5) and in the existing literature[42,49]. For example, the two right-mixing components $G^{\ulcorner}(t_E, t_N)$ and $G^{\ulcorner}_L(\tau, t_N)$ have almost the same definition, the only difference being that we use equilibrium time here instead of imaginary time. There is no apparently corresponding definition for the pre-mixing components in the usual finite temperature formalism, but they are connected to the mixing components at negative imaginary times (see Sec. I.B.1.2). They are basically the same as the mixing components, but the equilibrium time argument lies before the non-equilibrium time argument on the contour. Since such cases exist here, there are more components in Def. (I.B.9) than in Def. (I.A.5).

I.B.1.1 Convolution

For the formalism with two real time axes we have similar convolution rules as above, the only differences coming from the exact shape of the contour. To provide an example we will take a look at the right-mixing component of the convolution $A * B$, like we did in Sec. I.A.3.2 for the L-shaped contour.

$$
\begin{aligned}
(A * B)^{\ulcorner}(t_E, t_N) &= (A * B)_{31}(t_E, t_N) && \text{(I.B.15)} \\
&= \sum_{j=0}^{3} \int A_{3j}(t_E, \bar{\mathbf{t}})\, B_{j1}(\bar{\mathbf{t}}, t_N)\ \mathrm{d}\bar{\mathbf{t}} && \text{(I.B.16)} \\
&= \int_{-\infty}^{0} A_{30}(t_E, \bar{t}_E)\, B_{01}(\bar{t}_E, t_N)\ \mathrm{d}\bar{t}_E && \text{(I.B.17)} \\
&\quad + \int_{0}^{t_N} A_{31}(t_E, \bar{t}_N)\, B_{11}(\bar{t}_N, t_N)\ \mathrm{d}\bar{t}_N \\
&\quad + \int_{t_N}^{0} A_{32}(t_E, \bar{t}_N)\, B_{21}(\bar{t}_N, t_N)\ \mathrm{d}\bar{t}_N \\
&\quad + \int_{0}^{t_E} A_{33}(t_E, \bar{t}_N)\, B_{31}(\bar{t}_E, t_N)\ \mathrm{d}\bar{t}_E \\
&\quad + \int_{t_E}^{-\infty} A_{33}(t_E, \bar{t}_N)\, B_{31}(\bar{t}_E, t_N)\ \mathrm{d}\bar{t}_E
\end{aligned}
$$

In the second line, j marks the region where $\bar{\mathbf{t}}$ lies on the contour. With the suitable components plugged in:

$$\begin{aligned}(A * B)^{\ulcorner}(t_E, t_N) = &\int_{-\infty}^{0} A^{>E}(t_E, \bar{t}_E)\, B^{\llcorner}(\bar{t}_E, t_N)\, \mathrm{d}\bar{t}_E \\ &+ \int_{0}^{t_N} A^{\ulcorner}(t_E, \bar{t}_N)\, B^{<}(\bar{t}_N, t_N)\, \mathrm{d}\bar{t}_N \\ &+ \int_{t_N}^{0} A^{\ulcorner}(t_E, \bar{t}_N)\, B^{>}(\bar{t}_N, t_N)\, \mathrm{d}\bar{t}_N \\ &+ \int_{0}^{t_E} A^{>E}(t_E, \bar{t}_N)\, B^{\ulcorner}(\bar{t}_E, t_N)\, \mathrm{d}\bar{t}_E \\ &+ \int_{t_E}^{-\infty} A^{<E}(t_E, \bar{t}_N)\, B^{\ulcorner}(\bar{t}_E, t_N)\, \mathrm{d}\bar{t}_E\end{aligned} \tag{I.B.18}$$

The second and third line can be combined in a similar way as above.

$$\begin{aligned}(A * B)^{\ulcorner}(t_E, t_N) = &\int_{-\infty}^{0} A^{>E}(t_E, \bar{t}_E)\, B^{\llcorner}(\bar{t}_E, t_N)\, \mathrm{d}\bar{t}_E \\ &+ \int_{0}^{\infty} A^{\ulcorner}(t_E, \bar{t}_N)\, B^{AN}(\bar{t}_N, t_N)\, \mathrm{d}\bar{t}_N \\ &+ \int_{0}^{t_E} A^{>E}(t_E, \bar{t}_N)\, B^{\ulcorner}(\bar{t}_E, t_N)\, \mathrm{d}\bar{t}_E \\ &+ \int_{t_E}^{-\infty} A^{<E}(t_E, \bar{t}_N)\, B^{\ulcorner}(\bar{t}_E, t_N)\, \mathrm{d}\bar{t}_E\end{aligned} \tag{I.B.19}$$

This is the final result for the right-mixing component of the convolution on the contour with two real time axes, similar to the results in Sec. I.A.3.2. Below we will show the connection of this convolution to the convolution of the L-shaped contour in the limit of $\beta \to \infty$.

I.B.1.2 Equality of Green functions on the two Contours in the limit $\beta \to \infty$

In the limit of $\beta \to \infty$, we show that all the information contained in $G_L(\mathbf{t}, \mathbf{t}')$ (see Def. (I.A.5)) is also contained within $G(\mathbf{t}, \mathbf{t}')$. The connection is made possible by taking the expectation values in Def. (I.A.5) in the limit of $\beta \to \infty$. The right-mixing component

(Eq. (I.A.45)) of G_L, for $\tau \geq 0$, in the eigenbasis of $H(0)$ is:

$$G_L^{\ulcorner}(\overbrace{\tau}^{\geq 0}, t_N) = -i \,\langle \psi \,|\, c(\tau)\, c^\dagger(t_N) \,|\, \psi \rangle \tag{I.B.20}$$

$$= -i \sum_n \langle \psi \,|\, c \,|\, n \rangle \,\langle n \,|\, c^\dagger(t_N) \,|\, \psi \rangle \; e^{-\tau(E_n - E_0)} \tag{I.B.21}$$

For $\tau < 0$ which is needed for for the limit $\beta \to \infty$, we need to use the periodicity of fermionic Green functions[42] $(f(-\tau) = -f(\beta - \tau))$:

$$G_L^{\ulcorner}(\overbrace{\tau}^{<0}, t_N) = i \,\langle \psi \,|\, c^\dagger(t_N)\, c(\tau) \,|\, \psi \rangle \tag{I.B.22}$$

$$= i \sum_n \langle \psi \,|\, c^\dagger(t_N) \,|\, n \rangle \,\langle n \,|\, c \,|\, \psi \rangle \; e^{-\tau(E_0 - E_n)} \tag{I.B.23}$$

For the contour with two real axes we will look at the Fourier transform of the right-mixing component (Eq. (I.B.6)) with respect to equilibrium time. After some calculation we get:

$$G^{\ulcorner}(\omega, t_N) = \int_{-\infty}^{\infty} e^{i\omega t_E}\, G^{\ulcorner}(t_E, t_N) \; \mathrm{d}t_E \tag{I.B.24}$$

$$= -i\, 2\pi \sum_n \langle \psi \,|\, c \,|\, n \rangle \,\langle n \,|\, c^\dagger(t_N) \,|\, \psi \rangle \; \delta(\omega - (E_n - E_0)) \tag{I.B.25}$$

$$G^{\llcorner}(\omega, t_N) = \int_{-\infty}^{\infty} e^{i\omega t_E}\, G^{\llcorner}(t_E, t_N) \; \mathrm{d}t_E \tag{I.B.26}$$

$$= i\, 2\pi \sum_n \langle \psi \,|\, c^\dagger(t_N) \,|\, n \rangle \,\langle n \,|\, c \,|\, \psi \rangle \; \delta(\omega - (E_0 - E_n)) \tag{I.B.27}$$

A comparison of Eqs. (I.B.21), (I.B.23), (I.B.25) and (I.B.27) shows, the right-mixing component of the L-shaped contour can be expressed with an integral over the right-mixing and pre-right-mixing component of the contour with two real axes.

$$G_L^{\ulcorner}(\tau, t_N) = \frac{1}{2\pi} \int_{-\infty}^{\infty} e^{-\tau\omega} \; \left(G^{\ulcorner}(\omega, t_N)\, \theta(\tau) + G^{\llcorner}(\omega, t_N)\, \theta(-\tau)\right) \, \mathrm{d}\omega \tag{I.B.28}$$

The same holds true for the left-mixing component, Matsubara component, greater, and lesser component, showing the possibility of doing the computation of the Green function on the contour with two real time axes without information loss.

$$G_L^{\urcorner}(\tau, t_N) = \frac{1}{2\pi} \int_{-\infty}^{\infty} e^{-\tau\omega} \, \left(G^{\urcorner}(\omega, t_N)\, \theta(\tau) + G^{\lrcorner}(\omega, t_N)\, \theta(-\tau)\right) \mathrm{d}\omega \tag{I.B.29}$$

$$G_L^{M}(\tau, \tau') = \frac{1}{i\, 2\pi} \int_{-\infty}^{\infty} e^{-(\tau-\tau')\omega} \, \left(G^{>E}(\omega, t_N)\, \theta(\tau - \tau') + G^{<E}(\omega, t_N)\, \theta(\tau' - \tau)\right) \mathrm{d}\omega \tag{I.B.30}$$

$$G_L^{>N}(t_N, t'_N) = G^{>N}(t_N, t'_N) \tag{I.B.31}$$

$$G_L^{<N}(t_N, t'_N) = G^{<N}(t_N, t'_N) \tag{I.B.32}$$

From Eqs. (I.B.31) and (I.B.32) automatically follows that the retarded and advanced non-equilibrium components are also equal between the L-shaped contour and the contour with two real time axes.

I.B.1.3 Equality After Contour Convolution

Non-equilibrium DMFT makes heavy use of the contour convolution. To check if we can use the existing non-equilibrium DMFT framework for the contour with two real time axes, we need to show whether the relations Eqs. (I.B.28) to (I.B.32) between generic Green functions on the L-shaped contour and the contour with two real time axes hold true after convolution over their respective contours. In mathematical terms:

$$C \equiv A * B \qquad \text{(...on the contour with two real time axes)} \tag{I.B.33}$$

$$C_L \equiv A_L * B_L \qquad \text{(...on the L-shaped contour)} \tag{I.B.34}$$

Based on the properties of the Green function in the previous subsection (Sec. I.B.1.2) we require the following properties for A and B:

$$\forall \omega \leq 0 : \; A^{>E}(\omega) = A^{\ulcorner}(\omega, t_N) = A^{\urcorner}(t_N, \omega) = 0 \tag{I.B.35}$$

$$\forall \omega \geq 0 : \; A^{<E}(\omega) = A^{\llcorner}(\omega, t_N) = A^{\lrcorner}(t_N, \omega) = 0 \tag{I.B.36}$$

These assumptions are motivated by the Fourier transform of the Green function (Sec. VI.1), because we assume that the ground state is unique. We assume that these properties shall hold true for all generic functions on the contour with two real time axes. Then, we need to show the following if Eqs. (I.B.28) to (I.B.32) shall hold true after convolution:

$$C_L^{\ulcorner}(\tau, t_N) \overset{?}{=} \frac{1}{2\pi} \int_{-\infty}^{\infty} e^{-\tau\omega} \, \left(C^{\ulcorner}(\omega, t_N)\,\theta(\tau) + C^{\llcorner}(\omega, t_N)\,\theta(-\tau)\right) \mathrm{d}\omega \tag{I.B.37}$$

$$C_L^{\urcorner}(\tau, t_N) \overset{?}{=} \frac{1}{2\pi} \int_{-\infty}^{\infty} e^{-\tau\omega} \, \left(C^{\urcorner}(\omega, t_N)\,\theta(\tau) + C^{\lrcorner}(\omega, t_N)\,\theta(-\tau)\right) \mathrm{d}\omega \tag{I.B.38}$$

$$C_L^{M}(\tau, \tau') \overset{?}{=} \frac{1}{i\,2\pi} \int_{-\infty}^{\infty} e^{-(\tau-\tau')\omega} \, \left(C^{>E}(\omega, t_N)\,\theta(\tau-\tau') + C^{<E}(\omega, t_N)\,\theta(\tau'-\tau)\right) \mathrm{d}\omega \tag{I.B.39}$$

$$C_L^{>N}(t_N, t'_N) \overset{?}{=} C^{>N}(t_N, t'_N) \tag{I.B.40}$$

$$C_L^{<N}(t_N, t'_N) \overset{?}{=} C^{<N}(t_N, t'_N) \tag{I.B.41}$$

The detailed calculation for the right-mixing component is done here, in the main text. The corresponding calculations of the other components are located in the appendix. First, we start out by writing the definition of $C^{\ulcorner}(t_E, t_N)$.

$$\begin{aligned} C^{\ulcorner}(t_E, t_N) = & \int_{-\infty}^{0} A^{>E}(t_E, \bar{t}_E)\, B^{\llcorner}(\bar{t}_E, t_N)\ \mathrm{d}\bar{t}_E \\ & + \int_{0}^{t_N} A^{\ulcorner}(t_E, \bar{t}_N)\, B^{<N}(\bar{t}_N, t_N)\ \mathrm{d}\bar{t}_N \\ & + \int_{t_N}^{0} A^{\ulcorner}(t_E, \bar{t}_N)\, B^{>N}(\bar{t}_N, t_N)\ \mathrm{d}\bar{t}_N \\ & + \int_{0}^{t_E} A^{>E}(t_E, \bar{t}_E)\, B^{\ulcorner}(\bar{t}_E, t_N)\ \mathrm{d}\bar{t}_E \\ & + \int_{t_E}^{-\infty} A^{<E}(t_E, \bar{t}_E)\, B^{\ulcorner}(\bar{t}_E, t_N)\ \mathrm{d}\bar{t}_E \end{aligned} \tag{I.B.42}$$

The next step is to replace the integration over $\bar{t}_E$ with an integration in frequency space.

$$C^{\ulcorner}(t_E, t_N) = \frac{1}{4\pi^2} \int_{-\infty}^{\infty} \int_{-\infty}^{\infty} \int_{-\infty}^{0} A^{>E}(\omega')\, B^{\llcorner}(\omega'', t_N)\, e^{-i\omega'(t_E - \bar{t}_E)}\, e^{-i\omega''\bar{t}_E}\ \mathrm{d}\bar{t}_E\ \mathrm{d}\omega'\ \mathrm{d}\omega'' \tag{I.B.43}$$

$$+ \int_{0}^{\infty} A^{\ulcorner}(t_E, \bar{t}_N)\, B^{AN}(\bar{t}_N, t_N)\ \mathrm{d}\bar{t}_N$$

$$+ \frac{1}{4\pi^2} \int_{-\infty}^{\infty} \int_{-\infty}^{\infty} \int_{0}^{t_E} A^{>E}(\omega')\, B^{\ulcorner}(\omega'', t_N)\, e^{-i\omega'(t_E - \bar{t}_E)}\, e^{-i\omega''\bar{t}_E}\ \mathrm{d}\bar{t}_E\ \mathrm{d}\omega'\ \mathrm{d}\omega''$$

$$+ \frac{1}{4\pi^2} \int_{-\infty}^{\infty} \int_{-\infty}^{\infty} \int_{t_E}^{-\infty} A^{<E}(\omega')\, B^{\ulcorner}(\omega'', t_N)\, e^{-i\omega'(t_E - \bar{t}_E)}\, e^{-i\omega''\bar{t}_E}\ \mathrm{d}\bar{t}_E\ \mathrm{d}\omega'\ \mathrm{d}\omega''$$

$$= -\frac{i}{4\pi^2} \int_{-\infty}^{\infty} \int_{-\infty}^{\infty} A^{>E}(\omega')\, B^{\llcorner}(\omega'', t_N)\, \frac{e^{-it_E\omega'}}{\omega' - \omega'' - i0^+}\ \mathrm{d}\omega'\ \mathrm{d}\omega'' \tag{I.B.44}$$

$$+ \int_{0}^{\infty} A^{\ulcorner}(t_E, \bar{t}_N)\, B^{AN}(\bar{t}_N, t_N)\ \mathrm{d}\bar{t}_N$$

$$- \frac{i}{4\pi^2} \int_{-\infty}^{\infty} \int_{-\infty}^{\infty} A^{>E}(\omega')\, B^{\ulcorner}(\omega'', t_N)\, \frac{e^{-i\omega''t_E} - e^{-i\omega' t_E}}{\omega' - \omega''}\ \mathrm{d}\omega'\ \mathrm{d}\omega''$$

$$+ \frac{i}{4\pi^2} \int_{-\infty}^{\infty} \int_{-\infty}^{\infty} A^{<E}(\omega')\, B^{\ulcorner}(\omega'', t_N)\, \frac{e^{-it_E\omega''}}{\omega' - \omega'' - i0^+}\ \mathrm{d}\omega'\ \mathrm{d}\omega''$$

Here, the 0^+ is to be read as $\lim_{\eta \to 0^+} \eta$ and is needed for the regularization of the integrals over $\bar{t}_E$. This is the same technique, used to Fourier transform retarded and advanced Green functions[89] and is layed out in more detail in Sec. VI.3.1. The Fourier transform is trivial to perform with $\int_{-\infty}^{\infty} e^{ixp}\ \mathrm{d}p = 2\pi\,\delta(x)$ (Ref. 97).

$$C^{\ulcorner}(\omega, t_N) = -\frac{i}{2\pi} \int_{-\infty}^{\infty} A^{>E}(\omega)\, B^{\llcorner}(\omega'', t_N)\, \frac{1}{\omega - \omega'' - i0^+}\ \mathrm{d}\omega'' \tag{I.B.45}$$

$$+ \int_{0}^{\infty} A^{\ulcorner}(\omega, \bar{t})\, B^{AN}(\bar{t}, t_N)\ \mathrm{d}\bar{t}$$

$$- \frac{i}{2\pi} \int_{-\infty}^{\infty} A^{>E}(\omega')\, B^{\ulcorner}(\omega, t_N)\, \frac{1}{\omega' - \omega}\ \mathrm{d}\omega'$$

$$+ \frac{i}{2\pi} \int_{-\infty}^{\infty} A^{>E}(\omega)\, B^{\ulcorner}(\omega'', t_N)\, \frac{1}{\omega - \omega''}\ \mathrm{d}\omega''$$

$$+ \frac{i}{2\pi} \int_{-\infty}^{\infty} A^{<E}(\omega')\, B^{\ulcorner}(\omega, t_N)\, \frac{1}{\omega' - \omega - i0^+}\ \mathrm{d}\omega'$$

This equation could further simplified, using the Dirac identity[18] $\frac{1}{x \pm i0^+} = \mathcal{P}(\frac{1}{x}) \mp i\pi\delta(x)$, where $\mathcal{P}$ is the Cauchy principal value. We will do a similar approach (Sec. VI.3.2), that uses information about the products $A^{>E}(\omega)\, B^{\llcorner}(\omega'', t_N)$ and $A^{<E}(\omega')\, B^{\ulcorner}(\omega, t_N)$ and makes it easier to compare the result with the calculation on the L-shaped contour. After doing the calculation as layed out in Sec. VI.3.2 we arrive at:

$$\begin{aligned}
C^{\ulcorner}(\omega, t_N) = &-\frac{i}{2\pi} \int_{-\infty}^{\infty} A^{>E}(\omega)\, B^{\llcorner}(\omega'', t_N)\, \frac{1}{\omega - \omega'' + 0^+}\ \mathrm{d}\omega'' \\
&+ \int_{0}^{\infty} A^{\ulcorner}(\omega, \bar{t})\, B^{AN}(\bar{t}, t_N)\ \mathrm{d}\bar{t} \\
&- \frac{i}{2\pi} \int_{-\infty}^{\infty} A^{>E}(\omega')\, B^{\ulcorner}(\omega, t_N)\, \frac{1}{\omega' - \omega}\ \mathrm{d}\omega' \\
&+ \frac{i}{2\pi} \int_{-\infty}^{\infty} A^{>E}(\omega)\, B^{\ulcorner}(\omega'', t_N)\, \frac{1}{\omega - \omega''}\ \mathrm{d}\omega'' \\
&+ \frac{i}{2\pi} \int_{-\infty}^{\infty} A^{<E}(\omega')\, B^{\ulcorner}(\omega, t_N)\, \frac{1}{\omega' - \omega - 0^+}\ \mathrm{d}\omega' \\
&+ \frac{1}{2} \left(A^{>E}(\omega)\, B^{\llcorner}(\omega, t_N) - A^{<E}(\omega)\, B^{\ulcorner}(\omega, t_N) \right)
\end{aligned} \tag{I.B.46}$$

The last line has the dirac delta already integrated out, and vanishes according to the assumptions Eqs. (I.B.35) and (I.B.36). To compare this result with the result of the L-shaped contour the last step is to integrate over ω (Eq. (I.B.28)).

$$\begin{aligned}
\frac{1}{2\pi} \int_{-\infty}^{\infty} C^{\ulcorner}(\omega, t_N)\, e^{-\tau\omega}\ \mathrm{d}\omega = &-\frac{i}{4\pi^2} \int_{-\infty}^{\infty} \int_{-\infty}^{\infty} A^{>E}(\omega')\, B^{\llcorner}(\omega'', t_N)\, \frac{e^{-\tau\omega'}}{\omega' - \omega'' + 0^+}\ \mathrm{d}\omega'\ \mathrm{d}\omega'' \\
&+ \frac{1}{2\pi} \int_{-\infty}^{\infty} \int_{0}^{\infty} A^{\ulcorner}(\omega', \bar{t})\, B^{AN}(\bar{t}, t_N)\, e^{-\tau\omega'}\ \mathrm{d}\bar{t}\ \mathrm{d}\omega' \\
&- \frac{i}{4\pi^2} \int_{-\infty}^{\infty} \int_{-\infty}^{\infty} A^{>E}(\omega')\, B^{\ulcorner}(\omega'', t_N)\, \frac{e^{-\tau\omega''}}{\omega' - \omega''}\ \mathrm{d}\omega'\ \mathrm{d}\omega'' \\
&+ \frac{i}{4\pi^2} \int_{-\infty}^{\infty} \int_{-\infty}^{\infty} A^{>E}(\omega')\, B^{\ulcorner}(\omega'', t_N)\, \frac{e^{-\tau\omega'}}{\omega' - \omega''}\ \mathrm{d}\omega'\ \mathrm{d}\omega'' \\
&+ \frac{i}{4\pi^2} \int_{-\infty}^{\infty} \int_{-\infty}^{\infty} A^{<E}(\omega')\, B^{\ulcorner}(\omega'', t_N)\, \frac{e^{-\tau\omega''}}{\omega' - \omega'' - 0^+}\ \mathrm{d}\omega'\ \mathrm{d}\omega''
\end{aligned} \tag{I.B.47}$$

The corresponding calculation for the pre-right-mixing components yields:

$$
\begin{aligned}
\frac{1}{2\pi}\int_{-\infty}^{\infty} C^{\llcorner}(\omega, t_N)\, e^{-\tau\omega}\ \mathrm{d}\omega = -\frac{i}{4\pi^2}\int_{-\infty}^{\infty}\int_{-\infty}^{\infty} A^{>E}(\omega')\, B^{\llcorner}(\omega'', t_N)\, \frac{e^{-\tau\omega''}}{\omega' - \omega'' + 0^+}\ \mathrm{d}\omega'\ \mathrm{d}\omega'' \qquad \text{(I.B.48)}\\
-\frac{i}{4\pi^2}\int_{-\infty}^{\infty}\int_{-\infty}^{\infty} A^{<E}(\omega')\, B^{\llcorner}(\omega'', t_N)\, \frac{e^{-\tau\omega'}}{\omega' - \omega''}\ \mathrm{d}\omega'\ \mathrm{d}\omega''\\
+\frac{i}{4\pi^2}\int_{-\infty}^{\infty}\int_{-\infty}^{\infty} A^{<E}(\omega')\, B^{\llcorner}(\omega'', t_N)\, \frac{e^{-\tau\omega''}}{\omega' - \omega''}\ \mathrm{d}\omega'\ \mathrm{d}\omega''\\
+\frac{1}{2\pi}\int_{-\infty}^{\infty}\int_{0}^{\infty} A^{\llcorner}(\omega', \bar{t}_N)\, B^{AN}(\bar{t}_N, t_N)\, e^{-\tau\omega'}\ \mathrm{d}\bar{t}_N\ \mathrm{d}\omega'\\
+\frac{i}{4\pi^2}\int_{-\infty}^{\infty}\int_{-\infty}^{\infty} A^{<E}(\omega')\, B^{\ulcorner}(\omega'', t_N)\, \frac{e^{-\tau\omega'}}{\omega' - \omega'' - 0^+}\ \mathrm{d}\omega'\ \mathrm{d}\omega''
\end{aligned}
$$

In the case of the L-shaped contour, we start with the definition of the convolution.

$$
\begin{aligned}
C_L^{\ulcorner}(\tau, t_N) &= \int_0^{t_N} A_L^{\ulcorner}(\tau, \bar{t}_N)\, B_L^{<N}(\bar{t}_N, t_N)\ \mathrm{d}\bar{t}_N \qquad \text{(I.B.49)}\\
&\quad + \int_{t_N}^{0} A_L^{\ulcorner}(\tau, \bar{t}_N)\, B_L^{>N}(\bar{t}_N, t_N)\ \mathrm{d}\bar{t}_N\\
&\quad + \int_{-\infty}^{\infty} A_L^{M}(\tau - \bar{\tau})\, B_L^{\ulcorner}(\bar{\tau}, t_N)\ \mathrm{d}\bar{\tau}\\
&= \int_0^{\infty} A_L^{\ulcorner}(\tau, \bar{t})\, B_L^{AN}(\bar{t}, t_N)\ \mathrm{d}\bar{t}\\
&\quad + \int_{-\infty}^{\infty} A_L^{M}(\tau - \bar{\tau})\, B_L^{\ulcorner}(\bar{\tau}, t_N)\ \mathrm{d}\bar{\tau}
\end{aligned}
$$

Let us first start with the case $\tau \geq 0$. With the corresponding integration limits we get:

$$
\begin{aligned}
C_L^{\ulcorner}(\tau, t_N) &= \int_0^{\infty} A_L^{\ulcorner}(\tau, \bar{t}_N)\, B_L^{AN}(\bar{t}_N, t_N)\ \mathrm{d}\bar{t}_N \qquad \text{(I.B.50)}\\
&\quad + \int_{-\infty}^{0} A_L^{M}(\tau - \bar{\tau})\, B_L^{\ulcorner}(\bar{\tau}, t_N)\ \mathrm{d}\bar{\tau}\\
&\quad + \int_{0}^{\tau} A_L^{M}(\tau - \bar{\tau})\, B_L^{\ulcorner}(\bar{\tau}, t_N)\ \mathrm{d}\bar{\tau}\\
&\quad + \int_{\tau}^{\infty} A_L^{M}(\tau - \bar{\tau})\, B_L^{\ulcorner}(\bar{\tau}, t_N)\ \mathrm{d}\bar{\tau}
\end{aligned}
$$

In the next step, we replace the right-mixing and Matsubara components with Eqs. (I.B.28) and (I.B.30) and integrate out the τ.

$$\begin{aligned}
C_L^{\ulcorner}(\tau, t_N) = \frac{1}{2\pi} \int_{-\infty}^{\infty} \int_{0}^{\infty} \; & A^{\ulcorner}(\omega', \bar{t}_N) \, B^{AN}(\bar{t}_N, t_N) \, e^{-\tau\omega'} \; \mathrm{d}\bar{t}_N \, \mathrm{d}\omega' && \text{(I.B.51)} \\
& - \frac{i}{4\pi^2} \int_{-\infty}^{\infty} \int_{-\infty}^{\infty} \int_{-\infty}^{0} \; A^{>E}(\omega') \, e^{-(\tau-\bar{\tau})\omega'} \; B^{\llcorner}(\omega'', t_N) \, e^{-\bar{\tau}\omega''} \; \mathrm{d}\bar{\tau} \, \mathrm{d}\omega' \; \mathrm{d}\omega'' \\
& - \frac{i}{4\pi^2} \int_{-\infty}^{\infty} \int_{-\infty}^{\infty} \int_{0}^{\tau} \; A^{>E}(\omega') \, e^{-(\tau-\bar{\tau})\omega'} \; B^{\ulcorner}(\omega'', t_N) \, e^{-\bar{\tau}\omega''} \; \mathrm{d}\bar{\tau} \, \mathrm{d}\omega' \; \mathrm{d}\omega'' \\
& - \frac{i}{4\pi^2} \int_{-\infty}^{\infty} \int_{-\infty}^{\infty} \int_{\tau}^{\infty} \; A^{<E}(\omega') \, e^{-(\tau-\bar{\tau})\omega'} \; B^{\ulcorner}(\omega'', t_N) \, e^{-\bar{\tau}\omega''} \; \mathrm{d}\bar{\tau} \, \mathrm{d}\omega' \; \mathrm{d}\omega'' \\
= \frac{1}{2\pi} \int_{-\infty}^{\infty} \int_{0}^{\infty} \; & A^{\ulcorner}(\omega', \bar{t}_N) \, B^{AN}(\bar{t}_N, t_N) \, e^{-\tau\omega'} \; \mathrm{d}\bar{t}_N \, \mathrm{d}\omega' && \text{(I.B.52)} \\
& - \frac{i}{4\pi^2} \int_{-\infty}^{\infty} \int_{-\infty}^{\infty} \; A^{>E}(\omega') \, B^{\llcorner}(\omega'', t_N) \, \frac{e^{-\tau\omega'}}{\omega' - \omega'' + 0^+} \; \mathrm{d}\omega' \; \mathrm{d}\omega'' \\
& - \frac{i}{4\pi^2} \int_{-\infty}^{\infty} \int_{-\infty}^{\infty} \; A^{>E}(\omega') \, B^{\ulcorner}(\omega'', t_N) \, \frac{e^{-\tau\omega''} - e^{-\tau\omega'}}{\omega' - \omega''} \; \mathrm{d}\omega' \; \mathrm{d}\omega'' \\
& + \frac{i}{4\pi^2} \int_{-\infty}^{\infty} \int_{-\infty}^{\infty} \; A^{<E}(\omega') \, B^{\ulcorner}(\omega'', t_N) \, \frac{e^{-\tau\omega''}}{\omega' - \omega'' - 0^+} \; \mathrm{d}\omega' \; \mathrm{d}\omega''
\end{aligned}$$

Like above, the 0^+ stems from the regularization of the integral over τ.

These regularizations are possible, because we required $\forall\omega < 0 : \; A^{>E}(\omega) = B^{\ulcorner}(\omega, t_N) = 0$ and $\forall\omega > 0 : \; A^{<E}(\omega) = B^{\llcorner}(\omega, t_N) = 0$. A comparison of Eq. (I.B.47) and Eq. (I.B.52) shows that these equations are the same and this proves Eq. (I.B.37) for $\tau \geq 0$. The corresponding result for $\tau < 0$ is:

$$\begin{aligned}
C_L^{\ulcorner}(\tau, t_N) = \frac{1}{2\pi} \int_{-\infty}^{\infty} \int_{0}^{\infty} \; & A^{\llcorner}(\omega', \bar{t}_N) \, B^{AN}(\bar{t}_N, t_N) \, e^{-\tau\omega'} \; \mathrm{d}\bar{t} \; \mathrm{d}\omega' && \text{(I.B.53)} \\
& - \frac{i}{4\pi^2} \int_{-\infty}^{\infty} \int_{-\infty}^{\infty} \; A^{>E}(\omega') \, B^{\llcorner}(\omega'', t_N) \, \frac{e^{-\tau\omega''}}{\omega' - \omega'' + 0^+} \; \mathrm{d}\omega' \; \mathrm{d}\omega'' \\
& - \frac{i}{4\pi^2} \int_{-\infty}^{\infty} \int_{-\infty}^{\infty} \; A^{<E}(\omega') \, B^{\llcorner}(\omega'', t_N) \, \frac{e^{-\tau\omega'} - e^{-\tau\omega''}}{\omega' - \omega''} \; \mathrm{d}\omega' \; \mathrm{d}\omega'' \\
& + \frac{i}{4\pi^2} \int_{-\infty}^{\infty} \int_{-\infty}^{\infty} \; A^{<E}(\omega') \, B^{\ulcorner}(\omega'', t_N) \, \frac{e^{-\tau\omega'}}{\omega' - \omega'' - 0^+} \; \mathrm{d}\omega' \; \mathrm{d}\omega''
\end{aligned}$$

A comparison of Eq. (I.B.48) and Eq. (I.B.53) shows that these equations are the same and this proves Eq. (I.B.37) for $\tau < 0$. To summarize the calculation so far, we have shown that the right-mixing component of the convolution over the L-shaped contour can be expressed in convolutions over the contour with two real axes (Eqs. (I.B.28) and (I.B.37)). In the appendix (Sec. VI.4) it is shown that similar relations hold for the other components of the convolution, i.e. Eqs. (I.B.28) to (I.B.32) hold true after convolution. To show that these equations carry on the result of a convolution we relied on the properties Eqs. (I.B.35) and (I.B.36). Because the convolution in DMFT is iterated several times we need to check whether Eqs. (I.B.35) and (I.B.36) carry over to the result of a convolution. To this end, we will take a closer look at the right-mixing component.

$$\begin{aligned}\forall\omega \le 0:\ C^{\ulcorner}(\omega, t_N) = &-\frac{i}{2\pi}\int_{-\infty}^{\infty} \underbrace{A^{>E}(\omega)}_{=0}\ B^{\llcorner}(\omega'', t_N)\,\frac{1}{\omega - \omega'' + 0^+}\ \mathrm{d}\omega'' \\ &+ \int_0^{\infty} \underbrace{A^{\ulcorner}(\omega, \bar{t})}_{=0}\ B^{AN}(\bar{t}, t_N)\ \mathrm{d}\bar{t} \\ &- \frac{i}{2\pi}\int_{-\infty}^{\infty} A^{>E}(\omega')\ \underbrace{B^{\ulcorner}(\omega, t_N)}_{=0}\,\frac{1}{\omega' - \omega}\ \mathrm{d}\omega' \\ &+ \frac{i}{2\pi}\int_{-\infty}^{\infty} \underbrace{A^{>E}(\omega)}_{=0}\ B^{\ulcorner}(\omega'', t_N)\,\frac{1}{\omega - \omega''}\ \mathrm{d}\omega'' \\ &+ \frac{i}{2\pi}\int_{-\infty}^{\infty} A^{<E}(\omega')\ \underbrace{B^{\ulcorner}(\omega, t_N)}_{=0}\,\frac{1}{\omega' - \omega - 0^+}\ \mathrm{d}\omega' \\ &+ \frac{1}{2}\left(\underbrace{A^{>E}(\omega)}_{=0}\ B^{\llcorner}(\omega, t_N) - A^{<E}(\omega)\ \underbrace{B^{\ulcorner}(\omega, t_N)}_{=0}\right) \\ = 0 &\end{aligned} \tag{I.B.54}$$

The analogous equalities for the other components can easily be checked in the appendix, Sec. VI.4, where all components in Fourier space are listed. This means, if an algorithm on the L-shaped contour in the limit of $\beta \to \infty$ relies only on convolution and addition, we can use the contour with two real time axes instead.

I.B.2 Exploiting Symmetries at $T = 0$

I.B.2.1 Effective Contour

In this section we describe two effective contours to compute the impurity Green function. To compute the Green function of the impurity one does not need to use the full contour as depicted in Fig. I.B.2. The full contour is needed to (i) perform a consistent convolution, because the effective contour described below does not preserve time translational invariance on the equilibrium axis after convolution, and (ii) for the solution of the mapping problem (Sec. I.B.3), where we perform a Fourier transform with respect to equilibrium time to obtain e.g. Eq. (I.B.98). A closer inspection of Def. (I.B.9) shows that we did not perform the time-evolution along the infinite equilibrium axis starting from $-\infty$, but started from $t_E = 0$. One can show that this time-evolution path is valid for the computation of the impurity Green function. For example, the right-mixing component:

$$\begin{aligned} G^{\ulcorner}(t_E, t_N) &= -i \lim_{R\to\infty} \langle \psi \,|\, \mathcal{U}(-R,0)\, c(t_E)\, c^\dagger(t_N) \mathcal{U}(0,-R) \,|\, \psi \rangle && \text{(I.B.55)} \\ &= -i \lim_{R\to\infty} e^{-iE_\psi R} \, \langle \psi \,|\, c(t_E)\, c^\dagger(t_N) \,|\, \psi \rangle \; e^{iE_\psi R} && \text{(I.B.56)} \\ &= -i \, \langle \psi \,|\, c(t_E)\, c^\dagger(t_N) \,|\, \psi \rangle && \text{(I.B.57)} \end{aligned}$$

This is again the same formula as in Def. (I.B.9). Here E_ψ is the ground state energy of the system at $t_N = 0$, and the time-evolution operator applied to the ground state is just a phase factor that gets canceled from line two to three

This implies that the computation of the impurity Green function only involved two smaller contours depicted in Fig. I.B.3. Experience shows that for large $|t_E|$ the Green function tends to zero, so we only need to choose a suitable $t_{E,\max}$ when computing the Green function. If the algorithm employed does not allow a high enough $t_{E,\max}$, one usually uses a tool called linear prediction[98,99] (see Sec. VI.2).

The contours above do not include the pre-mixing components. This is not a problem, because the pre-mixing components of the Green function can be computed from the mixing

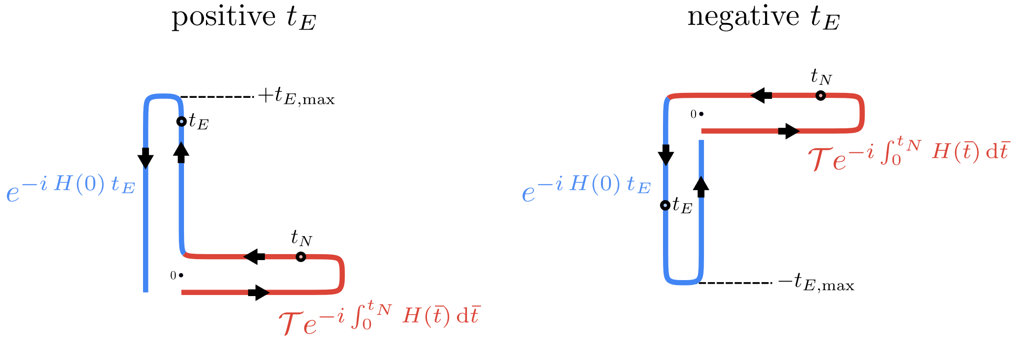

Figure I.B.3. Contours used for computing the impurity Green function.

components.

$$-\left(G^{\ulcorner}(t_E, t_N)\right)^* = -i\,\left(\langle\psi\,|\,c(t_E)\,c^\dagger(t_N)\,|\,\psi\rangle\right)^* \tag{I.B.58}$$

$$= -i\,\langle\psi\,|\,c(t_N)\,c^\dagger(t_E)\,|\,\psi\rangle \tag{I.B.59}$$

$$= G^{\lrcorner}(t_N, t_E) \tag{I.B.60}$$

Similarly for the pre-right-mixing component:

$$-\left(G^{\urcorner}(t_N, t_E)\right)^* = i\,\left(\langle\psi\,|\,c^\dagger(t_E)\,c(t_N)\,|\,\psi\rangle\right)^* \tag{I.B.61}$$

$$= i\,\langle\psi\,|\,c^\dagger(t_N)\,c(t_E)\,|\,\psi\rangle \tag{I.B.62}$$

$$= G^{\llcorner}(t_E, t_N) \tag{I.B.63}$$

Note that these two smaller contours and symmetries can only be used when computing the impurity Green function, whereas the contour convolutions necessary non-equilibrium DMFT involve the full contour of Fig. I.B.2.

I.B.2.2 Iterative Time-Evolution Scheme for Green Functions

Suppose we have a method (more on that later) to efficiently store states and apply operators to them. One possible method to efficiently compute the Green function is written in Alg. (I.B.4) and sketched in Fig. I.B.4. Like in many applications involving continuous functions we discretize the Green function along a grid of nodes or *time slices* with respect to equilibrium and non-equilibrium time. For example the right-mixing component:

$$G^{\ulcorner}(t_E, t_N) \longrightarrow G^{\ulcorner}(m\,\Delta t, n\,\Delta t) \tag{I.B.64}$$

$$m \in \mathbb{Z} \tag{I.B.65}$$

$$n \in \mathbb{N} \tag{I.B.66}$$

Algorithm I.B.4: Integration scheme for computing the Green function with Hamiltonian based solvers

We assume that we have the Green functions listed below up to some current $t_{N,max}$*. The non-equilibrium is by definition restricted to* $t_N \geq 0$*. We now want to compute them up to* $t_{N,max} + \Delta t$*, i.e. we want to compute:*

- $G^{>N}(t_{N,max} + \Delta t, t_N) \qquad \forall t_N \leq t_{N,max} + \Delta t$
- $G^{>N}(t_N, t_{N,max} + \Delta t) \qquad \forall t_N \leq t_{N,max} + \Delta t$
- $G^{<N}(t_{N,max} + \Delta t, t_N) \qquad \forall t_N \leq t_{N,max} + \Delta t$
- $G^{<N}(t_N, t_{N,max} + \Delta t) \qquad \forall t_N \leq t_{N,max} + \Delta t$
- $G^{\ulcorner}(t_E, t_{N,max} + \Delta t) \qquad \forall\, |t_E| \leq t_{E,max}$
- $G^{\llcorner}(t_E, t_{N,max} + \Delta t) \qquad \forall\, |t_E| \leq t_{E,max}$
- $G^{\urcorner}(t_{N,max} + \Delta t, t_E) \qquad \forall\, |t_E| \leq t_{E,max}$
- $G^{\lrcorner}(t_{N,max} + \Delta t, t_E) \qquad \forall\, |t_E| \leq t_{E,max}$

Furthermore, we assume that we know the time-evolved ground state $|\psi(t_{N,max})\rangle$ *and have stored in memory.*

1. *Time-evolve (Eqs.* (I.A.34) *and* (I.B.220)*)* $|\psi(t_{N,max})\rangle$ *to the next time slice*

$$|\psi(t_{N,max} + \Delta t)\rangle = \mathcal{U}(t_{N,max} + \Delta t, t_{N,max}))\;|\psi(t_{N,max})\rangle \tag{I.B.67}$$

2. *Apply creation and annihilation operators*

$$\big|\varphi(t_{N,max} + \Delta t)\big\rangle = c^{\dagger}\ \big|\psi(t_{N,max} + \Delta t)\big\rangle \tag{I.B.68}$$

$$\big|\chi(t_{N,max} + \Delta t)\big\rangle = c\ \big|\psi(t_{N,max} + \Delta t)\big\rangle \tag{I.B.69}$$

3. *For $t_N \in [t_{N,\ max} + \Delta t,\ t_{N,max}, t_{N,max} - \Delta t,\ \dots,\ 2\,\Delta t,\ 1\,\Delta t]$:*

   (a) *Compute Green functions*

$$G^{>N}(t_N, t_{N,max} + \Delta t) = -i\ \langle \psi(t_N)\,|\, c\,|\,\varphi(t_N)\rangle \tag{I.B.70}$$

$$G^{<N}(t_{N,max} + \Delta t, t_N) = i\ \langle \psi(t_N)\,\big|\, c^{\dagger}\,\big|\,\chi(t_N)\rangle \tag{I.B.71}$$

   (b) *Evolve $|\varphi\rangle$ and $|\chi\rangle$ (and also $|\psi\rangle$ if not stored in memory) backwards in time*

$$|\varphi(t_N - \Delta t)\rangle = \mathcal{U}(t_N - \Delta t, t_N)\ |\varphi(t_N)\rangle \tag{I.B.72}$$

$$|\chi(t_N - \Delta t)\rangle = \mathcal{U}(t_N - \Delta t, t_N)\ |\chi(t_N)\rangle \tag{I.B.73}$$

$$|\psi(t_N - \Delta t)\rangle = \mathcal{U}(t_N - \Delta t, t_N)\ |\psi(t_N)\rangle \tag{I.B.74}$$

4. *Apply creation and annihilation operators*

$$|\varphi_0(0)\rangle = c^{\dagger}\ |\psi(0)\rangle \tag{I.B.75}$$

$$|\chi_0(0)\rangle = c\ |\psi(0)\rangle \tag{I.B.76}$$

5. *For $t_E \in [0,\ 1\,\Delta t,\ 2\,\Delta t, \dots,\ t_{E,max}]$:*

   (a) *Compute Green function (E_ψ is the ground state energy of $H(0)$)*

$$G^{\ulcorner}(t_E, t_{N,max} + \Delta t) = -i\, e^{it_E E_\psi}\ \langle \varphi_0(t_E)\,|\,\varphi(0)\rangle \tag{I.B.77}$$

$$G^{\urcorner}(t_{N,max} + \Delta t, t_E) = i\, e^{it_E E_\psi}\ \langle \chi_0(t_E)\,|\,\chi(0)\rangle \tag{I.B.78}$$

(b) Time-evolve $|\varphi_0\rangle$ and $|\chi_0\rangle$

$$|\varphi_0(t_E + \Delta t)\rangle = e^{i\,\Delta t\,H(0)}\;|\varphi_0(t_E)\rangle \tag{I.B.79}$$

$$|\chi_0(t_E + \Delta t)\rangle = e^{i\,\Delta t\,H(0)}\;|\chi_0(t_E)\rangle \tag{I.B.80}$$

Because $|\varphi_0(t_E)\rangle$ and $|\chi_0(t_E)\rangle$ are the same for all t_N, they may be stored in memory if their size allows it.

6. For $t_E \in [0,\ -1\,\Delta t,\ -2\,\Delta t,\ \ldots,\ -t_{E,max}]$:

(a) Compute Green function (E_ψ is the ground state energy of $H(0)$)

$$G^{\ulcorner}(t_E, t_{N,max} + \Delta t) = -i\,e^{it_E E_\psi}\;\langle\varphi_0(t_E)\,|\,\varphi(0)\rangle \tag{I.B.81}$$

$$G^{\urcorner}(t_{N,max} + \Delta t, t_E) = i\,e^{it_E E_\psi}\;\langle\chi_0(t_E)\,|\,\chi(0)\rangle \tag{I.B.82}$$

(b) Time-evolve $|\varphi_0\rangle$ and $|\chi_0\rangle$

$$|\varphi_0(t_E - \Delta t)\rangle = e^{-i\,\Delta t\,H(0)}\;|\varphi_0(t_E)\rangle \tag{I.B.83}$$

$$|\chi_0(t_E - \Delta t)\rangle = e^{-i\,\Delta t\,H(0)}\;|\chi_0(t_E)\rangle \tag{I.B.84}$$

Because $|\varphi_0(t_E)\rangle$ and $|\chi_0(t_E)\rangle$ are the same for all t_N, they may be stored in memory if their size allows it.

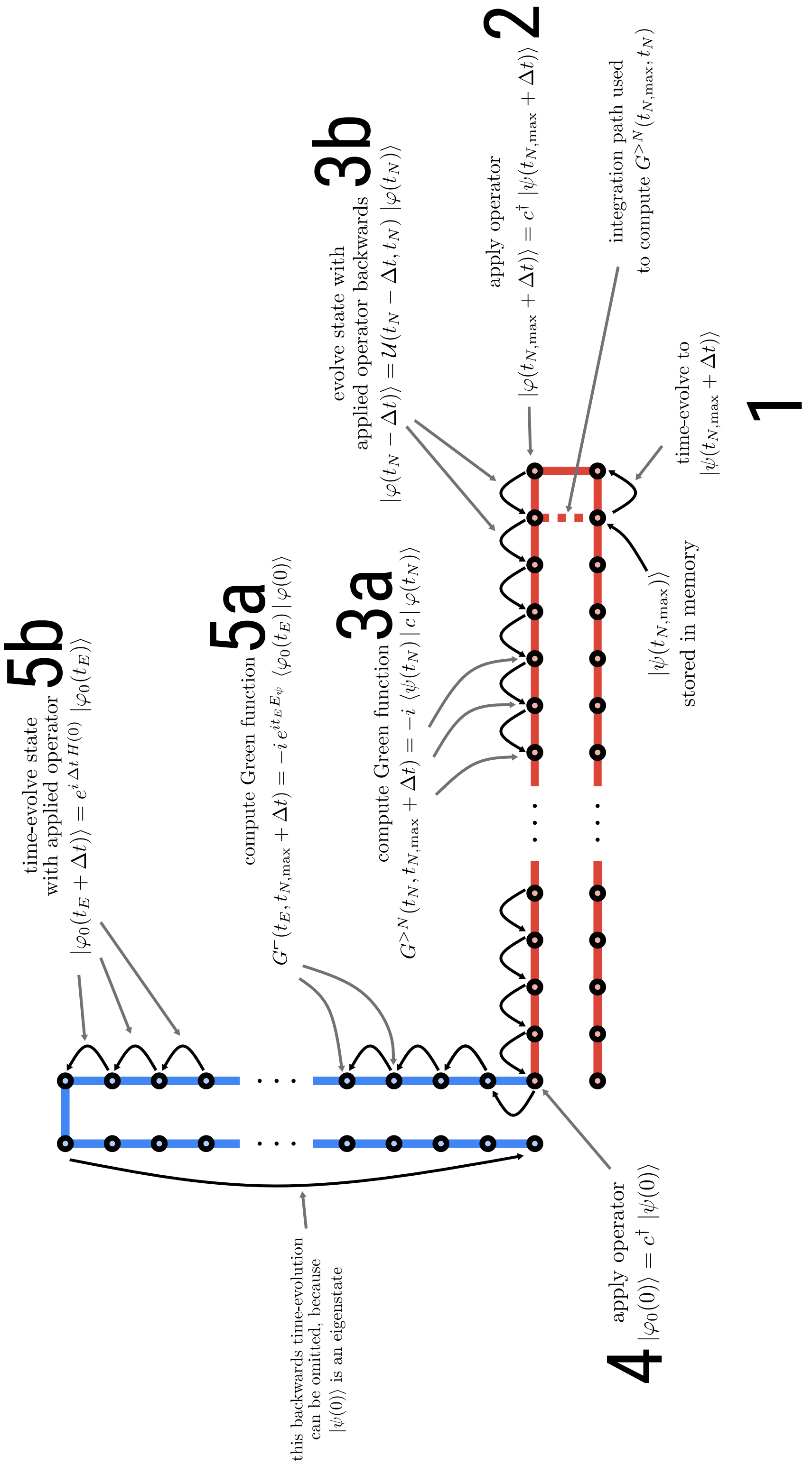

Figure I.B.4. Graphical illustration of Alg. (I.B.4), with the same numbering of steps. Only the computation of the greater and right-mixing component are shown.

I.B.3 Computation of the Anderson Impurity Hamiltonian Parameters

In this section we will follow and extend Refs. 49 and 50 to our contour with two real time axes. The goal is to compute the values of Hamiltonian parameters of the Anderson Impurity Model for a given hybridization function. The context here is the DMFT loop, where one computes the hybridization function from the previously obtained Green function and in turn needs to compute the Green function of the new iteration according to the new hybridization function. In order to obtain the impurity Green function of the new iteration with a Hamiltonian based solver, one needs to map the hybridization function to Hamiltonian parameters of the Anderson Impurity Model. Following Ref. 49 we split the hybridization function into two parts:

$$\Delta(\mathbf{t},\mathbf{t}') = \Delta_{-}(\mathbf{t},\mathbf{t}') + \Delta_{+}(\mathbf{t},\mathbf{t}') \tag{I.B.85}$$

The first hybridization function Δ_- is defined so that it is equal to the total hybridization function if one of the time arguments is on the equilibrium axis. The second hybridization function is simply the difference between the total hybridization function and the first hybridization function.

$$\Delta_{-}^{\ulcorner} = \Delta^{\ulcorner} \tag{I.B.86}$$

$$\Delta_{-}^{\llcorner} = \Delta^{\llcorner} \tag{I.B.87}$$

$$\Delta_{-}^{\urcorner} = \Delta^{\urcorner} \tag{I.B.88}$$

$$\Delta_{-}^{\lrcorner} = \Delta^{\lrcorner} \tag{I.B.89}$$

$$\Delta_{+} = \Delta - \Delta_{-} \tag{I.B.90}$$

Accompanying these two hybridization functions there are two baths coupled to the impurity with their own set of Hamiltonian parameters V_-, ϵ_- and V_+, ϵ_+. We will call the bath stemming from Δ_- initial bath or first bath and the bath stemming from Δ_+ second bath. The splitting of the original hybridization into the first and second hybridization function is performed to simplify the mapping problem. The first bath is used to describe the initial equilibrium state of the system and its correlations with states at non-zero non-equilibrium time, while the second bath deals with correlations that build up during the quench of the Hamiltonian parameters of the lattice system.

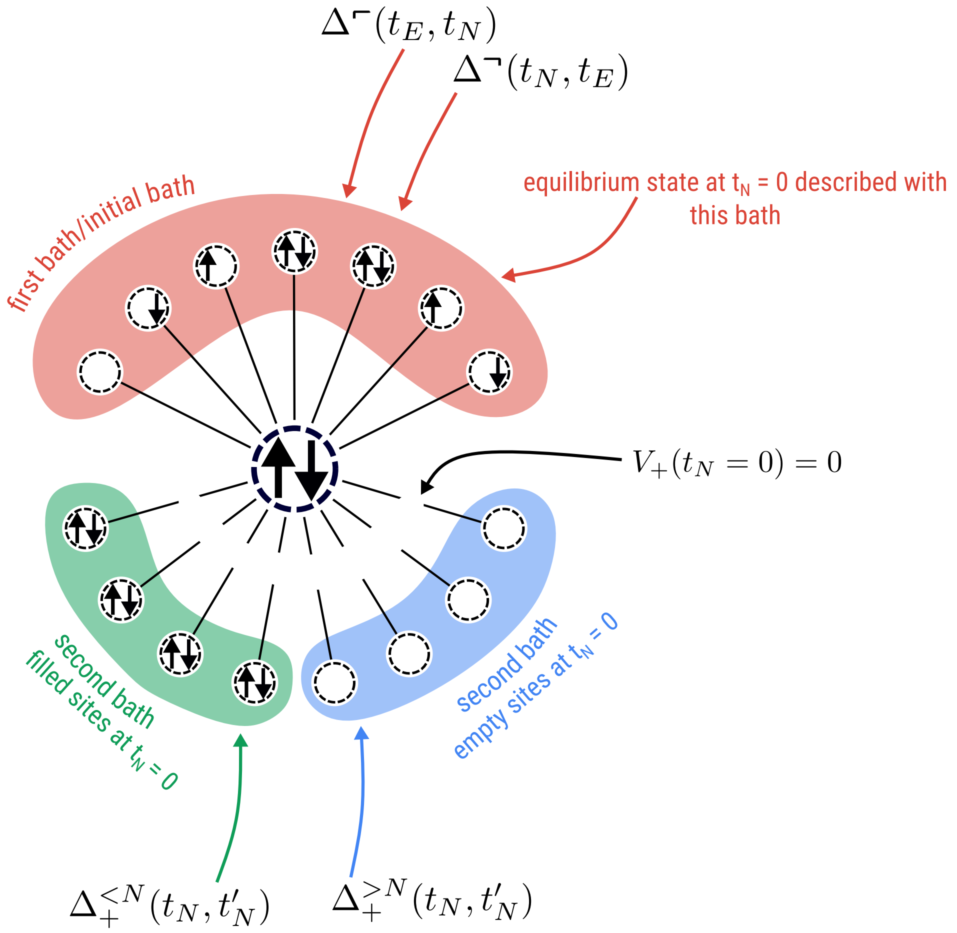

Figure I.B.5. Illustration of the two baths. The mixing components of the hybridization function $\Delta^{\ulcorner/\urcorner} = \Delta_{\_}^{\ulcorner/\urcorner}$ are used to obtain the Anderson Impurity Model Hamiltonian parameters of the first bath. The greater non-equilibrium and lesser non-equilibrium components of the second hybridization function $\Delta_+ = \Delta - \Delta_{\_}$ are used to obtain the Anderson Impurity Model Hamiltonian parameters of the second bath. By construction the second bath is decoupled from the impurity at $t_N = 0$. Note that the depicted occupation of the impurity and the first bath are just one basis state used to represent the state. The depicted occupation of the second bath is the actual basis state used at $t_N = 0$.

I.B.3.1 Initial Bath, $\Delta_{\_}$

The parameters $V_{\_}$ and $\epsilon_{\_}$ are obtained from the initial hybridization function $\Delta_{\_}$ which is by definition equal to the total hybridization function if at least one of the function arguments lies on the equilibrium axis of the contour. Because the non-equilibrium DMFT formalism with the non-equilibrium axis removed is equal to equilibrium DMFT, V_- and ϵ_- describe the initial equilibrium state and its correlations with states at non-zero non-equilibrium time.

To obtain a relation between V_-, ϵ_- and the hybridization function Δ, we start from Eq. (I.A.98) for the Anderson Impurity Model, where the removed site 0 is the impurity. In Eq. (I.A.98) for the Anderson Impurity Model all higher order terms vanish, because the bath sites are isolated after the removal of the impurity. We will drop the spin index for sake of brevity and arrive at:

$$\Delta(\mathbf{t},\mathbf{t}') = \sum_p V_p(\mathbf{t}) V_p(\mathbf{t}')^* \, g_p(\mathbf{t},\mathbf{t}') \tag{I.B.91}$$

Here g_p are the Green functions of isolated bath sites, emerging from the removal of the impurity. In explicit form they can be written as[42,49,50]:

$$g_p(\mathbf{t},\mathbf{t}') = -i \left[\theta_{\mathcal{C}}(\mathbf{t},\mathbf{t}') - \theta(-\epsilon+\mu)\right] \, e^{-i(\epsilon_p-\mu)(\mathbf{t}-\mathbf{t}')} \tag{I.B.92}$$

The subtraction $\mathbf{t}-\mathbf{t}'$ is meant in way that the information of the contour is ignored and subtraction is the difference of the numerical values of $\mathbf{t}$ and $\mathbf{t}'$. To get this result one needs to assume that the ϵ_p are not time-dependent, which is not a problem here as every time-dependency can be pulled into the hoppings V_p, as shown for example in Ref. 49. To simplify the calculation for the first bath one can transform the sum into an integral with $\rho(\epsilon) = \sum_p \delta(\epsilon - \epsilon_p)$. Thus, the hybridization function has the form:

$$\Delta(\mathbf{t},\mathbf{t}') = -i \int \rho(\epsilon) V(\epsilon,\mathbf{t}) \, V(\epsilon,\mathbf{t}')^* \, \left[\theta_{\mathcal{C}}(\mathbf{t},\mathbf{t}') - \theta(-\epsilon+\mu)\right] \, e^{-i(\epsilon-\mu)(\mathbf{t}-\mathbf{t}')} \, \mathrm{d}\epsilon \tag{I.B.93}$$

The bath density of states of the initial bath ρ_- can assumed to be constant and absorbed into the hybridization function[49]. The bath parameters will be discretized again later. In this subsection we deal with the initial bath only.

$$\Delta_-(\mathbf{t},\mathbf{t}') = -i \int V_-(\epsilon,\mathbf{t}) \, V_-(\epsilon,\mathbf{t}')^* \, \left[\theta_{\mathcal{C}}(\mathbf{t},\mathbf{t}') - \theta(-\epsilon+\mu)\right] \, e^{-i(\epsilon-\mu)(\mathbf{t}-\mathbf{t}')} \, \mathrm{d}\epsilon \tag{I.B.94}$$

To provide a better orientation: This is equation (41) from Ref. 49 with g already plugged in. Similar to in Ref. 49 we will use the use the fact that the bath hopping parameters cannot depend on equilibrium time and will use a Fourier transform. The whole reason we defined the contour with two real time axes is that this Fourier transform can easily be done!

First, we look at the left-mixing component of the hybridization function.

$$\Delta^{\neg}(t_N, t_E) = i \int V_-(\epsilon, t_N)\, V_-(\epsilon, 0)^*\, \theta(-\epsilon + \mu)\, e^{-i(\epsilon-\mu)(t_N - t_E)}\, \mathrm{d}\epsilon \tag{I.B.95}$$

The Fourier transform can easily be done with[97]:

$$\int_{-\infty}^{\infty} e^{it(x-a)}\, \mathrm{d}t = 2\pi\, \delta(x-a) \tag{I.B.96}$$

$$\begin{aligned}
\Delta^{\neg}(t_N, \omega) &= \int \Delta^{\neg}(t_N, t_E)\, e^{i\omega t_E}\, \mathrm{d}t_E && \text{(I.B.97)}\\
&= i\, 2\pi\, V_-(\mu-\omega, t_N)\, V_-(\mu-\omega, 0)^*\, \theta(\omega)\, e^{i\omega t_N} && \text{(I.B.98)}
\end{aligned}$$

Substituting $\epsilon = \omega - \mu$ gives us our intermediate result:

$$V_-(\epsilon, t_N) = -\frac{i}{2\pi}\, \frac{1}{V_-(\epsilon, 0)^*}\, e^{i(\epsilon-\mu)t_N}\, \Delta^{\neg}(t_N, \mu - \epsilon) \tag{I.B.99}$$

with the restriction $\epsilon < \mu$. The right-mixing component is dealt with similarly.

$$\begin{aligned}
\Delta^{\invneg}(t_E, t_N) &= -i \int V_-(\epsilon, 0)\, V_-(\epsilon, t_N)^*\, (1 - \theta(-\epsilon + \mu))\, e^{-i(\epsilon-\mu)(t_E - t_N)}\, \mathrm{d}\epsilon && \text{(I.B.100)}\\
&= -i \int V_-(\epsilon, 0)\, V_-(\epsilon, t_N)^*\, \theta(\epsilon - \mu)\, e^{-i(\epsilon-\mu)(t_E - t_N)}\, \mathrm{d}\epsilon && \text{(I.B.101)}
\end{aligned}$$

Again, the Fourier transform is easily done with Eq. (I.B.96).

$$\begin{aligned}
\Delta^{\invneg}(\omega, t_N) &= \int \Delta^{\invneg}(t_E, t_N)\, e^{i\omega t_E}\, \mathrm{d}t_E && \text{(I.B.102)}\\
&= -i\, 2\pi\, V_-(\omega+\mu, 0)\, V_-(\omega+\mu, t_N)^*\, \theta(\omega)\, e^{i\omega t_N} && \text{(I.B.103)}
\end{aligned}$$

Complex conjugate both sides of the equation and substitute $\epsilon = \omega + \mu$ an we will get our next intermediate result.

$$V_{-}(\epsilon, t_N) = -\frac{i}{2\pi}\,\frac{1}{V_{-}(\epsilon,0)^*}\,e^{i(\epsilon-\mu)t_N}\,\Delta^{\ulcorner}(\epsilon-\mu, t_N)^* \tag{I.B.104}$$

with the restriction $\epsilon > \mu$.

Now, combining Eq. (I.B.99) and Eq. (I.B.104) yields an expression for the hopping amplitude.

$$V_{-}(\epsilon, t_N) = -\frac{i}{2\pi}\,\frac{1}{V_{-}(\epsilon,0)^*}\,e^{i(\epsilon-\mu)t_N}\,\cdot\,\begin{cases}\Delta^{\urcorner}(t_N, \mu-\epsilon) & \text{if } \epsilon < \mu\\ \Delta^{\ulcorner}(\epsilon-\mu, t_N)^* & \text{if } \epsilon > \mu\end{cases} \tag{I.B.105}$$

and for $t = 0$:

$$|V_{-}(\epsilon,0)|^2 = -\frac{i}{2\pi}\,\left(\Delta^{\urcorner}(0,\mu-\epsilon)\,\theta(-\epsilon+\mu) + \Delta^{\ulcorner}(\epsilon-\mu,0)^*\,\theta(\epsilon-\mu)\right) \tag{I.B.106}$$

The Heaviside θ functions are mutually exclusive, and are already contained in $\Delta^{\urcorner}(0, \mu-\epsilon)$ and $Delta^{\ulcorner}(\epsilon-\mu, 0)^*$ (see Eqs. (I.B.98) and (I.B.103)). Furthermore, the left hand side of the equation is real. From this it follows that Fourier transformed hybridization functions at $t_N = 0$ must be purely imaginary and the complex conjugate operation is equal to sign inversion.

$$|V_{-}(\epsilon,0)|^2 = \frac{i}{2\pi}\,\left(\Delta^{\ulcorner}(\epsilon-\mu,0) - \Delta^{\urcorner}(0,\mu-\epsilon)\right) \tag{I.B.107}$$

We emphasize that in contrast to Ref. 49 no analytical continuation from the complex axis to the real axis is needed to compute the bath parameters.

To do a Fourier transform of e.g. $\Delta^{\urcorner}(t_N, t_E)$ needs the function on the infinite interval $t_E \in (-\infty, \infty)$. In practice, this data is impossible to obtain, so we use the tool linear prediction (Sec. VI.2) to extrapolate the data for $t_E > t_{E,\max}$. Sometimes, it is difficult to do a linear prediction for the functions $\Delta^{\urcorner}(t_N, t_E)$ and $\Delta^{\ulcorner}(t_E, t_N)$, because they do not tend to zero fast enough. To work around this problem, we rewrite Eq. (I.B.105). Here, we will use the convolution theroem:

$$\mathcal{F}[f * g] = (\mathcal{F}[f] \cdot \mathcal{F}[g]) \tag{I.B.108}$$

$$(f * g)(t) = \int f(\tilde{t})\, g(t - \tilde{t})\ \mathrm{d}\tilde{t} \tag{I.B.109}$$

We will again write equation I.B.105 as a sum similar to Eq. (I.B.107).

$$V_{-}(\epsilon, t_N) = -\frac{i}{2\pi} \frac{1}{V_{-}(\epsilon, 0)^*} \left(e^{i(\epsilon-\mu)t_N} \Delta^{\urcorner}(t_N, \mu - \epsilon) + e^{i(\epsilon-\mu)t_N} \Delta^{\ulcorner}(\epsilon - \mu, t_N)^* \right) \tag{I.B.110}$$

After Fourier transforming all terms of the right hand side separately and then combining them with the convolution theorem one arrives at the following result:

$$V_{-}(\epsilon, t_N) = -\frac{i}{2\pi} \frac{1}{V_{-}(\epsilon, 0)^*} \mathcal{F}[e^{-i\mu t_E} \left(\Delta^{\urcorner}(t_N, -(t_E - t_N)) + \Delta^{\ulcorner}(-(t_E - t_N), t_N)^*\right)] \tag{I.B.111}$$

We found that it is generally easier to perform a linear prediction for $(\Delta^{\urcorner}(t_N, -(t_E - t_N)) + \Delta^{\ulcorner}(-(t_E - t_N), t_N)^*)$ than for the two terms separately.

I.B.3.2 Rediscretization of Inital Bath

So far we have found a representation of the hoppings with continuous energies ϵ. Because a Hamiltonian based solver can only deal with a finite number of bath sites, one must integrate over intervals of the continuous solution to get a discretized result. Here, we choose the $\epsilon_{p,-}$ of the Hamiltonian to be equidistantly distributed over the relevant energy window with a distance of $\Delta\epsilon = \epsilon_{p,-} - \epsilon_{p-1,-}$

$$\text{continuous:} \qquad V_{-}(\epsilon, t_N) = f(\epsilon, t_N) \tag{I.B.112}$$

$$\text{discrete:} \qquad V_{p,-}(t_N) = \int_{\epsilon_p - \frac{\Delta\epsilon}{2}}^{\epsilon_p + \frac{\Delta\epsilon}{2}} V_{-}(\epsilon, t_N)\ \mathrm{d}\epsilon \tag{I.B.113}$$

One can easily verify that the discrete bath parameters solve Eq. (I.B.94) under the assumption that enough bath sites are used and discretization errors do not dominate.

I.B.3.3 Second Bath, Δ_+

As shown in Sec. I.B.1.2, Green functions where both arguments lie on the non-equilibrium time axis have the same value on (i) the contour with two real time axes and (ii) the L-shaped contour in the limit $\beta \to 0$. By construction, all the mixing components of the second bath are equal to zero (neglecting discretization errors), meaning that all hopping parameters of the second bath are equal to zero at $t_N = 0$. Thus, the bath parameters stemming from Δ_+ can be computed exactly the same as in Ref. 49. We will review the process briefly here. Note that the second bath can be viewed as two separated baths, one which is occupied at $t_N = 0$ and one which is empty $t_N = 0$.

For the second bath the same relation between the Hamiltonian parameters and the hybridization function as in Eqs. (I.B.91) and (I.B.93) must hold true.

$$\Delta(\mathbf{t}, \mathbf{t}') = -i \sum_p V_{p,+}(\mathbf{t}) V_{p,+}(\mathbf{t}')^* \; [\theta_C(\mathbf{t}, \mathbf{t}') - \theta(-\epsilon + \mu)] \; e^{-i(\epsilon_p - \mu)(\mathbf{t} - \mathbf{t}')} \tag{I.B.114}$$

At this point the occupation of the bath sites at $t_N = 0$ and the ϵ_p for the second bath can be chosen freely. The trick used in Ref. 49 is to separate the bath sites into occupied at $t_N = 0$ and unoccupied at $t_N = 0$ and to use two different values for $\epsilon_p(t_N = 0)$ and $\epsilon_p(t_N \neq 0)$. The initial value $\epsilon_p(t_N = 0)$ is chosen so that the occupation is either zero or one and the second value is set to $\epsilon_p(t_N \neq 0) = \mu$ so the exponential function in Eq. (I.B.114) vanishes. For our contour with two real time axes there is no need to use two different values for $\epsilon_p(t_N = 0)$ and $\epsilon_p(t_N \neq 0)$ and one can simply set:

$$\epsilon_p = \begin{cases} \mu - 0^+ & \text{if bath site } p \text{ is occupied at } t_N = 0 \\ \mu + 0^+ & \text{if bath site } p \text{ is unoccupied at } t_N = 0 \end{cases} \tag{I.B.115}$$

These settings of occupation and value for ϵ_p vastly simplify the computation of the bath parameters. As a reminder: We can freely choose the initial occupation and ϵ_p for the second bath, because the second bath is decoupled from the impurity at $t_N = 0$ by construction,

$V_+(0) = 0$. After plugging Eq. (I.B.115) into Eq. (I.B.93) we get:

$$-i\,\Delta_+^{<N}(t_N, t'_N) = \sum_{p,\text{occupied}} V_{p,+}(t_N)V_{p,+}(t'_N)^* \tag{I.B.116}$$

$$i\,\Delta_+^{>N}(t_N, t'_N) = \sum_{p,\text{unoccupied}} V_{p,+}(t_N)V_{p,+}(t'_N)^* \tag{I.B.117}$$

This is equation (52) in Ref. 49. The quantities $-i\,\Delta_+^{<N}(t_N, t'_N)$ and $i\,\Delta_+^{>N}(t_N, t'_N)$ can be viewed as matrices where the matrix indices are the time steps on the contour. Then, the computation of the path parameters $V_{p,+}(t_N)$ can be viewed as a matrix decomposition of the form $M = VV^\dagger$ and there are several different algorithms to do that, e.g. diagonalization of M. However, the low-rank Cholesky decomposition has some unique properties making it a well suited algorithm in this scenario. To use the Cholesky decomposition $-i\,\Delta_+^{<N}(t_N, t'_N)$ and $i\,\Delta_+^{>N}(t_N, t'_N)$ must be positive definite, which is shown to hold true in Ref. 49. A desirable property of the Cholesky decomposition is that the addition of a new time step on the non-equilibrium axis does not change the hopping amplitudes of the previous time steps. This would not hold true if one would use the diagonalization of M.

We will now describe a possible iterative process to find a good low-rank Cholesky decomposition of a matrix $M = VV^\dagger$ and follow Ref. 49. If $M_{t_n,t'_n} = -i\,\Delta_+^{<N}(t_N, t'_N)$, then $V_{t_n,p} = V_{+,p}(t_N)$ is the hopping matrix for the bath sites of the second bath that are occupied in the initial state. If $M_{t_n,t'_n} = i\,\Delta_+^{>N}(t_N, t'_N)$, then $V_{t_n,p} = V_{+,p}(t_N)$ is the hopping matrix for the bath sites of the second bath that are unoccupied in the initial state. This process is illustrated in Fig. I.B.6. The context here is that with every time-step addded on the non-equilibrium axis in the DMFT loop, we couple two new bath sites of the second to the impurity, one that was occupied in the initial state and one that was unoccupied in the initial state. This process continues until there are not any bath sites left to couple to the impurity due to the finite bath size. Then, one must find a suitable low-rank Cholesky approximation. The authors of Ref. 49 claim that one can use the classical exact Cholesky decomposition if the number of time steps is lower than the bath sites of the second bath. We cannot verify this fact, because M is numerical not positive definite due to the finite system size and finite time-step, which introduce discretization errors. Hence, we do not use the exact Cholesky decomposition, but solve a minimization problem from the very first time step on the non-equilibrium axis.

We will write M and V in block matrix form and assume that we already computed the low-rank Cholesky decomposition of the upper left block of M, which is the result of the previous iteration step.

$$M = \begin{pmatrix} \tilde{M} & m_r \\ m_l & m_d \end{pmatrix} \qquad V = \begin{pmatrix} \tilde{V} & 0 \\ v^\dagger & w \end{pmatrix} \qquad \tilde{M} \approx \tilde{V}\,\tilde{V}^\dagger \tag{I.B.118}$$

$$M \in \mathbb{C}^{N\times N} \quad \tilde{M} \in \mathbb{C}^{(N-1)\times(N-1)} \quad m_r \in \mathbb{C}^{(N-1)\times 1} \quad m_l \in \mathbb{C}^{1\times(N-1)} \quad m_d \in \mathbb{C}$$
$$V \in \mathbb{C}^{N\times N} \quad \tilde{V} \in \mathbb{C}^{(N-1)\times(N-1)} \quad v^\dagger \in \mathbb{C}^{1\times(N-1)} \quad w \in \mathbb{R}$$

V is a matrix that grows in p-dimension (columns) until the number of time steps is greater than the number of assigned bath sites of the second bath. If the number of time steps is greater than the number of assigned bath sites, we set w to zero und the non-zero entries of V can only grow in the time-dimension (rows). Now, under the assumption that we already found a good approximation for $\tilde{M} \approx \tilde{V}\,\tilde{V}^\dagger$, we want to find a good approximation for $M \approx VV^\dagger$, which results in the following minimization problem:

$$\left\|M - VV^\dagger\right\|^2 \tag{I.B.119}$$

$$= \left\| \begin{pmatrix} \tilde{M} & m_r \\ m_l & m_d \end{pmatrix} - \begin{pmatrix} \tilde{V} & 0 \\ v^\dagger & w \end{pmatrix} \begin{pmatrix} \tilde{V}^\dagger & v \\ 0 & w \end{pmatrix} \right\|^2 \tag{I.B.120}$$

$$= \left\| \begin{pmatrix} \tilde{M} & m_r \\ m_l & m_d \end{pmatrix} - \begin{pmatrix} \tilde{V}\,\tilde{V}^\dagger & \tilde{V}\,v \\ v^\dagger\,\tilde{V}^\dagger & v^\dagger\,v - w^2 \end{pmatrix} \right\|^2 \tag{I.B.121}$$

$$= \left\| \begin{pmatrix} \tilde{M} - \tilde{V}\,\tilde{V}^\dagger & m_r - \tilde{V}\,v \\ m_l - v^\dagger\,\tilde{V}^\dagger & m_d - v^\dagger\,v + w^2 \end{pmatrix} \right\|^2 \tag{I.B.122}$$

$$\approx \left\| \begin{pmatrix} 0 & m_r - \tilde{V}\,v \\ m_l - v^\dagger\,\tilde{V}^\dagger & m_d - v^\dagger\,v + w^2 \end{pmatrix} \right\|^2 \tag{I.B.123}$$

$\|\cdot\|$ is the Euclidean matrix norm. From the second last to the last line we used the fact that we already minimized $\left\|\tilde{M} - \tilde{V}\tilde{V}^\dagger\right\|^2$ in the previous time step. To find a good low-rank Cholesky decomposition we minimize Eq. (I.B.123) with respect to v if the maximum number of bath sites is reached and with respect to v and w if it is possible to couple more bath sites from the second bath to the impurity.

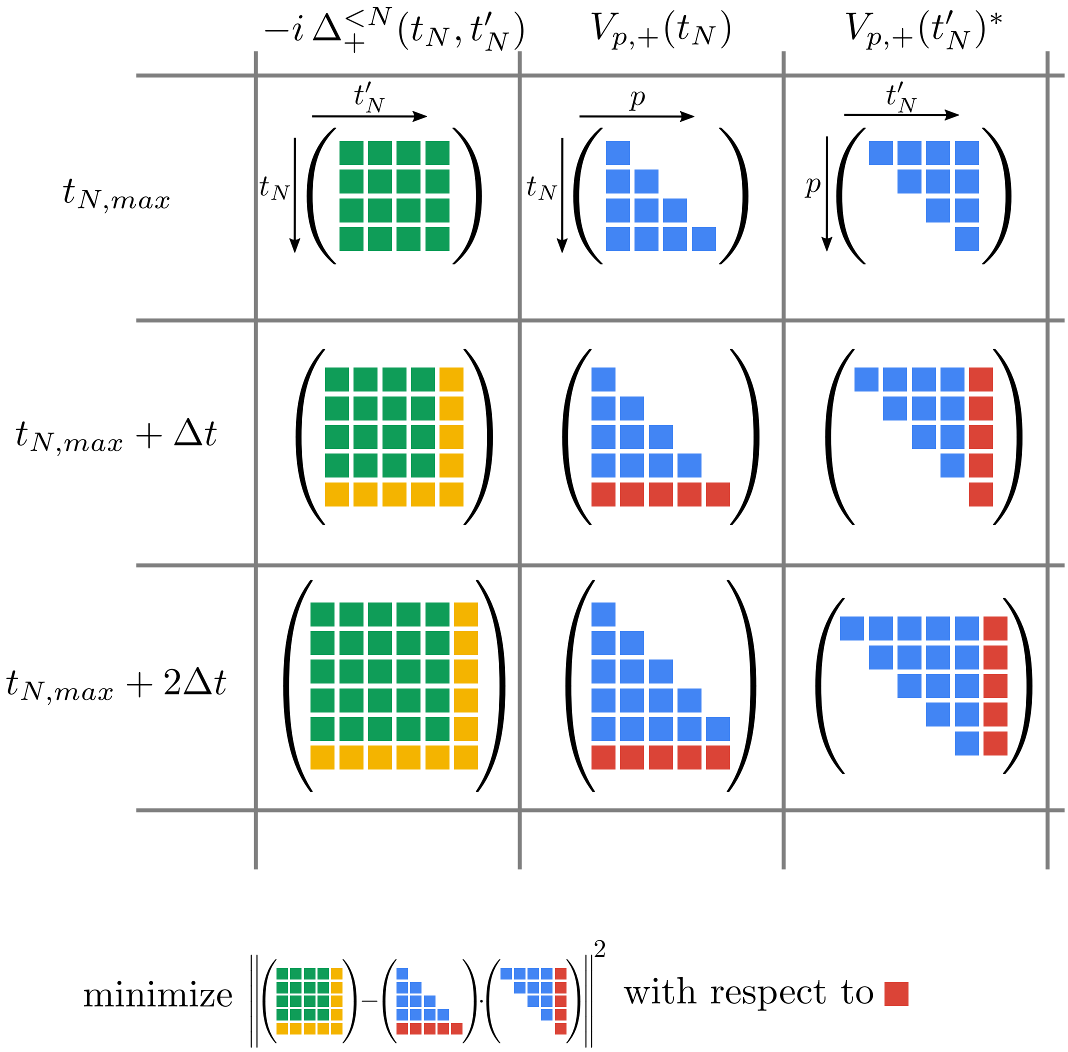

Figure I.B.6. Graphical representation of the low-rank Cholesky decomposition for 5 bath sites. Note that the matrices of the hopping amplitudes cannot grow anymore after 5 time steps in the p index. At every new time step new entries are added to $-i\,\Delta_{+}^{<N}(t_N, t'_N)$ (yellow), which results to the addition of a new row to V_+ (red).

Algorithm I.B.5: Summary: Computation of the bath parameters of the Anderson Impurity Model

In the present thesis we will always use 99 bath sites for the first bath and 100 bath sites for the second bath. Context: Here we consider the case, where the non-equilibrium DMFT loop is repeated for every subsequent time step (see Fig. I.A.3, top right) and *assume that the non-equilibrium DMFT loop is already converged up to some* $t_{N,max}$*. A vastly simplified version of the DMFT loop (Alg. (I.A.3)) reads as follows:*

$$\cdots \rightarrow \Delta^{(n-1)} \rightarrow G_{IMP}^{(n)} \rightarrow \Delta^{(n)} \rightarrow G_{IMP}^{(n+1)} \rightarrow \ldots \tag{I.B.124}$$

Here, (n) *is the DMFT loop iteration index. The impurity solver computes the impurity Green function up to* $t_{N,max} + \Delta t$ *and from which one obtains updated entries for the hybridization function* Δ *up to* $t_{N,max} + \Delta t$*. In order for a Hamiltonian based impurity solver to compute the Green function according to a hybridization function, one needs to compute suitable Hamiltonian parameters for the Anderson Impurity model. Because the DMFT loop is already converged up to some* $t_{N,max}$*, one only needs to compute the Hamiltonian parameters for* $t_N = t_{N,max} + \Delta t$ *here. Note that we choose the* $\epsilon_{p,-}$ *of the first bath to be equidistantly distributed over the relevant energy window with a distance of* $\Delta\epsilon = \epsilon_{p,-} - \epsilon_{p-1,-}$ *For all the equations below the following holds true:* $t'_N \leq t_N + \Delta t$*.*

1. *Compute the continuous hopping amplitudes of the first bath and discretize*

$$\begin{aligned} V_{-}(\epsilon, t_N + \Delta t) = -\frac{i}{2\pi}\frac{1}{V_{-}(\epsilon, 0)^*}\,\mathcal{F}[e^{-i\mu t_E}(\Delta^{\urcorner}(t_N, -(t_E - t_N - \Delta t)) \\ + \Delta^{\ulcorner}(-(t_E - t_N), t_N + \Delta t)^*)] \end{aligned} \tag{I.B.125}$$

$$V_{p,-}(t_N + \Delta t) = \int_{\epsilon_p - \frac{\Delta\epsilon}{2}}^{\epsilon_p + \frac{\Delta\epsilon}{2}} V_{-}(\epsilon, t_N + \Delta t)\ \mathrm{d}\epsilon \tag{I.B.126}$$

2. *Compute the resulting* $> N$ *and* $< N$ *components of the first hybridization function*

$$\Delta_{-}^{>N}(t_N+\Delta t,t'_N) = -i\int V_{-}(\epsilon,t_N+\Delta t)\,V_{-}(\epsilon,t'_N)^{*}\;[1-\theta(-\epsilon+\mu)]\; e^{-i(\epsilon-\mu)(t_N+\Delta t-t'_N)}\,\mathrm{d}\epsilon \tag{I.B.127}$$

$$\Delta_{-}^{>N}(t'_N,t_N+\Delta t) = -i\int V_{-}(\epsilon,t'_N)\,V_{-}(\epsilon,t_N+\Delta t)^{*}\;[1-\theta(-\epsilon+\mu)]\; e^{-i(\epsilon-\mu)(t'_N-t_N-\Delta t)}\,\mathrm{d}\epsilon \tag{I.B.128}$$

$$\Delta_{-}^{<N}(t_N+\Delta t,t'_N) = i\int V_{-}(\epsilon,t_N+\Delta t)\,V_{-}(\epsilon,t'_N)^{*}\,\theta(-\epsilon+\mu)\; e^{-i(\epsilon-\mu)(t_N+\Delta t-t'_N)}\,\mathrm{d}\epsilon \tag{I.B.129}$$

$$\Delta_{-}^{<N}(t'_N,t_N+\Delta t) = i\int V_{-}(\epsilon,t'_N)\,V_{-}(\epsilon,t_N+\Delta t)^{*}\,\theta(-\epsilon+\mu)\; e^{-i(\epsilon-\mu)(t'_N-t_N-\Delta t)}\,\mathrm{d}\epsilon \tag{I.B.130}$$

3. *Compute the resulting* $> N$ *and* $< N$ *components of the second hybridization function*

$$\Delta_{+}^{>N}(t_N+\Delta t,t'_N) = \Delta^{>N}(t_N+\Delta t,t'_N) - \Delta_{-}^{>N}(t_N+\Delta t,t'_N) \tag{I.B.131}$$

$$\Delta_{+}^{>N}(t'_N,t_N+\Delta t) = \Delta^{>N}(t'_N,t_N+\Delta t) - \Delta_{-}^{>N}(t'_N,t_N+\Delta t) \tag{I.B.132}$$

$$\Delta_{+}^{<N}(t_N+\Delta t,t'_N) = \Delta^{<N}(t_N+\Delta t,t'_N) - \Delta_{-}^{<N}(t_N+\Delta t,t'_N) \tag{I.B.133}$$

$$\Delta_{+}^{<N}(t'_N,t_N+\Delta t) = \Delta^{<N}(t'_N,t_N+\Delta t) - \Delta_{-}^{<N}(t'_N,t_N+\Delta t) \tag{I.B.134}$$

4. *Minimize Eq.* (I.B.123) *with respect to* v *and* w*, if new bath sites of the second bath can be coupled to the impurity. Minimize Eq.* (I.B.123) *with respect to* v *while keeping* $w = 0$*, if no new bath sites of the second bath can be coupled to the impurity. Set* $M_{t_n,t'_n} = -i\,\Delta_{+}^{<N}(t_N,t'_N)$*, to compute the new hopping amplitudes for the bath sites of the second bath that are occupied in the initial state. Set* $M_{t_n,t'_n} = i\,\Delta_{+}^{>N}(t_N,t'_N)$*, to compute the new hopping amplitudes for the bath sites of the second bath that are unoccupied in the initial state. Here, we have already coupled* p_{max} *bath sites to the initially occupied part of the second bath and additionally* p_{max} *bath sites of the initially unoccupied part of the second bath.*

> *The hopping amplitudes of the second bath are:*
>
> $$V_{+,p}(t_N + \Delta t) = v_p \tag{I.B.135}$$
>
> $$V_{+,p_{max}+1}(t_N + \Delta t) = w \tag{I.B.136}$$
>
> *Here, v_p is the p-th entry of vector v. The last equation can only be used if the number of time steps is lower than the number of bath sites in the second bath, i.e. there are still bath sites that can be coupled to the impurity.*

I.B.4 Numerical Solution of Integral Equation for G_k

I.B.4.1 Problem Statement

In this section we follow Ref. 42. In DMFT one must compute the momentum resolved Green function G_k from the impurity Green function G (see Eqs. (I.A.134) and (I.A.135)), which amounts to solving an integral equation on the contour. In this section we provide a solution on our new contour with two real time axes. The computation of G_k can be simplified to the solution of the following two equations:

$$G = G_k + G_k * \Delta * G - G_k * \varepsilon * G \tag{I.B.137}$$

$$= G_k + G * \Delta * G_k - G * \varepsilon * G_k \tag{I.B.138}$$

This is the combination of Eq. (I.A.134) and Eq. (I.A.135).

This means, to obtain G_k, we need to solve two equations of the following form for X:

$$Q = X + X * F_R \tag{I.B.139}$$

$$Q = X + F_L * X \tag{I.B.140}$$

with:

$$Q = G \tag{I.B.141}$$

$$X = G_k \tag{I.B.142}$$

$$F_L = G * \Delta - G * \varepsilon \tag{I.B.143}$$

$$F_R = \Delta * G - \varepsilon * G \tag{I.B.144}$$

To numerically solve Eqs. (I.B.139) and (I.B.140), we follow Appendix A of Ref. 42 and discretize the relevant integrals. These two equations can be solved on the non-equilibrium axis time slice by time slice. As a general note for this section, the advanced and retarded components in this section occur only strictly within integrals. Thus, if the first and second time argument are equal, no special care has to be taken regarding the Heaviside step function contained in their definitions and the retarded component is simply the difference between the greater and lesser and vice versa for the advanced component.

I.B.4.2 $t_N = 0$

On the equilibrium axis the convolution $*$ in Eqs. (I.B.139) and (I.B.140) is reduced to a multiplication in ω-space. The different components of Eq. (I.B.139) can be written as:

$$Q^{RE}(\omega) = X^{RE}(\omega) + X^{RE}(\omega)\, F_R^{RE}(\omega) \tag{I.B.145}$$

$$Q^{AE}(\omega) = X^{AE}(\omega) + X^{AE}(\omega)\, F_R^{AE}(\omega) \tag{I.B.146}$$

$$Q^{>E}(\omega) = X^{>E}(\omega) + X^{>E}(\omega)\, F_R^{AE}(\omega) + X^{RE}(\omega)\, F_R^{>E}(\omega) \tag{I.B.147}$$

$$Q^{<E}(\omega) = X^{<E}(\omega) + X^{<E}(\omega)\, F_R^{AE}(\omega) + X^{RE}(\omega)\, F_R^{<E}(\omega) \tag{I.B.148}$$

With the solutions:

$$X^{RE}(\omega) = \frac{Q^{RE}(\omega)}{1 + F_R^{RE}(\omega)} \tag{I.B.149}$$

$$X^{AE}(\omega) = \frac{Q^{AE}(\omega)}{1 + F_R^{AE}(\omega)} \tag{I.B.150}$$

$$X^{>E}(\omega) = \frac{Q^{>E}(\omega) - X^{RE}(\omega)\, F_R^{>E}(\omega)}{1 + F_R^{AE}(\omega)} \tag{I.B.151}$$

$$X^{<E}(\omega) = \frac{Q^{<E}(\omega) - X^{RE}(\omega)\, F_R^{<E}(\omega)}{1 + F_R^{AE}(\omega)} \tag{I.B.152}$$

There is also a similar solution when one starts from Eq. (I.B.140). Now, we can do an inverse Fourier transform and get the mixing components of X at $t_N = 0$.

$$X^{\ulcorner}(t_E - t'_E, 0) = X^{\lrcorner}(0, t'_E - t_E) = X^{>E}(t_E, t'_E) = \frac{1}{2\pi} \int_{-\infty}^{\infty} e^{-i\omega(t_E - t'_E)} X^{>E}(\omega)\ \mathrm{d}\omega \tag{I.B.153}$$

$$X^{\urcorner}(0, t'_E - t_E) = X^{\llcorner}(t_E - t'_E, 0) = X^{<E}(t_E, t'_E) = \frac{1}{2\pi} \int_{-\infty}^{\infty} e^{-i\omega(t_E - t'_E)} X^{<E}(\omega)\ \mathrm{d}\omega \tag{I.B.154}$$

I.B.4.3 $t_N \neq 0$

Here we assume that the contour is discretized in time steps of Δt and that for the calculation of an entry of X all other entries with lower non-equilibrium time are already known. For example, if we want to calculate $X^{\ulcorner}(t_E, t_N)$ we assume that we have already computed all $X^{\ulcorner}(t_E, t_N - m \cdot \Delta t)$, where $m > 0$ and $t_N - m \cdot \Delta t \geq 0$.

We will discretize the integrals with a summation:

$$\int_{t_0}^{t_1} f(t)\ \mathrm{d}t \approx \sum_m w_m\, f(t_0 + m\Delta t) \tag{I.B.155}$$

Here w_m are the weights chosen to discretize the integral. Examples of usable weights are the trapezoid rule or Simpson's rule[42], which is used in the present thesis.

I.B.4.3.1 Right-Mixing Component

The right-mixing component of X can be computed from Eq. (I.B.139), which reads in integral notation:

$$\begin{aligned} Q^{\ulcorner}(t_E, t_N) = X^{\ulcorner}(t_E, t_N) & \\ & + \int_{-\infty}^{0} X^{>E}(t_E, \bar{t}_E) \left(F_R^{\llcorner}(\bar{t}_E, t_N) - F_R^{\ulcorner}(\bar{t}_E, t_N)\right) \mathrm{d}\bar{t}_E \\ & + \int_{0}^{t_N} X^{\ulcorner}(t_E, \bar{t}_N)\, F_R^{AN}(\bar{t}_N, t_N)\, \mathrm{d}\bar{t}_N \\ & + \int_{\infty}^{\infty} X^{RE}(t_E, \bar{t}_E)\, F_R^{\ulcorner}(\bar{t}_E, t_N)\, \mathrm{d}\bar{t}_E \end{aligned} \tag{I.B.156}$$

Of the three integrals above, only the second one contains unknown information by our assumption that we already computed all entries with non-equilibrium time lower than t_N. When we discretize the second integral only the last term of the sum contains unknown entries of X, i.e. $X^{\ulcorner}(t_E, t_N)$ is not yet determined, while we already computed $X^{\ulcorner}(t_E, t'_N)$ with $t'_N < t_N$ by assumption. The solution of the equation above can be written as:

$$X^{\ulcorner}(t_E, t_N) = \frac{Q^{\ulcorner}(t_E, t_N) - R^{\ulcorner}(t_E, t_N)}{1 + w_N \left(F_R^{<N}(t_N, t_N) - F_R^{>N}(t_N, t_N)\right)} \tag{I.B.157}$$

where w_N is the last weight of the integral approximation:

$$\begin{aligned} \int_0^{t_N} X^{\ulcorner}(t_E, \bar{t}_N)\, F_R^{AN}(\bar{t}_N, t_N)\, \mathrm{d}\bar{t}_N \approx w_0 X^{\ulcorner}(t_E, 0)\, F_R^{AN}(0, t_N) & \\ & + w_1\, X^{\ulcorner}(t_E, \Delta t)\, F_R^{AN}(\Delta t, t_N) \\ & + w_2\, X^{\ulcorner}(t_E, 2\Delta t)\, F_R^{AN}(2\Delta t, t_N) \\ & + \ldots \\ & + w_N\, X^{\ulcorner}(t_E, t_N)\, F_R^{AN}(t_N, t_N) \\ & = \sum_{m=0}^{N} w_m\, X^{\ulcorner}(t_E, m \cdot \Delta t)\, F_R^{AN}(m \cdot \Delta t, t_N) \end{aligned}$$

and $R^{\ulcorner}(t_E, t_N)$ is the rest of the known integral quantities combined into one term:

$$\begin{aligned} R^{\ulcorner}(t_E, t_N) = & \int_{-\infty}^{0} X^{>E}(t_E, \bar{t}_E)\ \left(F^{\llcorner}_{R}(\bar{t}_E, t_N) - F^{\ulcorner}_{R}(\bar{t}_E, t_N)\right)\, \mathrm{d}\bar{t}_E \\ & + \int_{\infty}^{\infty} X^{RE}(t_E, \bar{t}_E)\, F^{\ulcorner}_{R}(\bar{t}_E, t_N)\, \mathrm{d}\bar{t}_E \\ & + \sum_{m=0}^{N-1} w_m\, X^{\ulcorner}(t_E, m \cdot \Delta t)\, F^{AN}_{R}(m \cdot \Delta t, t_N) \end{aligned} \tag{I.B.158}$$

The first two integrals must also be discretized, but they are written in continuous from here for the sake of brevity.

I.B.4.3.2 Pre-Right-Mixing Component

In a similar manner, the solution of the pre-right-mixing component yields:

$$X^{\llcorner}(t_E, t_N) = \frac{Q^{\llcorner}(t_E, t_N) - R^{\llcorner}(t_E, t_N)}{1 + w_N\left(F^{<N}_{R}(t_N, t_N) - F^{>N}_{R}(t_N, t_N)\right)} \tag{I.B.159}$$

with:

$$\begin{aligned} R^{\llcorner}(t_E, t_N) = & \int_{-\infty}^{0} X^{<E}(t_E, \bar{t}_E)\ \left(F^{\llcorner}_{R}(\bar{t}_E, t_N) - F^{\ulcorner}_{R}(\bar{t}_E, t_N)\right)\, \mathrm{d}\bar{t}_E \\ & + \int_{\infty}^{\infty} X^{RE}(t_E, \bar{t}_E)\, F^{\llcorner}_{R}(\bar{t}_E, t_N)\, \mathrm{d}\bar{t}_E \\ & + \sum_{m=0}^{N-1} w_m\, X^{\llcorner}(t_E, m \cdot \Delta t)\, F^{AN}_{R}(m \cdot \Delta t, t_N) \end{aligned} \tag{I.B.160}$$

I.B.4.3.3 Left-Mixing Component

The computation of the left-mixing component $X^{\urcorner}(t_N, t_E)$ is very similar to the right-mixing component, with the difference that we use Eq. (I.B.140).

$$X^{\urcorner}(t_E, t_N) = \frac{Q^{\urcorner}(t_E, t_N) - R^{\urcorner}(t_N, t_E)}{1 + w_N\left(F^{>N}_{L}(t_N, t_N) - F^{<N}_{L}(t_N, t_N)\right)} \tag{I.B.161}$$

with:

$$
\begin{aligned}
R^{\urcorner}(t_N, t_E) = &\int_{-\infty}^{0} \left(F_L^{\lrcorner}(t_N, \bar{t}_E) - F_L^{\urcorner}(t_N, \bar{t}_E)\right)\, X^{<E}(\bar{t}_E, t_E)\, \mathrm{d}\bar{t}_E \\
&+ \int_{-\infty}^{\infty} F_L^{\urcorner}(t_N, \bar{t}_E)\, X^{AE}(\bar{t}_E, t_E)\, \mathrm{d}\bar{t}_E \\
&+ \sum_{m=0}^{N-1} w_m\, F_L^{RN}(t_N, m \cdot \Delta t)\, X^{\urcorner}(m \cdot \Delta t, t_N)
\end{aligned}
\tag{I.B.162}
$$

I.B.4.3.4 Pre-Left-Mixing Component

In a similar manner, the solution of the pre-left-mixing component yields:

$$
X^{\lrcorner}(t_E, t_N) = \frac{Q^{\lrcorner}(t_E, t_N) - R^{\lrcorner}(t_N, t_E)}{1 + w_N \left(F_L^{>N}(t_N, t_N) - F_L^{<N}(t_N, t_N)\right)}
\tag{I.B.163}
$$

with:

$$
\begin{aligned}
R^{\lrcorner}(t_N, t_E) = &\int_{-\infty}^{0} \left(F_L^{\lrcorner}(t_N, \bar{t}_E) - F_L^{\urcorner}(t_N, \bar{t}_E)\right)\, X^{>E}(\bar{t}_E, t_E)\, \mathrm{d}\bar{t}_E \\
&+ \int_{-\infty}^{\infty} F_L^{\lrcorner}(t_N, \bar{t}_E)\, X^{AE}(\bar{t}_E, t_E)\, \mathrm{d}\bar{t}_E \\
&+ \sum_{m=0}^{N-1} w_m\, F_L^{RN}(t_N, m \cdot \Delta t)\, X^{\lrcorner}(m \cdot \Delta t, t_N)
\end{aligned}
\tag{I.B.164}
$$

I.B.4.3.5 Greater and Lesser Components

The solution of the non-equilibrium greater and lesser components of X is very similar to the previous components, with the difference that one must distinguish whether $t_N > t'_N$, $t_N < t'_N$, or $t_N = t'_N$, because different unknown entries of X emerge when taking care of the three different cases. For the sake of brevity whe define a general component $C \in \{<, >\}$. Note that Green functions denoted with C here are *not* the causal Green function used in other settings, but either the lesser or greater component.

The first case is $t_N > t'_N$, and then one can use Eq. (I.B.140) to solve the non-equilibrium greater and lesser components of X, with the solution:

$$X^{>N}(t_N, t'_N) = \frac{Q^{>N}(t_N, t'_N) - R_L^{>N}(t_N, t'_N)}{1 + w_N \left(F_L^{>N}(t_N, t_N) - F_L^{<N}(t_N, t_N)\right)} \tag{I.B.165}$$

$$X^{<N}(t_N, t'_N) = \frac{Q^{<N}(t_N, t'_N) - R_L^{<N}(t_N, t'_N)}{1 + w_N \left(F_L^{>N}(t_N, t_N) - F_L^{<N}(t_N, t_N)\right)} \tag{I.B.166}$$

with:

$$\begin{aligned} R_L^{CN} = {} & \int_{-\infty}^{0} \left(F_L^{\lrcorner}(t_N, \bar{t}_E)\, X^{\llcorner}(\bar{t}_E, t'_N)\right) - \left(F_L^{\urcorner}(t_N, \bar{t}_E)\, X^{\ulcorner}(\bar{t}_E, t'_N)\right)\, \mathrm{d}\bar{t}_E \\ & + \int_{0}^{t'_N} F_L^{CN}(t_N, \bar{t}_N)\, X^{AN}(\bar{t}_N, t'_N)\, \mathrm{d}\bar{t}_N \\ & + \sum_{m=0}^{N-1} w_m\, F_L^{RN}(t_N, m \cdot \Delta t)\, X^{CN}(m \cdot \Delta t, t_N) \end{aligned} \tag{I.B.167}$$

The second case, $t_N < t'_N$, can be solved in the same way with the use of Eq. (I.B.140).

$$X^{>N}(t_N, t'_N) = \frac{Q^{>N}(t_N, t'_N) - R_R^{>N}(t_N, t'_N)}{1 + w_N \left(F_R^{<N}(t'_N, t'_N) - F_R^{>N}(t'_N, t'_N)\right)} \tag{I.B.168}$$

$$X^{<N}(t_N, t'_N) = \frac{Q^{<N}(t_N, t'_N) - R_R^{<N}(t_N, t'_N)}{1 + w_N \left(F_R^{<N}(t'_N, t'_N) - F_R^{>N}(t'_N, t'_N)\right)} \tag{I.B.169}$$

with:

$$\begin{aligned} R_R^{CN} = {} & \int_{-\infty}^{0} \left(F_L^{\lrcorner}(t_N, \bar{t}_E)\, X^{\llcorner}(\bar{t}_E, t'_N)\right) - \left(F_L^{\urcorner}(t_N, \bar{t}_E)\, X^{\ulcorner}(\bar{t}_E, t'_N)\right)\, \mathrm{d}\bar{t}_E \\ & + \int_{0}^{t_N} X^{RN}(t_N, \bar{t}_N)\, F_R^{CN}(\bar{t}_N, t'_N)\, \mathrm{d}\bar{t}_N \\ & + \sum_{m=0}^{N-1} w_m\, X^{CN}(t_N, m \cdot \Delta t)\, F_R^{AN}(m \cdot \Delta t, t'_N) \end{aligned} \tag{I.B.170}$$

The third case, $t_N = t'_N$, is a bit more involved and one cannot solve for the greater and lesser component separately, but must solve both at the same time. One can solve for Eq. (I.B.140) or Eq. (I.B.139). We will present the solution of the latter here:

$$
\begin{aligned}
X^{>N}(t_N, t_N) &= \frac{\left(Q^{>N}(t_N, t_N) - R_R\right)\left(1 - w_N\, F_R^{>N}(t_N, t_N)\right)}{1 + w_N\left(F_R^{<N}(t_N, t_N) - F_R^{>N}(t_N, t_N)\right)} \\
&\quad - \frac{\left(Q^{<N}(t_N, t_N) - R_R\right)\left(-w_N\, F_R^{>N}(t_N, t_N)\right)}{1 + w_N\left(F_R^{<N}(t_N, t_N) - F_R^{>N}(t_N, t_N)\right)} \qquad \text{(I.B.171)} \\
X^{<N}(t_N, t_N) &= \frac{\left(Q^{<N}(t_N, t_N) - R_R\right)\left(1 + w_N\, F_R^{<N}(t_N, t_N)\right)}{1 + w_N\left(F_R^{<N}(t_N, t_N) - F_R^{>N}(t_N, t_N)\right)} \\
&\quad - \frac{\left(Q^{>N}(t_N, t_N) - R_R\right)\left(w_N\, F_R^{<N}(t_N, t_N)\right)}{1 + w_N\left(F_R^{<N}(t_N, t_N) - F_R^{>N}(t_N, t_N)\right)} \qquad \text{(I.B.172)}
\end{aligned}
$$

with:

$$
\begin{aligned}
R_R = \int_{-\infty}^{0} &\left(F_L^{\lrcorner}(t_N, \bar{t}_E)\, X^{\llcorner}(\bar{t}_E, t'_N)\right) - \left(F_L^{\urcorner}(t_N, \bar{t}_E)\, X^{\ulcorner}(\bar{t}_E, t'_N)\right)\, \mathrm{d}\bar{t}_E \qquad \text{(I.B.173)} \\
&+ \sum_{m=0}^{N-1} w_m\, X^{>N}(t_N, m \cdot \Delta t)\, F_R^{<N}(m \cdot \Delta t, t_N) \\
&+ \sum_{m=0}^{N-1} w_m\, X^{<N}(t_N, m \cdot \Delta t)\, F_R^{>N}(m \cdot \Delta t, t_N)
\end{aligned}
$$

I.B.4.4 Stabilization

To stabilize the computation we will perform a damping on the Green function and the hybridization function on the equilibrium axis:

$$G^{\ulcorner}(t_E, t_N) \longrightarrow G^{\ulcorner}(t_E, t_N)\, e^{-\alpha |t_E|} \qquad \text{(I.B.174)}$$

$$G^{\llcorner}(t_E, t_N) \longrightarrow G^{\llcorner}(t_E, t_N)\, e^{-\alpha |t_E|} \qquad \text{(I.B.175)}$$

$$G^{\urcorner}(t_N, t_E) \longrightarrow G^{\urcorner}(t_N, t_E)\, e^{-\alpha |t_E|} \qquad \text{(I.B.176)}$$

$$G^{\lrcorner}(t_N, t_E) \longrightarrow G^{\lrcorner}(t_N, t_E)\, e^{-\alpha |t_E|} \qquad \text{(I.B.177)}$$

I.B.5 Existing Non-Equilibrium Impurity Solvers

This section serves as a brief overview over the existing impurity solvers and their respective limitations. For more in-depth information see Refs. 39, 42, 46, and 51. The state of the art methods for equilibrium DMFT are the so called Continuous-Time Quantum Monte Carlo (CTQMC) solvers. A general feature of many interesting Hamiltonians is that they are separable into two different parts, where each part is diagonalizable trivially on their own but the combination of the two parts is is not. An example is the hopping term and interaction term of the Hubbard model, with the hopping term being diagonal in k-space and the interaction term being diagonal in real space. The general strategy of CTQMC is to split the Hamiltonian into these separate parts, expanding the partition function in powers of one of those Hamiltonians, and do an importance sampling with Monte Carlo methods over the resulting sum. For weak-coupling CTQMC (CT-INT; or the more generalized CT-AUX) this means expanding the partition function in powers of the interaction term H_{imp} (see Def. (2)).

$$\frac{Z}{Z_0} = \sum_{n=0}^{\infty} \frac{(-i)^n}{n!} \int_{\mathcal{C}} ... \int_{\mathcal{C}} U(\mathbf{t_1}) ... U(\mathbf{t_n}) \prod_s \left\langle (n_s(\mathbf{t_1}) - \alpha_s) ... (n_s(\mathbf{t_n}) - \alpha_s) \right\rangle_{S_0} \, \mathrm{d}\mathbf{t_1} ... \mathrm{d}\mathbf{t_n} \tag{I.B.178}$$

Here, the expectation value is taken with respect to the action $S_0 = -i \int_{\mathcal{C}} H_{\text{hyb}}(\mathbf{t}) + H_{\text{bath}}(\mathbf{t}) \, \mathrm{d}\mathbf{t}$, $Z_0 = \operatorname{tr} e^{S_0}$, and the α cause a chemical potential shift to avoid one kind of sign problem, which is described below. Due to Wick's theorem, it is possible to calculate the coefficients in Eq. (I.B.178) which are however complex weights w_c, $\frac{Z}{Z_0} = \sum_c w_c$. They can be used as a probability distribution for importance sampling after:

$$\begin{aligned}
\langle O \rangle_w &= \frac{\sum_c w_c \, O_c}{\sum_c w_c} = \frac{\sum_c |w_c| \, \phi_c \, O_c}{\sum_c |w_c| \, \phi_c} = \frac{\sum_c |w_c| \, \phi_c \, O_c}{\sum_c |w_c| \, \phi_c} \underbrace{\frac{\sum_c |w_c|}{\sum_c |w_c|}}_{=1} \\
&= \frac{\frac{\sum_c |w_c| \, \phi_c \, O_c}{\sum_c |w_c|}}{\frac{\sum_c |w_c| \, \phi_c}{\sum_c |w_c|}} \\
&= \frac{\langle \phi \, O \rangle_{|w|}}{\langle \phi \rangle_{|w|}} \qquad\qquad (\phi_c = e^{i \operatorname{Arg}(w_c)})
\end{aligned} \tag{I.B.179}$$

The so called sign problem is that, although this mapping is well defined, the sampled expectation value in the denominator $\left\langle \phi \right\rangle_{|w|}$ may be very small with relatively large uncertainties, which renders the sampled expectation value $\left\langle O \right\rangle_{w}$ not accurate enough. Although certain basis transformations with respect to w_c can reduce or eliminate the sign problem in special cases, there probably is no general solution to the sign problem as this would imply $P = NP$ (see Ref. 44).

In the same vein, it is possible to expand the partition function in powers of H_{hyb}, which is called strong-coupling CTQMC (CT-HYB). Then the partition function is given by:

$$Z = \left\langle \sum_{n=0}^{\infty} \frac{(-i)^n}{n!} \int_{\mathcal{C}} ... \int_{\mathcal{C}} H_{\text{hyb}}(\mathbf{t_1}) ... H_{\text{hyb}}(\mathbf{t_n}) \; \mathrm{d}\mathbf{t_1} ... \mathrm{d}\mathbf{t_n} \right\rangle_{S_0} \tag{I.B.180}$$

With $S_0 = -i \int_{\mathcal{C}} H_{\text{imp}}(\mathbf{t}) + H_{\text{bath}}(\mathbf{t}) \; \mathrm{d}\mathbf{t}$. After tracing out the bath it is possible to do an importance sampling of the sum in Eq. (I.B.180), where the weights are again in general complex.

Both of these two sampling methods are well defined and make no approximation, except for statistical errors from the finite sample size, but suffer to varying degree from the sign problem that gets exponentially worse with increasing non-equilibrium time t_N, inverse temperature β, and the number of particles N (see Refs. 39, 42, and 44). This is best understood by looking at the relative error of the sampled expectation value of ϕ:

$$\frac{1}{\sqrt{N_{\text{samples}}}} \frac{\sqrt{\mathrm{Var}(\phi)_{|w|}}}{\left| \left\langle \phi \right\rangle_{|w|} \right|} = \frac{1}{\sqrt{N_{\text{samples}}}} \frac{\sqrt{\left\langle |\phi|^2 \right\rangle_{|w|} - |\left\langle \phi \right\rangle_{|w|}|^2}}{\left| \left\langle \phi \right\rangle_{|w|} \right|} \tag{I.B.181}$$

$$= \frac{1}{\sqrt{N_{\text{samples}}}} \frac{\sqrt{1 - |\left\langle \phi \right\rangle_{|w|}|^2}}{\left| \left\langle \phi \right\rangle_{|w|} \right|} \tag{I.B.182}$$

$$\xrightarrow[\left| \left\langle \phi \right\rangle_{|w|} \right| \ll 1]{} \frac{1}{\sqrt{N_{\text{samples}}} \left| \left\langle \phi \right\rangle_{|w|} \right|} \tag{I.B.183}$$

The expectation value of the phase can be related to the ratio of two partition functions:

$$\left\langle \phi \right\rangle_{|w|} = \frac{\sum_c |w_c| \phi_c}{\sum_c |w_c|} = \frac{\sum_c w_c}{\sum_c |w_c|} = \frac{Z_w}{Z_{|w|}} \tag{I.B.184}$$

In equilibrium, the partition function can be related to β which is the inverse temperature, N the number of particles, and the free energy density f with $Z = e^{-\beta N f}$, meaning the relative error can be expressed as[44]:

$$\frac{|\Delta\phi|}{|\left\langle \phi \right\rangle_{|w|}|} \approx \frac{1}{\sqrt{N_{\text{samples}}}\left|\left\langle \phi \right\rangle_{|w|}\right|} = \frac{e^{\beta N (f_w - f_{|w|})}}{\sqrt{N_{\text{samples}}}} \tag{I.B.185}$$

With real time evolution in quantum Monte Carlo, the expectation value of the phase shrinks exponentially with increasing real time $\left\langle \phi \right\rangle_{|w|} \propto e^{-\alpha\, t_{max}}$ (see Ref. 42), which means the relative error grows exponentially with increasing time:

$$\frac{|\Delta\phi|}{|\left\langle \phi \right\rangle_{|w|}|} \approx \frac{1}{\sqrt{N_{\text{samples}}}\left|\left\langle \phi \right\rangle_{|w|}\right|} \propto \frac{e^{\alpha\, t_{N,max}}}{\sqrt{N_{\text{samples}}}} \tag{I.B.186}$$

This means that if one increases the inverse temperature, the number of particles, and/or the maximum time, while keeping the relative error constant, the number of needed samples grows exponentially.

For fermionic systems it strongly depends on the investigated system how severe the sign problem is. In equilibrium it can be completely eliminated in some very special cases[39]. Furthermore, the sign problem is more severe for strong-coupling CTQMC than for weak-coupling CTQMC, where short simulation can be reached[42]. In general, low temperatures are not accessible to the above mentioned sampling methods, and there are alternatives in equilibrium[41,100,101], however there are exceptions where even in non-equilibrium setups CTQMC can be used[52,53]. In non-equilibrium, as a rule of thumb the sign problem is more severe than in equilibrium[39,42]. The severity depends on several factors such as filling, particle-hole symmetry, and more[39].

If one wants to reach long simulation times in non-equilibrium, the best current option may be to use the Non-Crossing Approximation (NCA) or its generalizations[42,46]. The Non-Crossing Approximation is the lowest order of the strong-coupling perturbation theory, where ones does a Taylor expansion of the partition function with respect to the hybridization function, like in Eq. (I.B.180). After a basis transformation to the impurity Hilbert space, the expansion can be expressed as a sum of Feynman diagrams[14]. For NCA, only diagrams with no crossing in them are kept for the result. As mentioned before, the great advantage of

NCA is that it possible to reach long simulation times (see e.g. Ref 102). The disadvantage is that it is not a controlled approximation, in the sense that there is no parameter that can be arbitrarily tuned to get a better result like the number of samples for Monte Carlo methods or the discarded weight/cutoff for Matrix Product Based approaches. It is for example known that in equilibrium the Fermi-liquid behavior is not correctly reproduced by NCA if $T \ll T_k$ (see Refs. 46, 103, and 104). This problem can be reduced by truncating at higher orders (One-Crossing Approximation) with higher computational cost, yet the problem still remains that NCA is not a controlled approximation and it usually takes a great deal of experience to know in which parameter regions the results are usable.

Other solvers that are not related to this work but are relevant to the field include the Configuration Interaction[47] (CI) method, which can be used as a solver for DMFT[86], and the inchworm method[45], a Monte Carlo sampling method alleviating the dynamical sign problem, and the Auxiliary Master Equation Approach[48] (AMEA), where steady states can be investigated.

A relatively new category of equilibrium impurity solvers is based on Matrix Product States[68–70,105,106] or Tensor Product States[41,71], which recently have been used for up to five orbitals[71]. In Ref. 51, such an approach has been extended to single-orbital non-equilibrium setups, however the only published application of the solver has been restricted to non-correlated initial states, i. e. the initial state of the lattice system is a product state.

$$|\psi(0)\rangle = (|\uparrow_1\rangle + |\downarrow_1\rangle) \otimes (|\uparrow_2\rangle + |\downarrow_2\rangle) \otimes ... \tag{I.B.187}$$

In Ref. 51 the computational cost with respect to (non-equilibrium) time increases exponentially, and the number of bath sites is relatively low in comparison to the present thesis.

With Tensor Network based approaches the impurity Green function can be computed directly on the real[41,69] or imaginary[106] axis at zero temperature after mapping the hybridization to a corresponding Hamiltonian[49]. Tensor Product State based solvers do not suffer from the sign problem but do suffer from the problem of growing matrix dimensions if the entanglement entropy is large. In the present thesis, we also develop a Matrix Product States based solver to directly compute the Green function on two real time axis (see Sec. I.B.1) at zero temperature. To calculate the ground state we use DMRG[30] and for the time-evolution we use swap gates[30,72] in combination with the Suzuki-Trotter decomposition of the time-evolution operator, a method introduced in Ref. 41. We will show in Subpart I.C that this new solver can simulate quenches with correlated initial states.

I.B.6 Matrix Product States and Techniques

This section serves as a brief recapitulation of Matrix Product States (MPS) and the techniques used for time-evolution. For a more in-depth introduction see Ref. 30. The MPS formalism is a clever way to rewrite a quantum state into a tensor product.

> **Definition I.B.10: Matrix Product State (MPS) and Matrix Product Operator (MPO)**
>
> *A Matrix Product State $|\psi\rangle$ is a quantum state on a lattice with N lattice sites that is stored in the form:*
>
> $$|\psi\rangle = \sum_{\{s_i\}} A^{s_1}_{[1]}\, A^{s_2}_{[2]}\, \dots\, A^{s_{N-1}}_{[N-1]}\, A^{s_N}_{[N]}\, |s_1, s_2, \dots, s_{N-1}, s_N\rangle \tag{I.B.188}$$
>
> $$A^{s_1}_{[1]} \in \mathbb{C}^{d_1 \times 1 \times q_1} \tag{I.B.189}$$
>
> $$A^{s_N}_{[N]} \in \mathbb{C}^{d_N \times p_N \times 1} \tag{I.B.190}$$
>
> $$A^{s_i}_{[i]} \in \mathbb{C}^{d_i \times p_i \times q_i} \tag{I.B.191}$$
>
> $$q_{i-1} = p_i \tag{I.B.192}$$
>
> *The subscript $[i]$, that indicates the lattice site, is from here on omitted and implied by the superscript s_i. The local Hilbert space dimension of site i is denoted by d_i and the used matrix dimensions p_i and q_i are called bond dimension. There is also a similar method to store operators in matrix product form:*
>
> $$O = \sum_{\{s_i\}} W^{s_1,s_1'}_{[1]}\, \dots\, W^{s_N,s_N'}_{[N]}\, |s_1, s_2, \dots, s_{N-1}, s_N\rangle \langle s_1', s_2', \dots, s_{N-1}', s_N'| \tag{I.B.193}$$

This is basically a compression algorithm. Instead of storing $\prod_i d_i$ entries we only need to keep $\sum_i d_i\, p_i\, q_i$ entries. There is a convention for a graphical representation of Matrix

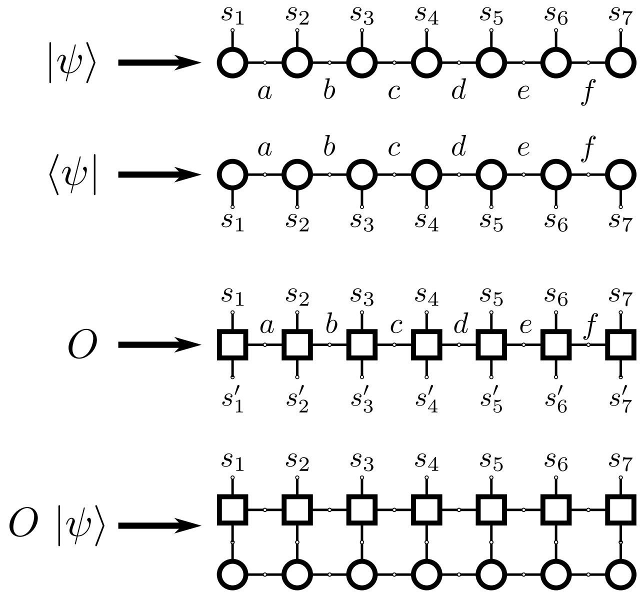

Figure I.B.7. Graphical representation of $|\psi\rangle$, $\langle\psi|$ in MPS form. Also shown is an operator O in Matrix Product Operator (MPO) form and the operator application $O\,|\psi\rangle$. Connected lines stand for a sum over all possible index value which is called matrix product or tensor contraction, depending on the tensor type.

Product States and for Matrix Product Operators depicted in Fig. I.B.7. The convention is that connected indices stand for a summation over the index values of the connected indices. In the case of Fig. I.B.7 the graph of $|\psi\rangle$ stands for:

$$\sum_{a\ldots f} A^{s_1}_{a}\, A^{s_2}_{a,b}\, A^{s_3}_{b,c}\, A^{s_4}_{c,d}\, A^{s_5}_{d,e}\, A^{s_6}_{e,f}\, A^{s_7}_{f} \tag{I.B.194}$$

For $\langle\psi|$ we take the complex conjugate of every entry.

The great advantage of the MPS representation is, that we have efficient methods to compute the ground state[26] of a Hamiltonian and the time-evolution of a state[27] without leaving the MPS representation. Usually, in the framework of MPS, the Singular Value Decomposition (SVD) (see Ref. 30) is used to compress a tensor.

Definition I.B.11: Singular Value Decomposition (SVD)

The Singular Value Decomposition decomposes a matrix M into a product of three matrices U, D, $V^\dagger$ with the following properties:

$$M = U D V^\dagger \qquad M \in \mathbb{C}^{p\times q} \tag{I.B.195}$$

$$U^\dagger U = \mathbb{1} \qquad U \in \mathbb{C}^{p\times m} \tag{I.B.196}$$

$$D \in \left\{\mathrm{diag}(x) \mid x \in \mathbb{R}_+^m\right\} \tag{I.B.197}$$

$$V^\dagger V = \mathbb{1} \qquad V^\dagger \in \mathbb{C}^{m\times q} \tag{I.B.198}$$

The entries of the diagonal matrix D are called singular values. Compression of the MPS is done by cutting of smaller singular values in D, reducing it from a $m \times m$ matrix to a $\tilde{m} \times \tilde{m}$ matrix, where $\tilde{m} < m$.

When truncating the diagonal matrix D of a quantum state one must keep the sum of all squared entries to one $\sum_i D_{i,i}^2 = 1$ by renormalizing with the singular values which are kept after truncation. In the present thesis we use the MPS library ITensor[107]. An important technical detail, when truncating the diagonal matrix D, is how many singular values are kept. In ITensor this is controlled by a parameter called cutoff, which is defined in Def. (I.B.12)

Definition I.B.12: Cutoff

Let ϵ be the cutoff. When the smallest singular values are discarded, the number of discarded singular values is maximized while keeping by the following inequality to hold true:

$$\frac{\sum_{i\in discarded} D_{i,i}^2}{\sum_i D_{i,i}^2} < \epsilon \tag{I.B.199}$$

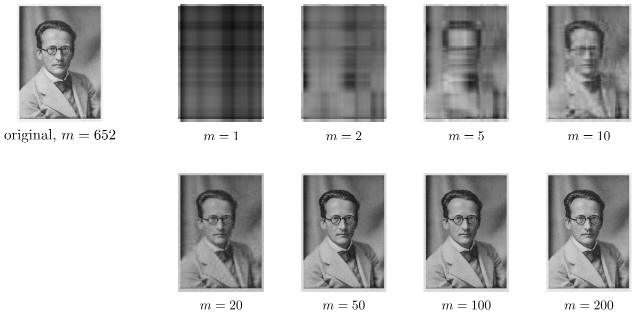

original, $m = 652$ $m = 1$ $m = 2$ $m = 5$ $m = 10$

$m = 20$ $m = 50$ $m = 100$ $m = 200$

Figure I.B.8. Compressed images[108] of Erwin Schrödinger. Shown are various compressions where the orignal image was decomposed with an SVD into three matrices and multiplied back again.

The MPS representation of a quantum state is not unique. This stems from the fact that we can insert a matrix Y an its inverse between two adjacent MPS tensors.

$$|\psi\rangle = \sum_{\{s_i\}} A^{s_1} \ldots A^{s_k} A^{s_{k+1}} \ldots A^{s_N} |s_1, s_2, \ldots, s_{N-1}, s_N\rangle \tag{I.B.200}$$

$$= \sum A^{s_1} \ldots \underbrace{A^{s_k} Y}_{\tilde{A}^{s_k}} \underbrace{Y^{-1} A^{s_{k+1}}}_{\tilde{A}^{s_{k+1}}} \ldots A^{s_N} |s_1, s_2, \ldots, s_{N-1}, s_N\rangle \tag{I.B.201}$$

$$= \sum A^{s_1} \ldots \tilde{A}^{s_k} \tilde{A}^{s_{k+1}} \ldots A^{s_N} |s_1, s_2, \ldots, s_{N-1}, s_N\rangle \tag{I.B.202}$$

$$\tag{I.B.203}$$

This gauge invariance is used to bring the MPS into so called right-, left-, and mixed-canonical form. To understand this we first need to define right-, and left-normalized tensors.

> **Definition I.B.13: Tensor and MPS gauges**
>
> *A tensor is left-normalized if it the following condition holds true.*
>
> $$\sum_i A^{s_i,\dagger} A^{s_i} = \mathbb{1} \tag{I.B.204}$$
>
> *A tensor is right-normalized if it the following condition holds true.*
>
> $$\sum_i A^{s_i} A^{s_i,\dagger} = \mathbb{1} \tag{I.B.205}$$

Figure I.B.9. Graphical representation of a left-normalized tensor and a right-normalized tensor. Triangles pointing to the right are left-normalized tensors (because they collapse to the right when contracting), while triangles pointing to the left are right-normalized tensors.

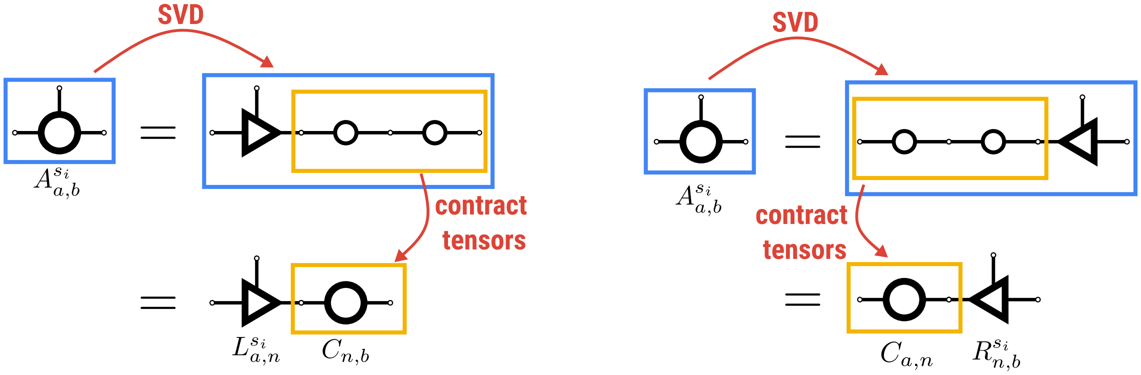

Figure I.B.10. Decomposition of a tensor A^{s_i} into a $L^{s_i} \cdot C$ where L is left-normalized, and into $C \cdot R^{s_i}$ where R is right-normalized.

> *If every tensor of an MPS is left-normalized, the MPS is called left-canonical. If every tensor of an MPS is right-normalized, the MPS is called right-canonical. If every tensor left of a certain lattice site is left-normalized and every tensor right of the lattice site is right-normalized it is a mixed-canonical MPS. An example of a mixed canonical MPS can be seen in Fig. I.B.11.*

It is possible to change between the different gauges with an SVD. The interested reader is referred to section 4 of Ref. 30 for more details, but for here it is sufficient to know that we can transform an arbitrary tensor into a product of a left-normalized tensor and a matrix, or a matrix and a right-normalized tensor (see Fig. I.B.10). This is depicted in Fig. I.B.10. The process on how to move the center site and change the gauge is drawn in Fig. I.B.11. For the MPS based impurity solver we need to apply MPO that act onto two lattice sites. The application of the MPO is algorithmically very similar to the other operations and is shown in Fig. I.B.12 and the calculation of an expectation value of an operator that acts only on one lattice is very efficient and depicted in Fig. I.B.13. Ground state search is possible with the

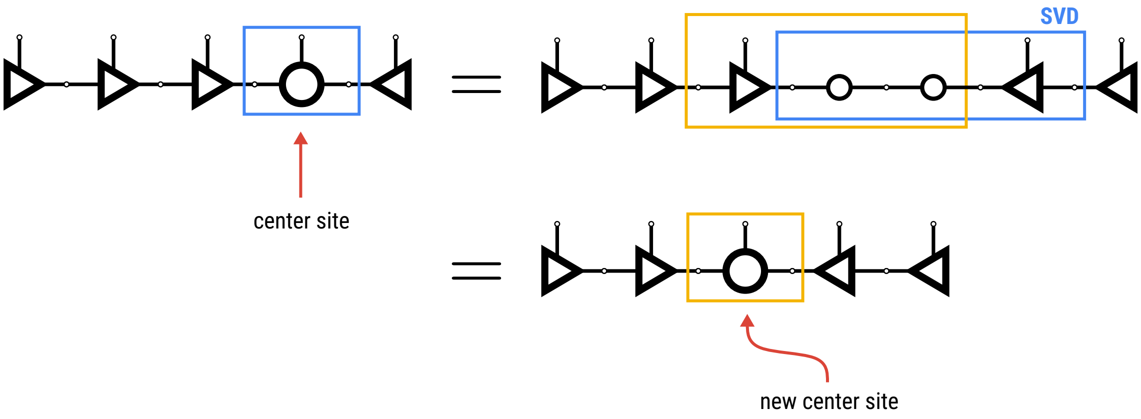

Figure I.B.11. The center site of a mixed canonical MPS with five lattice sites is moved with an SVD.

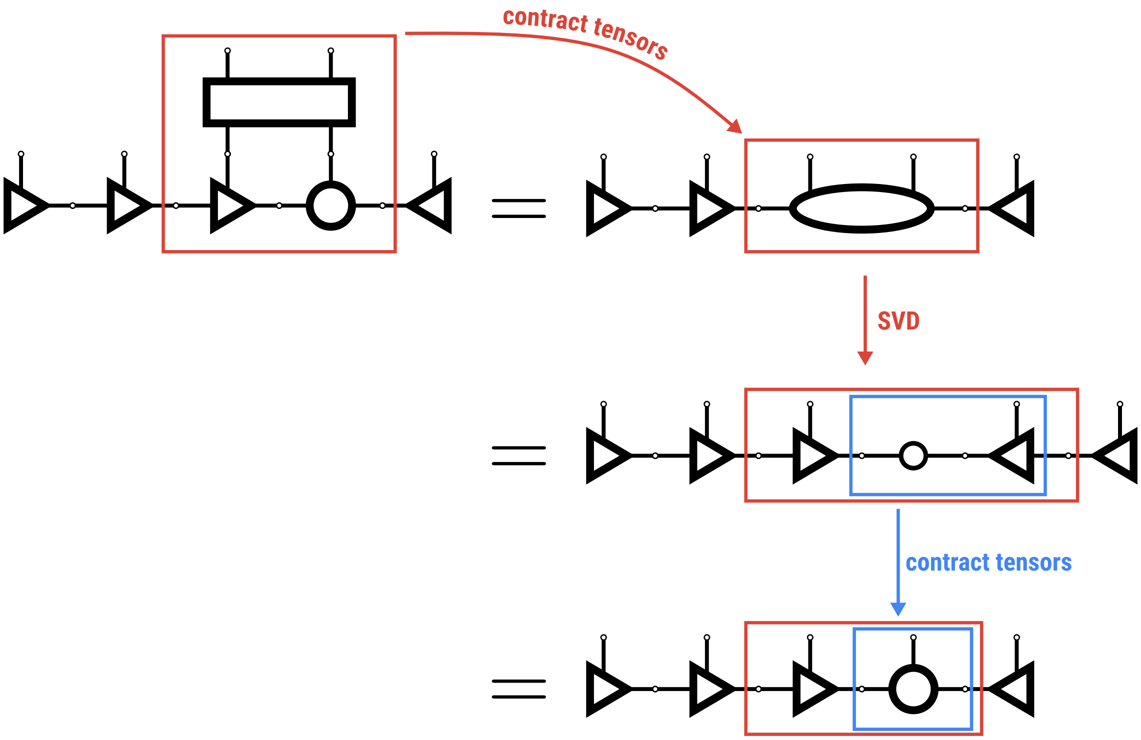

Figure I.B.12. Application of a two-site MPO to an MPS and subsequent transformation to a valid MPS.

Density Matrix Renormalization Group[26,30] (DMRG), where the energy is locally minimized on the tensor level and a variational search is performed[30]. The time-evolution is done in this thesis by a Suzuki-Trotter splitting[73] as outlined below. There are other techniques available[31,109], but not used here. The matrix exponential of two non-commuting matrices A

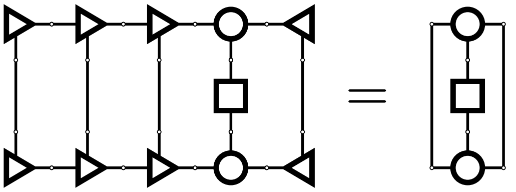

Figure I.B.13. Graphical representation of the computation of the expectation value of an operator that acts only on one site. The tensor multiplications to the left and to the right collapse according to Fig. I.B.9.

and B, $e^{\tau(A+B)}$, can be be approximated by the following expression.

$$e^{\frac{\tau}{2}A}\,e^{\tau B}\,e^{\frac{\tau}{2}A} = \left(\mathbb{1} + \frac{\tau}{2}A + \frac{\tau^2}{8}A^2\right)\left(\mathbb{1} + \tau B + \frac{\tau^2}{2}B\right)\left(\mathbb{1} + \frac{\tau}{2}A + \frac{\tau^2}{8}A^2\right) + \mathcal{O}\left(\tau^3\right) \tag{I.B.206}$$

$$= \mathbb{1} + \tau(A+B) + \frac{\tau^2}{2}\left(A^2 + AB + BA + B^2\right) + \mathcal{O}\left(\tau^3\right) \tag{I.B.207}$$

$$= e^{\tau(A+B)} + \mathcal{O}\left(\tau^3\right) \tag{I.B.208}$$

This is useful when the matrix exponential of the separated terms, $e^{\tau A}$ and $e^{\tau B}$, can be computed without problems. This means the exponential of a sum of three or more non-commuting operators can be split by recursively peeling off one operator.

$$e^{\tau(A+B+C)} = e^{\tau(A+(B+C))} \tag{I.B.209}$$

$$= e^{\frac{\tau}{2}A}\,e^{\tau(B+C)}\,e^{\frac{\tau}{2}A} + \mathcal{O}\left(\tau^3\right) \tag{I.B.210}$$

$$= e^{\frac{\tau}{2}A}\left(e^{\frac{\tau}{2}B}\,e^{\tau C}\,e^{\frac{\tau}{2}B} + \mathcal{O}\left(\tau^3\right)\right)e^{\frac{\tau}{2}A} + \mathcal{O}\left(\tau^3\right) \tag{I.B.211}$$

$$= e^{\frac{\tau}{2}A}\,e^{\frac{\tau}{2}B}\,e^{\tau C}\,e^{\frac{\tau}{2}B}\,e^{\frac{\tau}{2}A} + \mathcal{O}\left(\tau^3\right) \tag{I.B.212}$$

For the Anderson Impurity Model (AIM) one can peel off the single hybridization terms in this way. To this end we rewrite the AIM Hamiltonian (Def. (2)):

$$
\begin{aligned}
H &= H_{\mathrm{imp}} + \sum_p H_{p,\uparrow} + \sum_p H_{p,\downarrow} && \text{(I.B.213)}\\
H_{\mathrm{imp}} &= U\left(n_{0,\uparrow} - \frac{1}{2}\right)\left(n_{0,\downarrow} - \frac{1}{2}\right) - \mu\, n_{0,s} && \text{(I.B.214)}\\
H_{p,s} &= V_{p,s}(t)\, c^{\dagger}_{0,s} c_{p,s} + V^{*}_{p,s}(t)\, c^{\dagger}_{p,s} c_{0,s} + \left(\epsilon_{p,s} - \mu\right) n_{p,s} && \text{(I.B.215)}\\
e^{\tau H} &= e^{\tau\left(H_{\mathrm{imp}} + \sum_p H_{p,\uparrow} + \sum_p H_{p,\downarrow}\right)} && \text{(I.B.216)}\\
&= e^{\frac{\tau}{2} H_{\mathrm{imp}}}\, e^{\frac{\tau}{2}\sum_p H_{p,\uparrow}}\, e^{\tau \sum_p H_{p,\downarrow}}\, e^{\frac{\tau}{2}\sum_p H_{p,\uparrow}}\, e^{\frac{\tau}{2} H_{\mathrm{imp}}} + \mathcal{O}\left(\tau^3\right) && \text{(I.B.217)}\\
&= e^{\frac{\tau}{2} H_{\mathrm{imp}}} \left(\prod_{p=N_b}^{1} e^{\frac{\tau}{2} H_{p,\downarrow}}\right)\left(\prod_{p=1}^{N_b} e^{\frac{\tau}{2} H_{p,\downarrow}}\right) && \text{(I.B.218)}\\
&\quad \left(\prod_{p=N_b}^{1} e^{\frac{\tau}{2} H_{p,\uparrow}}\right)\left(\prod_{p=1}^{N_b} e^{\frac{\tau}{2} H_{p,\uparrow}}\right) e^{\frac{\tau}{2} H_{\mathrm{imp}}} + \mathcal{O}\left(\tau^3\right)
\end{aligned}
$$

N_b is the number of bath sites. To apply these operators within the MPS framework we need a valid MPS geometry for the state. The Anderson Impurity Model couples the impurity with every bath site, which can be interpreted as a star geometry (Fig. I.B.14, top left). To use MPS we need a linear geometry[41,51] and the local Hilbert space dimension d should be as low as possible, because the computational cost grows like $\mathcal{O}(d^3)$. To minimize the d, we can split the two spin directions into two connected star geometries[41]. Then, the Anderson Impurity Model can be viewed as a spin-less fermion model with special long-ranged hopping amplitudes and a local interaction term that affects only two sites corresponding to the spin-up site $0_\uparrow$ and spin-down site $0_\downarrow$ of the impurity (Fig. I.B.14, top right).

$$
\begin{aligned}
H = &\sum_{i_\uparrow} v_{i_\uparrow}\, c^{\dagger}_{0_\uparrow} c_{i_\uparrow} + v^{*}_{i_\uparrow}\, c^{\dagger}_{i_\uparrow} c_{0_\uparrow} + \left(\epsilon_{i_\uparrow} - \mu\right) n_{i_\uparrow} && \text{(I.B.219)}\\
&+ \sum_{i_\downarrow} v_{i_\downarrow}\, c^{\dagger}_{0_\downarrow} c_{i_\downarrow} + v^{*}_{i_\downarrow}\, c^{\dagger}_{i_\downarrow} c_{0_\downarrow} + \left(\epsilon_{i_\downarrow} - \mu\right) n_{i_\downarrow}\\
&+ U\left(n_{0_\uparrow} - \frac{1}{2}\right)\left(n_{0_\downarrow} - \frac{1}{2}\right)
\end{aligned}
$$

Note that this splitting of spins does not always pay off in the general (non-Anderson Impurity Model) case, because there might be a strong correlation between the different spin flavors

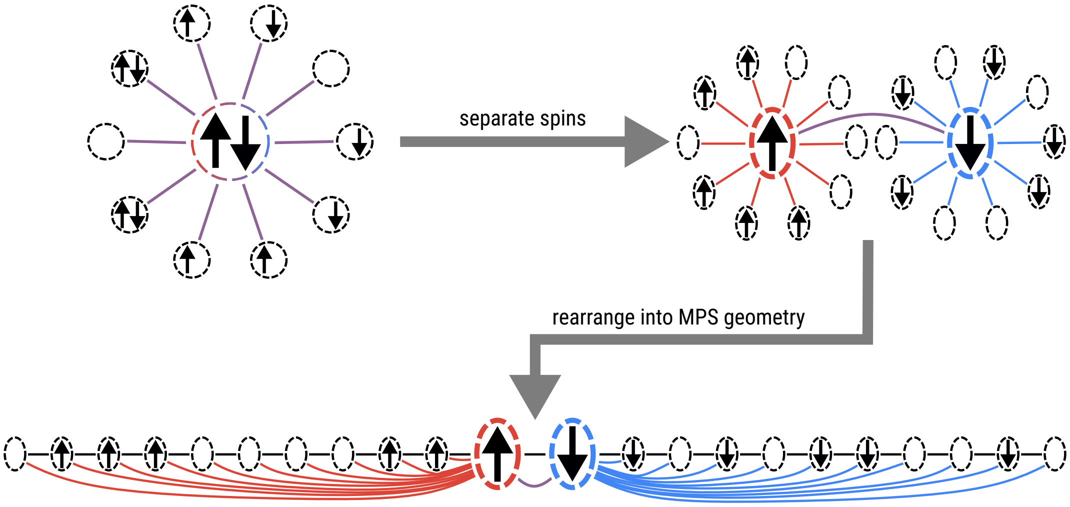

Figure I.B.14. The Mapping of the star geometry to a valid MPS geometry. The solid lines in the bottom graph mark the nearest-neighbor connections in the MPS geometry, while the colored lines stand for interaction terms in the Anderson Impurity Model Hamiltonian.

on the same or neighboring lattice sites. For the Anderson Impurity Model this splitting works well, because the spin-up and spin-down electrons in the bath do not interact with each other directly and are only connected via the impurity. Finally, the model with split spins is brought into a linear geometry which can be represented as a MPS (Fig. I.B.14, bottom). A problem with this geometry and time-evolution via the Suzuki-Trotter splitting as outlined above is that one would have to repeatedly apply long-ranged MPO, i.e. the interactions of the Hamiltonian are not of the nearest-neighbor kind, for which MPS are particular well suited. A solution was presented in Ref. 41 by applying so called swap gates with the local time-evolution operators which effectively move the impurity through the lattice while doing a time-evolution step. This process is explained in more detail in the next section. Another technical point is that for the time-evolution we need to compute the time-ordered product of the matrix exponential. This is approximated in the present thesis by taking the mean of the Hamiltonian between two consecutive time steps and doing a time-evolution as if the Hamiltonian was constant.

$$\mathcal{T} e^{-i\int_{t_0}^{t_0+\Delta t} H(\bar{t}) d\bar{t}} \approx e^{-\frac{i\Delta t}{2}(H(t_0)+H(t_0+\Delta t))} \tag{I.B.220}$$

When one computes the Green function with Matrix Product States it is possible to extrapolate the Green function to longer simulation times with linear prediction. This is summarized in Sec. VI.2.

I.B.7 Swap Gates

Ref. 41 introduced swap gates[30,72] to compute the time evolution of the Anderson Impurity Model where the usage of the star basis in the MPS formalism introduces long ranged interactions. A swap gate changes the order of two neighboring lattice sites, including the fermionic ordering[41], and the graphical representation in the MPS notation is depicted in Fig. I.B.15. The fermionic ordering used in this thesis is the same as the MPS geometry in Fig. I.B.14.

$$\begin{aligned}
&\left|n_{N_b,\uparrow}, n_{N_b,\downarrow}, n_{N_b-1,\uparrow}, n_{N_b-1,\downarrow}, \dots, n_{0,\uparrow}, n_{0,\uparrow}\right\rangle \\
&\quad = \left(c^\dagger_{N_b,\uparrow}\right)^{n_{N_b,\uparrow}} \left(c^\dagger_{N_b-1,\uparrow}\right)^{n_{N_b-1,\uparrow}} \dots \left(c^\dagger_{2,\uparrow}\right)^{n_{2,\uparrow}} \left(c^\dagger_{1,\uparrow}\right)^{n_{1,\uparrow}} \\
&\qquad \left(c^\dagger_{0,\downarrow}\right)^{n_{0,\downarrow}} \left(c^\dagger_{0,\downarrow}\right)^{n_{0,\downarrow}} \\
&\qquad \left(c^\dagger_{1,\downarrow}\right)^{n_{1,\downarrow}} \left(c^\dagger_{2,\downarrow}\right)^{n_{2,\downarrow}} \dots \left(c^\dagger_{N_b-1,\downarrow}\right)^{n_{N_b-1,\downarrow}} \left(c^\dagger_{N_b,\downarrow}\right)^{n_{N_b,\downarrow}} |0\rangle
\end{aligned} \tag{I.B.221}$$

Here, N_b is the number of bath sites and site 0 is the impurity. As mentioned above, in the fermionic ordering employed here, the Anderson Impurity Model can be viewed as a spin-less fermion model, meaning we can ignore the spin for now. When changing the fermionic ordering of a basis state in the occupation basis, one has to multiply the state with -1 if both lattice

Figure I.B.15. Graphical representation of a swap gate (left) and a combination of a swap gate and a general operator that acts on two neighboring sites (right).

site are occupied. In matrix representation this can be written as:

$$S_{i,i+1} = \begin{array}{c} \\ \langle 0,0| \\ \langle 0,1| \\ \langle 1,0| \\ \langle 1,1| \end{array} \begin{array}{cccc} |0,0\rangle & |0,1\rangle & |1,0\rangle & |1,1\rangle \\ \end{array} \hspace{-0pt}$$

$$S_{i,i+1} = \begin{array}{c|cccc} & |0,0\rangle & |0,1\rangle & |1,0\rangle & |1,1\rangle \\ \hline \langle 0,0| & 1 & 0 & 0 & 0 \\ \langle 0,1| & 0 & 0 & 1 & 0 \\ \langle 1,0| & 0 & 1 & 0 & 0 \\ \langle 1,1| & 0 & 0 & 0 & -1 \end{array} \tag{I.B.222}$$

This has the property $S^2_{i,i+1} = 1$ and can be written in spin-less fermion notation as:

$$S_{i,i+1} = 1 + c_i^\dagger c_{i+1} + c_{i+1}^\dagger c_i - n_i - n_{i+1} \tag{I.B.223}$$

With a bit of effort one can verify the following statements:

$$\begin{aligned} \forall \alpha, \beta : \quad & S_{i,i+1}\, Q^\alpha_{i-1}\, Q^\beta_i\, S_{i,i+1} = Q^\alpha_{i-1}\, Q^\beta_{i+1} \\ \alpha, \beta \in \{1,2,3,4\} \qquad & Q_i = (\mathbb{1}_i,\, c_i^\dagger,\, c_i,\, c_i^\dagger\, c_i) \end{aligned} \tag{I.B.224}$$

Since $\mathbb{1}_i$, $c_i^\dagger$, c_i, and $c_i^\dagger\, c_i$ form an operator basis, we can write every operator $O_{i,j}$ that acts non-trivially on only two lattice sites i and j as:

$$O_{i,j} = \sum_{\alpha,\beta} O_{\alpha,\beta}\, Q^\alpha_i\, Q^\beta_j \tag{I.B.225}$$

This means we can apply every operator of the form Eq. (I.B.225) by swapping sites with swap gates until the relevant sites are nearest-neighbors and then apply $O_{i,i+1}$ and then swap the sites back to their original places. In Sec. I.B.6, we peeled of the single hybridization terms from the time-evolution operator one by one. Without swap gates an expensive computational step would be application of $e^{\frac{\tau}{2} H_{p,s}}$ to the Matrix Product State. To work around this problem the impurity is swapped back and forth through the bath, so that it neighbors every bath site and the application of $e^{\frac{\tau}{2} H_{p,s}}$ is a simple nearest-neighbor operation. This can best be viewed in the graphical MPS notation as shown in Fig. I.B.16. Another optimization is that we can combine a time-evolution operator and a swap gate into a single operator (Fig. I.B.15, right hand side) to cut the computational cost, because the multiplication of two gates is way cheaper than two successive applications of two operators.

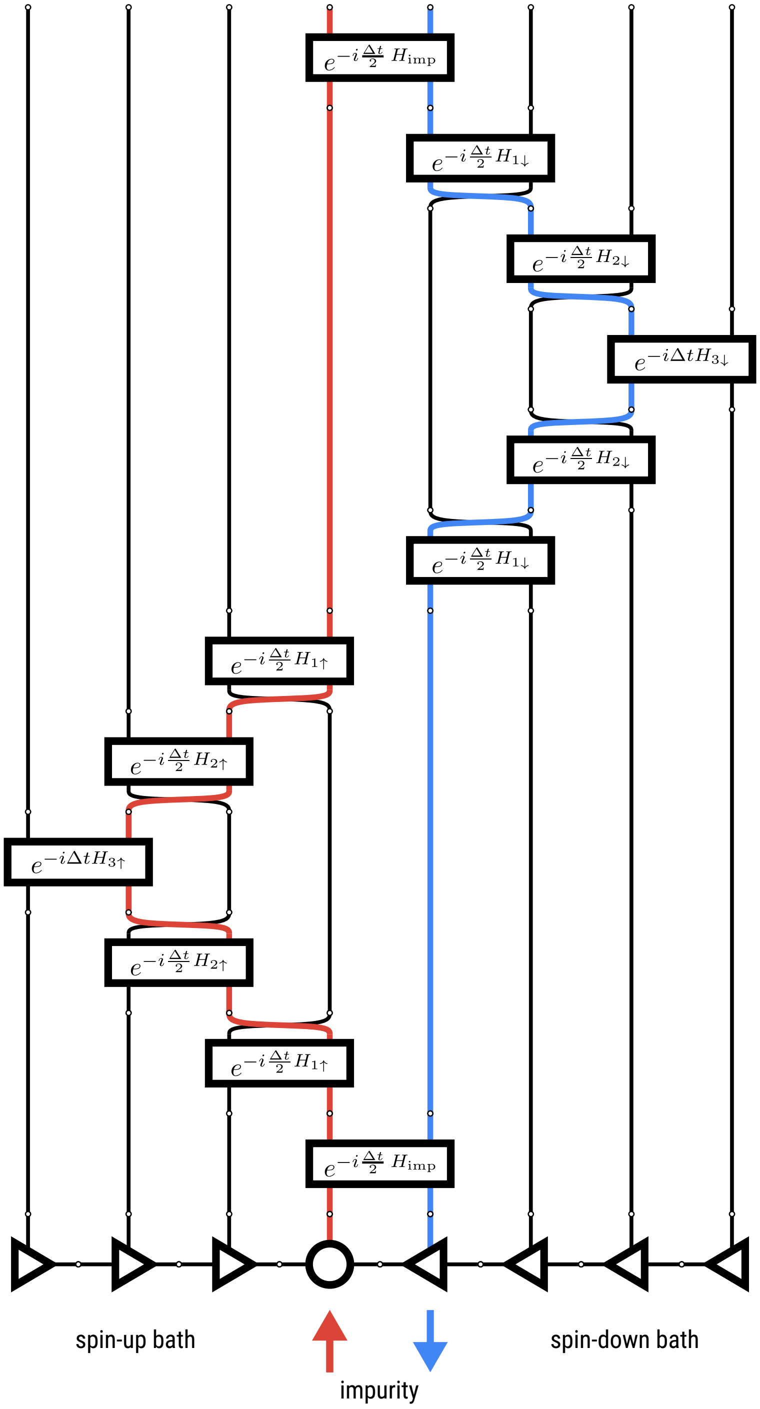

Figure I.B.16. Graphical representation of one time step of Δt (adapted from Ref. 110). Step by step, we swap one spin of the impurity along the bath and handle the single interactions with the bath, one site at a time. Note that when we swap from the center to the side of the chain, we first apply the time-evolution operator and then swap gate, and when we swap back to the center we first apply the swap gate and then the time-evolution operator.

I.B.8 Summary: New Solver on Real Time Contour

The theoretical ingredients of the new solver are distributed over Part I. We summarize the necessary steps of the solver here. Note that there is a similar list of steps in Alg. (I.A.3). Here, the actual steps we programmed are presented. The solver is operated in such a way that we repeat the DMFT loop for every subsequent time step like described in the top right of Fig. I.A.3.

Algorithm I.B.6: Summary of non-equilibrium DMFT with the new solver

Let $H(t)$ be the Hamiltonian of the lattice system. For every $t_N \in \{0,\ \Delta t,\ 2\Delta t,\ \ldots\}$ do:

0.
- *If $t_N = 0$, then start with an initial guess for the equilibrium impurity Green function.*

  When no good guess is available and the solution is suspected to be metallic, one can usually start from the semicircular density of states.
- *If $t_N \neq 0$, one can use the values of the Green function from the last time step on the non-equilibrium axis, i.e. the first initial guess for the Green function is:*

$$G^{\rceil}(t_N, t_E) = G^{\rceil}(t_N - \Delta t, t_E) \tag{I.B.226}$$

$$G^{\lceil}(t_E, t_N) = G^{\lceil}(t_E, t_N - \Delta t) \tag{I.B.227}$$

$$G^{>N}(t_N, t'_N) = G^{>N}(t_N - \Delta t, t'_N) \tag{I.B.228}$$

$$G^{>N}(t'_N, t_N) = G^{>N}(t'_N, t_N - \Delta t) \tag{I.B.229}$$

$$G^{<N}(t_N, t'_N) = G^{>N}(t_N - \Delta t, t'_N) \tag{I.B.230}$$

$$G^{<N}(t'_N, t_N) = G^{<N}(t'_N, t_N - \Delta t) \tag{I.B.231}$$

For all:

$$t'_N \leq t_N \tag{I.B.232}$$

$$|t_E| \leq t_{E,max} \qquad (= 20 \textit{ in the present thesis}) \tag{I.B.233}$$

1. *Compute G_k from the impurity Green function G and then the new Δ from G_k like described in Sec. I.B.4. If the investigated lattice is the Bethe lattice one can instead compute the updated hybridization function with: $\Delta(\mathbf{t}, \mathbf{t}') = v(\mathbf{t})\, G^{(n)}_{IMP}(\mathbf{t}, \mathbf{t}')\, v(\mathbf{t}')^*$, for all $\mathbf{t} \leq t_N$ and $\mathbf{t}' \leq t_N$ (according to Fig. I.A.3, bottom)*

2. *Compute the hopping amplitudes of the Anderson Impurity Model with Alg. (I.B.5) to set the bath parameters. Note that $t_{N,max}$ in Alg. (I.B.5) corresponds to $t_N - \Delta t$ here.*

3. *Compute the Green function of the Anderson Impurity Model, for all $\mathbf{t} \leq t_N$ and $\mathbf{t}' \leq t_N$ (according to Fig. I.A.3, bottom), like described in Alg. (I.B.4). Use MPS and swap gates for the time-evolution like described in Secs. I.B.6 and I.B.7. Note that $t_{N,max}$ in Alg. (I.B.4) corresponds to $t_N - \Delta t$ here.*

4. *Go back to step 1 and repeat until the Green function and hybridization function at t_N are converged. If they are converged, then increase $t_N \to t_N + \Delta t$ and go to step 0.*

The total computational cost of the solver cannot be easily quantified in advance, because the required matrix dimension m to represent the quantum state of the Anderson Impurity Model as an MPS up to a certain accuracy (see the keyword *discarded weight* in Ref. 30) depends on the type of quench investigated in $H(t)$ and on how close one operates to the Mott transition. The computational cost of MPS operations goes like $\mathcal{O}(m^3)$. Additionally, with the naïve integration scheme we use here we need to compute the Green function $G(\mathbf{t}, \mathbf{t}')$ for every combination of $\mathbf{t}$ and $\mathbf{t}'$. Suppose that we want the non-equilibrium DMFT loop to converge up to some $t_{N,max}$. Then there is a computational cost of the order of $\mathcal{O}(t^2_{N,max} + t_{N,max}\, t_{E,max})$. Because the required matrix dimension is a function of time the total computational cost is of the order of $\mathcal{O}(\sum_{t_N} (t_N + t_{E,max} + m(t_N)^3)\, \Delta t)$.

Subpart I.C

New Solver: Tests and First Results

I.C.1 Model

To test our new non-equilibrium DMFT solver, we replicate and extend the simulations done in Ref. 52 and the subsequent Ref. 53, where the authors used weak-coupling CTQMC (see Sec. I.B.5) as the solver. We investigate the Hubbard model at half-filling on the Bethe lattice, simulating the situation where the initial state is the ground state at zero temperature and the system is time-evolved after a quench in the interaction parameter U. For an easier comparison with Ref. 52 we will use a different notation for time in this subpart of the present thesis and t denotes what is the non-equilibrium time t_N in the rest of Part I. We will provide energies in units of hopping, and times in units of inverse hopping.

$$H = -\sum_{\langle i,j\rangle,s} c^{\dagger}_{i,s} c_{j,s} + c^{\dagger}_{j,s} c_{j,s} + U(t) \sum_{i} \left(n_{i,\uparrow} - \frac{1}{2} \right) \left(n_{i,\downarrow} - \frac{1}{2} \right) \tag{I.C.1}$$

$$U(t) = \begin{cases} U_0 & \text{if } t \leq 0 \\ U_1 & \text{if } t > 0 \end{cases} \tag{I.C.2}$$

In Ref. 46, several quenches of this kind with $U_0 > 0$ and non-zero temperature $\beta = 5$ were investigated as a proof of concept for the Non-Crossing Approximation and its generalizations. Usually, action based solvers cannot do DMFT at zero temperature, because the L-shaped contour would have to go to infinity on the imaginary axis. The authors of Ref. 52 and 53 circumvented this problem by considering only the non-interacting initial state of $U_0 = 0$. In this case the Green function only needs to be computed on the real axis with the impurity solver because the self-energy is strictly zero if one of the time arguments lies on the imaginary axis[53].

$$\forall \tau : \quad \Sigma^{\lceil}_{L}(\tau, t) = \Sigma^{\rceil}_{L}(t, \tau) = 0 \tag{I.C.3}$$

This simplifies the computations since all components can be related to the real time branch of the Green function[53]. In Ref. 52, the double occupancy per lattice site, the momentum

Table I.C.1. Summary of the main parameters used for the simulations in this thesis. The step numbers inside the parenthesis refer to those in Fig. I.B.4. The cutoff is defined in Def. (I.B.12). The linear prediction is described in Sec. VI.2.

cutoff, equilibrium axis (step 5b)	10^{-08}
cutoff, forward time-evolution (step 1)	10^{-10}
cutoff, backwards time-evolution (step 3b)	10^{-08}
time step	10^{-2}
bath sites, first bath	99
bath sites, second bath	100
$t_{E,max}$, impurity solver	20
$t_{E,max}$, linear prediction	100

distribution, and its discontinuity at the Fermi-level were calculated:

$$d(t) = \left\langle n_{0,\uparrow}(t)\, n_{0,\downarrow}(t) \right\rangle \tag{I.C.4}$$

$$n_\epsilon(t) = \left\langle c^\dagger_{\epsilon_k}(t)\, c_{\epsilon_k}(t) \right\rangle \tag{I.C.5}$$

$$\Delta n(t) = \lim_{\epsilon \to 0^+} \left(n_{-\epsilon}(t) - n_\epsilon(t) \right) \tag{I.C.6}$$

In the case of $U_0 = 0$, the initial double occupancy can easily be calculated, because the two spin directions do not interact:

$$U_0 = 0: \qquad d(0) = \left\langle n_{0,\uparrow}(0)\, n_{0,\downarrow}(0) \right\rangle = \left\langle n_{0,\uparrow}(0) \right\rangle \left\langle n_{0,\downarrow}(0) \right\rangle = \frac{1}{2}\frac{1}{2} = \frac{1}{4} \tag{I.C.7}$$

In the present thesis, we measure the same quantities and furthermore investigate different quenches with $U_0 \neq 0$, which is now possible with our new solver at zero temperature.

To use a Matrix Product State based solver, one must choose suitable values for the cutoff and other parameters. They are specified in table I.C.1. To compensate for small numerical errors, we enforce particle-hole symmetry by averaging pairs of hopping amplitudes to. Let $\tilde{V}_{-/+}$ be the hopping amplitude obtained with Alg. (I.B.5). The actual hopping amplitudes V_- of the first bath used for the impurity solver are computed as follows.

$$V_-(\epsilon, t) = \frac{1}{2} \left(\tilde{V}_-(\epsilon, t) + \tilde{V}_-(-\epsilon, t)^* \right) \tag{I.C.8}$$

The same holds true for the second bath where we average over two corresponding bath orbitals that are occupied and empty in the initial state. In Sec. I.B.3 we explain that we couple two bath sites to the impurity for every time slice, where one of those bath sites is initially occupied and the other is initially empty. Let p be a bath site of the second bath that is initially empty and $\overline{p}$ be the bath site of the second bath that gets coupled to the impurity at the same time slice. Since $\Delta_+^{<N}(t,t') = \Delta_+^{>N}(t,t')^*$ holds true when the system is particle-hole symmetric[49], we enforce particle-hole symmetry for the second bath in the following way:

$$\overbrace{V_{+,p}(t)}^{\text{init. occ.}} = \frac{1}{2}\left(\overbrace{\tilde{V}_{+,p}(t)}^{\text{init. occ.}} + \overbrace{\tilde{V}_{+,\overline{p}}(t)^*}^{\text{init. empty}}\right) \tag{I.C.9}$$

$$\underbrace{V_{+,\overline{p}}(t)}_{\text{init. empty}} = \frac{1}{2}\left(\underbrace{\tilde{V}_{+,p}(t)}_{\text{init. occ.}} + \underbrace{\tilde{V}_{+,\overline{p}}(t)^*}_{\text{init. empty}}\right)^* \tag{I.C.10}$$

Spin symmetry is enforced by taking the average of the hopping amplitudes of spin-up and spin-down. We do not numerically enforce half-filling at the impurity level, but we check that the initial state is in the correct particle sector at the impurity after performing the ground state search with DMRG. We start with an initial state of the Anderson Impurity Model that is half-filled on the whole system. This means that the number of spin-up electrons in the initial state of the impurity and the first bath is $\frac{1+N_{b,-}}{2}$, where $N_{b,-}$ is the number of bath sites of the first bath. The second bath, which is initially decoupled from the impurity, contains additional $\frac{N_{b,+}}{2}$ spin-up electrons, where $N_{b,+}$ is the number of bath sites of the second bath. The number of spin-down electrons is equal to number spin-up electrons in each bath of the initial state.

I.C.2 Double Occupancy

I.C.2.1 Comparison with Existing Results ($U_0 = 0$)

In Fig. I.C.1 the results of the double occupancy taken from Ref. 52 are shown. One of the main results of the referenced publications 52 and 53 is that there is fast thermalization at $U_1 = U_c^{dyn} = 3.2$, indicated by a fast convergence to zero of the discontinuity $\Delta n(t)$ at the Fermi-level, and a qualitatively different behavior of the system depending on whether $U_1 < U_c^{dyn}$ or $U_1 > U_c^{dyn}$. This will be examined in Sec. I.C.3.

Here, we will focus on the double occupancy, where the qualitatively different behavior with U_1 can also be seen, albeit not as well as with the momentum distribution. When $U_1 < U_c^{dyn}$, the double occupancy quickly decays from its initial value and slowly thermalizes afterwards[52]. For $U_1 > U_c^{dyn}$, Ref. 52 points out an oscillating behavior that is well understood in the atomic limit[52]. In Fig. I.C.2 a comparison between the double occupancy taken from Ref. 52 and the one computed with our new solver is shown. The time series align very well, with maximum differences of only about $4 \cdot 10^{-3}$. Filling conservation with our solver holds up very well and the difference between the single up/down expectation value and the analytic value at half-filling is very small: $|\langle n_\uparrow(t)\rangle - 0.5| \lessapprox 10^{-4}$, whereas in Ref. 52 the difference[111] is $|\langle n_\uparrow(t)\rangle - 0.5| \lessapprox 10^{-3}$. This may explain some of the small deviations in Fig. I.C.2.

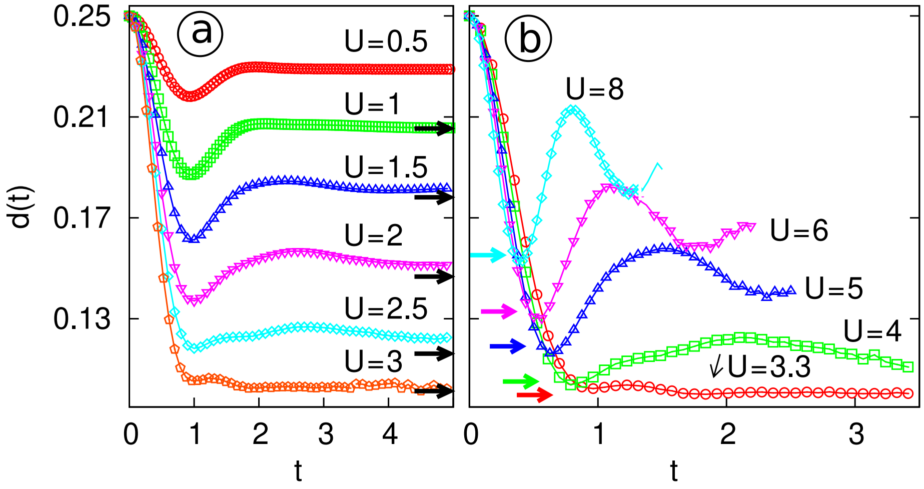

Figure I.C.1. Plot taken from Ref. 52 ($U_0 = 0$). The double occupancy is shown as a function of time for different U_1. The left column is for values of $U_1 < 3.2$, while the quenches $U_1 > 3.2$ are in the right column.

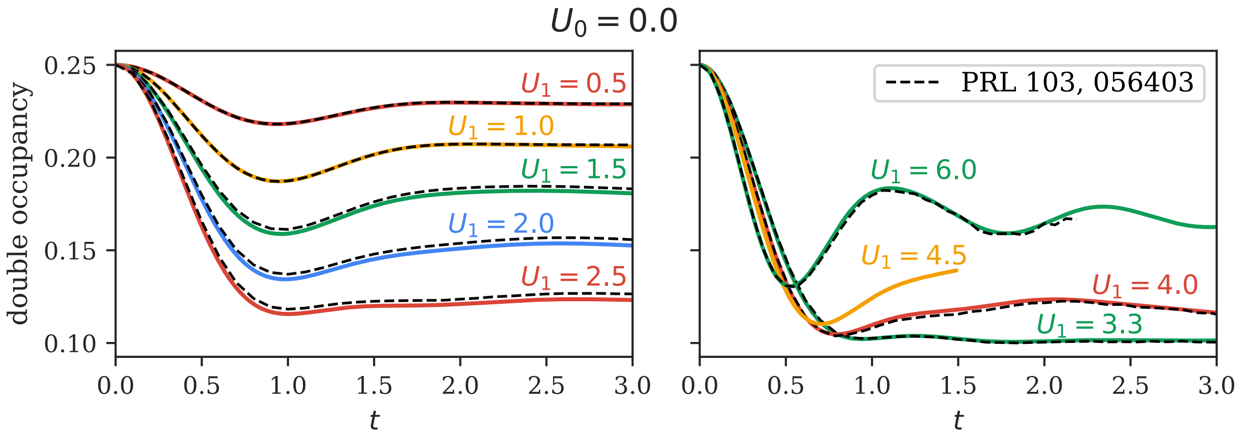

Figure I.C.2. Double occupancy per site as a function of time for $U_0 = 0$, calculated with our new solver. The dashed lines are taken from Ref. 52 for comparison.

I.C.2.2 New Results, Interacting Initial States

One great improvement of the new solver is that we are not restricted to specific parameter ranges and we can simulate different initial interaction strengths $U_0 \neq 0$. The time series for the double occupancies can be seen in Fig. I.C.3 and the overall appearance agrees very well with the first expectations one would have on how the system would behave after the quench. For $U_1 < U_0$, the system increases the number of double occupations versus the initial state, while it decreases the number of double occupations $U_1 > U_0$. For small U_1, the double occupancy appears to exhibit damped oscillations, possibly for all U_1 on the left column of Fig. I.C.3. We show the double occupancy including larger times for a few cases in Fig. I.C.4, where the damped oscillations are more clearly visible. For larger U_1 (right column of Fig. I.C.3), we see again an oscillating behavior like for $U_0 = 0$ that is well understood in the atomic limit[52]. An apparent shift of U_c^{dyn} towards larger U_1 of the onset of this oscillating behavior will be discussed in Sec. I.C.3.4.

Crossings at Constant U_1

An interesting phenomenon can be observed when we group the double occupancy time series by U_1, as shown in Figs. I.C.5 and I.C.6. If U_0 and U_1 are both small, time series with the same U_1 intersect each other at nearly the same time of $t \approx 0.55$ in units of inverse hoppings. At the crossing point the double occupancy is about the same as the equilibrium double occupancy of U_1. The double occupancies also appear to converge to approximately this same value at large times, when U_1 is not too large. Furthermore, for very small U_1 there seems to be a second crossing point at $t \approx 1.65$. These crossings vanish at higher $U_1 \approx 3.5$. This suggests that there may be an effective model for the Bethe lattice based on the Taylor series with respect to U which is a reasonable approximation for small U, even in non-equilibrium situations. We also investigated the behavior of the crossing points for equal U_1 with respect to the time step and the cutoff. The results can be seen in Fig. I.C.7. They show only a slight dependence on these computational parameters, with the area enclosed by the crossing points staying approximately constant.

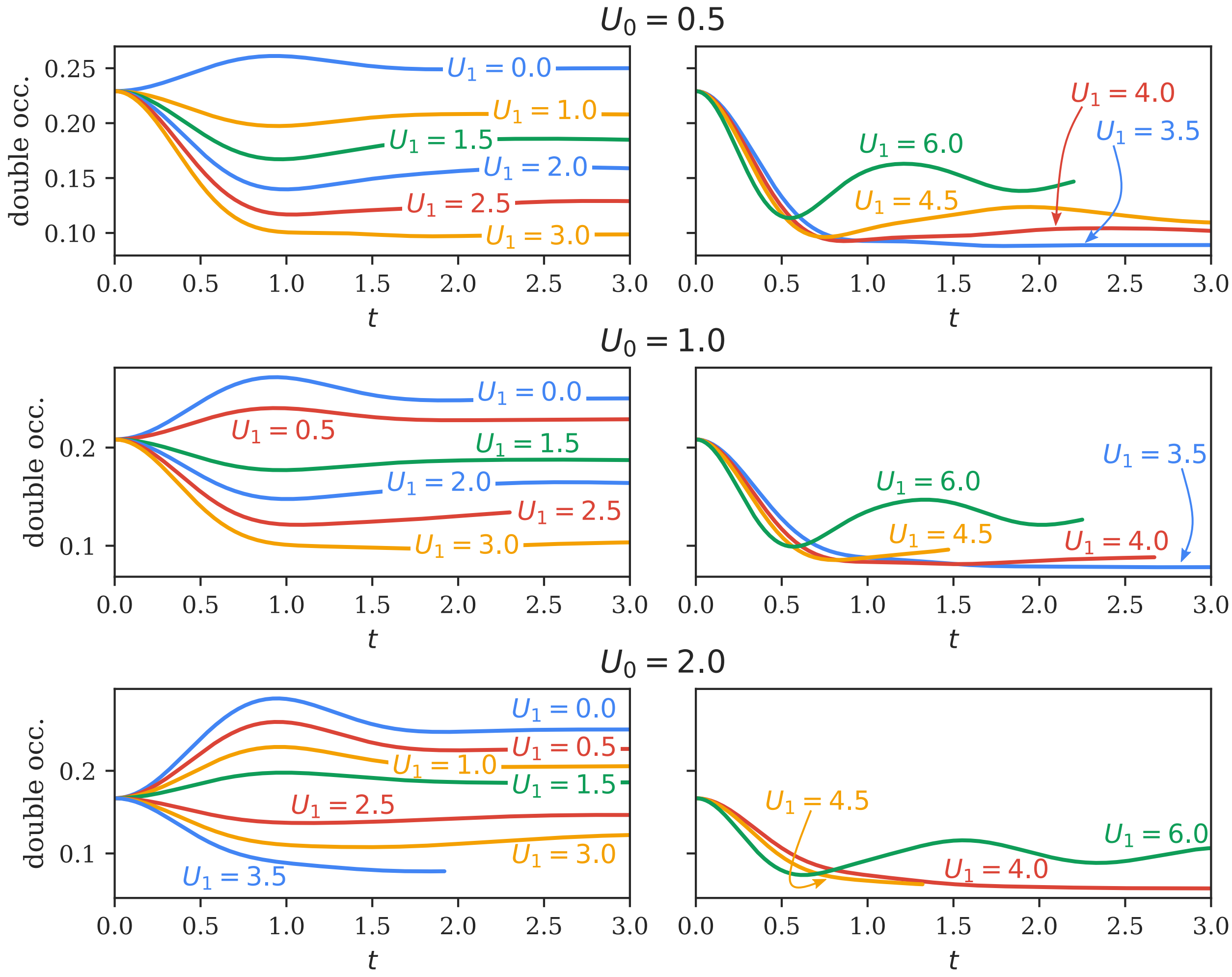

Figure I.C.3. Double occupancy per site as a function of time for $U_0 \neq 0$. Some of the time series end at earlier times $t < 3$, which is not due to a limitation of the solver. These simulations were stopped there during the exploration of the parameter space.

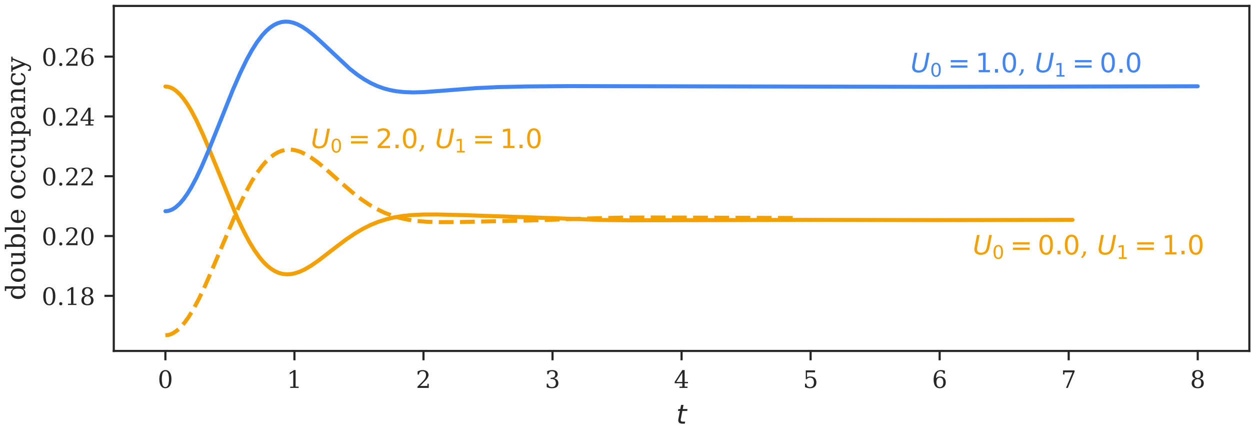

Figure I.C.4. Examples of a few quenches where we performed simulations to longer times than the value of $t = 3$, which is used in the rest of the present part. The maximum time here is arbitrary and not a consequence of the computational cost.

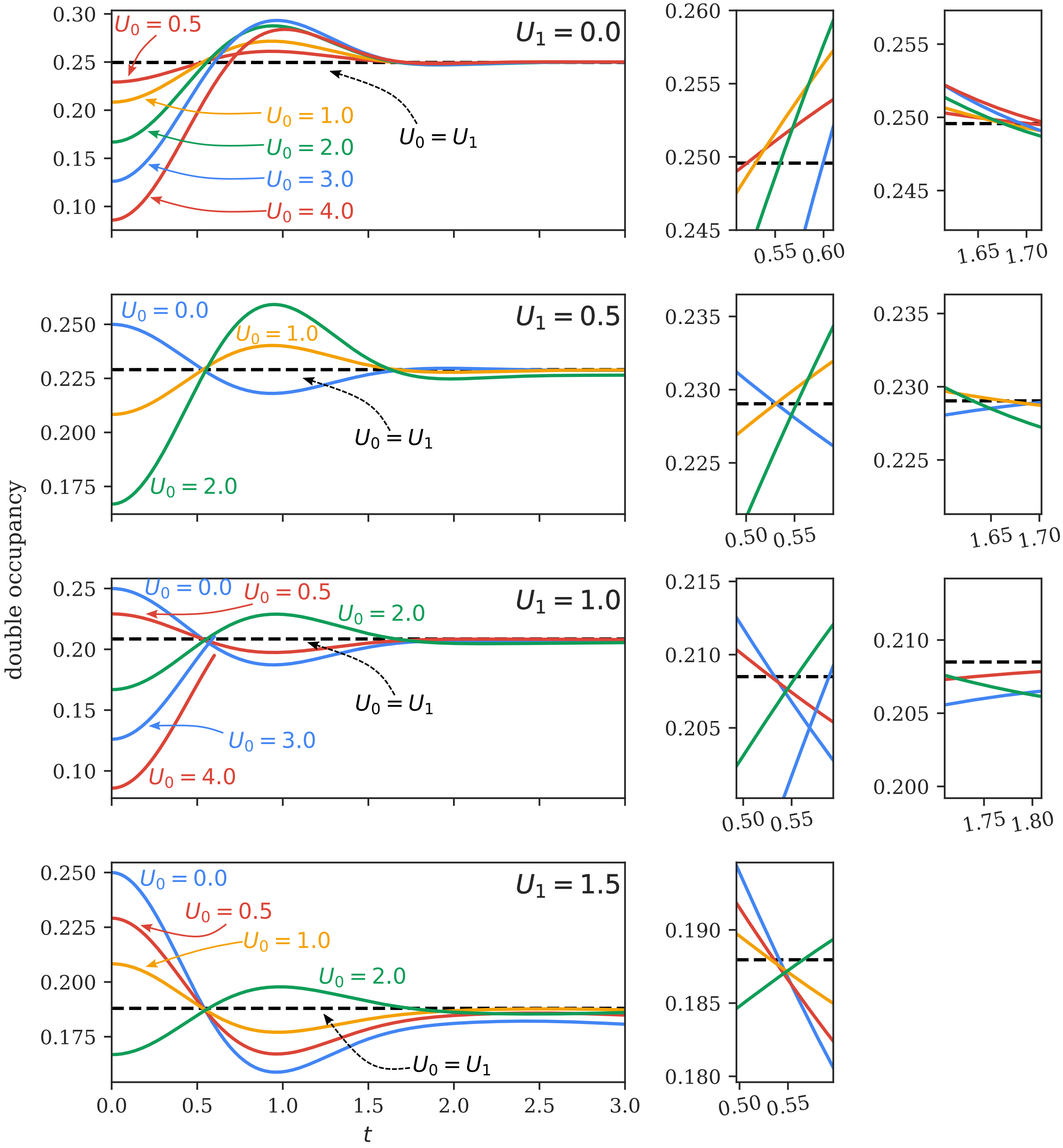

Figure I.C.5. Double occupancy as a function of time for several U_0 grouped by U_1. For small U_1, there are crossings at $t \approx 0.55$, at which the double occupancies are almost the same as the equilibrium double occupancy of U_1. For $U_1 = 0.5$ and $U_1 = 1$, there seems to be a second crossing point at $t \approx 1.6$. The small plots on the right hand side, all on the same scale, zoom in on the crossing areas.

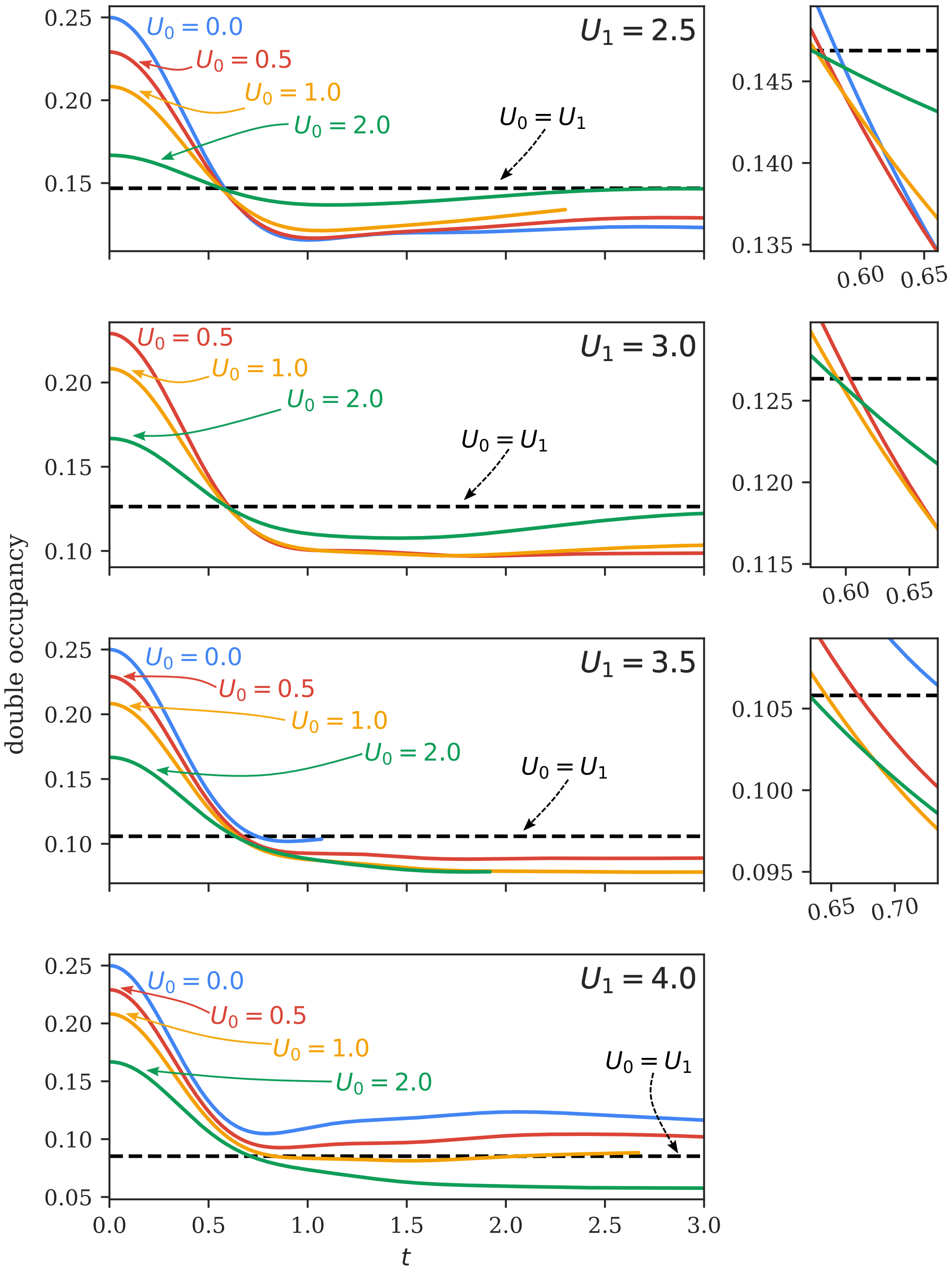

Figure I.C.6. Double occupancy as a function of time for several U_0 grouped by U_1. For small U_1, there are crossings at $t \approx 0.55$, at which the double occupancies are almost the same as the equilibrium double occupancy of U_1. The small plots on the right hand side, all on the same scale, zoom in on the crossing areas. The crossing points apparently dissolve around $U_1 \approx 3.5$.

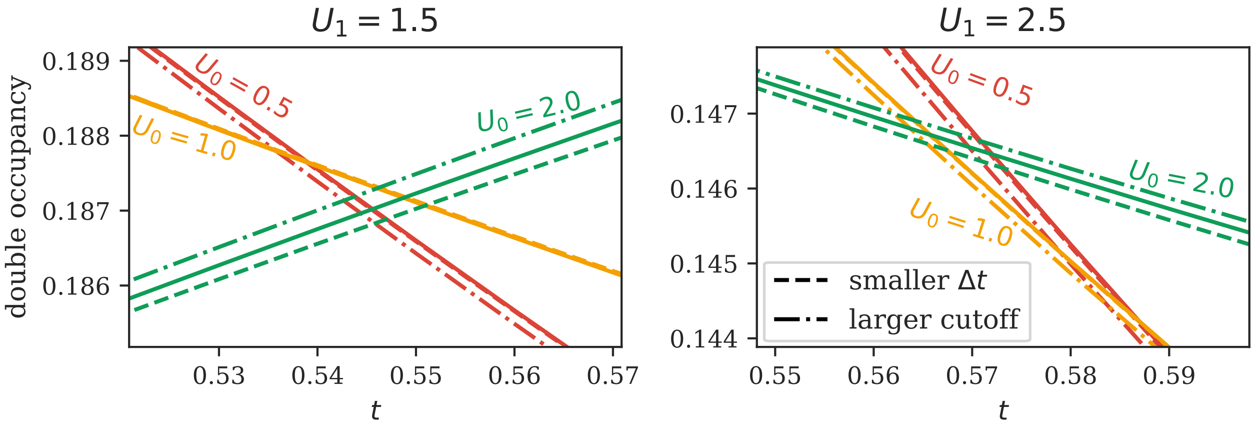

Figure I.C.7. Influence of computational parameters on the crossings of the double occupancy as a function of time, plotted for several U_0 and grouped by U_1. The axes are centered around the crossing regions mentioned above. The solid lines mark simulations with the main parameter tuples used for this thesis. The dashed lines mark simulations with a smaller time step $\Delta t = \frac{\Delta t_{main}}{2}$. The dash-dotted lines mark simulations with a larger cutoff of 10^{-8} for forward time-evolution and 10^{-6} for backward time-evolution after the creation/annihilation operator has been applied. Some dashed and dash-dotted lines are not visible to the eye, because they are on top of their corresponding solid lines. It can be seen that the intersection area stays almost the same for the different parameter sets and there is no clear trend visible of a growing or shrinking crossing area.

I.C.3 Momentum Distribution and Discontinuity of Time-Dependent Occupation

One of the main results of Ref. 52 is that at $U_0 = 0$ there is fast thermalization at $U_1 = U_c^{dyn} = 3.2$, indicated by a fast convergence to zero of the discontinuity $\Delta n(t)$ at the Fermi-level, and a qualitatively different behavior of the system depending on whether $U_1 < U_c^{dyn}$ or $U_1 > U_c^{dyn}$. When $U_1 < U_c^{dyn}$, the authors of Ref. 52 find that the discontinuity settles on a prethermalization plateau, before tending to zero on long time scales. On the other hand, when $U_1 > U_c^{dyn}$, they report collapse-and-revival oscillations, where the time series of the discontinuity forms a damped oscillation with zero as minimal value. The results of Ref. 52 are shown in Fig. I.C.8. In the present thesis, we will not determine whether the system thermalizes after the quench for $U_0 > 0$, but will investigate the behavior of the discontinuity of the momentum distribution at the Fermi-level.

In order to compute the momentum distribution $\langle n_\epsilon(t)\rangle = \mathrm{Im}(G_\epsilon^<(t,t))$, one must solve the following integral equation on the contour, like described in Sec. I.B.4. Note that $\epsilon = \epsilon_k$ corresponds to the energy of the free-particle eigenstate k.

$$G = G_\epsilon + G_\epsilon * \Delta * G - G_\epsilon * \varepsilon * G \tag{I.C.11}$$

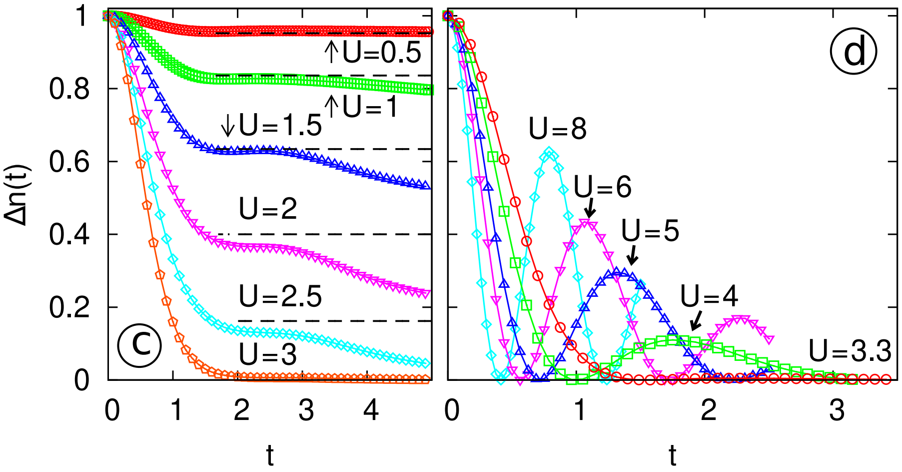

Figure I.C.8. Plot taken from Ref. 52 ($U_0 = 0$). The discontinuity of the momentum distribution as a function of time is shown for different U_1. The left column is for values of $U_1 < 3.2$, while the quenches $U_1 > 3.2$ are on the right column.

On the contour with two real time axes this poses a small problem because there may be $G^{\ulcorner}_{\epsilon}(t_E, t_N)$ (or other mixing components) that decay very slowly to zero with respect to t_E, and the momentum resolved Green function may not have converged to zero by the maximum t_E calculated, altering the results. To circumvent this problem we damp the Green function and the hybridization function with an exponentially decaying function after performing the linear prediction (Sec. VI.2), which amounts to convoluting the Green function with a Lorentz peak in ω-space. For the single components this means:

$$G^{\ulcorner}(t_E, t_N) \longrightarrow G^{\ulcorner}(t_E, t_N)\, e^{-\alpha|t_E|} \tag{I.C.12}$$

$$G^{\llcorner}(t_E, t_N) \longrightarrow G^{\llcorner}(t_E, t_N)\, e^{-\alpha|t_E|} \tag{I.C.13}$$

$$G^{\urcorner}(t_N, t_E) \longrightarrow G^{\urcorner}(t_N, t_E)\, e^{-\alpha|t_E|} \tag{I.C.14}$$

$$G^{\lrcorner}(t_N, t_E) \longrightarrow G^{\lrcorner}(t_N, t_E)\, e^{-\alpha|t_E|} \tag{I.C.15}$$

$$G^{>N}(t_N, t_N) \longrightarrow G^{>N}(t_N, t_N) \tag{I.C.16}$$

$$G^{<N}(t_N, t_N) \longrightarrow G^{<N}(t_N, t_N) \tag{I.C.17}$$

Note that the non-equilibrium components stay unaltered. We did the calculation with several different dampings $\alpha \in \{\frac{1}{5}, \frac{1}{6}, \frac{1}{7}, \dots, \frac{1}{20}\}$ for later extrapolation to $\alpha = 0$ (see below). Although such an approach generally seems to work for continuous functions, it is more difficult in the present case, because the discontinuity of the momentum distribution at $\epsilon = 0$, which is the quantity of interest here, becomes convoluted with the damping function.

I.C.3.1 Momentum Distribution at Finite Broadening

To give a general impression of the time-dependent momentum distribution we present the data with the lowest damping $\alpha = \frac{1}{20}$ in Figs. I.C.9 to I.C.13. The number of nodes for ϵ is equal to 200, which are equally distributed over the range $[-2, 2]$. In these plots, areas where the absolute values of the slope of $\langle n_\epsilon(t) \rangle$ with respect to ϵ is greater than 0.4 are marked in red to indicate the area with a possible discontinuity at $\alpha = 0$. In Fig. I.C.9 we see that the results qualitatively align very well with the results of Ref. 52 (Fig. I.C.8). For $U_1 \lesssim 3.2$ there is a shrinking and plateauing gap, while for $U_1 \gtrsim 3.2$ we see the collapse-and-revival regime indicated by the shrinking and growing red areas. These results stay almost unchanged in the cases of $U_0 = 0.5$ and $U_0 = 1.0$, where we see a potential rapid convergence to zero of the discontinuity at $U_1 \approx 3.5$. However, at $U_0 = 2$ there is rapid convergence at $U_1 = 4$, whereas at $U_0 = 0$, the case $U_1 = 4$ shows oscillations. This indicates that there is an increasing U_c^{dyn} with increasing U_0. Because the data points with respect to U_1 are rather sparse, we cannot determine whether there is a range of U_1 where the rapid convergence happens or whether it is one singular U_1. The behavior of the red regions in other cases also suggests that U_c^{dyn} shifts to higher values when U_0 grows. For example, the size of the red region is larger for the quench $U_0 = 1$, $U_1 = 2$ than for $U_0 = 0$, $U_1 = 2$. In Sec. I.C.3.4 (Fig. I.C.18), we will show that after extrapolating the data to zero broadening, one can indeed see a clear shift towards larger U_1 when the initial coupling U_0 is increased.

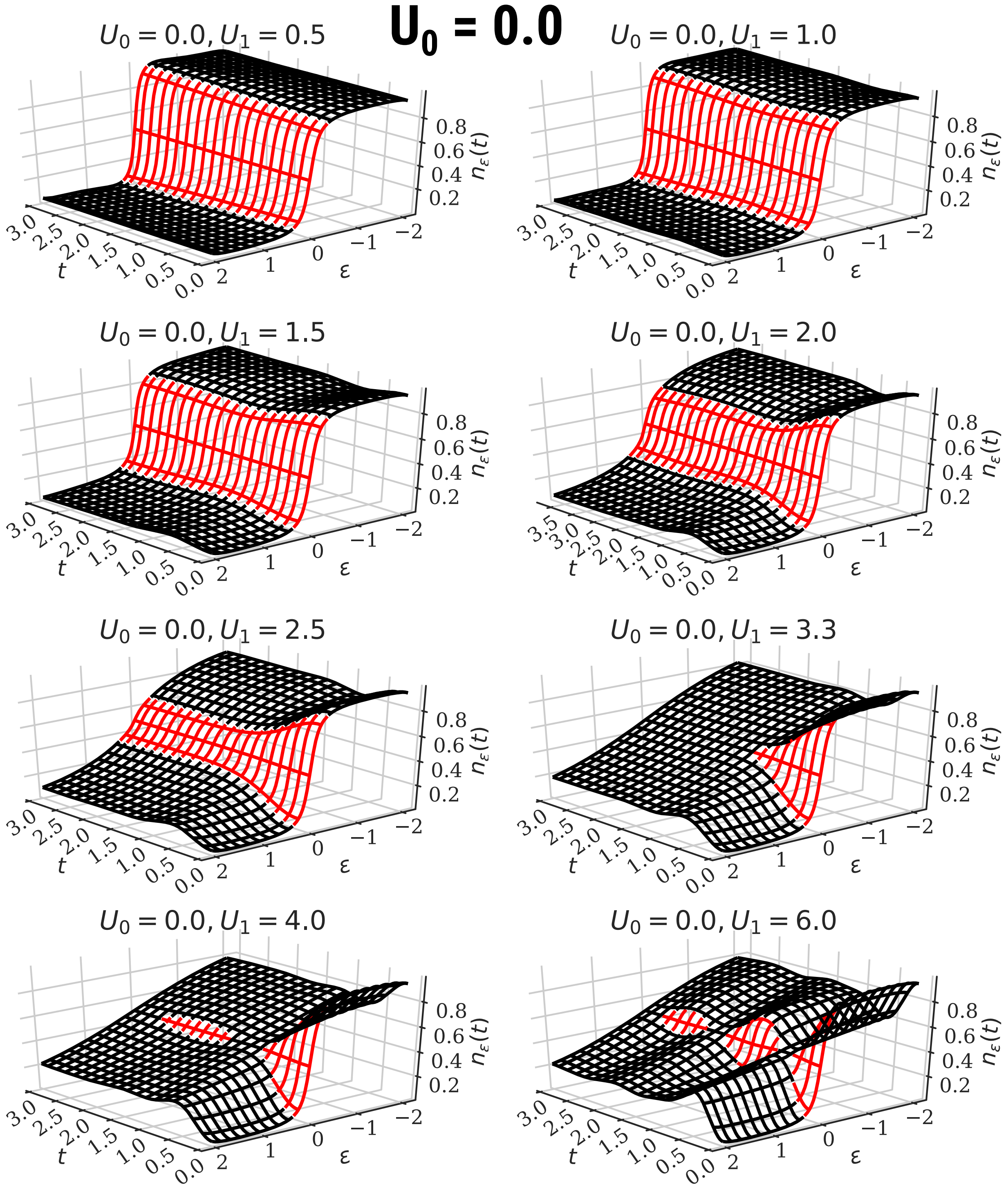

Figure I.C.9. $\langle n_\epsilon(t) \rangle$ for $U_0 = 0$ and several values of U_1. In this figure there is an applied broadening of $\alpha = \frac{1}{20}$. The red regions mark where the absolute value of the slope of $\langle n_\epsilon(t) \rangle$ with respect to ϵ is greater than 0.4.

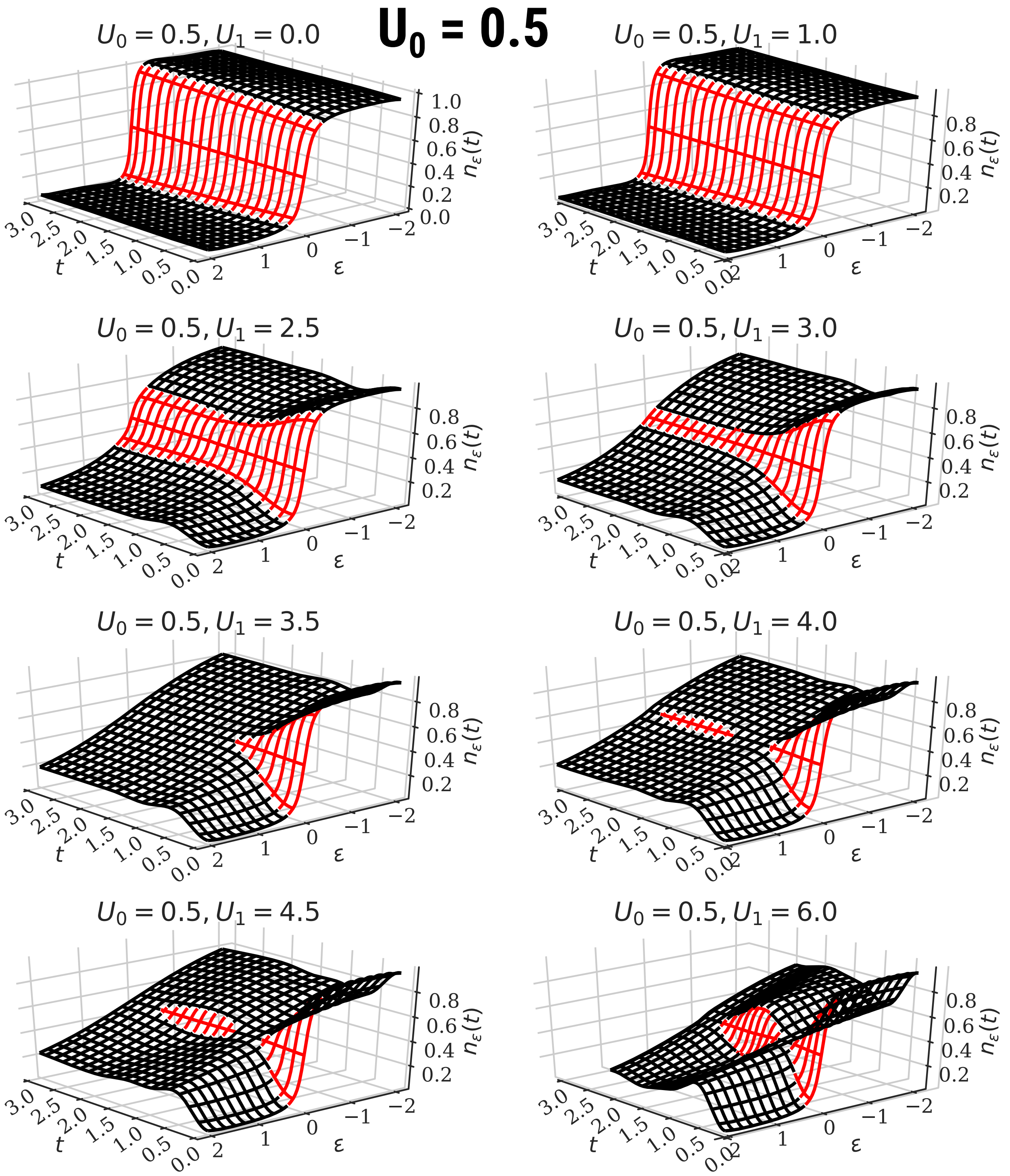

Figure I.C.10. $\langle n_\epsilon(t)\rangle$ for $U_0 = 0.5$ and several values of U_1. In this figure there is an applied broadening of $\alpha = \frac{1}{20}$. The red regions mark where the absolute value of the slope of $\langle n_\epsilon(t)\rangle$ with respect to ϵ is greater than 0.4.

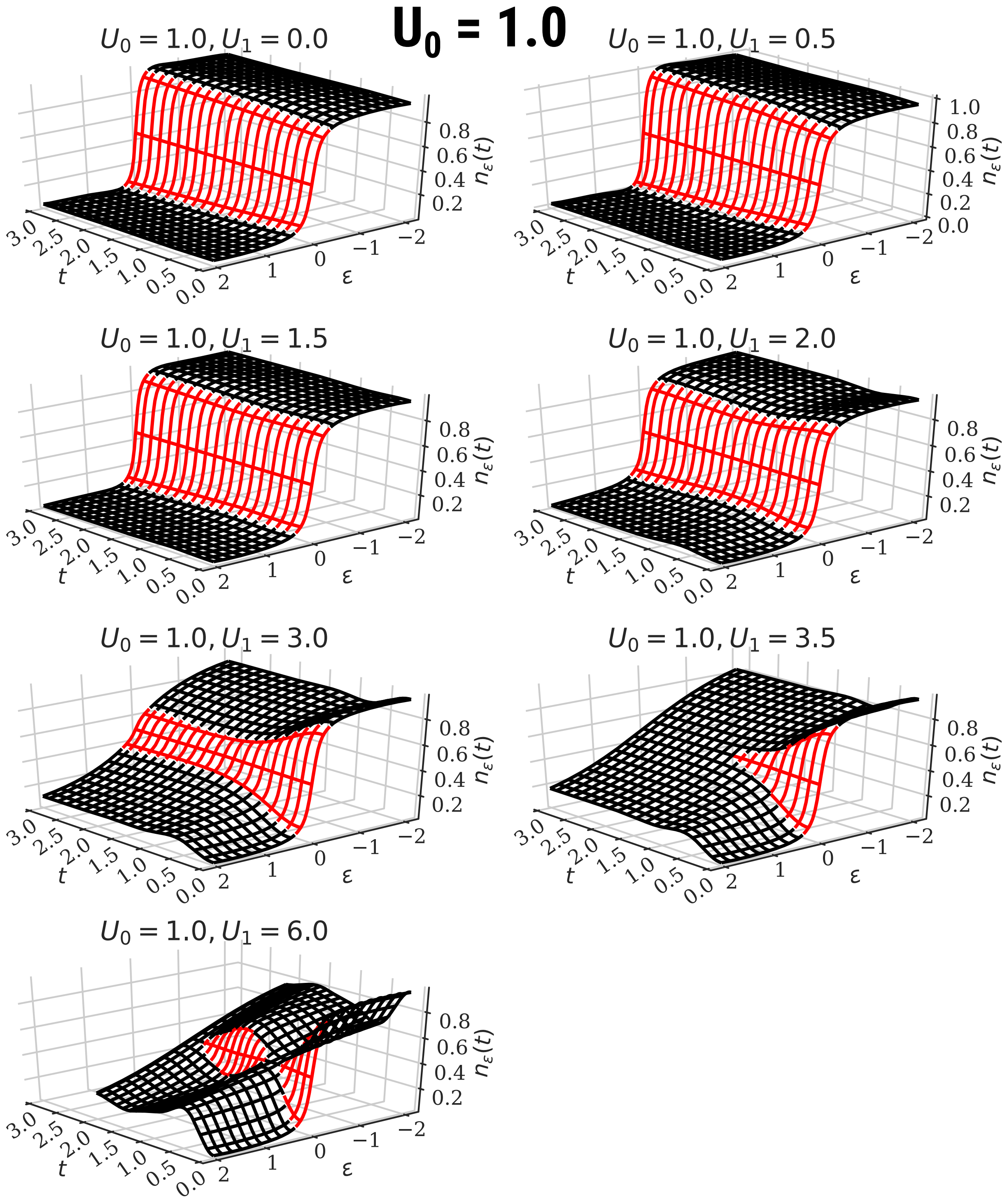

Figure I.C.11. $\langle n_\epsilon(t)\rangle$ for $U_0 = 1$ and several values of U_1. In this figure there is an applied broadening of $\alpha = \frac{1}{20}$. The red regions mark where the absolute value of the slope of $\langle n_\epsilon(t)\rangle$ with respect to ϵ is greater than 0.4.

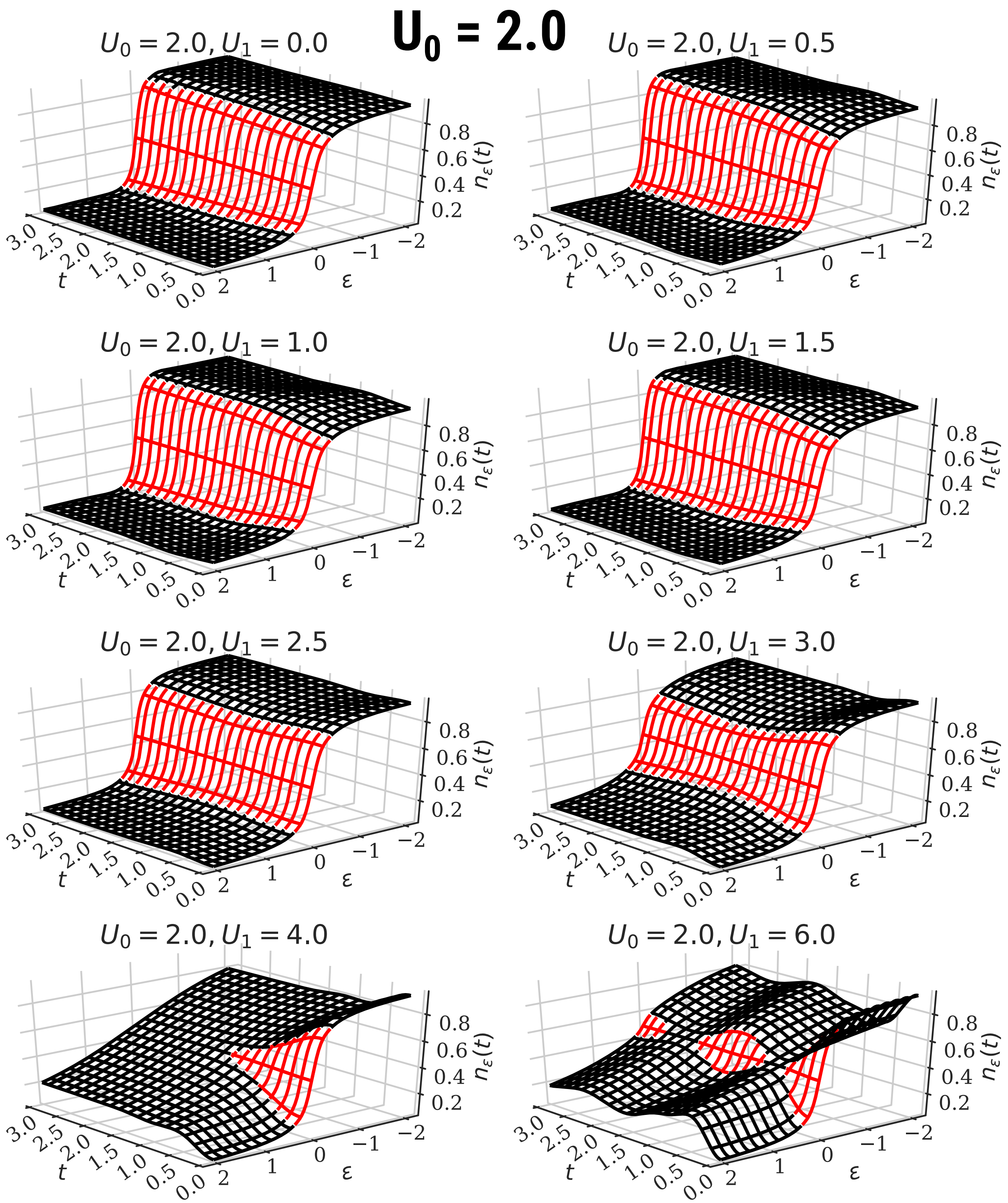

Figure I.C.12. $\langle n_\epsilon(t) \rangle$ for $U_0 = 2$ and several values of U_1. In this figure there is an applied broadening of $\alpha = \frac{1}{20}$. The red regions mark where the absolute value of the slope of $\langle n_\epsilon(t) \rangle$ with respect to ϵ is greater than 0.4.

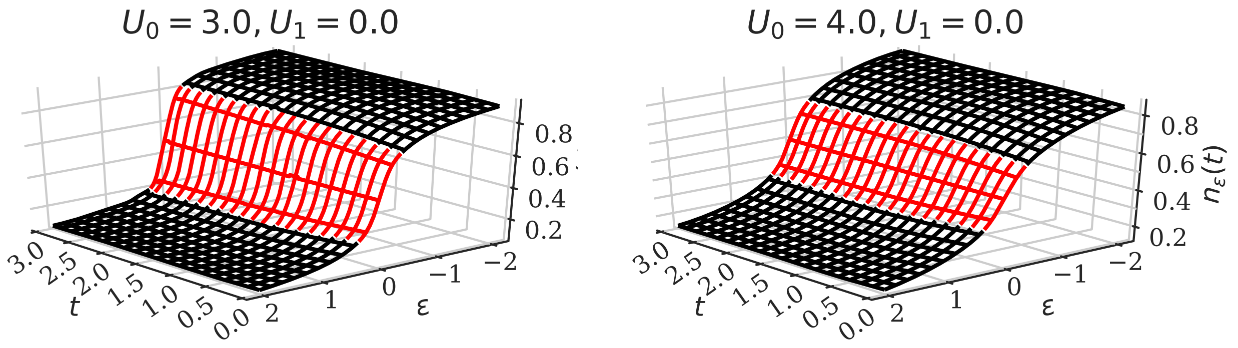

Figure I.C.13. $\langle n_\epsilon(t)\rangle$ for $U_0 = 3$, $U_0 = 4$, and $U_1 = 0$. In this figure there is an applied broadening of $\alpha = \frac{1}{20}$. The red regions mark where the absolute value of the slope of $\langle n_\epsilon(t)\rangle$ with respect to ϵ is greater than 0.4.

I.C.3.2 Extrapolation to Zero Broadening

To test if the broadened momentum distribution is consistent with Ref. 52 we extrapolate with a series of polynomial fits to zero damping/broadening. This is described in Alg. (I.C.7) and illustrated in Fig. I.C.14. When solving Eq. (I.C.11) the particle-hole symmetry can be violated by numerical errors, possibly introduced by the linear prediction (Sec. VI.2). For extrapolating the discontinuity to zero damping, we re-introduce particle-hole symmetry for the momentum distribution by averaging over ϵ and $-\epsilon$.

$$\langle n_{\epsilon,\alpha}(t)\rangle \longleftarrow \frac{1}{2}\left(\langle n_{\epsilon,\alpha}(t)\rangle + \langle n_{-\epsilon,\alpha}(t)\rangle\right) \tag{I.C.18}$$

Algorithm I.C.7: Extrapolation of the discontinuity to zero broadening

1. *For every α do a polynomial fit of 4^{th} degree for $\langle n_{\epsilon,\alpha}(t)\rangle$ with respect to ϵ in the range $-1.5 \leq \epsilon \leq -0.25$.*

   $$\langle n_{\epsilon,\alpha}(t)\rangle \approx p_n(\epsilon,\alpha,t) \tag{I.C.19}$$

   Assuming particle-hole symmetry, set the gap $g(\alpha,t)$ for this particular α to:

   $$g(\alpha,t) = 2\,p_n(\epsilon=0,\alpha,t) - 1 \tag{I.C.20}$$

2. *Do a do a polynomial fit of 4^{th} degree for $g(\alpha,t)$ with respect to α.*

   $$g(\alpha,t) \approx p_g(\alpha,t) \tag{I.C.21}$$

3. *The extrapolated gap at $\epsilon = 0$ is $p_g(\alpha=0,t)$.*

Note that we first fit the gap for every α and then extrapolate to $\alpha = 0$. To test the stability of the fit, we perform a bootstrap like analysis where we do the steps described in Alg. (I.C.7) 128 times and every time we omit 50 % of the ϵ and α points.

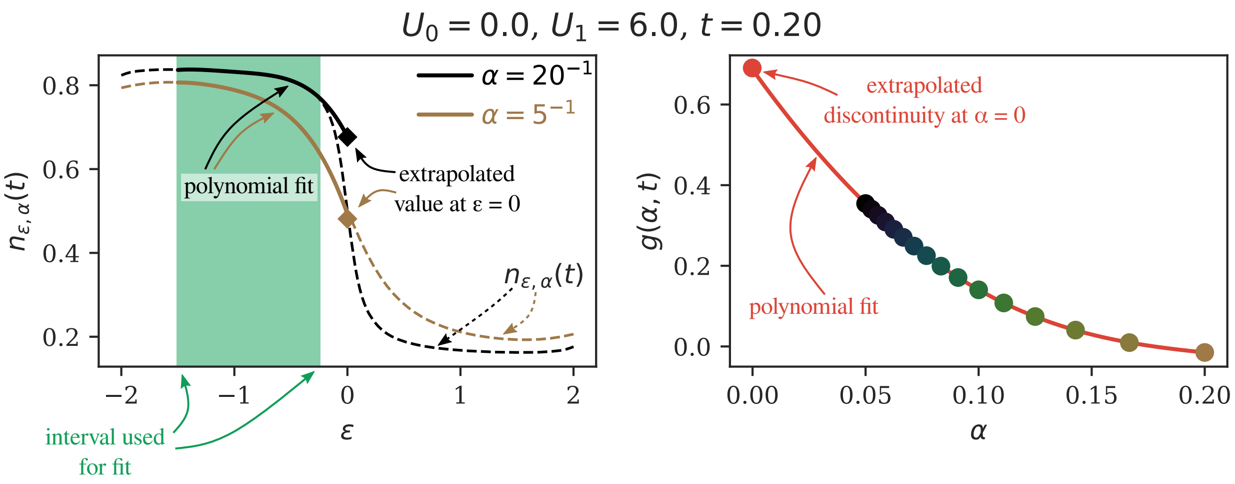

Figure I.C.14. Illustration of the extrapolation process described in Alg. (I.C.7). On the left hand side, the fit of the broadened momentum distribution with a polynomial of 4^{th} degree is shown for two values of α. On the right hand side, the resulting gap $g(\alpha, t) = 2\,p_n(\epsilon = 0, \alpha, t) - 1$ is shown for each α and extrapolated to $\alpha = 0$.

An alternative approach, that has slightly bigger computational cost, is to first extrapolate the momentum distribution to $\alpha = 0$ and then to determine the gap as described in Alg. (I.C.8) and illustrated in Fig. I.C.15.

Algorithm I.C.8: Extrapolation of the discontinuity to zero broadening (unused alternative)

1. *For every ϵ do a polynomial fit of 4^{th} degree for $\langle n_{\epsilon,\alpha}(t)\rangle$ with respect to α.*

$$\langle n_{\epsilon,\alpha}(t)\rangle \approx p_n(\epsilon, \alpha, t) \tag{I.C.22}$$

The momentum distribution with zero broadening is now approximated with:

$$\langle n_{\epsilon,\alpha}(t)\rangle = p_n(\epsilon, \alpha = 0, t) \tag{I.C.23}$$

2. *Do a polynomial fit of the extrapolated momentum distribution in the range $-1.5 \leq \epsilon \leq -0.25$ with respect to ϵ.*

$$\langle n_{\epsilon}(t)\rangle \approx p_g(\epsilon, t) \tag{I.C.24}$$

> *3. Using particle-hole symmetry, the extrapolated gap at* $\epsilon = 0$ *is* $2\,p_g(\epsilon = 0, t) - 1$.

Both methods yield almost identical results, which depend on the exact fit intervals and the polynomial degree. The uncertainty of the discontinuity, determined by the bootstrap-like method for either of these two algorithms seems to be smaller generally when the discontinuity is small. However, for some quenches there appears to be an instability which produces large jumps, visible for example in the top right of Fig. I.C.17 below. The reason for these instabilities may be overfitting in the vicinity of the discontinuity. Indeed, in Fig. I.C.15 we see that the momentum distribution appears to be overestimated below the discontinuity and underestimated above the discontinuity. A similar peak at small $|\epsilon|$ can be seen when computing the equilibrium occupation function $-\frac{\mathrm{Im}(G^{<E}(\omega))}{2\,\mathrm{Im}(G^{RE}(\omega))}$ (not shown), which should be a simple step function. The origin of the small overfitting is probably the linear prediction (Sec. VI.2) of the Green function in equilibrium time. The occurrence and frequency of the instabilities depends rather noticeably on the fit range in ϵ. Further research regarding a stable approximation for large t_E should be done because stable computations of G_ϵ are of prime importance when doing simulations on a different geometry than the Bethe lattice, since G_ϵ is then needed to compute the hybridization function. The two algorithms produce almost identical results, including error bars. In the following we will take the results from Alg. (I.C.7).

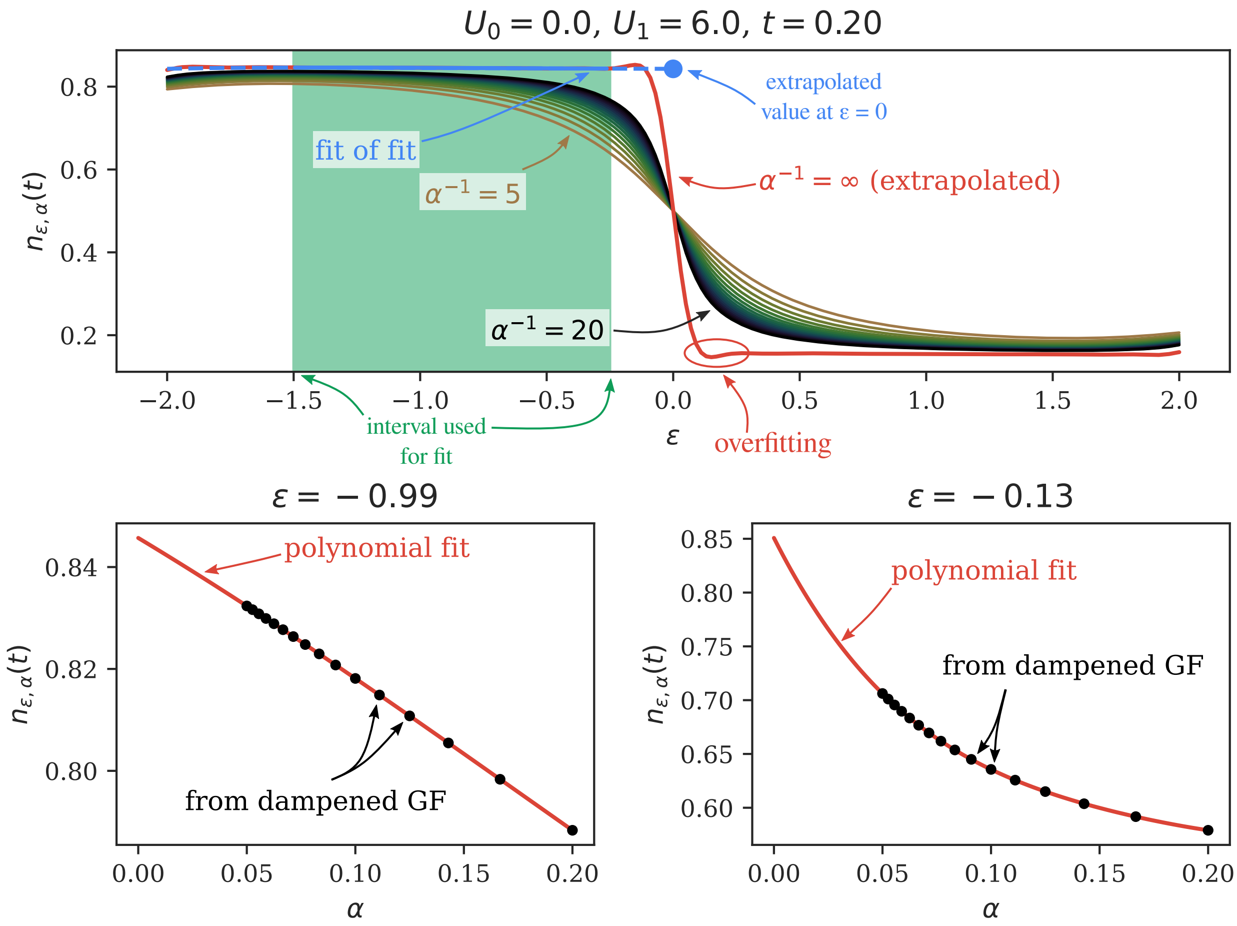

Figure I.C.15. Illustration of Alg. (I.C.8). Top row: $n_{\epsilon,\alpha}(t)$ at $t = 0.2$ as a function of ϵ for the different dampings of the Green function, the extrapolation to zero damping (red), and the polynomial fit of the extrapolation (blue). In the example shown, there appears to be an overfitting in the vicinity of the discontinuity, probably stemming from the linear prediction of the Green function. In order to extract the discontinuity to zero damping the red line is fitted with a polynomial in a suitable energy range ($-1.5 \leq \epsilon \leq -0.25$) and extrapolated to $\epsilon = 0$ (blue). Bottom row: Polynomial fit of 4th degree, in α, to perform the extrapolation, for two different ϵ. The dots show the $\langle n_{\epsilon,\alpha}(t)\rangle$ obtained from the deconvolution of the damped Green function G (Eq. (I.C.11)) and the solid lines depict the polynomial fit.

I.C.3.3 Comparison with Existing Results ($U_0 = 0$)

The results of the extrapolation for $U_0 = 0$ can be seen in Fig. I.C.16. Although we essentially perform a fit of a fit, the results are in very good agreement with Ref. 52, with a qualitative change in behavior at $U_1 = U_c^{dyn} \approx 3.2$: For $U_1 < U_c^{dyn}$, there is a shrinking and plateauing discontinuity, while for $U_1 > U_c^{dyn}$ the discontinuity reaches zero and oscillates afterwards.

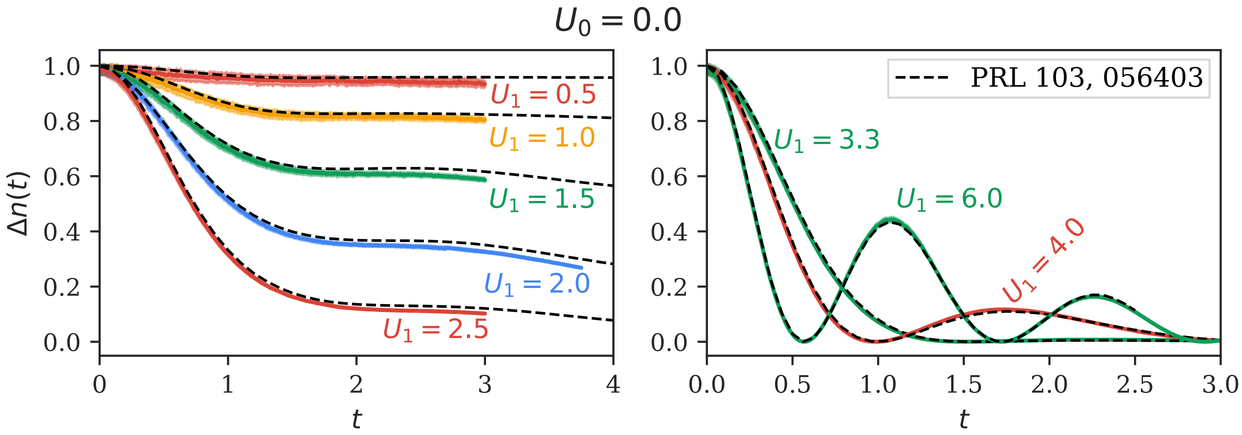

Figure I.C.16. Approximate discontinuity at the fermi level as a function of time for $U_0 = 0$, computed with Alg. (I.C.7). The light colored regions mark the uncertainty (1 σ) stemming from the bootstrap-like analysis described below Alg. (I.C.7). They are hard to see in this plot, because the standard deviation of the bootstrap samples is small. The dashed lines are taken from Ref. 52 for comparison.

I.C.3.4 New Results, Interacting Initial States

In Fig. I.C.17 we present the discontinuities at the Fermi-level computed with Alg. (I.C.7). As a general rule of thumb, it seems that Alg. (I.C.7) is not as stable for $U_0 \neq 0$ as it is for $U_0 = 0$ and we see some jumps in some time series of Fig. I.C.17, especially at $U_0 = 0.5$. The extrapolation tends to yield smaller error bars at larger U_1 in the right hand column. The temporal behavior of the discontinuity resembles that of the double occupancy (Fig. I.C.3): It curves towards higher values for $0 < U_1 < U_0$, and towards lower values for $U_1 > U_0$. When $U_1 < U_0$, the maximum of the discontinuity first increases with increasing U_1 (different from the double occupancy), and the discontinuities of the time series decrease monotonically with increasing U_1, which also continues for $U_1 > U_0$.

In line with the behavior already observed in Sec. I.C.3.1, the data show that U_c^{dyn} increases with increasing U_0. At $U_1 = 3.0$ for example, the value of the discontinuity at large times increases from about 0.04 at $U_0 = 0.5$ to about 0.5 at $U_0 = 2.0$. At $U_1 = 4.0$, there is a large oscillation in time for $U_0 = 0$, which becomes smaller in amplitude for $U_0 = 0.5$ and is not present anymore at $U_0 = 2.0$, where the discontinuity instead exhibits fast convergence to zero. To better visualize that U_c^{dyn} increases, we plot the minimum of the discontinuity in the interval $t \in [0, 3]$ in Fig. I.C.18, showing an apparent shift of the curves for increasing U_0 towards larger U_1.

We also note that the time scale of the collapse-and-revival oscillations increases with increasing U_0, which can be seen if we compare the time of the first local maximum of the discontinuity of $U_1 = 6$ for the different U_0.

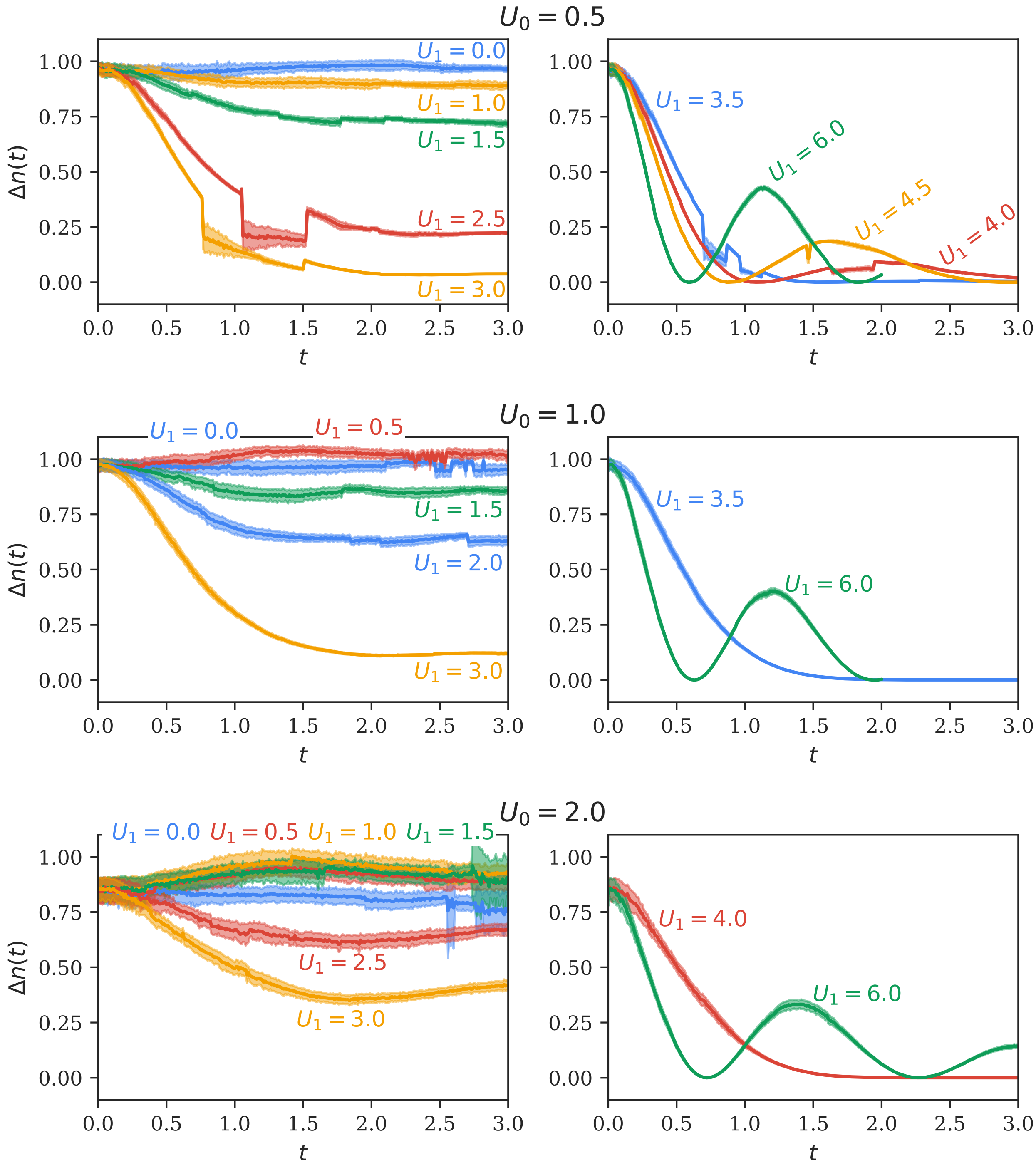

Figure I.C.17. Approximate discontinuity at the fermi level as a function of time for $U_0 > 0$, computed with Alg. (I.C.7). The light colored regions mark the uncertainty (1 σ) stemming from the bootstrap-like analysis described below Alg. (I.C.7).

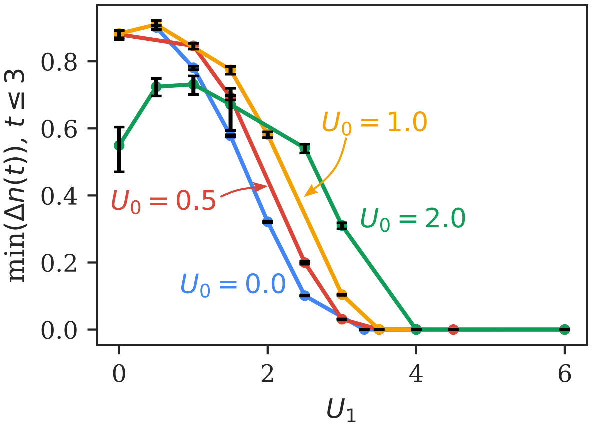

Figure I.C.18. Minimal discontinuity in the interval $t \in [0, 3]$ as a function of U_1, taken from Figs. I.C.16 and I.C.17. It can clearly be seen that for growing U_0 the lines and their intersect with zero move to higher U_1. For the computation of the minimum the large jumps in the discontinuities of $U_0 = 0.5$, $U_1 = 2.5$ and $U_0 = 0.5$, $U_1 = 3.0$ were discarded. The error bars mark the uncertainty $(1\ \sigma)$ stemming from the bootstrap-like analysis described below Alg. (I.C.7). At $U_1 = 1.5$ the large error bars belong to $U_0 = 2.0$.

I.C.4 Energy

With the momentum distribution we can compute the kinetic energy and the potential energy per lattice site of the system. Again, there is the difficulty that the kinetic energy gets altered by the damping of the Green function and we need to extrapolate to zero damping of the Green function as described in Alg. (I.C.9).

> **Algorithm I.C.9: Extrapolation of the kinetic energy to zero broadening**
>
> 1. *For every α compute the kinetic energy $E_{kin}(t,\alpha)$.*
>
> $$E_{kin}(t,\alpha) = \int_{-2}^{2} \epsilon \, \langle n_{\epsilon,\alpha}(t) \rangle \, \frac{\sqrt{4-\epsilon^2}}{2\pi} \, \mathrm{d}\epsilon \tag{I.C.25}$$
>
> 2. *Do a do a polynomial fit of 4^{th} degree for $E_{kin}(t,\alpha)$ with respect to α.*
>
> $$E_{kin}(t,\alpha) \approx p_E(\alpha,t) \tag{I.C.26}$$
>
> 3. *The extrapolated kinetic energy is $p_E(\alpha=0,t)$.*

The results of the extrapolation to $\alpha = 0$ are presented in Fig. I.C.19 for several different quenches. We applied the same bootstrap-like algorithm described below Alg. (I.C.7) but find, that the uncertainty is smaller the line width in Fig. I.C.19, thus we will not show the uncertainties here. An important quality criterion for non-equilibrium DMFT solvers is that the total energy per lattice site stays constant when the Hamiltonian is constant. For the simulation setup in this section, this means a constant energy after the quench. We find that the total energy stays constant within a reasonable margin with our new solver. The observed small changes with respect to time may mostly stem from the extrapolation to $\alpha = 0$. This is indicated by the fact that the total energy, extrapolated to $\alpha = 0$, changes the least with respect to time when it changes the least with respect to α. In Fig. I.C.20 we present the total energy per lattice site before and after the quench. Note that the total energy per lattice site after the quench is a linear function with respect to U_1, since the kinetic energy immediately

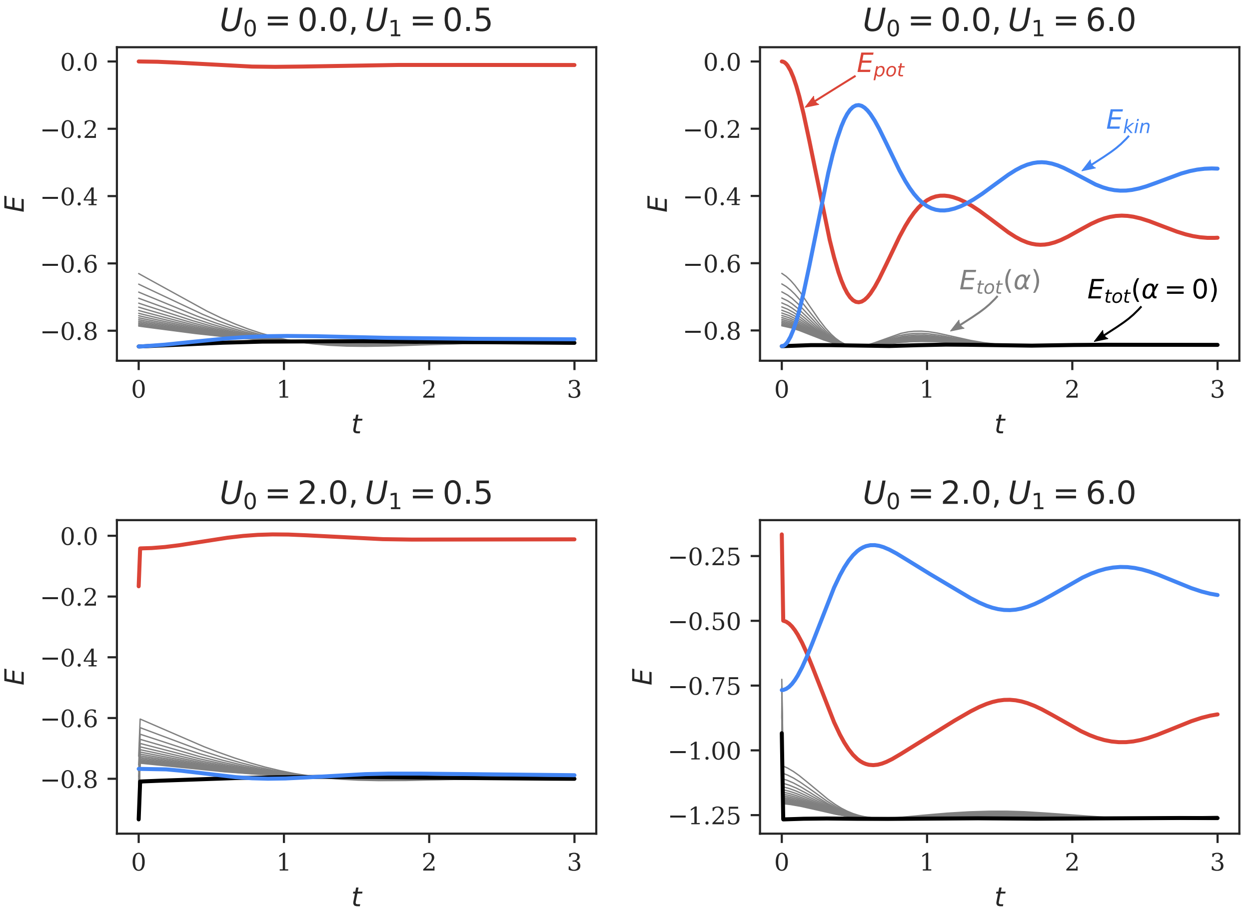

Figure I.C.19. Potential energy (red), kinetic energy extrapolated with a polynomial to zero broadening (blue), total energy for various broadenings (thin gray lines), and extrapolated total energy (black) as a function of time for several quenches.

after the quench must be the same as immediately before because of its sudden nature, and the potential energy is a linear function with respect to U.

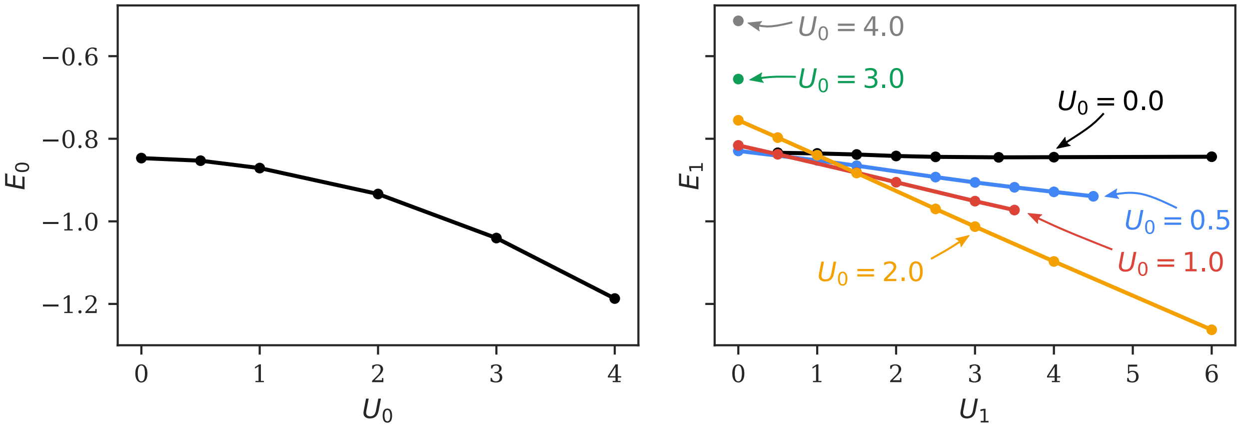

Figure I.C.20. Total energy per site before the quench (E_0, left) as a function of U_0 and total energy per site after the quench (E_1, right) as a function of U_1.

I.C.5 Convergence and Computational Scaling

The relevant control parameters for Matrix Product State based DMFT solvers are the time-step and the cutoff (Def. (I.B.12)). In Fig. I.C.21 we present a comparison of the double occupancy, for a computationally difficult quench, computed with the cutoff used for the simulations in this section and several other cutoffs. We find that the results converge very well with decreasing cutoff and additionally note that the double occupancy of Ref. 52 for this specific quench appear to become statistically unstable beyond $t \approx 2$ while our new solver remains stable (see Fig. I.C.2). Even the larger cutoffs, where the simulations are quantitatively different than the simulation with the main cutoff, seem to at least indicate a good qualitative description of the behavior. On the relevant scales there is no difference in the double occupancies of the simulation with the main cutoff and a simulation with a magnitude smaller cutoff.

The main obstacle for reaching long times with Matrix Product State based solvers is the increasing entanglement entropy after the quench. This in turn increases the required matrix dimensions involved in the computation, which are shown in Figs. I.C.21 and I.C.22.

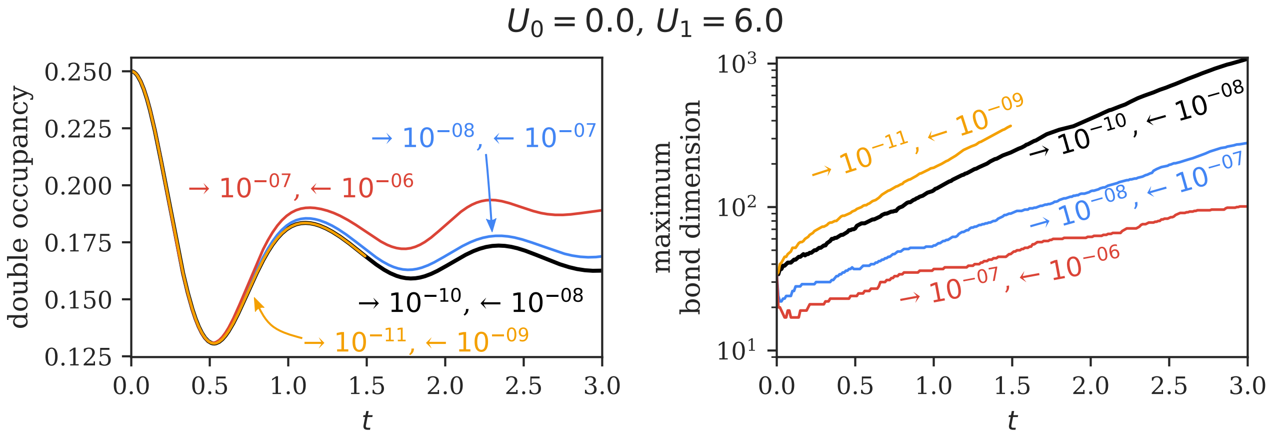

Figure I.C.21. Left: Double occupancy as a function of time for $U_0 = 0$ and $U_1 = 6$ for several cutoff parameters. The first number, after the rightwards arrow, indicates the cutoff used for forward time-evolution, while the second number, after the leftwards arrow, indicates the cutoff used for backwards time-evolution after the creation/annihilation operator has been applied to the state. The black line marks the main parameter tuple used for the simulations of the thesis. Right: Maximum bond dimension of $|\psi(t)\rangle$ of the Anderson Impurity Model as a function of time.

We see an exponential increase in bond dimension similar to Ref. 51. The most expensive calculation in the process is the Singular Value Decomposition of an MPS matrix which has the computational cost of $\mathcal{O}(m^3)$, where m is the bond dimension of the Matrix Product State. We performed our simulations for all independent components (spin-up, spin-down, right-mixing, left-mixing, greater non-equilibrium, lesser non-equilibrium) in parallel with HTCondor[112]. As a rule of thumb for this setup: For the lower bond dimensions in Fig. I.C.22, one iteration for one t_N of the DMFT loop takes $\approx$ 10 minutes, for the higher bond dimensions in Fig. I.C.22 it can take several hours to complete. There is no general description on how the entanglement entropy grows, because it depends on the type of quench investigated. For the quenches performed here, we find that the bond dimension m, which is indirectly linked to the entanglement entropy, grows like $m \propto e^{\mathrm{const}\, t}$. This means that the computational cost, for the type of quench investigated here, grows like $\mathcal{O}(e^{3\, \mathrm{const}\, t})$. Note that the bond dimension is not an observable and different geometric orderings of the underlying Matrix Product State may lower the required bond dimension. Another possibility to lower the bond dimension may be to find a different mapping for the second bath (see Sec. I.B.3), where the ϵ are distributed over a suitable energy range and not set to $\epsilon_p = \mu$, possibly allowing the time-dependent hopping amplitudes to converge in time when there is a steady-state. Future research in this area may prove to be fruitful and provide better orderings of the Matrix Product State. Note that the bond dimensions depicted in Figs. I.C.21 and I.C.22 are for the MPS of $|\psi(t)\rangle$. Most of the computations need to be performed for the MPS representations of $c\, |\psi(t)\rangle$ and $c^\dagger\, |\psi(t)\rangle$. They have a much lower bond dimension, because the application of these operators remove states from $|\psi(t)\rangle$. For example in the MPS representation of $c\, |\psi(t)\rangle$ we do not need to store basis states where the impurity of $|\psi(t)\rangle$ is empty and vice versa for $c^\dagger\, |\psi(t)\rangle$. Furthermore, we use the conservation of quantum numbers (particle number, spin) in ITensor[107], which means the tensors of the MPS is split up into different blocks for the different quantum numbers and the bond dimension we provide here is the total bond dimension of all blocks. The computational cost is dominated by the size of the largest block.

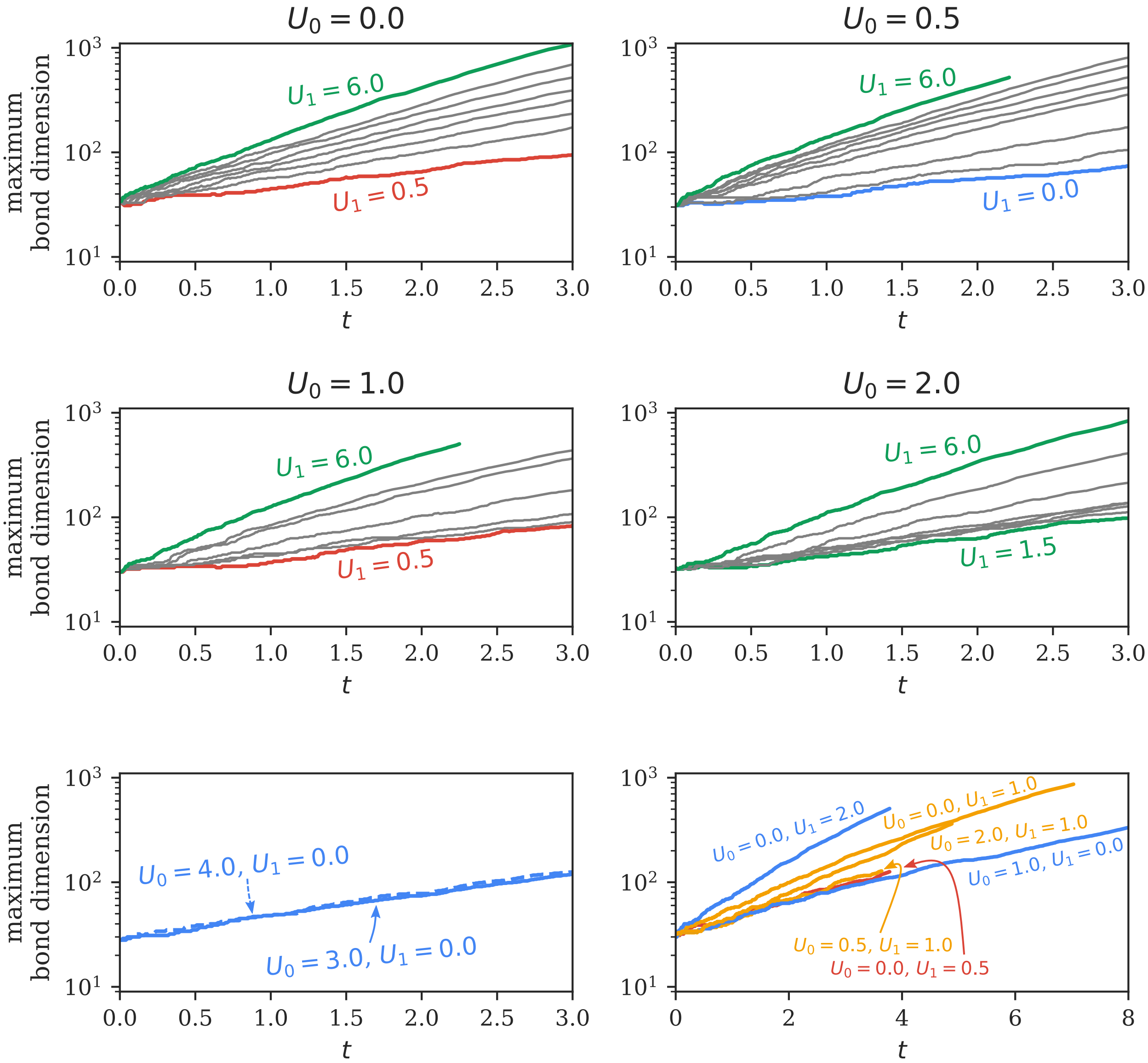

Figure I.C.22. Maximum bond dimension of $|\psi(t)\rangle$ of the Anderson Impurity Model as a function of time at constant cutoff. The plots are grouped by U_0, except for the bottom row where $U_0 = 3$ and $U_0 = 4$ are shown. In each plot, only two time series are colored to provide a better overview. For the simulation parameters see table I.C.1. In the bottom right we show the maximum bond dimension of longer runs, some of which appear in Fig. I.C.4.

I.C.6 Conclusions

In the previous sections we replicated and extended the results of Ref. 52 with which our results agree very well for the quenches with $U_0 = 0$ at zero temperature for the double occupancy and momentum distribution. The authors of Ref. 52 were only able to simulate this particular quench at zero temperature, by using the fact that the self-energy vanishes on the imaginary axis of the L-shaped contour. We demonstrated that the new solver does not have this restriction and can simulate different quenches with $U_0 \neq 0$.

Because the new solver is Hamiltonian based, any observable local to the impurity, such as the double occupancy, can be directly measured at the impurity. This is not the case for the momentum distribution, which is not a local observable. To obtain the momentum distribution, one must solve a contour integral equation as described in Sec. I.B.4. A difficulty here is the integration with respect to equilibrium time from $-\infty$ to ∞. Since one cannot time-evolve from $-\infty$ to ∞, one must extrapolate the values of the Green function for large equilibrium times from small times by linear prediction and stabilize the computation by damping the Green function, corresponding to a convolution in energy space. In the previous section it was seen that this complicates the determination of the exact height of a step like function like the momentum distribution. Further research should be done in this area to minimize the influence of the linear prediction and the damping. Note that on the Bethe lattice this is only a problem for the evaluation of the data, because one does not need G_k to do a DMFT loop. Even for different lattice geometries, where G_k is needed for the k-sum in the DMFT loop, damping probably is not a big problem since the k-sum will likely suppress its negative effects. This claim is supported by the fact that, in equilibrium, MPS based solvers can be used to reliable predict material properties[41,71], and the same linear prediction and damping scheme needs to be done there.

Another difference of Hamiltonian based solvers to established non-equilibrium solvers like e.g. the Non-Crossing Approximation (NCA) or CTQMC is in the implementation of the self-consistency scheme. For the established solvers it is viable to do a global update of the Green function, meaning that every time slice of $G(\mathbf{t}, \mathbf{t}')$ is updated at once for every iteration of the DMFT loop (Fig. I.A.3, top left). Although this is also possible to do with Hamiltonian based solvers, it probably is, in general, better to do several DMFT loops after increasing the maximum non-equilibrium time by one time step[49] (Fig. I.A.3, top right). This may pose a problem for Hamiltonian based solvers, if the goal is to reach as long simulation times as are possible with NCA ($\mathcal{O}(t_N = 100)$).

In general, the new solver is not restricted to any parameter region as long as the entanglement entropy stays low, because a growing entanglement entropy means growing matrix dimensions in the Matrix Product state (MPS) formalism. The matrix dimension is a bottleneck for the MPS time-evolution, because the computational cost goes with $\mathcal{O}(m^3)$, where m is the matrix dimension of a MPS matrix. As mentioned in Sec. I.C.5, there is room for future improvement here, e.g. testing different MPS geometries or finding a different mapping for the second bath where the ϵ are distributed over a suitable energy range and not bound to $\epsilon_p = \mu$, possibly allowing the time-dependent hopping amplitudes to converge in time when there is a steady-state. Note that the finite matrix dimension is the only approximation done with respect to the representation of the quantum state and we can freely change any parameter of the Hamiltonian or the system without any other approximations. This includes the hopping amplitude and the chemical potential, and any quenches there could be simulated without any change to the algorithm.

Part II

Impact ionization and multiple photon absorptions in the two-dimensional photoexcited Hubbard model (arXiv:2007.16201)

This part of the thesis contains Ref. 113,

F. Maislinger and H. G. Evertz, “Impact ionization and multiple photon absorptions in the two-dimensional photoexcited hubbard model,” arXiv preprint arXiv:2007.16201 (2020).

While DMFT fully accounts for temporal correlations on the impurity, a disadvantage of this method is the neglect of spatial correlations between the lattice sites[64]. An ongoing area of research is the dynamics of photoinduced excitations of the Hubbard model[55,61,62], where spatial correlations may qualitatively alter the results. One important quantity in this field is the time-dependent double occupancy after a short photon pulse, which is potentially important for e.g. the solar power industry, because it is linked to the number of mobile charge carriers. A crucial question here is whether the double occupancy increases further *after* the incoming photon pulse, indicating that an excited electron with sufficient energy excited further electrons from the lower Hubbard band. This effect has been shown to exist with DMFT[55,61,62]. To test if this is still the case with spatial correlations taken into account, we simulated a 4 × 3 Hubbard model, using Lánczos-based methods[24]. For a better understanding of the contributing eigenstates, we computed the eigenstate spectrum of the time-evolved quantum states by Fourier transforming the Loschmidt amplitude, a method which was independently developed for the present study and also introduced by other authors in Ref. 114. We analyzed the emerging multiphoton absorptions by applying a gaussian filter, a method that was, to our knowledge, not used in prior publications. All simulations in this paper were programmed from the ground up in *Python*, using only the general purpose libraries *numpy*[115,116] and *scipy*[117], by the author of this thesis. The calculations and analysis were performed under guidance from H. G. Evertz. Most of the text (excluding the abstract and summary) was initially written by the author of this thesis and then modified and finalized together with H. G. Evertz.

Impact ionization and multiple photon absorptions in the two-dimensional photoexcited Hubbard model

Florian Maislinger[1] and Hans Gerd Evertz[1]

[1] *Institute of Theoretical and Computational Physics, Graz*
University of Technology, 8010 Graz, Austria

(Dated: 31 July 2020)

We study the non-equilibrium response of a 4×3 Hubbard model at $U = 8$ under the influence of a short electric field pulse, with the main focus on multiple photon excitations and on the change of double occupancy after the pulse. The behavior mainly depends on the driving frequency of the electric field. The largest change of double occupancy occurs during the pulse. For frequencies below the Mott gap, we observe multiphoton excitations at large field intensities. For frequencies beyond the gap energy, there is a region where Auger recombination reduces the double occupancy after the pulse. Impact ionization (Multi Exciton Generation), namely a growing double occupancy after the pulse, occurs for frequencies larger than twice the Mott gap. From the Loschmidt amplitude we compute the eigenstate spectrum of the quantum state after the pulse, observing multiple distinct photon excitation peaks, in line with expectations from a quasiparticle picture. We introduce a technique with which we analyze the time evolution of double occupancy in each peak individually. The long-term behavior of the double occupancy almost only depends on the absorbed energy, and we explore the connection of this property to the Eigenstate Thermalization Hypothesis.

II.1 Introduction

One exciting area of research is the influence of photoexcitations on strongly correlated electron systems. In strongly correlated materials, one generally cannot neglect the electron-electron interaction when describing and predicting material properties, because strong localization and Coulomb interaction effects play an important role[118]. In the context of computational material science this means that one of its most prominent approaches, the Density Function Theory (DFT)[1], fails to reliably predict the correct properties[118]. There are several possible but computationally expensive routes one can take to tackle this problem. One of them is to map the many body Hamiltonian to a Hubbard type model and to use Dynamical Mean Field Theory (DMFT)[64] to solve it. The approach we choose here is to consider small lattice sizes, akin to nano crystals or quantum dots[119–122], and to use precise techniques related to exact diagonalization to compute the ground state and the time evolution.

An important effect for, e.g., the solar power industry is impact ionization[65,123,124], also called Multiple Exciton Generation (MEG)[122,125–127], Carrier Multiplication (CM)[122], or Multi Carrier Generation (MCG)[124], where an excited electron with kinetic energy larger than the band or Mott gap of the material generates additional excitations through electron-electron scattering. Impact ionization has been observed experimentally[125–131]. It would allow to raise the theoretical efficiency limit of solar cells from approximately 30%[59] to approximately 60%[60]. However, impact ionization cannot be used to significantly increase the efficiency of classical silicon based solar cells[132], because the electron-phonon scattering process is faster by an order of magnitude than the relevant electron-electron scattering processes[133]. In strongly interacting Mott insulators, on the other hand, the relevant electron-electron scattering processes can be much faster than electron-phonon scattering processes due to strong localization and Coulomb interaction mentioned above. It has therefore been proposed to use Mott insulators for photovoltaic purposes[65,123,134].

Impact ionization has been numerically confirmed to exist for the infinite dimensional hypercubic lattice in a DMFT calculation[55] and a quantum Boltzmann approach[63], and in DMFT calculations for a correlated layer connected to two metallic leads[61] and for models of $LaVO_3$ and $YTiO_3$[62]. The drawback of DMFT is that it neglects spatial correlations[64]. In the present paper, we take such correlations into full account. We examine the 4×3 Hubbard model, exposed to a short laser pulse[55–58,102,135,136]. We use Lánczos-based methods[24] to compute the ground state, and a related scaling method[137] to compute the time evolution. An independent study by Kauch et. al.[58] observed impact ionization in Hubbard models, with the focus on different geometries, disorder, and the quasiparticle spectrum.

When the intensity of the electric field is high, one enters the domain of nonlinear optics, where multiphoton absorption processes [125,138–150] become relevant. With multiphoton absorption it is possible to reach excited states beyond a gap, even when the energy of a single photon is smaller than the gap. Multiphoton absorption is a single physical process described by Quantum Electrodynamics[151], different from the consecutive absorption of single photons[138]. Experimentally, the necessary field strengths are achieved by focusing a pulsed laser beam onto a very small (order of 10^{-9} cm^2) area[139]. Relevant applications include multiphoton microscopy[139,140] and high-resolution three dimensional polymerization of photoresists[141–143]. High resolution in comparison to single photon absorption is achieved because of the nonlinear dependence of multiphoton absorption on the field intensity[143,144]. The effect can be utilized in a variety of materials including molecules[138,145], nano-crystals[146–148], cuprates[149,150], and chalcogenide glasses[144]. We observe multiphoton absorption at high electric field intensity with a driving frequency below the Mott gap size.

An interesting phenomenon that has been observed for many quantum systems is that the long time mean of the expectation value of an observable can tend to a value which depends only on the energy of the initial state. This is the topic of the so called Eigenstate Thermalization Hypothesis (ETH)[152,153]. The dependence on energy only can be understood when the initial state is dominated by a single peak in the eigenstate spectrum of the Hamiltonian and the relevant observable varies slowly in eigenenergy. In the present paper, we observe and explain a similar dependence on energy only, for states with support in a very large energy range.

In Sec. II.2 we provide an overview over the model, briefly present numerical methods, and discuss expectations based on a quasiparticle picture. Sec. II.3.1 shows the time dependence of the double occupancy during and after the photo pulse, including impact ionization. We calculate the emerging eigenstate spectrum from the Loschmidt amplitude in Sec. II.3.2, observing a clear peaked structure with distances in multiple of the photon energy. The time evolution of the individual peaks is analyzed in Sec. II.3.3. The long time behavior of the double occupancy is mostly governed by the amount of absorbed energy during the pulse. A connection to the Eigenstate Thermalization Hypothesis is explored in Sec. II.3.4.

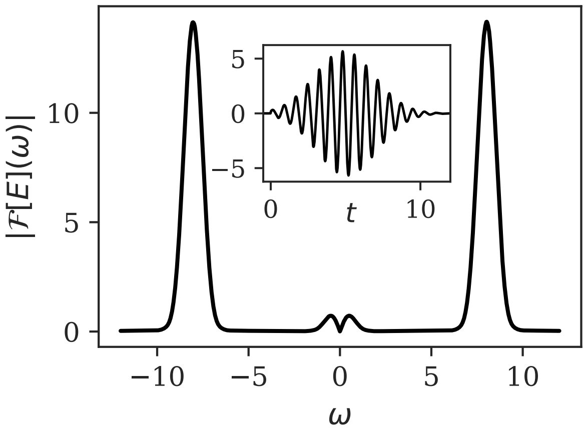

Figure II.1. Electric field pulse, for $\Omega = 8$ and $I_0 = 0.71$. Inset: time domain. Main figure: absolute value of the Fourier transform of the electric field. The two peaks are of Gaussian shape with a width of $\tilde{\sigma} = \frac{1}{2}$.

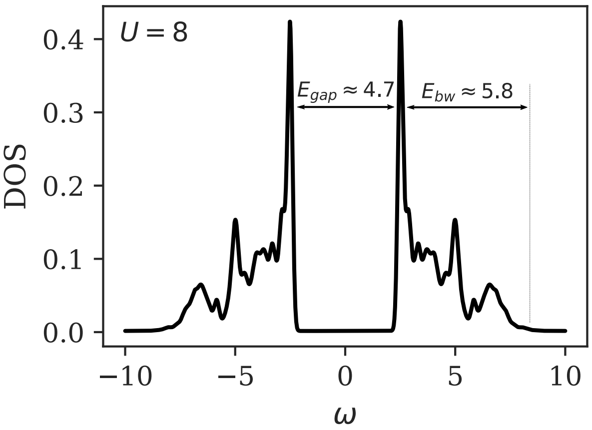

Figure II.2. Equilibrium density of states of $H(0)$, at half filling and $U = 8$ on the 4×3 lattice, convoluted with a Gaussian peak of width $\sigma = \frac{1}{10}$ for smoothness.

II.2 Model

We investigate a 4×3 Hubbard model with open boundary conditions and nearest-neighbor hopping $v_{ij}(t)$,

$$H(t) = H_0(t) + H_1 \tag{II.1a}$$

$$H_0(t) = -\sum_{\langle ij\rangle,s} v_{ij}(t)\; c^{\dagger}_{i,s} c_{j,s} \tag{II.1b}$$

$$H_1 = U \sum_i \left(n_{i,\uparrow} - \frac{1}{2}\right)\left(n_{i,\downarrow} - \frac{1}{2}\right) \tag{II.1c}$$

at half-filling, $\sum_i n_{i,\uparrow} = \sum_i n_{i,\downarrow} = \frac{N}{2}$, $N = 12$.

The initial state at time $t = 0$ is the ground state, calculated with the Lánczos method[24]. At time $t > 0$ the system is irradiated by an electric field $\vec{E}$ of frequency Ω, in plane with the $2d$ system, and angled at 45° to the lattice. We incorporate the field into the Hubbard model by the Peierls phase[43,54], $\phi(t) = \int_{x_i}^{x_j} \vec{A}(x,t)\ \mathrm{d}\vec{x}$, where $\vec{A}$ is the vector potential, with $\vec{E} = -\frac{\partial \vec{A}}{\partial t}$. Then all nearest-neighbor hopping amplitudes obtain the same time-dependent complex phase factor

$$v_{ij}(t) = v\ e^{i\phi(t)}\ . \tag{II.2}$$

We employ a Gaussian shaped light pulse[55–58], centered at time $t_i = 5v^{-1}$, with a width of $\sigma = 2v^{-1}$ and intensity I_0, see Fig. II.1, so that

$$\phi(t) = -I_0\ e^{-\frac{(t-t_i)^2}{2\sigma^2}} \left(\cos\left(\Omega\left(t - t_i\right)\right) - \cos\left(-\Omega\, t_i\right)\right)\ . \tag{II.3}$$

We investigate the model at $U = 8v$. In the following, all energies will be specified in units of the hopping amplitude v and all times in units of v^{-1}.

Our main observable of interest is the total double occupancy of the system:

$$d = \sum_i n_{i,\uparrow} n_{i,\downarrow} \tag{II.4}$$

as a measure of excitations of the system. We will use an increasing double occupancy after the incoming photon pulse as a measure for impact ionization[55].

We approximate the time-evolution operator $\mathcal{U}$ by

$$\mathcal{U}(t_0 + \Delta t, t_0) = \mathcal{T} e^{-i\int_{t_0}^{t_0+\Delta t} H(\bar{t})d\bar{t}} \tag{II.5a}$$

$$\approx e^{-\frac{i\Delta t}{2}(H(t_0)+H(t_0+\Delta t))} \tag{II.5b}$$

We use a modified scaling and squaring method to compute the action of the matrix exponential on the state[117,137]. Convergence of the simulations was verified by using several different time steps, $\Delta t = 10^{-2} \cdot 2^{-n}$, $n \in \{0,1,2,3,4\}$. For a detailed description of a similar numerical setup see Ref. 57. The density of states was calculated with $H(0)$ from the Fourier transform of $-i\theta(t)\left(\langle GS|c_{i,\uparrow}(t)\, c^{\dagger}_{i,\uparrow}|GS\rangle + \langle GS|c^{\dagger}_{i,\uparrow}\, c_{i,\uparrow}(t)|GS\rangle\right)$ (Ref. 69), averaging over all sites i.

II.2.1 Quasiparticle picture

The density of states is shown in Fig. II.2. There is a gap of $E_{gap} \approx 4.7$ and the width of the Hubbard bands is $E_{bw} \approx 5.8$. The reaction of the system to the pulse will depend on the value of Ω. The excitations expected to happen in the single particle picture are illustrated in Fig. II.3. When $\Omega < E_{gap}$, then the system should not react to the pulse, because an incoming photon does not carry enough energy to excite electrons. When $E_{gap} < \Omega < E_{gap} + 2E_{bw}$,

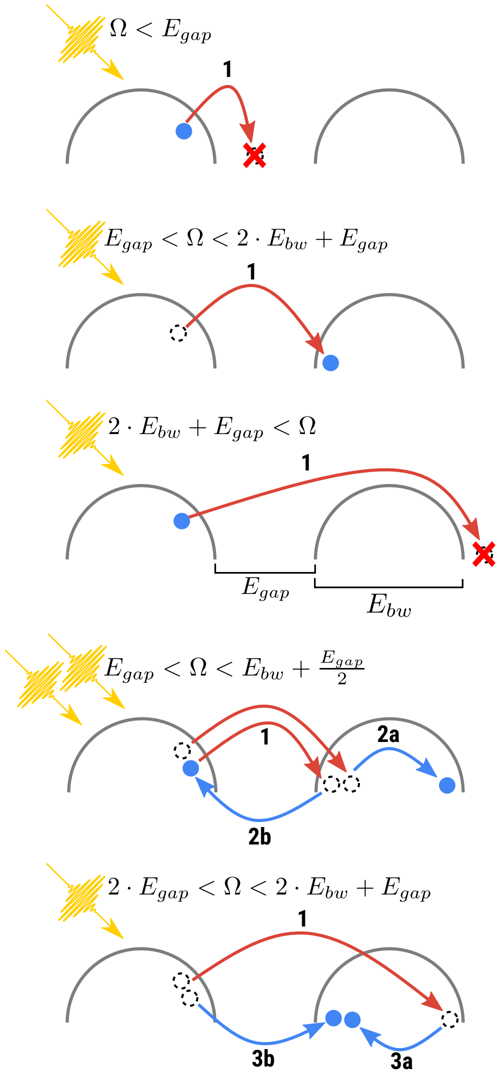

Figure II.3. Expected excitation processes in the quasiparticle picture, for different ranges of the photon energy Ω. In each subfigure, the horizontal axis represents energy and the semicircles schematically depict the lower and upper Hubbard bands. An electron is excited by a photon (step 1) into the upper Hubbard band, given that the photon energy is not too low (first subfigure) or too high (third subfigure). For the energy range depicted in the fourth subfigure, Auger recombination can reduce the number of excited electrons (step 2). At higher photon energies (last subfigure), a single photon can lead to two excited electrons via impact ionization (step 3).

a photon can excite an electron to the upper Hubbard band, leaving behind a hole, and for $\Omega > E_{gap} + 2E_{bw}$, no final state is available, so the photon should not be absorbed.

Electron scattering can later modify the number of excited electrons. When $E_{gap} < \Omega < E_{bw} + \frac{E_{gap}}{2}$ (third subfigure of Fig. II.3), Auger recombination[65], can reduce the number of excited electrons. Conversely, when $2\ E_{gap} < \Omega < 2\ E_{bw} + E_{gap}$ (and also $E_{gap} < E_{bw}$), then an excited electron can subsequently transfer enough energy by scattering processes to excite another electron into the upper Hubbard band. Thus a single photon can produce two excited electrons in this process of impact ionization[55,58,61,62,65].

Note that this is an idealized view. In non-equilibrium, the spectral function is time dependent[56–58,63,102,145,154–157] and there is a photo-induced insulator-metal transition in the Hubbard model in various setups[56–58,135,155,156,158–160]. Such an insulator-metal transition has also been observed in experiment in quasi one- and two-dimensional materials[161–166]. We also note that the incoming photon pulse has a finite width $\tilde{\sigma} = \frac{1}{2}$ in frequency, due to the finite width of the Gaussian peak in the time domain (see Fig. II.1).

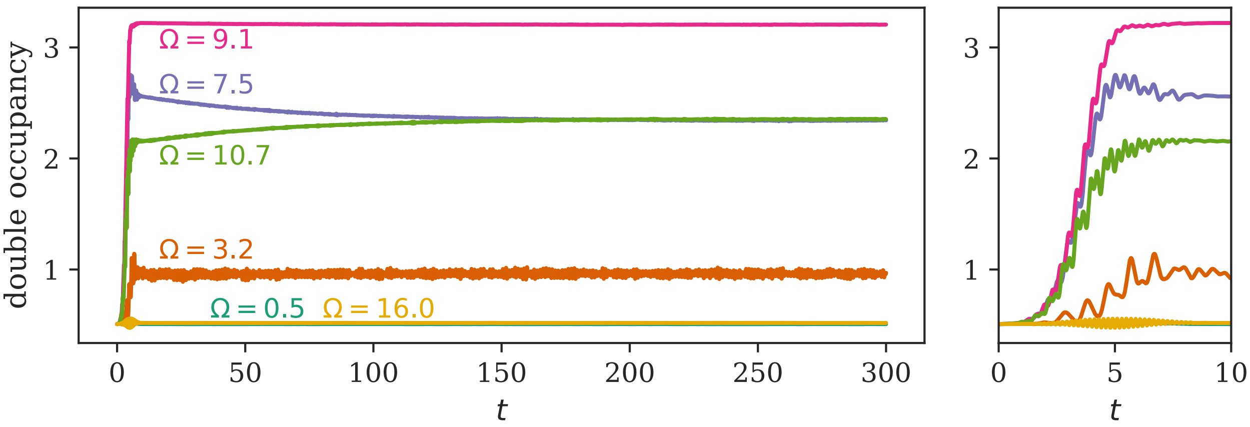

Figure II.4. Double occupancy as a function of time for $I_0 = 0.71$ and several different Ω. The right hand side shows the double occupancy for short times, where the electric field pulse acts.

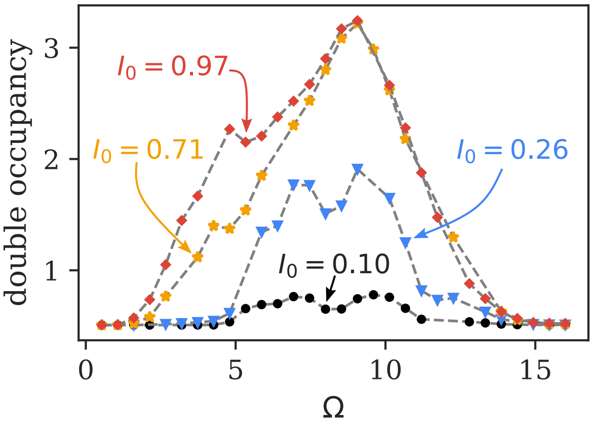

Figure II.5. Double occupancy at $t = 20$ after the pulse as a function of Ω and several different intensities I_0. For small I_0 the response is in good agreement with the quasiparticle picture according to the density of states. To minimize small oscillations with respect to time we show averages over times from $t = 17.5$ to $t = 22.5$. Color codes for the intensity I_0.

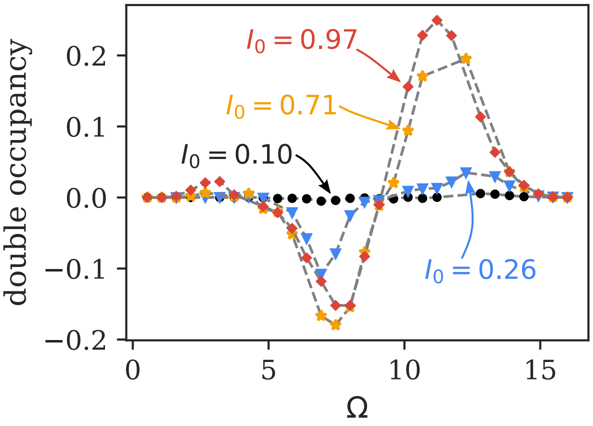

Figure II.6. Further change of double occupancy after the pulse. Shown is the difference between the values at $t = 300$ and $t = 20$. To minimize small oscillations with respect to time we used occupancies averaged over intervals with length 5 around $t = 20$ resp. $t = 297.5$. Color codes for the intensity I_0.

II.3 Results

II.3.1 Time evolution of the double occupancy

In Fig. II.4 we show the time evolution of the double occupancy for several photon energies Ω at an intensity of $I_0 = 0.71$. The overall behavior is mostly in agreement with expectations from the quasiparticle picture, except for $\Omega = 3.2$ below the gap.

For all Ω, there are initial oscillations with a frequency of roughly 2Ω. At large times, the double occupancy converges to a constant value, up to small fluctuations.

For very small and very large photon energies, the double occupancy oscillates slightly during the pulse but then returns to almost exactly its original value.

At frequencies Ω between E_{gap} and $E_{gap}+2E_{bw}$, where absorption is expected, the double occupancy rises quickly during the pulse, i.e., elecrons are excited across the gap and energy is transferred into the system. Note that after the pulse has decayed, the Hamiltonian $H(t)$ becomes the time-independent bare $H(0)$ again, so that energy is then conserved. At $\Omega = 9.1$, just below the region where impact ionization is expected, the double occupancy stays (almost) constant after the pulse. At $\Omega = 10.7$, the double occupancy shows the expected impact ionization behavior, noticeably rising further after the pulse, which was also observed by Kauch et al.[58]. We note that the corresponding time scale is large compared to the electron hopping time[55,58,62]

At $\Omega = 7.5$, the double occupancy goes down after the pulse, compatible with the expected Auger recombination, beginning already after the pulse maximum at time $t = 5$.

Remarkably, at $\Omega = 3.2$, below E_{gap}, where the quasiparticle picture would forbid excitations, Fig. II.4 exhibits a sizeable increase of the double occupancy. We will later show that this is due to multiphoton excitations.

In Fig. II.5 we display the double occupancy at $t = 20$ after the pulse, for different intensities I_0 and different frequencies Ω. There is a strong nonlinear dependence on I_0. We will show in Sec. II.3.2 that it occurs together with multiple photon excitations. Indeed, for Ω below E_{gap}, a sizeable excitation of double occupations does not occur for small intensities, but only at large I_0, as would be expected for multiphoton absorption.

The energy absorbed by the Hubbard system matches the change in double occupancy in Fig. II.5 closely, which will be further explored in Sec. II.3.4.

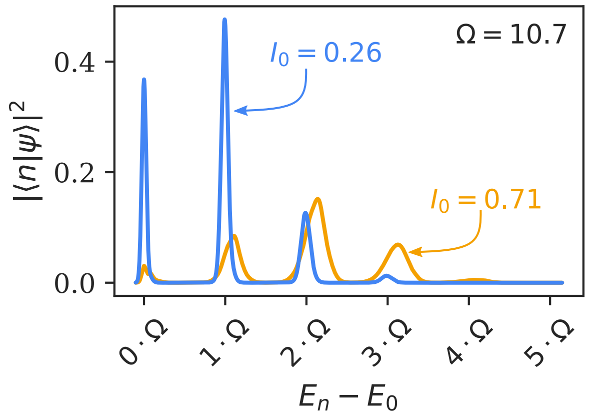

Figure II.7. Eigenstate spectrum at $t = 20$ for $\Omega = 10.7 > 2E_{gap}$ at two values of the electric field intensity.

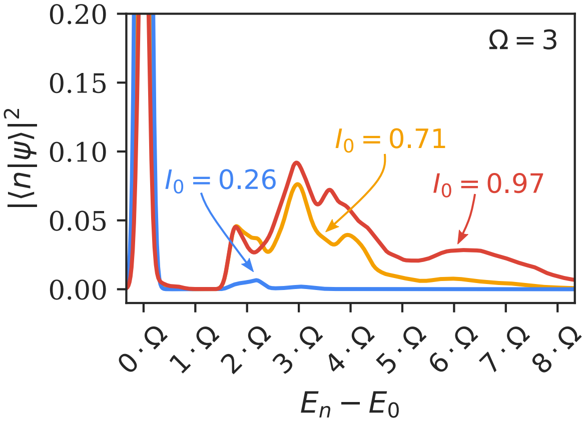

Figure II.8. Eigenstate spectrum at $t = 20$ for $\Omega = 3 < E_{gap}$ at different field intensities. The first peak at $0 \cdot \Omega$ is dominant for all three cases. Its height is ≈ 1.4 for $I_0 = 0.26$, ≈ 0.8 for $I_0 = 0.71$, and ≈ 0.3 for $I_0 = 0.97$.

In Fig. II.6 we show the further change of double occupancy after the pulse, from $t = 20$ to $t = 300$ where it has converged well for all Ω. In the energy range $2\ E_{gap} < \Omega < E_{gap} + 2\ E_{bw}$ the double occupancy increases, i.e., there is impact ionization, as suggested by the quasiparticle picture. Impact ionization is larger at higher intensities. We will show below that this is again connected to the absorption of several photons during the pulse. Notably, when the intensity is large, impact ionization even occurs at small $\Omega < E_{gap}$. The double occupancy decreases after the pulse in a range of lower values of Ω. For the small I_0, this range closely matches the expectation $E_{gap} < \Omega < E_{bw} + \frac{E_{gap}}{2}$ from the single particle picture, while at $I_0 = 0.71$ and $I_0 = 0.97$, the range extends to larger energies. We will discuss these processes further in Sec. II.3.3.

II.3.2 Eigenstate spectrum

For a better understanding of the excited state after the pulse, we examine the eigenstate spectrum of $|\psi(t)\rangle$. To this end we compute the Fourier transform of the Loschmidt amplitude, with respect to an auxiliary time span τ (Refs. 114, 167–169).

$$L(\tau) = \langle\psi(t)|\ e^{-i\tau H(0)}\ |\psi(t)\rangle \quad \text{(II.6a)}$$

$$\int_{-\infty}^{\infty} e^{i\omega\tau} L(\tau)\,\mathrm{d}\tau = 2\pi \sum_n |\langle n|\psi(t)\rangle|^2\ \delta(\omega - E_n) \quad \text{(II.6b)}$$

Eq. (II.6b) can also be viewed as the probability distribution of work done on the system[170] by the electric field. In Eq. (II.6b), the sum runs over all eigenstates $|n\rangle$ of $H(0)$, and E_n is the energy of $|n\rangle$. Through Eq. (II.6b) we obtain the energy spectrum of an arbitrary state, while only using the tool of time-evolution. This is very useful here, because the large Hilbert space dimension prohibits full diagonalization of the Hamiltonian. We note that the eigenstate spectrum is independent of time after the pulse has decayed, because then the Hamiltonian $H(t)$ reverts back to the initial Hamiltonian $H(0)$.

We damped the time evolution in Eq. (II.6a) with $\exp(-t^2/(2\sigma^2))$, $\sigma = 5/\sqrt{2}$, thus widening the spectra by $\tilde{\sigma} = 1/\sigma \approx 0.3$.

In Fig. II.7 we show the resulting spectrum for the case of $\Omega = 10.7$, after the pulse has decayed. The spectrum has a very distinct peaked structure, with the distances between the peaks close to Ω. The excited state $|\psi(t)\rangle$ thus consists of groups of eigenstates of $H(0)$ close to multiples of the photon energy. At low intensity, $I_0 = 0.26$, the peaks are narrow, and excitations at 1Ω and 2Ω dominate. For large intensity $I_0 = 0.71$, the peaks are wider, shifted slightly to higher energies, and they include higher multiples of Ω. The ground state is then almost depleted, in line with the saturation of double occupancy in Fig. II.5. Since 2Ω is larger than $E_{gap} + 2E_{bw}$ here, peaks beyond 1Ω must correspond to the sequential excitation of several electrons from the lower to the upper Hubbard band, by several photons. We will investigate these peaks individually in Sec. II.3.3. Below the gap, $\Omega < E_{gap}$, Fig. II.5 showed that the double occupancy is increased by the light pulse when the intensity I_0 is large, even though single photon absorption is energetically forbidden. In Fig. II.8 we show corresponding eigenstate spectra for $\Omega = 3$ at different intensities I_0. At small $I_0 = 0.26$, where there is very little absorption, Fig. II.8 shows that $|\psi(t)\rangle$ has almost returned to the ground state (slightly widened in the plot), with an additional small excitation at 2Ω. At larger intensity $I_0 = 0.71$, however, states with higher multiples of the photon energy have become excited. Thus the increase in double occupancy here is indeed due to multiphoton absorption. The largest amplitude in Fig. II.8 is from three-photon excitations at $3\Omega = 9$, where the available phase space is the largest as indicated by the highest absorption values in Figs. II.4 and II.5. At excitation energy 4Ω, both 4-photon absorption and two sequential two-photon absorptions can contribute. At $5\Omega = 15$ and beyond, the end of the bandwidth has been reached, so that the excitations, still sizeable in Fig. II.8, must correspond to sequential absorptions. We note that since the density of states develops a small in-gap density after electron excitations [56–58,102,155], additional processes with single-photon absorption will also be possible after the initial two-photon absorption has taken place.

II.3.3 Time evolution of individual photon-absorption peaks

Knowing the structure of the eigenstate spectrum, one can gain considerable additional insight into the development of $|\psi(t)\rangle$. Here we introduce a technique to decompose a state $|\psi(t)\rangle$ into states $|f_i(t)\rangle$ with support around the individual photon peaks. We isolate the contribution of a photon peak to $|\psi(t)\rangle$ by applying a filter,

$$\left|\varphi(t, \sigma_f, E_f)\right\rangle = \frac{1}{\mathcal{N}(t)}\, e^{-\frac{(H(0)-E_f)^2}{2\sigma_f^2}} \, |\psi(t)\rangle \; . \quad \text{(II.7)}$$

We take $\mathcal{N}(t)$ such that $\langle\varphi(t)|\varphi(t)\rangle = 1$. This is a Gaussian peak centered around E_f. Expanding $|\varphi(t)\rangle$ in the eigenbasis of $H(0)$ shows that basis states which are energetically too far away from E_f are discarded in $|\varphi(t)\rangle$. Note that the filtering from $|\psi(t)\rangle$ to $|\varphi(t)\rangle$ is very similar to doing a time-evolution.

Suppose that we have derived a number of distinct states $|f_i(t)\rangle$ from a state $|\psi(t)\rangle$ with the filtering procedure above. To find the best representation $\left|\psi'(t)\right\rangle$ of $|\psi(t)\rangle$ that is a linear combination of filter results $|f_i(t)\rangle$ we use:

$$\left|\psi'(t)\right\rangle = \sum_i \alpha_i(t)\,|f_i(t)\rangle \quad \text{(II.8)}$$

and choose the coefficients $\alpha_i(t)$ such that $\left|\,|\psi(t)\rangle - \left|\psi'(t)\right\rangle\right|^2$ is minimized. We will look at the expectation value of an operator O with respect to the single states $|f_i(t)\rangle$, including the coefficients $\alpha_i(t)$:

$$\langle O\rangle_i = |\alpha_i(t)|^2 \,\langle f_i(t)|O|f_i(t)\rangle \quad \text{(II.9a)}$$

$$\langle O\rangle_{\text{non-diag}} = \sum_{i\neq j} \bar{\alpha}_i(t)\,\alpha_j(t)\,\langle f_i(t)|O|f_j(t)\rangle \quad \text{(II.9b)}$$

(with the time dependence not denoted). Specifically for the photon peaks we define $|f_i(t)\rangle$ as follows:

$$|f_i(t)\rangle = \left|\varphi\left(t, \frac{\Omega}{3}, E_{GS} + i\cdot\Omega\right)\right\rangle \quad \text{(II.10)}$$

In other words, $|f_i(t)\rangle$ is a filtered state centered around the energy that is i times Ω above the ground state energy, filtered with a width of $\sigma_f = \frac{\Omega}{3}$. Note that each filtered state still contains many eigenstates, so that observables, like the double occupancy, remain time dependent even after the light pulse.

We find that the set of filtered states $|f_i(t)\rangle$ provides a good representation of the original state $|\psi(t)\rangle$ at all times. The absolute value of the overlap between the filtered states $\left|\langle f_i(t)|f_j(t)\rangle\right|$ is about $5\cdot 10^{-2}$ when they are Ω apart, 10^{-4} when 2Ω apart, and 10^{-8} when they are 3Ω apart. The norm squared of the difference between the original time-evolved state and the best approximation $\left|\,|\psi(t)\rangle - \sum_i \alpha_i(t)\,|f_i(t)\rangle\,\right|^2$ is of the order of 10^{-2}. The relative difference between the expectation value of the double occupancy of the original states and the sum of filtered state contributions Eqs. (II.9a) and (II.9b) is of the order of 0.5 %.

We examine two cases, $\Omega = 10.7$ where the double occupancy increases, and $\Omega = 7.5$ where it decreases after the pulse. In both cases we find that during the pulse, the initial rise of the photon peaks occurs sequentially, delayed by roughly one hopping time for each additional photon, in line with the expected sequential nature of photon absorptions at these values of Ω.

The eigenstate spectra of the two states after the pulse are shown in Figs. II.9 and II.10 (center row). At every time t, we separately filter out each peak and cal-

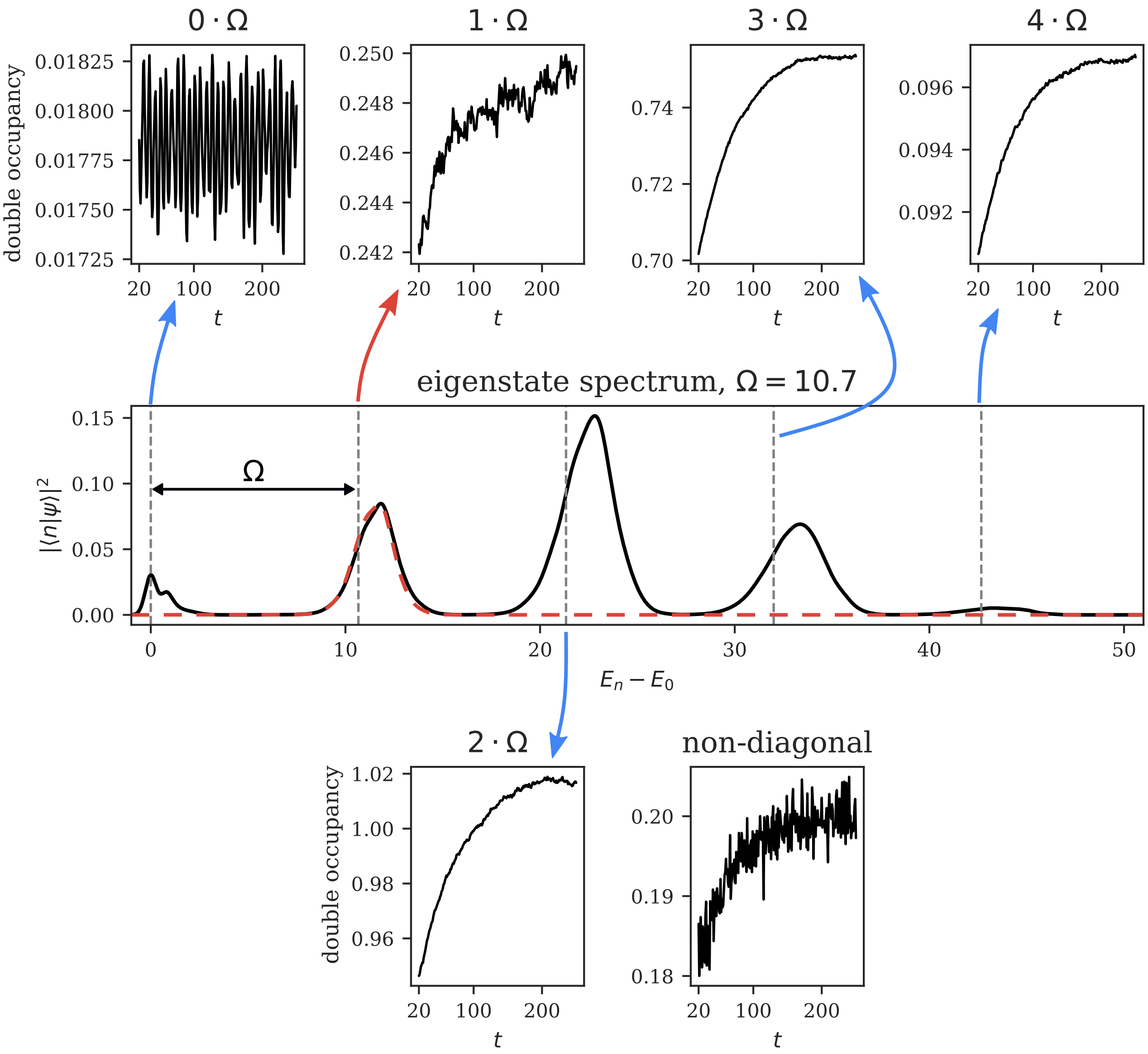

Figure II.9. Double occupancy of the different peaks as a function of time, computed with Eqs. (II.9a) and (II.9b), for $\Omega = 10.7$ and $I_0 = 0.71$. The center row displays the eigenstate spectrum computed with Eq. (II.6b), showing peaks with a distance of $\approx \Omega$. The red dashed curve in the center row shows the eigenstate spectrum after filtering for one specific peak. The top and bottom rows display the contributions of the filtered peaks to the double occupancy.

culate the double occupancy according to Eq. (II.9a), including the coefficient $|\alpha_i(t)|^2$. The results are shown in Fig. II.9 and Fig. II.10 (top and bottom rows).

For $\Omega = 10.7$, we saw in Fig. II.4 that there is an increase of double occupancy after the pulse, in line with the impact ionization expected in the quasiparticle picture. Fig. II.9 shows that indeed each photon peak and also the non-diagonal part contribute to the increase. The largest contributions to the double occupancy and to its increase come from the states with two and three absorbed photons, each of which can separately contribute to the impact ionization process sketched in Fig. II.3.

At $\Omega = 7.5$, absorption of up to 6 photons is visible, and the remaining contribution of the ground state is tiny. Now $|\psi(t)\rangle$ has a decreasing double occupancy as a function of time. The individual peaks

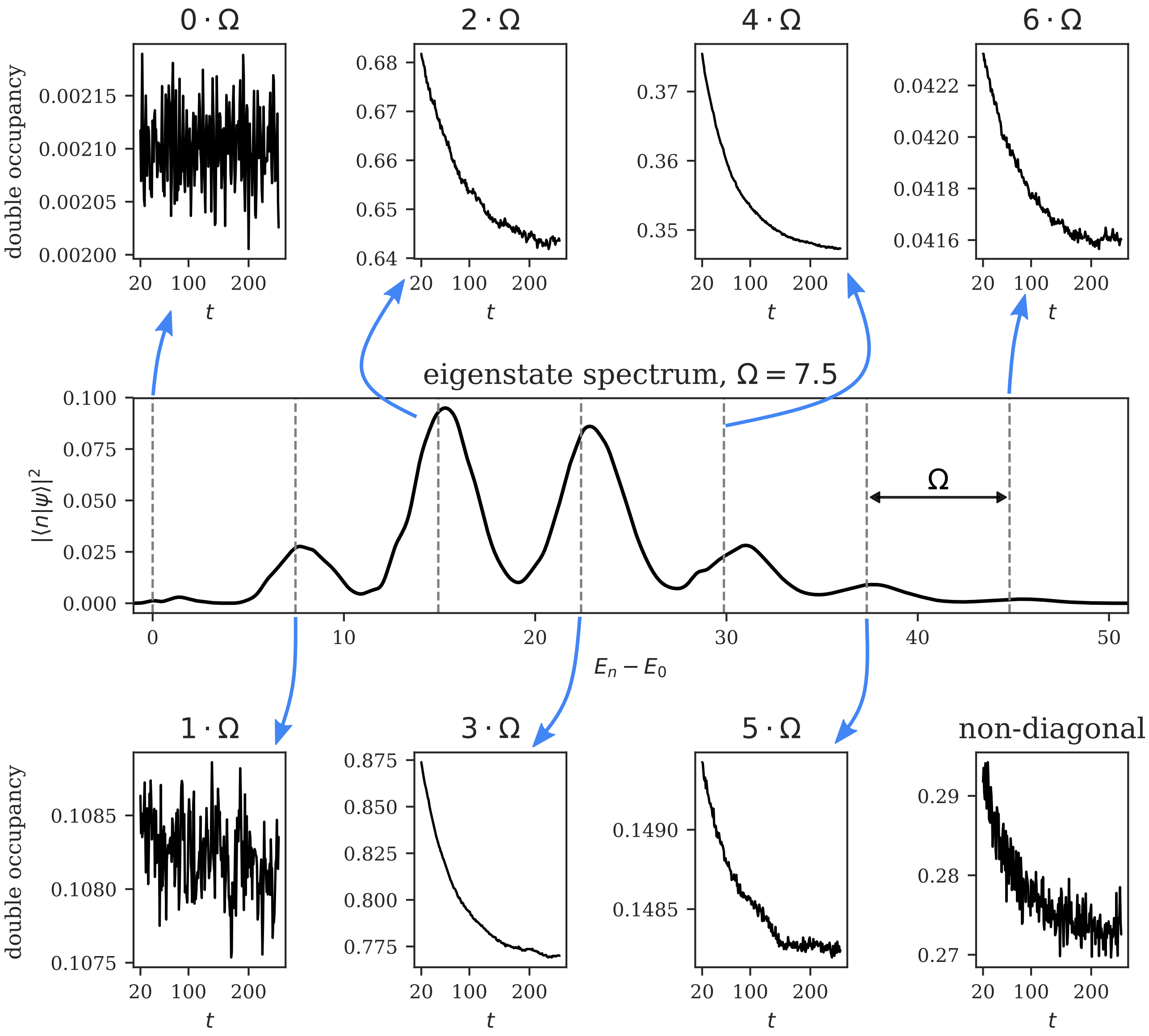

Figure II.10. Double occupancy of the different peaks as a function of time, computed with Eqs. (II.9a) and (II.9b), for $\Omega = 7.5$ and $I_0 = 0.71$. The center row displays the eigenstate spectrum computed with Eq. (II.6b), showing peaks with a distance of $\approx \Omega$. The top and bottom rows display the contributions of the filtered peaks to the double occupancy.

in Fig. II.10 all contribute to this decrease, with the notable exception of the single photon peak, for which the double occupancy stays almost constant.

This difference in behavior is in line with Auger recombination in the quasiparticle picture, shown in Fig. II.3 (fourth subfigure), which is only possible when at least two electrons are excited into the upper Hubbard band. Thus this decay channel is absent in the single photon peak. The upper bound for this process is $\Omega < E_{bw} + \frac{E_{gap}}{2} \approx 8.1$ for two initially excited electrons, matching the observed Ω-range of decay at small intensities in Fig. II.6. The range in Fig. II.6 is wider at larger intensities, $I_0 = 0.71$ and 0.97, where absorption of more photons becomes important (Figs. II.7 and II.10), thus allowing Auger-like processes with more initial photons and larger energy range. Furthermore, for more initially excited electrons there are more decay channels, suggesting a stronger decrease of double occupancy, in agreement with the behavior of the large 3Ω peak in Fig. II.10, which shows the largest change in double occupancy after the pulse.

II.3.4 Eigenstate Thermalization

Another way to learn about the photoexcited system is to look at the double occupancy as a function of absorbed energy, shown in Fig. II.11. Interestingly, whereas the double occupancy at time $t = 20$ depends on intensity and frequency separately, after convergence at long simulation times it depends almost only on the absorbed energy, with an almost linear relation between those two quantities.

In many physical systems it has been observed that long time averages of some expectation values are actually close to a microcanonical average, which has been discussed under the name of Eigenstate Thermalization Hypothesis (ETH)[152,153,171].

When the Hamiltonian is not time-dependent (long after the light pulse in our case), a quantum state under unitary time-evolution can be written in the eigenbasis of the Hamiltonian:

$$|\psi(t)\rangle = \sum_n e^{-i(t-t_0)E_n}\, \alpha_n\, |n\rangle\,, \quad \alpha_n = \langle n|\psi(t_0)\rangle \tag{II.11}$$

The mean of the expectation value of an observable O is

$$\overline{\langle O(t)\rangle} := \frac{1}{t-t_0}\int_{t_0}^{t} \langle O(t')\rangle\, \mathrm{d}t' \tag{II.12a}$$

$$= \sum_{m,n} \alpha_m^* \alpha_n \langle m|O|n\rangle\, \frac{\int_{t_0}^{t} e^{-i(t'-t_0)(E_n-E_m)}\, \mathrm{d}t'}{t-t_0} \tag{II.12b}$$

Under the assumption of no degeneracy, only the diagonal contributions survive for long times:

$$\overline{\langle O(t)\rangle} \xrightarrow[t\gg t_0]{} \sum_n \langle n|O|n\rangle\, |\langle n|\psi\rangle|^2 \tag{II.13}$$

The Eigenstate Thermalization Hypothesis[152,153,171] tries to explain the peculiar observation that this long-time mean of $\langle O(t)\rangle$ often coincides with a microcanonical average, where we take the average of the expectation values of the eigenstates in a small energy window ΔE around $E_\psi = \sum_n E_n\, |\langle n|\psi\rangle|^2$, For $t \gg t_0$:

$$\overline{\langle O(t)\rangle} \overset{?}{=} \langle O\rangle_{mc} \equiv \frac{1}{\mathcal{N}} \sum_{\substack{n\\ |E_n - E_\psi| < \Delta E}} \langle n|O|n\rangle \tag{II.14}$$

This is rather surprising, because the left hand side of the equation above depends on the specific coefficients of the state in the eigenbasis $|\langle n|\psi\rangle|^2$, while the right hand side does not. One possible explanation is that for many physical situations the state has a single peak in the eigenstate spectrum and in addition, the difference between two expectation values of two separate eigenstates is small when the difference between their eigenenergies is small:

$$E_m \approx E_n \;\Rightarrow\; \langle m|O|m\rangle \approx \langle n|O|n\rangle \tag{II.15}$$

In our case, however, we do not have a single peak in the eigenstate spectrum, but a series of peaks that stretch over almost the whole eigenenergy range, as can be seen in Figs. II.9 and II.10. We now show that eigenstate thermalization still holds when there is an almost linear relation between the eigenenergies and the expectation values of their respective eigenvalues (Fig. II.12, inset) in the energy range(s) where $|\psi(t_0)\rangle$ has an overlap with the eigenstates:

$$\langle n|O|n\rangle = a\cdot E_n + b + \epsilon(E_n) \tag{II.16a}$$

$$|\epsilon(E_n)| \le M \tag{II.16b}$$

with M the maximum deviation from the linear behavior. Then the long-time average of $\langle O(t)\rangle$ has the same linear behavior as a function of E_ψ with at most the same maximum deviation M, no matter how peaked the structure of $|\psi(t_0)\rangle$ is in the eigenstate spectrum. Namely, for large $t \gg t_0$, where Eq. (II.13) holds, we have

$$\begin{aligned} &\left|\overline{\langle O(t)\rangle} - a\,E_\psi - b\right| = \\ &= \left|\sum_n \langle n|O|n\rangle\, |\langle n|\psi\rangle|^2 - a\,E_\psi - b\right| \\ &= \left|\sum_n (a\cdot E_n + b + \epsilon(E_n))\, |\langle n|\psi\rangle|^2 - a\,E_\psi - b\right| \\ &= \left|\sum_n \epsilon(E_n)\, |\langle n|\psi\rangle|^2\right| \;\le\; M \end{aligned} \tag{II.17}$$

Similarly, for the difference between the long time average and the microcanonical average Eq. (II.14)

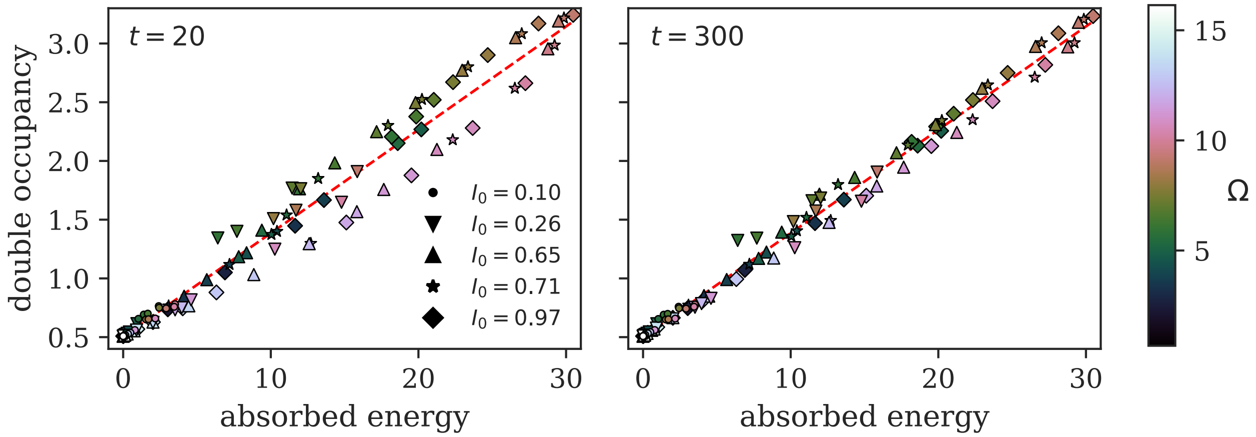

Figure II.11. Double occupancy as a function of absorbed energy from the pulse, for time $t = 20$ after the pulse and for $t = 300$ after convergence. Different colors mark different pulse frequencies Ω. For long simulation times, the double occupancies tend to a linear function. To reduce the effect of short-time oscillations, the figures show averages over the double occupancy in time intervals of length 5 around $t = 20$, resp. $t = 297.5$.

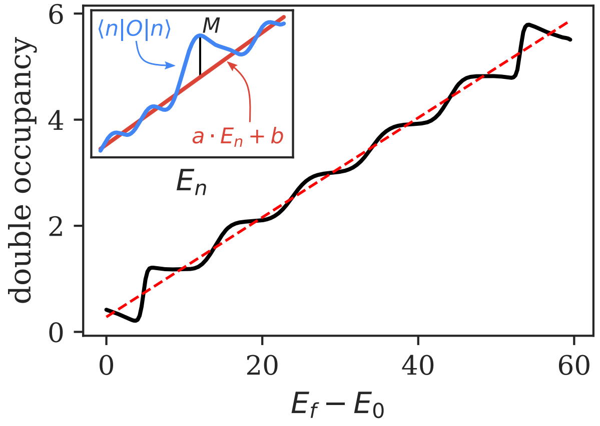

Figure II.12. Double occupancy as a function of energy for uniformly sampled states of the 4×3 Hubbard model, each projected onto a narrow energy range around energies E_f. The slope of the linear fit agrees to within a few percent with the one in Fig. II.11. Inset: Sketch of expectation values of an operator O that is well approximated by a linear function with respect to the eigenenergies E_n.

$$\left|\overline{\langle O(t)\rangle} - \langle O\rangle_{mc}\right| \;\leq\; M + M' + |a|\frac{\Delta E}{\mathcal{N}} \tag{II.18}$$

with ΔE and $\mathcal{N}$ from Eq. (II.14) and M' the maximum deviation from linear behaviour within the small energy range ΔE. The upper bounds apply when $|\psi\rangle$ has support only from eigenstates where the deviation Eq. (II.16b) is maximal.

We examined the linearity Eq. (II.16a) of the double occupancy in the Hubbard model by uniformly sampling states from the hypersphere of normed states[172]. For each value of E_f in Fig. II.12, we took a sample of $N_r = 9$ states $|r\rangle$, projected and normalized each state to a small range around E_f by $|r_f\rangle = \frac{1}{N} e^{-\frac{(H-E_f)^2}{2}} |r\rangle$, and plotted the averaged double occupancy $d(E_f) = \frac{1}{N_r} \sum_{r_f} \langle r_f|\sum_i n_{i\uparrow} n_i \downarrow|r_f\rangle$, which is similar to the microcanonical average Eq. (II.14), since contributions that are nondiagonal in eigenstates cancel stochastically. The approximately linear behavior in Fig. II.12 was verified for a smaller 3×2 system where exact diagonalization is still possible.

Fig. II.12 indicates that for the Hubbard model, the double occupancy of eigenstates is indeed close to linear in the eigenstate energies, like Eq. (II.16a), with the same slope as in Fig. II.11. The steps in the figure correspond to individual double occupations.

In our case, the double occupancy after the light pulse converges (up to small fluctuations) at large times t. The converged value, shown in Fig. II.11, is then the same as the long time average. Taking into account the actual eigenstate spectra of the excited states, the convergence towards linear behavior in Fig. II.11 indeed corresponds to Eq. (II.17).

II.4 Summary

We investigated the non-equilibrium response of a strongly correlated Mott insulator to a short light pulse, using exact-diagonalization based calculations on a 4×3 Hubbard model for a large range of light intensities and of photon energies Ω. The pulse excites electrons into the upper Hubbard band, quickly increasing the number of doubly occupied sites. At sufficiently large photon energies, we observed impact ionization (also seen in Ref. 58), namely a further increase in the double occupancy over time after the light pulse had ended. Conversely, at lower photon energies, we observed Auger recombination with a reduction in double occupancy.

We calculated the eigenstate spectra of the non-equilibrium states, i.e. the probability distribution of the work done by the light pulse, as the Fourier transform of the Loschmidt amplitude. The resulting spectra exhibit distinct peaks at distances of about Ω, corresponding to the absorption of multiple photons. The absorption rate is strongly nonlinear in light intensity. Multiphoton absorption was identified for small photon energies below the band gap, which leads to electron excitations when the light intensity is large.

We introduced a technique, using tools similar to time evolution, to isolate photon peaks in the eigenstate spectra. This enabled us to investigate the non-equilibrium evolution of double occupancy in individual photon peaks. We showed for example that, as expected from the quasiparticle picture of Auger recombination, double occupations excited by a single photon do not contribute to the overall reduction over time which occurs at intermediate light frequencies.

We found that at large times, the double occupancy moves towards a function that only depends on the absorbed energy, reminiscent of the Eigenstate Thermalization Hypothesis. Eigenstate Thermalization is usually observed for states with support in a narrow region of eigenenergies. We showed that the observed dependence on energy alone will also happen for states which contain a wide range of eigenenergies, when the relevant observable is almost a linear function of energy.

The analysis of eigenstate spectra via the Loschmidt amplitude and the filtering of the relevant energy ranges provided valuable insight into multiple photon absorptions and should prove to be useful tools to investigate strongly correlated systems, when full diagonalization is not possible, but the computation of the time-evolution is accessible.

Acknowledgements

The authors acknowledge financial support by the Austrian Science Fund (FWF) through SFB ViCoM, F4104. We thank K. Held, A. Kauch, and D. Bauernfeind for stimulating and fruitful initial discussions. The computational resources were provided by TU Graz.

Part III

Front Dynamics of Spin Chains

This part of the thesis contains the publications Ref. 173 and Ref. 174,

V. Eisler and F. Maislinger, “Hydrodynamical phase transition for domain-wall melting in the XY chain,” Physical Review B 98, 161117 (2018).

V. Eisler and F. Maislinger, “Front dynamics in the XY chain after local excitations,” SciPost Physics 8, 37 (2020).

In the large U limit, the Hubbard model reduces to the quantum Heisenberg spin-model[175]. When the coupling of one component of the spins becomes negligible, e.g. because of strong crystal anisotropy, the Heisenberg model becomes the quantum XY spin-model[176], which has the following Hamiltonian:

$$H = -\sum_{i=1}^{n-1} \frac{1+\gamma}{4}\,\sigma_i^x\,\sigma_{i+1}^x + \frac{1-\gamma}{4}\,\sigma_i^y\,\sigma_{i+1}^y - \frac{h}{2}\sum_i \sigma_i^z \tag{III.1}$$

With strong anisotropy ($\gamma = 1$) the XY model becomes the Transverse Field Ising (TI) model, where the peculiar fact was recently discovered that in one dimension the rescaled magnetization profiles of the time-evolved Jordan-Wigner excitation are the same for different magnetic field strengths[177]. Here, the Jordan-Wigner excitation corresponds to a series of operators applied to the symmetry broken ground state. These profiles were found to be numerically[177] and analytically[178] identical to the particle density profile of free fermions in one dimension, where the initial state is fully filled in half of the chain and empty in the other half of the chain. Based on these results we analyzed a different model, namely the XY model instead of the TI model, with the same initial state. We performed the computations of the expectation values and entanglement entropy with the Matrix Product State approach, to check the correctness of other approaches, which are a Pfaffian approach, a semi-classical approach, and a form-factor approach.

The contribution of Florian Maislinger to both publications was doing the Matrix Product State calculations and explorations in parameter space to check for interesting results in the time series of the magnetization profile, correlation functions, and the entanglement entropy. He also contributed to the semiclassical calculations in Subpart III.A and programmed the simulations for both publications from the ground up in C++ using the ITensor library[107], and in Python. Viktor Eisler did the calculations and programming of the other approaches. The bulk of the text of both publications was written by Viktor Eisler, while Florian Maislinger contributed the parts which are relevant to Matrix Product States.

Subpart III.A

Hydrodynamical phase transition for domain-wall melting in the XY chain (Phys. Rev. B 98, 161117(R))

Hydrodynamical phase transition for domain-wall melting in the XY chain

Viktor Eisler[1] and Florian Maislinger[1]

[1] *Institute of Theoretical and Computational Physics, Graz*
University of Technology, 8010 Graz, Austria

We study the melting of a domain wall, prepared as a certain low-energy excitation above the ferromagnetic ground state of the XY chain. In a well defined parameter regime the time-evolved magnetization profile develops sharp kink-like structures in the bulk, showing features of a phase transition in the hydrodynamic scaling limit. The transition is of purely dynamical nature and can be attributed to the appearance of a negative effective mass term in the dispersion. The signatures are also clearly visible in the entanglement profile measured along the front region, which can be obtained by covariance-matrix methods despite the state being non-Gaussian.

III.A.1 Article

Uncovering the mechanism of phase transitions belongs to one of the most spectacular achievements of statistical physics. The abrupt changes in the properties of matter, in response to the tuning of a control parameter, could be understood through simple concepts such as order parameter, symmetry breaking, or free energy. While the theory is well established for systems in thermal equilibrium, and can even be extended to quantum phase transitions at zero temperature[179], it is far from obvious how these concepts generalize to the nonequilibrium scenario.

Due to this ambiguity, there has been various attempts to lift the definition of a phase transition into the dynamical regime. In the particular context of quantum quenches[66,180], dynamical quantum phase transitions (DQPT) were introduced by analogy, via the definition of a dynamical free energy density[181]. It is simply given via the overlap between initial and time-evolved states, and DQPT manifests itself in the nonanalytic real-time behavior of this return probability, see[182] for a recent review. Despite not being a conventional observable, the return probability and the signatures of a DQPT could directly be detected in a recent experiment[183].

On the other hand, in a number of approaches the definition of dynamical phases is based on the time-asymptotic behavior of an order parameter that shows abrupt changes when crossing the phase boundaries. Dynamical phase transitions based on a suitable order parameter have been identified for quench protocols of various closed many-body systems[52,184,185] and the studies have even been extended to the open-system scenario[186,187]. Furthermore, connections between the different concepts of a DQPT, based on dynamical free energy vs. order parameter, have recently been pointed out[188,189].

Here we shall address the question whether a phase transition in simple quantum chains might occur due to the presence of initial spin gradients, which drive the system towards a nonequilibrium steady state (NESS). In the context of Markovian open system dynamics, such an example was found earlier for a boundary driven open XY spin chain, where the emergence of long range order was observed in the NESS below a critical value $h < h_c$ of a model parameter[190]. Although the phenomenon seems robust enough against the details of incoherent driving[191], no counterpart of the phase transition under closed unitary dynamics has been found so far.

To mimic the effect of gradients imposed at the boundaries in the open system setup, here we prepare instead a domain-wall initial state and then let the system evolve under its own unitary dynamics. The domain wall is created as a simple low-lying excitation above the ferromegnatic (symmetry-broken) ground state of the XY chain. Our main result is illustrated on Fig. III.A.1, where the qualitative change in the time-evolved and properly normalized magnetization profiles is clearly visible. The phase transition point h_c exactly coincides with the one found in Ref.[190], and is signalled by an infinite slope in the center of the profile, whereas kinks are developing in the bulk for $h < h_c$. The nonanalytical behavior appears only in the hydrodynamical limit, shown by the solid lines in Fig. III.A.1. However, in contrast to Ref.[190], our results on the correlations indicate that the NESS itself is similar to the symmetry-restored ground state of the chain and does not show any criticality around h_c. Hence we use the term hydrodynamical phase transition to distinguish between the two behaviors.

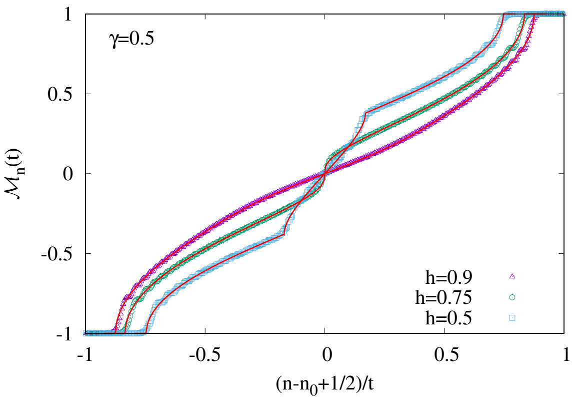

Figure III.A.1. Normalized magnetization profiles (symbols) at $t = 200$ compared to the hydrodynamic solution (red solid lines) in (III.A.10). The phase transition is located at $h_c = 1 - \gamma^2 = 0.75$.

The Hamiltonian of the XY chain is given by

$$H = -\sum_{n=1}^{N-1}\left(\frac{1+\gamma}{4}\sigma_n^x\sigma_{n+1}^x + \frac{1-\gamma}{4}\sigma_n^y\sigma_{n+1}^y\right) - \frac{h}{2}\sum_{n=1}^{N}\sigma_n^z \tag{III.A.1}$$

where σ_n^α are Pauli matrices on site n, γ is the anisotropy and h is a transverse magnetic field. The XY model can be mapped to a chain of free fermions via a Jordan-Wigner (JW) transformation, by introducing the Majorana operators

$$a_{2j-1} = \prod_{k=1}^{j-1}\sigma_k^z\sigma_j^x, \qquad a_{2j} = \prod_{k=1}^{j-1}\sigma_k^z\sigma_j^y, \tag{III.A.2}$$

satisfying anticommutation relations $\{a_k, a_l\} = 2\delta_{k,l}$. While the open boundaries in Eq. (III.A.1) are most suitable for numerical investigations of the dynamics on finite size chains, for the analytical treatment one should impose antiperiodic boundary conditions $\sigma_{N+1}^{x,y} = -\sigma_1^{x,y}$ on the spins, such that H can be brought into a diagonal form by a Fourier transform and a Bogoliubov rotation[192].

We focus on the parameter regime $0 < \gamma \leq 1$ and $0 \leq h < 1$, where the model is in a gapped ferromagnetic phase, with magnetic order in the x direction. In particular, in the limit $N \to \infty$, the ground state is twofold degenerate, with $|0\rangle_{\mathrm{NS}}$ and $|0\rangle_{\mathrm{R}}$ located in the Neveu-Schwarz (NS) and Ramond (R) sectors, corresponding to ± 1 eigenvalues of the parity operator $P = \prod_{k=1}^{N}\sigma_k^z$, which commutes with the Hamiltonian $[H, P]$=0. Since both of the ground states are parity eigenstates, their magnetization is vanishing. However, starting from the symmetry-broken ground state $|\Uparrow\rangle$, a domain wall initial state can be prepared via a JW excitation, i.e. acting with a single Majorana operator as

$$|\mathrm{JW}\rangle = a_{2n_0-1}|\Uparrow\rangle, \qquad |\Uparrow\rangle = \frac{|0\rangle_{\mathrm{NS}} + |0\rangle_{\mathrm{R}}}{\sqrt{2}}. \tag{III.A.3}$$

In numerical calculations we always consider domain walls localized in the middle of the chain, $n_0 = N/2 + 1$.

Our primary goal is to calculate the magnetization profile in the time evolved state

$$\mathrm{e}^{-iHt}|\mathrm{JW}\rangle = \frac{|\phi_t\rangle_{\mathrm{NS}} + |\phi_t\rangle_{\mathrm{R}}}{\sqrt{2}} \tag{III.A.4}$$

being a superposition of states from the two parity sectors. Both can be obtained by rewriting the excitation in (III.A.3) in the fermionic eigenbasis of the Hamiltonian, leading to a superposition of single-particle states. These can then be trivially time evolved and yield[193]

$$|\phi_t\rangle_{\mathrm{NS}} = \frac{1}{\sqrt{N}}\sum_{q\in\mathrm{NS}}\mathrm{e}^{-i\epsilon_q t}\mathrm{e}^{-iq(n_0-1)}\mathrm{e}^{i\theta_q/2}|q\rangle_{\mathrm{NS}}, \tag{III.A.5}$$

where the single-particle dispersion ϵ_q and the Bogoliubov phase θ_q are given by

$$\begin{aligned}\epsilon_q &= \sqrt{(\cos q - h)^2 + \gamma^2\sin^2 q}\,,\\ \mathrm{e}^{i(\theta_q+q)} &= \frac{\cos q - h + i\gamma\sin q}{\epsilon_q}\,.\end{aligned} \tag{III.A.6}$$

The result for $|\phi_t\rangle_{\mathrm{R}}$ is completely analogous to (III.A.5), with the sum running over momenta $p \in R$. In turn, the normalized magnetization can be cast in the form

$$\mathcal{M}_n(t) = \frac{\langle\mathrm{JW}|\sigma_n^x(t)|\mathrm{JW}\rangle}{\langle\Uparrow|\sigma_n^x|\Uparrow\rangle} = \mathrm{Re}\,{}_{\mathrm{R}}\langle\phi_t|\hat{\mathcal{M}}_n|\phi_t\rangle_{\mathrm{NS}}\,, \tag{III.A.7}$$

where, in the limit $N \gg 1$, the form factors read[194,195]

$${}_{\mathrm{R}}\langle p|\hat{\mathcal{M}}_n|q\rangle_{\mathrm{NS}} = -\frac{i}{N}\frac{\epsilon_p + \epsilon_q}{2\sqrt{\epsilon_p\epsilon_q}}\frac{\mathrm{e}^{i(n-1/2)(q-p)}}{\sin\frac{q-p}{2}}. \tag{III.A.8}$$

Combining the results (III.A.5)-(III.A.8) and considering the thermodynamic limit, one ends up with a double integral formula for the magnetization[196]. Interestingly, this is exactly the same expression as the one found earlier for the transverse Ising (TI) chain[178], except that the form of the dispersion and the Bogoliubov angle (III.A.6) are now more general. In fact, it is the very presence of the XY anisotropy that will give rise to a peculiar dynamical behavior. The hydrodynamical phase transition is encoded in the $q \ll 1$ expansion of the dispersion

$$\epsilon_q \approx \Delta + \frac{h-h_c}{2\Delta} q^2 + c\, q^4 , \qquad \text{(III.A.9)}$$

where $\Delta = 1-h$ is the excitation gap and $h_c = 1-\gamma^2$ is a critical field. The coefficient c has a lengthy expression in terms of h and γ, satisfying $c > 0$ for any $h < h_c$. In contrast, the mass term in Eq. (III.A.9) becomes negative below the critical field.

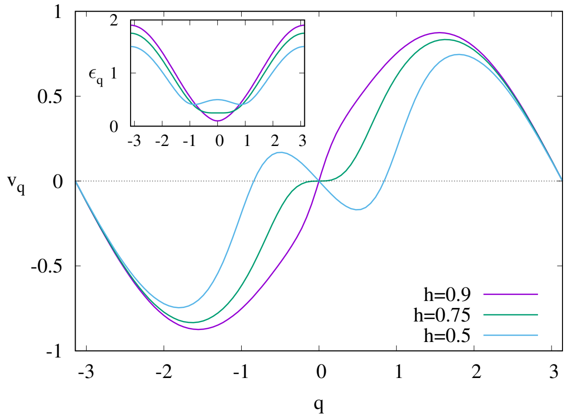

Figure III.A.2. Single-particle velocities v_q and dispersion ϵ_q (inset).

While a negative effective mass has no effect on the ground-state properties, it will play a crucial role in the dynamics. Indeed, in a well-defined limit, the shape of the melting domain wall is entirely determined by the group velocities $v_q = \frac{\mathrm{d}\epsilon_q}{\mathrm{d}q}$. These are shown on Fig. III.A.2 for $\gamma = 0.5$, and three different magnetic fields above, below and at the critical value h_c. In case $h < h_c$, the negative slope of v_q around $q \to 0$ leads to the development of a new local maximum, which eventually gives rise to a nonanalytic behavior in the hydrodynamic profiles of various observables. In particular, introducing the scaling variable $\nu = (n - n_0 + 1/2)/t$, the magnetization profile reads

$$\mathcal{M}_n(t) = 1 - 2 \int_{-\pi}^{\pi} \frac{\mathrm{d}q}{2\pi} \Theta(v_q - \nu), \qquad \text{(III.A.10)}$$

where $\Theta(x)$ is the Heaviside step function. The result (III.A.10) follows rigorously from a stationary-phase analysis[197] of the integral representation of $\mathcal{M}_n(t)$, and has a clear physical interpretation. Namely, each single-particle excitation carries a spin-flip[198–201] and thus the magnetization along a fixed ray follows from the integrated density of excitations whose speed exceeds ν. Hence, for $h < h_c$ the nonanalytical behavior of the density is a consequence of the new branch of solutions around the local maximum for negative momenta.

The comparison between the profiles and the hydrodynamic scaling function is shown on Fig. III.A.1. The magnetization at $t = 200$ and various h were calculated for an open chain of size $N = 400$ using the Pfaffian formalism described in[178]. One has an excellent agreement with clear signatures of the developing kink for $h < h_c$. The hydrodynamic profile in general depends on the details of the dispersion and is hard to obtain analytically, since the solution of $v_q = \nu$ leads to a fourth-order equation. Nevertheless, one expects a universal behavior to emerge around the edge of the front[202]. Indeed, the stationary phase calculation around $v_{q_*} = v_{max}$ can be extended to capture the fine structure of the front[203–206], suggesting the following choice for the scaling variable

$$X = (n - n_0 + 1/2 + \theta'_{q_*}/2 - v_{q_*} t) \left(\frac{2}{|v''_{q_*}| t} \right)^{1/3} . \qquad \text{(III.A.11)}$$

In turn, the edge magnetization is given by[207]

$$\mathcal{M}_n(t) = 1 - 2 \left(\frac{2}{|v''_{q_*}| t} \right)^{1/3} \rho(X) , \qquad \text{(III.A.12)}$$

where $\rho(X) = \left[\mathrm{Ai}'(X)\right]^2 - X \mathrm{Ai}^2(X)$ is just the diagonal part of the Airy kernel[208].

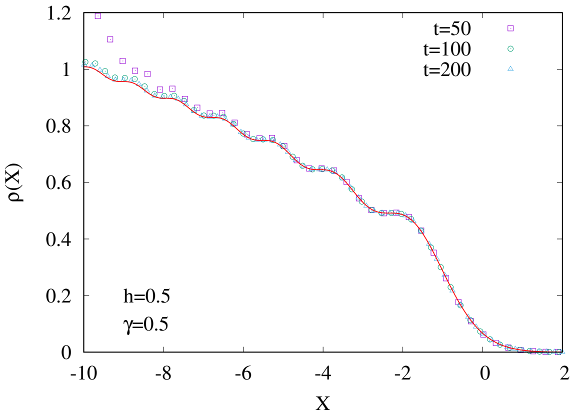

Figure III.A.3. Edge scaling of the magnetization profile, with the scaling variable X and function $\rho(X)$ defined by Eqs. (III.A.11) and (III.A.12), respectively.

The edge scaling (III.A.12) is tested against numerical calculations for $h = \gamma = 0.5$ in Fig. III.A.3, showing an excellent agreement already for moderately large times. Note that the larger deviation towards the bulk for $t = 50$ is due to the presence of the kink in the profile. In fact, one could ask whether zooming on around the kink would yield a similar universal fine structure as for the edge. However, in the latter case the density has a nonuniversal bulk contribution superimposed, which spoils the step structure. It is also worth noting that the edge scaling (III.A.12) for the XY chain can not be derived from a simple higher-order extension of the hydrodynamical picture[209].

The signatures of the hydrodynamical phase transition are also visible on the entanglement profiles, as measured by the von Neumann entropy between the segment $A = [1, N/2 + r]$ and B the rest of the system. Although the XY chain maps to free fermions, extracting the entropy via covariance-matrix techniques for Gaussian states[210,211] requires some additional care. Indeed, the initial state is excited from the symmetry-broken ground state of the model, which is inherently non-Gaussian[212]. This difficulty can, however, be overcome by the following considerations. Let us denote by $\rho_{\Uparrow}$ the reduced density matrix (RDM) arising from the time evolved state (III.A.4) after tracing out the degrees of freedom in B. The arrow indicates the choice of the symmetry-broken ground state in (III.A.3) and the entropy of the RDM is given by $S(\rho_{\Uparrow}) = -\mathrm{Tr}\, \rho_{\Uparrow} \ln \rho_{\Uparrow}$. In fact, one could equally well have defined $\rho_{\Downarrow}$ starting from the spin-reversed initial state, with the entropies of the two RDMs satisfying $S(\rho_{\Uparrow}) = S(\rho_{\Downarrow})$ due to obvious symmetry reasons. The main trick is now to consider the convex combination

$$\rho_G = \frac{\rho_{\Uparrow} + \rho_{\Downarrow}}{2}, \qquad \text{(III.A.13)}$$

which removes all the parity-odd contributions from the RDMs, albeit still mixing parity-even terms from the two sectors NS and R. However, in the thermodynamic limit all the expectation values of local operators become equal in both sectors[212], hence ρ_G is equivalent to a Gaussian RDM where the excitation is created upon the parity-symmetric ground state $|0\rangle_{\mathrm{NS}}$.

Due to its Gaussianity, the entropy of ρ_G can now be obtained by applying the covariance-matrix formalism as shown in Ref.[213]. Indeed, the effect of the Majorana excitation can be represented in a Heisenberg picture

$$a'_k = a_{2n_0-1} a_k a_{2n_0-1} = \sum_{l=1}^{2N} Q_{k,l} a_l, \qquad \text{(III.A.14)}$$

as an orthogonal transformation on the Majoranas, with matrix elements $Q_{k,l} = \delta_{k,l}(2\delta_{k,2n_0-1} - 1)$. Similarly, time evolving the state corresponds to the transformation

$$a'_k(t) = \mathrm{e}^{iHt} a'_k \mathrm{e}^{-iHt} = \sum_{l=1}^{2N} R_{k,l} a'_l, \qquad \text{(III.A.15)}$$

with matrix elements $R_{k,l}$ given as in Ref.[178]. Hence ρ_G corresponds to a RDM associated to the Gaussian state with covariance matrix

$$\tilde{\Gamma} = R\, Q\, \Gamma\, Q^T R^T, \qquad \text{(III.A.16)}$$

where $i\Gamma_{k,l} = {}_{\mathrm{NS}}\langle 0|a_k a_l|0\rangle_{\mathrm{NS}} - \delta_{k,l}$. Note that the matrix $\tilde{\Gamma}$ is exactly the one that appears in the Pfaffian by the calculation of the magnetization[178].

Although the entropy of ρ_G follows simply via the eigenvalues of the reduced covariance matrix $\tilde{\Gamma}_A$[210,211], one still has to relate it to the entropy of the non-Gaussian RDM $\rho_{\Uparrow}$ that we are interested in. To this end, one can make use of the inequality for convex combinations of density matrices[214,215]

$$S(\sum_i \lambda_i \rho_i) \le \sum_i \lambda_i S(\rho_i) - \sum_i \lambda_i \ln \lambda_i\, . \qquad \text{(III.A.17)}$$

Furthermore, it is also known that the inequality is saturated if the ranges of ρ_i are pairwise orthogonal. Applying it to Eq. (III.A.13), the orthogonality condition is clearly satisfied due to $\langle \Uparrow | \Downarrow \rangle = 0$ and hence one arrives at

$$S(\rho_{\Uparrow}) = S(\rho_G) - \ln 2\, . \qquad \text{(III.A.18)}$$

The entropy can thus be exactly evaluated using Gaussian techniques.

The result for the profile ΔS, measured from the $t = 0$ value, is shown on Fig. III.A.4 at time $t = 200$, against the rescaled cut position. The parameters are chosen to be identical to Fig. III.A.1, and a kink for $h = 0.5$ emerges again at the value of r/t equal to the local maximum of the velocity v_q. Furthermore, the entropy growth for the half-chain ($r/t = 0$) clearly converges towards the value $\ln 2$, which can be interpreted as a restoration of the spin-flip symmetry in the NESS. Note also the light dip in the middle for $h = h_c = 0.75$, which is the consequence of a much slower convergence towards the NESS at criticality. The entropy profiles obtained by the Gaussian technique have also been compared to the results of density-matrix renormalization group[30] calculations, finding an excellent agreement and thus justifying the result in Eq. (III.A.18).

We finally consider the normalized equal-time spin-correlation functions $\mathcal{C}_{m,n}(t) = {}_{\mathrm{NS}}\langle \phi_t | \hat{\mathcal{M}}_m \hat{\mathcal{M}}_n | \phi_t \rangle_{\mathrm{NS}}$ which can be studied via the form-factor approach by inserting a resolution

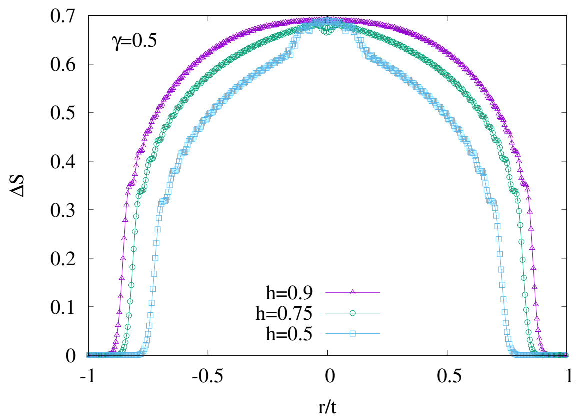

Figure III.A.4. Entanglement profiles as a function of the rescaled distance r of the cut from the middle of the chain. The entropy difference ΔS from the initial state value is shown at $t = 200$ for the same parameter values as in Fig. III.A.1.

of the identity between the operators. Although in general all the multi-particle form factors are nonvanishing, the dominant contribution to the correlations comes from the single-particle terms

$$\mathcal{C}_{m,n}(t) \simeq \sum_{p} {}_{\mathrm{NS}}\langle \phi_t | \hat{\mathcal{M}}_m | p \rangle_{\mathrm{R}} \, {}_{\mathrm{R}}\langle p | \hat{\mathcal{M}}_n | \phi_t \rangle_{\mathrm{NS}} \, . \tag{III.A.19}$$

The above expression can again be evaluated in the hydrodynamic scaling limit and for $m < n$ yields[216]

$$\mathcal{C}_{m,n}(t) \simeq 1 - 2 \int_{-\pi}^{\pi} \frac{\mathrm{d}q}{2\pi} \Theta(v_q - \mu)\Theta(\nu - v_q) \, , \tag{III.A.20}$$

where μ is defined analogously to ν. The integral in (III.A.20) gives the number of excitations with velocities between the rays defined by μ and ν, and has again a simple interpretation. In fact, it is directly related to the difference of the magnetizations along those rays and thus shows similar nonanalytical behavior for $h < h_c$.

In the NESS limit $t \to \infty$ with m, n fixed, Eq. (III.A.20) predicts long-range magnetic order $\mathcal{C}_{m,n}(t) \to 1$. Together with $\mathcal{M}_n(t) \to 0$, this behavior is characteristic of the ground state $|0\rangle_{\mathrm{NS}}$ at large separations $n - m \gg 1$. Furthermore, a careful numerical analysis shows that $\mathcal{C}_{m,n}(t)$ converges towards the proper ground-state value even for small separations of the spins. Indeed, in the ferromagnetic regime the normalized correlators deviate from unity by a term decaying exponentially with the distance[217]. The source of the discrepancy is the approximation in (III.A.19), which neglects the contribution of the multi-particle form factors. A detailed analysis of the correlations will be presented elsewhere[218].

In conclusion, our studies of domain-wall melting in the XY chain have revealed a phase transition, manifest in the emergence of kinks in the profiles of various observables. While the critical point $h_c = 1 - \gamma^2$ coincides with the one found earlier for open-system dynamics[190], the transition exists only in the hydrodynamic regime, and does not survive the NESS limit. In contrast, the latter one seems to be given by the parity-symmetric ground state, which does not show any criticality around h_c.

Although demonstrated on a simple free-fermion example, there is good reason to believe that this phenomenon carries over to generic integrable systems, where the proper hydrodynamic description has only recently been identified[219,220] and applied to initial states with domain walls[221,222]. In particular, the emergence of kinks in the magnetization profile has been observed for the XXZ chain at large anisotropies, resulting from the velocity maxima of the various quasi-particle families that govern the hydrodynamics[221]. While the mechanism seems to be closely related to the one presented here, it is unclear whether a hydrodynamical phase transition point exists in the XXZ case, since all the profiles considered in[221] belong to the kink phase.

Finally, it remains to be understood whether the finite increase of entropy after the JW excitation could be interpreted within a framework similar to the one introduced for local operator insertions in conformal field theories[223]. While the results have been checked against the lattice equivalent of local primary excitations for the transverse Ising chain in Ref.[213], it would be interesting to see whether the field theory treatment could be generalized to include the massive case and the non-local operators considered here.

We thank H. G. Evertz and M. Fagotti for discussions. The authors acknowledge funding from the Austrian Science Fund (FWF) through Project No. P30616-N36, and through SFB ViCoM F41 (Project P04).

III.A.2 Supplemental Material

III.A.2.1 Fermionization of XY Hamiltonian

In order to obtain the many-body eigenstates of the XY chain, it is useful to consider periodic H_+ or antiperiodic H_- chains, instead of the open one in Eq. (III.A.1). These are given by

$$H_s = -\frac{1}{2}\sum_{n=1}^{N}\left(\frac{1+\gamma}{2}\sigma_n^x\sigma_{n+1}^x + \frac{1-\gamma}{2}\sigma_n^y\sigma_{n+1}^y + h\sigma_n^z\right), \tag{III.A.21}$$

where the boundary conditions are $\sigma_{N+1}^x = s\sigma_1^x$ and $\sigma_{N+1}^y = s\sigma_1^y$ for $s=\pm$. Since H_s commutes with the parity P, it can be written in a block-diagonal form

$$H_s = \frac{1-sP}{2}H_{\mathrm{R}} + \frac{1+sP}{2}H_{\mathrm{NS}}, \qquad P = \prod_{n=1}^{N}\sigma_n^z\,. \tag{III.A.22}$$

The parity subspaces are the Ramond (R) and Neveu-Schwarz (NS) sectors, defining two different Hamiltonians. In terms of Majorana operators, obtained via the Jordan-Wigner transformation (III.A.2), both of them can be brought into the quadratic form

$$H_{\mathrm{R/NS}} = \frac{i}{2}\sum_{j=1}^{N}\left(\frac{1+\gamma}{2}a_{2j}a_{2j+1} - \frac{1-\gamma}{2}a_{2j-1}a_{2j+2} + ha_{2j-1}a_{2j}\right), \tag{III.A.23}$$

where the two Hamiltonians differ only in the boundary conditions $a_{2N+1} = \pm a_1$ and $a_{2N+2} = \pm a_2$ being periodic for R and antiperiodic for the NS sector. Each sector can be simultaneously diagonalized by a joint Fourier and Bogoliubov transformation

$$a_{2j-1} = \frac{1}{\sqrt{N}}\sum_{q\in\mathrm{R/NS}} \mathrm{e}^{-iq(j-1)}\mathrm{e}^{i\theta_q/2}(b_q^\dagger + b_{-q}), \qquad a_{2j} = \frac{-i}{\sqrt{N}}\sum_{q\in\mathrm{R/NS}} \mathrm{e}^{-iqj}\mathrm{e}^{-i\theta_q/2}(b_q^\dagger - b_{-q}), \tag{III.A.24}$$

where the allowed values of the momenta are $q_k = \frac{2\pi}{N}k$ for R and $q_k = \frac{2\pi}{N}(k+1/2)$ for NS, respectively, with $k = -N/2, \dots, N/2-1$. Note that the site index j in the Fourier transformation is shifted by one for odd Majorana operators. This is a dual representation in terms of which the Bogoliubov angle must satisfy

$$\mathrm{e}^{i(\theta_q+q)} = \frac{\cos q - h + i\gamma\sin q}{\epsilon_q}, \qquad \epsilon_q = \sqrt{(\cos q - h)^2 + \gamma^2\sin^2 q}\,. \tag{III.A.25}$$

In fact, the above definition ensures that θ_q is a continuous and smooth function in its full domain $q \in [-\pi, \pi]$, for arbitrary parameters $0 < \gamma \le 1$ and $0 \le h < 1$ in the ferromagnetic phase. The diagonal form of the Hamiltonian and its many-particle eigenstates then read

$$H_{\mathrm{R/NS}} = \sum_{q\in\mathrm{R/NS}} \epsilon_q b_q^\dagger b_q + \mathrm{const}, \qquad |q_1, q_2, \dots, q_m\rangle_{\mathrm{R/NS}} = \prod_{i=1}^{m} b_{q_i}^\dagger|0\rangle_{\mathrm{R/NS}}\,. \tag{III.A.26}$$

Finally, it should be pointed out that the boundary condition on the spins selects the parity of the many-particle basis: $m = 2\ell$ is even for the spin-periodic Hamiltonian H_+, and $m = 2\ell+1$ is odd for the spin-antiperiodic one H_-.

III.A.2.2 Form factor approach

To calculate the time evolution of the magnetization, one also needs the corresponding form factors of the σ^x operator. In fact, it is more convenient to consider the matrix elements normalized by the equilibrium magnetization, which in the large N limit reads[194,195]

$$
{}_{\mathrm{R}}\langle p|\hat{\mathcal{M}}_n|q\rangle_{\mathrm{NS}} = \frac{{}_{\mathrm{R}}\langle p|\sigma_n^x|q\rangle_{\mathrm{NS}}}{{}_{\mathrm{R}}\langle 0|\sigma_n^x|0\rangle_{\mathrm{NS}}} = -\frac{i}{N}\frac{\cosh\frac{\Delta_p-\Delta_q}{2}\sinh\frac{\Delta_p+\Delta_q}{2}}{\sqrt{\sinh\Delta_p\sinh\Delta_q}}\frac{\mathrm{e}^{i(n-1/2)(q-p)}}{\sin\frac{q-p}{2}}. \tag{III.A.27}
$$

The above definition of the form factors is well-suited for the parameter regime $\sqrt{1-\gamma^2} < h < 1$, i.e. in the non-oscillatory ferromagnetic phase[217], where the auxiliary parameter Δ_q is defined via

$$
\sinh\Delta_q = \frac{\sqrt{1-\gamma^2}}{\gamma\sqrt{\gamma^2+h^2-1}}\epsilon_q. \tag{III.A.28}
$$

In the oscillatory phase $0 < h < \sqrt{1-\gamma^2}$ the form factors can be obtained by analytic continuation[194], i.e. by introducing the variable $\tilde{\Delta}_q = \Delta_q + i\pi/2$. In fact, the form-factor formula (III.A.27) can even be further simplified by making use of the identity

$$
\cosh\frac{\Delta_p-\Delta_q}{2}\sinh\frac{\Delta_p+\Delta_q}{2} = \frac{1}{2}(\sinh\Delta_p + \sinh\Delta_q). \tag{III.A.29}
$$

Substituting (III.A.28) and (III.A.29) into (III.A.27), one obtains immediately Eq. (III.A.8). Using these form factors and taking the thermodynamic limit, Eq. (III.A.7) for the magnetization can be written out as a double integral

$$
\mathcal{M}_n(t) = \mathrm{Im}\int_{-\pi}^{\pi}\frac{\mathrm{d}p}{2\pi}\int_{-\pi}^{\pi}\frac{\mathrm{d}q}{2\pi}\frac{\epsilon_p+\epsilon_q}{2\sqrt{\epsilon_p\epsilon_q}}\frac{\mathrm{e}^{i(n-n_0+1/2)(q-p)}}{\sin\frac{q-p}{2}}\mathrm{e}^{i(\theta_q-\theta_p)/2}\mathrm{e}^{i(\epsilon_p-\epsilon_q)t}. \tag{III.A.30}
$$

Using the properties $\epsilon_{-q} = \epsilon_q$ and $\theta_{-q} = -\theta_q$, the above expression can be written as $\mathcal{M}_n(t) = \mathcal{M}_n^e(t) + \mathcal{M}_n^o(t)$ with only two nonvanishing contributions

$$
\begin{aligned}
\mathcal{M}_n^e(t) &= \int_{-\pi}^{\pi}\frac{\mathrm{d}p}{2\pi}\int_{-\pi}^{\pi}\frac{\mathrm{d}q}{2\pi}\frac{\epsilon_p+\epsilon_q}{2\sqrt{\epsilon_p\epsilon_q}}\frac{\cos\left[(n-n_0+1/2)(q-p)\right]}{\sin\frac{q-p}{2}}\sin\frac{\theta_q-\theta_p}{2}\cos(\epsilon_p-\epsilon_q)t\,,\\
\mathcal{M}_n^o(t) &= \int_{-\pi}^{\pi}\frac{\mathrm{d}p}{2\pi}\int_{-\pi}^{\pi}\frac{\mathrm{d}q}{2\pi}\frac{\epsilon_p+\epsilon_q}{2\sqrt{\epsilon_p\epsilon_q}}\frac{\sin\left[(n-n_0+1/2)(q-p)\right]}{\sin\frac{q-p}{2}}\cos\frac{\theta_q-\theta_p}{2}\cos(\epsilon_p-\epsilon_q)t\,.
\end{aligned} \tag{III.A.31}
$$

Hence the magnetization is the sum of an even and an odd function $\mathcal{M}_n^{e,o}(t) = \pm\mathcal{M}_{2n_0-1-n}^{e,o}(t)$ under reflections with respect to the initial domain wall position. Note that, in general, the even term has a contribution of much smaller magnitude, and it vanishes completely in the hydrodynamic scaling limit. Moreover, in the limit $\gamma = 1$ of a transverse Ising chain, the even part $\mathcal{M}_n^e(t) = 0$ vanishes identically even for finite times.

The normalized correlation functions $\mathcal{C}_{m,n}(t) = {}_{\mathrm{NS}}\langle\phi_t|\hat{\mathcal{M}}_m\hat{\mathcal{M}}_n|\phi_t\rangle_{\mathrm{NS}}$ can also be studied through the form factor approach. The standard trick is to insert an identity between the two operators, written in terms of the eigenbasis

$$
\mathbb{1} = \sum_p |p\rangle\langle p| + \sum_{p_1,p_2}|p_1,p_2\rangle\langle p_1,p_2| + \sum_{p_1,p_2,p_3}|p_1,p_2,p_3\rangle\langle p_1,p_2,p_3| + \ldots \tag{III.A.32}
$$

Thus, in contrast to the magnetization which could be exactly evaluated using only single-particle form factors, the situation for the correlations is much more complicated as an infinite series of many-particle matrix elements appear. Nevertheless, it is reasonable to expect that the dominant contribution to the correlations still comes from the single-particle sector. Hence, we will consider this approximate expression, given by (III.A.19) in the main text, which for $N \to \infty$ can be converted into the integral form

$$
\mathcal{C}_{m,n}(t) \simeq \int\frac{\mathrm{d}q_1}{2\pi}\int\frac{\mathrm{d}q_2}{2\pi}\mathrm{e}^{-i(\theta_{q_1}-\theta_{q_2})/2}\mathrm{e}^{i(\epsilon_{q_1}-\epsilon_{q_2})t}\int\frac{\mathrm{d}p}{2\pi}\frac{\epsilon_p+\epsilon_{q_1}}{2\sqrt{\epsilon_p\epsilon_{q_1}}}\frac{\epsilon_p+\epsilon_{q_2}}{2\sqrt{\epsilon_p\epsilon_{q_2}}}\frac{\mathrm{e}^{-i(m-n_0+1/2)(q_1-p)}}{\sin\frac{q_1-p}{2}}\frac{\mathrm{e}^{i(n-n_0+1/2)(q_2-p)}}{\sin\frac{q_2-p}{2}}. \tag{III.A.33}
$$

III.A.2.3 Stationary phase calculations

The profiles in the hydrodynamic scaling limit can be obtained by stationary phase arguments, and their derivation closely follows the lines of Refs.[203–206]. Let us consider first the magnetization as given by Eq. (III.A.30). In the limit $n - n_0 \gg 1$ and $t \gg 1$, the integrand is highly oscillatory and thus the main contribution comes from around the points q_s where the stationarity condition is satisfied

$$v_{q_s} t = n - n_0 + 1/2 + \theta'_{q_s}/2, \qquad v_q = \frac{\mathrm{d}\epsilon_q}{\mathrm{d}q}. \tag{III.A.34}$$

The stationary phase condition for the integral over p is exactly the same. Moreover, the integrand has a pole at $p = q$ which suggests the change of variables $Q = q - p$ and $P = (q + p)/2$. In the new variables, the stationarity condition is $Q_s = 0$ for arbitrary values of P. One shall thus expand the integrand in (III.A.30) around $Q = 0$, setting

$$\frac{\epsilon_p + \epsilon_q}{2\sqrt{\epsilon_p \epsilon_q}} \approx 1, \qquad \sin\frac{q-p}{2} \approx \frac{Q}{2}, \tag{III.A.35}$$

to arrive at

$$2\,\mathrm{Re}\int_{-\pi}^{\pi} \frac{\mathrm{d}P}{2\pi} \int_{-\infty}^{\infty} \frac{\mathrm{d}Q}{2\pi i} \frac{\mathrm{e}^{i(n-n_0+1/2+\theta'_P - v_P t)Q}}{Q}. \tag{III.A.36}$$

To carry out the integration around the pole, we use a formal identity in complex analysis as well as the integral representation of the Heaviside theta function

$$\frac{1}{Q} = i\pi\delta(Q) + \lim_{\delta\to 0}\frac{1}{Q + i\delta}, \qquad \Theta(x) = -\lim_{\delta\to 0}\int_{-\infty}^{\infty}\frac{\mathrm{d}Q}{2\pi i}\frac{\mathrm{e}^{-iQx}}{Q + i\delta}. \tag{III.A.37}$$

In the hydrodynamic regime one can neglect the term θ'_P and introduce the scaling variable $\nu = (n - n_0 + 1/2)/t$, which brings us to the result (III.A.10) in the main text.

In general, the hydrodynamic profile is found by solving the equation $v_q = \nu$. Special attention is needed around the maximum $v_{q_*} = v_{max}$ of the velocities, where the solutions coalesce at momentum q_*. To get the fine structure of the front edge, one has to expand the dispersion around q_* as

$$\epsilon_q \approx \epsilon_{q_*} + v_{q_*}(q - q_*) + \frac{\epsilon'''_{q_*}}{6}(q - q_*)^3. \tag{III.A.38}$$

Furthermore, one can introduce the following rescaled variables

$$X = (n - n_0 + 1/2 + \theta'_{q_*}/2 - v_{q_*} t)\left(\frac{-2}{\epsilon'''_{q_*} t}\right)^{1/3}, \quad Q = \left(\frac{-2}{\epsilon'''_{q_*} t}\right)^{-1/3}(q - q_*), \quad P = \left(\frac{-2}{\epsilon'''_{q_*} t}\right)^{-1/3}(p - q_*). \tag{III.A.39}$$

Substituting (III.A.38) and (III.A.39) into (III.A.7), one arrives at the following integral

$$\left(\frac{-2}{\epsilon'''_{q_*} t}\right)^{1/3} \mathrm{Im}\int \frac{\mathrm{d}P}{2\pi}\int\frac{\mathrm{d}Q}{2\pi}\frac{\mathrm{e}^{iX(Q-P)}\mathrm{e}^{i(Q^3-P^3)/3}}{(Q-P)/2}. \tag{III.A.40}$$

Using the integral representation of the Airy kernel

$$K(X,Y) = \lim_{\delta\to 0}\int\frac{\mathrm{d}P}{2\pi}\int\frac{\mathrm{d}Q}{2\pi}\frac{\mathrm{e}^{-iXP}\mathrm{e}^{-iP^3/3}\mathrm{e}^{iYQ}\mathrm{e}^{iQ^3/3}}{i(P - Q - i\delta)} = \frac{\mathrm{Ai}(X)\mathrm{Ai}'(Y) - \mathrm{Ai}'(X)\mathrm{Ai}(Y)}{X - Y}, \tag{III.A.41}$$

one recovers (III.A.12) of the main text, where the diagonal terms of the Airy kernel[208] can be obtained as

$$\rho(X) = \lim_{Y\to X} K(X,Y) = \left[\mathrm{Ai}'(X)\right]^2 - X\mathrm{Ai}^2(X). \tag{III.A.42}$$

The stationary phase calculation for the approximation of the correlation function in (III.A.33) is very similar to that for the magnetization. Indeed, introducing the new set of variables

$$Q_1 = q_1 - p, \qquad Q_2 = q_2 - p, \qquad P = \frac{q_1 + p}{2}, \tag{III.A.43}$$

and expanding around $Q_1 = 0$ and $Q_2 = 0$, one obtains

$$\mathcal{C}_{m,n}(t) \simeq 4 \int \frac{\mathrm{d}P}{2\pi} \int \frac{\mathrm{d}Q_1}{2\pi} \frac{\mathrm{e}^{-i(m-n_0+1/2+\theta'_P - v_P t)Q_1}}{Q_1} \int \frac{\mathrm{d}Q_2}{2\pi} \frac{\mathrm{e}^{i(n-n_0+1/2+\theta'_P - v_P t)Q_2}}{Q_2}. \tag{III.A.44}$$

Applying (III.A.37) in both the Q_1 and Q_2 integrals, the result can again be written with the help of step functions. Using the property $\Theta(x-x_1)\Theta(x-x_2) = \Theta(x - \max(x_1, x_2))$, and introducing the scaling variable $\mu = (m - n_0 + 1/2)/t$ analogously to ν, one arrives at

$$\mathcal{C}_{m,n}(t) \simeq 1 - 2\int_{-\pi}^{\pi} \frac{\mathrm{d}P}{2\pi} \Theta(v_P - \mu) + 2\int_{-\pi}^{\pi} \frac{\mathrm{d}P}{2\pi} \Theta(v_P - \nu), \tag{III.A.45}$$

where we assumed $\mu < \nu$. Finally, the difference of the step functions can also be rewritten as a product as in (III.A.20).

Subpart III.B

Front dynamics in the XY chain after local excitations (SciPost Phys. 8, 037)

Front dynamics in the XY chain after local excitations

Viktor Eisler, Florian Maislinger

Institut für Theoretische Physik, Technische Universität Graz, Petersgasse 16, A-8010 Graz, Austria

Abstract

We study the time evolution of magnetization and entanglement for initial states with local excitations, created upon the ferromagnetic ground state of the XY chain. For excitations corresponding to a single or two well separated domain walls, the magnetization profile has a simple hydrodynamic limit, which has a standard interpretation in terms of quasiparticles. In contrast, for a spin-flip we obtain an interference term, which has to do with the nonlocality of the excitation in the fermionic basis. Surprisingly, for the single domain wall the hydrodynamic limit of the entropy and magnetization profiles are found to be directly related. Furthermore, the entropy profile is additive for the double domain wall, whereas in case of the spin-flip excitation one has a nontrivial behaviour.

III.B.1 Introduction

The nonequilibrium dynamics of integrable quantum many-body systems has been the focus of intensive research[66]. The interest in these peculiar models, characterized by the existence of a large set of conservation laws, comes from two main perspectives. On one hand, they show relaxation towards generalized stationary ensembles that are not described by conventional statistical mechanics[224]. On the other hand, owing to the presence of stable quasiparticle excitations, integrable models have anomalous transport properties[225]. A recent milestone in understanding the transport driven by an initial inhomogeneity has been the formulation of generalized hydrodynamics (GHD)[219,220], which gives accurate predictions for the profiles of conserved densities in an appropriate spacetime scaling limit.

The simplest paradigm of an inhomogeneous initial state is a domain wall, separating domains of spins with different magnetizations. Letting the system evolve, the domain wall starts to melt, giving rise to an expanding front region characterized by a nonzero spin current. The resulting magnetization profiles were studied in various integrable spin models such as the XX chain[199,203,226], the transverse Ising (TI)[206,227,228], the XY[229] as well as the XXZ chains[219,222,230–233]. Rather generically one finds ballistic transport, with the exception of the isotropic Heisenberg chain where a diffusive behaviour is observed instead[234–239]. The common feature in all of the examples above is that the domain wall is oriented along the z-axis, and thus the magnetization is a local operator in the fermionic representation of the corresponding spin chain. In particular, for models with fermion-number conservation, the transverse magnetization itself corresponds to a locally conserved density, which makes the problem directly amenable to GHD techniques.

Recently, however, domain walls created upon the symmetry-broken ferromagnetic ground states of TI or XY chains have been considered[173,177,178]. The ordering in these chains occurs in the longitudinal component of the magnetization, which is a highly nonlocal string operator in the fermionic picture, being nontrivially related to the local conserved densities. Hence, even though one has a free-fermion model at hand, it is a priori unclear whether a hydrodynamic description still holds for this observable. Nevertheless, in[173,178] it has been shown that, for domain walls excited by a single local fermion operator, the longitudinal magnetization profile has the usual hydrodynamic scaling limit one would naively expect. Namely, the profile is determined by noninteracting quasiparticles carrying the fraction of a spin-flip and traveling at the corresponding group velocity.

In the present work we extend these studies to excitations that can be written as the product of two local fermion operators. In the spin language they describe a double domain wall, and if the distance between them is sufficiently large, we find that the magnetization profile factorizes in the hydrodynamic scaling limit. In other words, the quasiparticle excitations created at the two domain walls are completely independent. In contrast, the situation becomes nontrivial if the fermionic excitations act on neighbouring sites, even though the product of two adjacent domain walls is just a spin-flip and thus perfectly local in the spin-representation. Indeed, it turns out that this composite fermionic excitation leads to interference effects between the quasiparticle modes, encoded in the form factors of the spin operator. This interference term yields a significant contribution to the hydrodynamic profile, which can be found analytically via stationary phase analysis.

We also study in detail the correlation functions and the entanglement entropy for the single domain wall excitation. Interestingly, both of them can be directly related to the magnetization. For the correlations we derive a relation which holds also for finite times if the separation of the spins is much larger than the correlation length. On the other hand, for the entropy we propose an ansatz that is motivated by recent results for single-mode quasiparticle excitations in a free massive quantum field theory (QFT)[240,241]. Our ansatz works perfectly in the hydrodynamic regime, thereby creating an exact relation between the magnetization and entanglement profiles. Furthermore, we observe that the entropy becomes additive for the double domain wall excitation, whereas for the spin-flip one has again a nontrivial behaviour due to the above mentioned interference terms.

The paper is structured as follows. We start by introducing the model in Sec. III.B.2. The magnetization dynamics is studied in Sec. III.B.3 for three different local excitations as well as for a local quench. The correlation functions are investigated in Sec. III.B.4, followed by the study of the entropy profiles in Sec. III.B.5. We discuss our findings in Sec. III.B.6, and the technical details of the calculations are reported in three Appendices.

III.B.2 Model

We consider an XY spin chain of length N described by the Hamiltonian

$$H = -\sum_{n=1}^{N-1} \left(\frac{1+\gamma}{4} \sigma_n^x \sigma_{n+1}^x + \frac{1-\gamma}{4} \sigma_n^y \sigma_{n+1}^y \right) - \frac{h}{2} \sum_{n=1}^{N} \sigma_n^z \, , \tag{III.B.1}$$

where σ_n^α are Pauli matrices located at site n, h and γ denote the transverse magnetic field and the XY anisotropy, respectively. We restrict ourselves to the parameter regime $0 < h < 1$ and $0 < \gamma \leq 1$ where the chain is in a gapped ferromagnetic phase, with $\gamma = 1$ corresponding to the TI chain.

The Hamiltonian (III.B.1) is diagonalized through a standard procedure[217], by first introducing Majorana fermions via a Jordan-Wigner transformation

$$a_{2j-1} = \prod_{k=1}^{j-1} \sigma_k^z \, \sigma_j^x \, , \qquad a_{2j} = \prod_{k=1}^{j-1} \sigma_k^z \, \sigma_j^y \, , \tag{III.B.2}$$

satisfying anticommutation relations $\{a_k, a_l\} = 2\delta_{k,l}$. While (III.B.1) describes an open chain which is most suitable for our numerical calculations, the analytical treatment of the problem requires to consider either periodic ($s = +$) or antiperiodic ($s = -$) boundary conditions, $\sigma_{N+1}^x = s\sigma_1^x$ and $\sigma_{N+1}^y = s\sigma_1^y$. Due to the global spin-flip symmetry of the model, the corresponding Hamiltonians can then be split into two parts

$$H_s = \frac{1-s\mathcal{P}}{2} H_{\mathrm{R}} + \frac{1+s\mathcal{P}}{2} H_{\mathrm{NS}} \, , \qquad \mathcal{P} = \prod_{n=1}^{N} \sigma_n^z \, . \tag{III.B.3}$$

In terms of the Majorana fermions, the corresponding symmetry sectors are described by the Hamiltonians

$$H_{\mathrm{R/NS}} = \frac{i}{2} \sum_{j=1}^{N} \left(\frac{1+\gamma}{2} a_{2j} a_{2j+1} - \frac{1-\gamma}{2} a_{2j-1} a_{2j+2} + h a_{2j-1} a_{2j} \right) , \tag{III.B.4}$$

which differ in the boundary conditions $a_{2N+1} = \pm a_1$ and $a_{2N+2} = \pm a_2$ being periodic for the Ramond (R) and antiperiodic for the Neveu-Schwarz (NS) sectors.

In order to diagonalize (III.B.4), one performs a Fourier transformation followed by a Bogoliubov rotation

$$\begin{aligned} a_{2j-1} &= \frac{1}{\sqrt{N}} \sum_{q\in \mathrm{R/NS}} \mathrm{e}^{-iqj} \mathrm{e}^{i(\theta_q+q)/2} (b_q^\dagger + b_{-q}), \\ a_{2j} &= \frac{-i}{\sqrt{N}} \sum_{q\in \mathrm{R/NS}} \mathrm{e}^{-iqj} \mathrm{e}^{-i(\theta_q+q)/2} (b_q^\dagger - b_{-q}), \end{aligned} \tag{III.B.5}$$

where the Bogoliubov angle and the dispersion are given by

$$\mathrm{e}^{i(\theta_q+q)} = \frac{\cos q - h + i\gamma \sin q}{\epsilon_q}, \qquad \epsilon_q = \sqrt{(\cos q - h)^2 + \gamma^2 \sin^2 q}\,. \tag{III.B.6}$$

Note that the above definition ensures that the function θ_q is continuous within the Brillouin zone $q \in [-\pi, \pi]$. To satisfy the proper boundary conditions, the allowed values of the momenta are $q_k = \frac{2\pi}{N} k$ for R and $q_k = \frac{2\pi}{N}(k + 1/2)$ for NS, respectively, with $k = -N/2, \dots, N/2 - 1$ and N even. The diagonalized Hamiltonian and its K-particle eigenstates are then given by

$$H_{\mathrm{R/NS}} = \sum_{q\in \mathrm{R/NS}} \epsilon_q b_q^\dagger b_q + \mathrm{const}, \qquad |q_1, q_2, \dots, q_K\rangle_{\mathrm{R/NS}} = \prod_{i=1}^{K} b_{q_i}^\dagger |0\rangle_{\mathrm{R/NS}}\,. \tag{III.B.7}$$

It should be stressed that the eigenstates with K even belong to the spin-periodic Hamiltonian H_+, whereas the eigenstates of the spin-antiperiodic H_- have odd K.

In the thermodynamic limit $N \to \infty$, the periodic chain H_+ has a doubly degenerate ground state with ferromagnetic ordering along the x-axis, denoted by $|\Uparrow\rangle$ and $|\Downarrow\rangle$, respectively. Note however, that for finite N the actual ground states in both symmetry sectors are given by

$$|0\rangle_{\mathrm{NS}} = \frac{1}{\sqrt{2}}(|\Uparrow\rangle + |\Downarrow\rangle), \qquad |0\rangle_{\mathrm{R}} = \frac{1}{\sqrt{2}}(|\Uparrow\rangle - |\Downarrow\rangle), \tag{III.B.8}$$

which are separated by an exponentially small gap and both have vanishing magnetizations.

III.B.3 Magnetization dynamics

We are interested in the dynamics of the magnetization of various initial states, excited locally from the ferromagnetic ground state $|\Uparrow\rangle$ and time-evolved under the Hamiltonian H in (III.B.1). The locality of the excitation is understood in terms of the Majorana basis, which implies that these excitations may become highly non-local in the spin-basis representation. In fact, the latter will correspond to domain-wall excitations and one is interested in how the inhomogeneity spreads out under unitary time evolution. On the other hand, since the order-parameter magnetization is not conserved, even a single spin-flip excitation (which is local in terms of the spins) will lead to nontrivial dynamics. For the study of domain-wall melting, we will also consider for comparison a local quench setup where two separate chains are initially prepared in oppositely magnetized ground states, and subsequently joined together.

The time-evolved magnetization can be extracted in a number of different ways. On the numerical side, we apply matrix product state (MPS) calculations[30,107] in an open-chain geometry. To ensure that we obtain the proper ferromagnetic (symmetry-broken) ground state $|\Uparrow\rangle$, we introduced a small longitudinal field $h_x > 0$ in the Hamiltonian $H - h_x \sum_i \sigma_i^x$ for the first few sweeps and set $h_x = 0$ afterwards, until convergence is reached. The excitations are then created by acting with the matrix product operator representation of the corresponding spin-excitation. Finally, the time evolution was implemented with the finite two-site time-dependent variational principle (TDVP) algorithm[31].

On the other hand, we also employed Pfaffian techniques for the numerical evaluation of the magnetization. For the simple domain-wall excitation these were described in Ref.[178], but the calculations can easily be generalized for the other local excitations we deal with. In all of the examples we observed a perfect agreement with the results of MPS calculations.

Finally, we also present analytical results based on form-factor calculations. To this end, one has to first express the excited initial state $|\psi_0\rangle = (|\psi_0\rangle_{\mathrm{R}} + |\psi_0\rangle_{\mathrm{NS}})/\sqrt{2}$ in the fermion basis, which is then time-evolved with the corresponding Hamiltonian in both symmetry sectors as

$$|\psi_t\rangle_{\mathrm{R/NS}} = \mathrm{e}^{-itH_{\mathrm{R/NS}}} |\psi_0\rangle_{\mathrm{R/NS}} \, . \tag{III.B.9}$$

Once $|\psi_0\rangle_{\mathrm{R/NS}}$ is written as a linear combination of the K-particle eigenstates (III.B.7), the time evolution is trivial

$$\mathrm{e}^{-itH_{\mathrm{R/NS}}} |q_1, q_2, \ldots, q_K\rangle_{\mathrm{R/NS}} = \mathrm{e}^{-it\sum_{k=1}^{K} \epsilon_{q_k}} |q_1, q_2, \ldots, q_K\rangle_{\mathrm{R/NS}} \, , \tag{III.B.10}$$

since the Hamiltonian $H_{\mathrm{R/NS}}$ is diagonal in this basis. It is useful to introduce the normalized magnetization which can be evaluated as

$$\mathcal{M}_n(t) = \frac{{}_{\mathrm{R}}\langle\psi_t|\sigma_n^x|\psi_t\rangle_{\mathrm{NS}}}{{}_{\mathrm{R}}\langle 0|\sigma_n^x|0\rangle_{\mathrm{NS}}} \, . \tag{III.B.11}$$

Note that, since the operator σ_n^x changes the parity of the state, the only non-vanishing contribution to the expectation value is between different parity sectors. In turn, the calculation of $\mathcal{M}_n(t)$ boils down to evaluating multiple sums over the momenta with the form factors ${}_{\mathrm{R}}\langle p_1, \ldots, p_L|\sigma_n^x|q_1, \ldots, q_K\rangle_{\mathrm{NS}}$, which are known explicitly from previous studies[194,195,242]. In the following we always consider the thermodynamic limit $N \to \infty$, where the sums over momenta can be turned into integrals and the expressions for the form factors are summarized in Appendix III.B.7.1.

III.B.3.1 Single domain wall

Our first example is a single domain wall, which has already been considered for the TI[178] as well as for the XY chains[173]. For completeness, we revisit here the results obtained previously for the normalized magnetization. The single domain wall is an excitation $|\psi_0\rangle = D_{n_1}|\Uparrow\rangle$ created by the operator

$$D_{n_1} = \prod_{j=1}^{n_1-1} \sigma_j^z \, \sigma_{n_1}^x = a_{2n_1-1} \, . \tag{III.B.12}$$

As remarked before, D_{n_1} is strictly local in terms of the fermions, whereas in the spin representation it creates spin-flips all over the sites $j < n_1$. In the eigenbasis of the Hamiltonian it corresponds to a linear combination of one-particle states

$$|\psi_0\rangle = \frac{1}{\sqrt{N}} \sum_q \mathrm{e}^{-iq(n_1-1/2)} \mathrm{e}^{i\theta_q/2} |q\rangle \, , \tag{III.B.13}$$

where we have suppressed the subscripts R/NS of the symmetry sector for notational simplicity. One thus only needs the form factors between one-particle states, which has a relatively simple form (III.B.51) given in Appendix III.B.7.1. Performing the time evolution (III.B.9) via (III.B.10) and inserting the result into (III.B.11), one arrives at

$$\mathcal{M}_n(t) = \int_{-\pi}^{\pi} \frac{\mathrm{d}p}{2\pi} \int_{-\pi}^{\pi} \frac{\mathrm{d}q}{2\pi} \frac{\epsilon_p + \epsilon_q}{2\sqrt{\epsilon_p \epsilon_q}} \frac{\mathrm{e}^{i(n-n_1+1/2)(q-p)}}{i\sin\left(\frac{q-p}{2}\right)} \mathrm{e}^{i(\theta_q-\theta_p)/2} \mathrm{e}^{-i(\epsilon_q-\epsilon_p)t} \, . \tag{III.B.14}$$

The above expression simplifies considerably in appropriate scaling limits. Indeed, noting that the integral receives the dominant contribution due to a pole at $q = p$ in the integrand of (III.B.14), one can change variables as $Q = q - p$ and $P = (q+p)/2$, and perform a stationary phase analysis as described in Appendix III.B.7.2. In turn, one obtains

$$\mathcal{M}_n(t) = 1 - 2\int_{-\pi}^{\pi} \frac{\mathrm{d}P}{2\pi} \Theta(v_P - \nu) \, , \qquad \nu = \frac{n - n_1 + 1/2}{t} \, , \tag{III.B.15}$$

which is the so-called hydrodynamic scaling limit. Here $\Theta(x)$ is the Heaviside step function, $v_P = \frac{\mathrm{d}\epsilon_P}{\mathrm{d}P}$ is the group velocity of the single-particle excitations and ν is the ray variable, with the distance measured from the initial location $n_1 - 1/2$ of the domain wall. The result (III.B.15) has a simple semiclassical interpretation, which has been applied many times to understand front dynamics in quantum chains[198,200,201,243]. Namely, the magnetization is transported by single-particle excitations, each carrying an elementary spin-flip, which contribute to the hydrodynamic profile at a given ray only if their velocity $v_P > \nu$.

Another interesting scaling regime emerges around the edge of the front $\nu \approx v_{max}$, given by the maximum speed of excitations. In order to understand the fine structure of the edge, a higher order stationary phase analysis has to be performed around the momentum q_* which yields the maximum velocity $v_{q_*} = v_{max}$. As shown in Appendix III.B.7.2, this leads to the following result

$$\mathcal{M}_n(t) \approx 1 - 2\left(\frac{2}{|v''_{q_*}|t}\right)^{1/3} \rho(X) \,, \qquad X = (n - n_1 + 1/2 + \theta'_{q_*}/2 - v_{q_*} t)\left(\frac{2}{|v''_{q_*}|t}\right)^{1/3} . \tag{III.B.16}$$

In other words, with the proper choice of the scaling variable X measuring the distance from the edge, and after appropriate rescaling, the fine structure of the magnetization front is given via the function

$$\rho(X) = \mathcal{K}_{Ai}(X,X) = \left[\mathrm{Ai}'(X)\right]^2 - X\mathrm{Ai}^2(X) \,. \tag{III.B.17}$$

Note that $\rho(X)$ is nothing else but the diagonal part of the Airy-kernel $\mathcal{K}_{Ai}(X,Y)$[208], which appears in a number of front evolution problems related to free-fermion edge universality[202,203,205,206,209,244–246].

The results (III.B.15) and (III.B.16) have already been tested against numerical calculations for various parameters of the XY chain, where the notable feature of a hydrodynamic phase transition at $h_c = 1 - \gamma^2$ was observed[173]. Indeed, this phase transition can be understood by the appearance of a second local maximum in the group velocities v_q for $h < h_c$, which in turn leads to kinks in the bulk of the hydrodynamic magnetization profile[173].

Finally, it should be noted that the analytical result was obtained by following the time evolution of one-particle states building up the domain wall. Strictly speaking, these states are eigenstates of H_- only, i.e. the time evolution has to be performed with antiperiodic boundary conditions on the spin chain. However, since the form factor calculations are carried out directly in the thermodynamic limit, the boundaries actually do not play any role.

III.B.3.2 Double domain wall

We now move on to consider more complicated excitations, that are created by acting with the operator

$$D_{n_1,n_2} = \sigma^x_{n_1-1} \prod_{j=n_1}^{n_2-1} \sigma^z_j \, \sigma^x_{n_2} = -i \, a_{2n_1-2} \, a_{2n_2-1} \,, \tag{III.B.18}$$

where $n_2 > n_1$ is assumed. In terms of fermions this is a two-local operator, i.e. supported on two sites only. In contrast, D_{n_1,n_2} is again nonlocal in the spin representation, and it is easy to see that it describes a double domain wall, located at sites n_1 and n_2, respectively. Using (III.B.5), the excited initial state can be written as

$$|\psi_0\rangle = \frac{1}{N}\sum_q \mathrm{e}^{iq(n_2-n_1)}\mathrm{e}^{-i\theta_q}\,|0\rangle - \frac{1}{N}\sum_{q_1,q_2} \mathrm{e}^{-iq_1(n_1-1/2)}\mathrm{e}^{-iq_2(n_2-1/2)}\mathrm{e}^{-i(\theta_{q_1}-\theta_{q_2})/2}\,|q_1,q_2\rangle \,. \tag{III.B.19}$$

We shall restrict ourselves to the case $n_2 - n_1 \gg 1$, i.e. when the two domain walls are spatially well separated, such that the sum in the first term of (III.B.19) becomes highly oscillatory and can be neglected. The initial state then involves only two-particle excitations and the time evolved state can be written as

$$|\psi_t\rangle = -\frac{1}{N}\sum_{q_1,q_2} \mathrm{e}^{-iq_1(n_1-1/2)}\mathrm{e}^{-iq_2(n_2-1/2)}\mathrm{e}^{-i(\theta_{q_1}-\theta_{q_2})/2}\mathrm{e}^{-i(\epsilon_{q_1}+\epsilon_{q_2})t}\,|q_1,q_2\rangle \,. \tag{III.B.20}$$

The magnetization $\mathcal{M}_n(t)$ can thus be expressed as a quadruple integral via two-particle form factors ${}_{\mathrm{R}}\langle p_1, p_2|\sigma_n^x|q_1, q_2\rangle_{\mathrm{NS}}$, that are reported in (III.B.53) in Appendix III.B.7.1. The result can be simplified, similarly to the single domain wall case, by analyzing the pole-structure of the form factors combined with a stationary phase approximation. The poles appear for momenta satisfying $q_1 = p_1$ and $q_2 = p_2$ or $q_1 = p_2$ and $q_2 = p_1$. For the first pole one obtains two independent stationary phase conditions

$$v_{P_i} t - (-1)^i \theta'_{P_i} - (n - n_i + 1/2) = 0\,, \tag{III.B.21}$$

where $P_i = (q_i + p_i)/2$ for $i = 1, 2$. Note that this pole corresponds to a process where the incoming momenta are matched with the outgoing ones at each domain wall separately. In contrast, at the second pole an incoming momentum of the first domain wall must match with an outgoing momentum of the second domain wall. However, as shown in Appendix III.B.7.2, after the exchange of the outgoing momenta and under the assumption $n_2 - n_1 \gg 1$, the stationary phase condition cannot be satisfied. Thus only the first pole gives a contribution to the integral and leads to the result

$$\mathcal{M}_n(t) = \prod_i \int \frac{\mathrm{d}P_i}{2\pi} \left[1 - 2\,\Theta\left(v_{P_i} - \nu_i\right)\right], \qquad \nu_i = \frac{n - n_i + 1/2}{t}\,. \tag{III.B.22}$$

The hydrodynamic scaling limit of the profile in (III.B.22) has thus a factorized form with again a very simple physical interpretation. The ray variables ν_i now measure the distances from the corresponding initial domain wall locations $n_i - 1/2$, where quasiparticles with velocity v_{P_i} are emitted, each carrying a spin-flip. If, for a given pair of particles, one has $v_{P_1} > \nu_1$ and $v_{P_2} > \nu_2$ then both of the particles have reached site n at time t, hence the spin is flipped twice and one has a positive contribution. If, on the other hand, $v_{P_1} < \nu_1$ and $v_{P_2} > \nu_2$, then only one particle has arrived and the contribution is negative. The profile is then obtained by summing the contributions over all pairs.

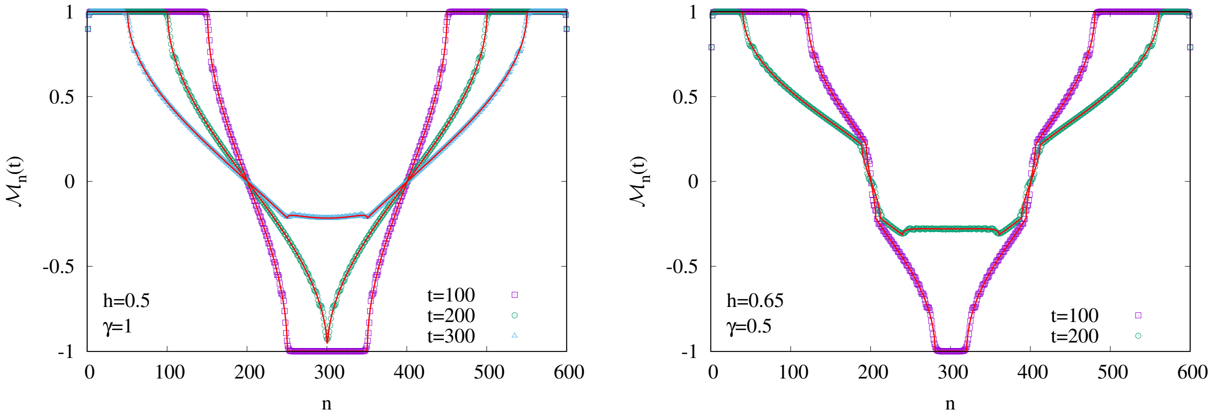

Figure III.B.1. Magnetization profiles after a double domain wall excitation for different times and various h and γ. The solid red lines show the approximation (III.B.22). The parameters are $N = 600$, $n_1 = 201$ and $n_2 = 401$.

In Fig. III.B.1 we show the results of our MPS simulations together with the result (III.B.22). One can see a perfect agreement, even after the two fronts propagating from different locations overlap in the middle. In particular, one observes the emergence of two cusps at the ends of the overlap region, which follows from the factorized form of (III.B.22), i.e. one multiplies two single domain wall front profiles, each having square-root singularities at their edges. Moreover, this also implies that the outer edge of the front is still described by the same scaling (III.B.16) as for the single domain wall. On the right of Fig. III.B.1 there are extra kinks to be seen, which is due to the fact that one has $h < h_c$ there, i.e. one is beyond the hydrodynamical phase transition point.

III.B.3.3 Single spin-flip

After having discussed the evolution of domain walls, we now study a very simple excitation, in the form of a single flipped spin. Naively, one would think that this excitation has a trivial hydrodynamic limit, and the flipped spin just disperses. However, since the magnetization is not conserved under the XY dynamics, it turns out that the profile is far from being trivial. In fact, the operator that creates a spin-flip at site n_1 is just $\sigma^z_{n_1} = -ia_{2n_1-1}a_{2n_1}$, which is strictly local in the spin representation, but is again two-local, i.e. a product of two adjacent Majoranas in the fermionic picture. Hence, this form is more reminiscent of a double domain wall excitation, with the exception that they are now created at neighbouring sites. Rewriting the excitation in the fermionic basis one has

$$|\psi_0\rangle = m^z\,|0\rangle - \frac{1}{N}\sum_{q_1,q_2} \mathrm{e}^{-iq_1(n_1-1/2)}\mathrm{e}^{-iq_2(n_1+1/2)}\mathrm{e}^{i(\theta_{q_1}-\theta_{q_2})/2}\,|q_1,q_2\rangle\ , \tag{III.B.23}$$

where the ground-state contribution is now proportional to the transverse magnetization

$$m^z = \langle 0|\sigma^z_n|0\rangle = -\int_{-\pi}^{\pi}\frac{\mathrm{d}q}{2\pi}\mathrm{e}^{i(\theta_q+q)}\,, \tag{III.B.24}$$

and thus cannot be neglected.

The calculation of $\mathcal{M}_n(t)$ follows the same steps as in the previous cases. Note, in particular, that the two-particle contribution in (III.B.23) has almost the same form as (III.B.19) for the double domain wall with $n_2 = n_1 + 1$, except for the sign of the Bogoliubov phases. After time evolving and taking the expectation value with $|\psi_t\rangle$, one has now cross terms where the form factors ${}_{\mathrm{R}}\langle 0|\sigma^x_n\,|q_1,q_2\rangle_{\mathrm{NS}}$ appear, see (III.B.52). However, since they have no poles, it is easy to see that their contribution is negligible in the scaling limit we are interested in. On the other hand, the two-particle form factors now yield a contribution from both of the poles. Indeed, the stationarity condition is, up to the sign of the θ'_{P_i} term, is the same as (III.B.21) for the double domain wall with $n_2 = n_1 + 1$. However, in the limit of $t \gg 1$ and $|n - n_1| \gg 1$, the two equations are essentially the same. Hence, the process in which an incoming momentum of the first domain wall scatters into an outgoing momentum of the neighbouring one is equally well permitted and yields a sizable contribution.

Carrying out the stationary phase analysis in detail (see Appendix III.B.7.2), one arrives at the following result in the hydrodynamic limit

$$\mathcal{M}_n(t) = (m^z)^2 + \left[1 - 2\int_{-\pi}^{\pi}\frac{\mathrm{d}P}{2\pi}\,\Theta\left(v_P - \tilde{\nu}\right)\right]^2 - \left|m^z + 2\int_{-\pi}^{\pi}\frac{\mathrm{d}P}{2\pi}\mathrm{e}^{iP}\mathrm{e}^{i\theta_P}\Theta\left(v_P - \tilde{\nu}\right)\right|^2\,, \tag{III.B.25}$$

where the ray variable $\tilde{\nu} = \frac{n-n_1}{t}$ is slightly changed compared to (III.B.15), since the distance is now measured from the location n_1 of the spin-flip. The profile can be written as the sum of three terms, where the first one is simply the ground-state contribution. The second one corresponds to the factorized result for the double domain wall and the third one describes a kind of interference term, where the momenta of the excitations building up the two domain walls are exchanged. There is no simple semiclassical interpretation of this interference term, since the quasiparticles contribute with a phase factor. The result (III.B.25) is compared against our numerical calculations in Fig. III.B.2 with an excellent agreement.

It is also interesting to have a look at the edge behaviour of the profile. Performing the higher order stationary phase analysis (see Appendix III.B.7.2), one is led to the following result

$$\mathcal{M}_n(t) \approx 1 - 2\left(\frac{2}{|v''_{q_*}|t}\right)^{1/3}\tilde{\rho}(\tilde{X})\,,\qquad \tilde{X} = (n - n_1 - v_{q_*}t)\left(\frac{2}{|v''_{q_*}|t}\right)^{1/3}\,, \tag{III.B.26}$$

where the scaling function is given by

$$\tilde{\rho}(\tilde{X}) = \left[2 + 2\,m^z\cos\!\left(\theta_{q_*} + q_*\right)\right]\mathcal{K}_{Ai}(\tilde{X},\tilde{X})\,. \tag{III.B.27}$$

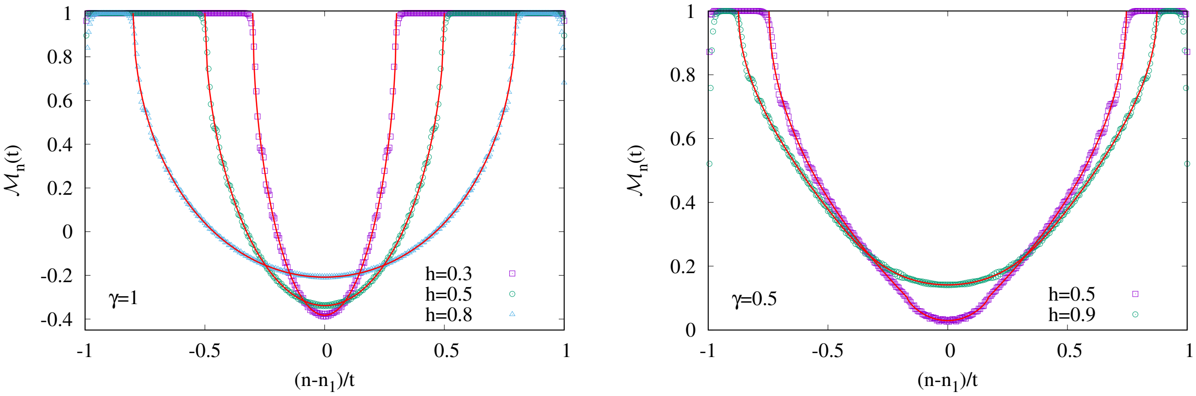

Figure III.B.2. Magnetization profiles after a spin-flip excitation for various h and γ. The red solid lines show the approximation (III.B.25). The parameters are $N = 400$, $n_1 = 200$ and $t = 200$.

The result is thus very similar to the one for the domain wall in (III.B.16), however the scaling function $\tilde{\rho}(\tilde{X})$ acquires a nontrivial prefactor, which depends explicitly on the transverse magnetization m^z, and even on the Bogoliubov phase evaluated at q_* where the quasiparticle velocity has its maximum. In particular, this phase factor vanishes for the TI chain and one has a factor of 2 difference with respect to $\rho(X)$. This explains the numerical findings of Ref.[177] where the very same setup was studied. We checked the validity of the edge scaling (III.B.26) in Fig. III.B.3 for various parameter values and found a very good agreement, there are however some differences in the convergence towards the scaling function $\tilde{\rho}(\tilde{X})$.

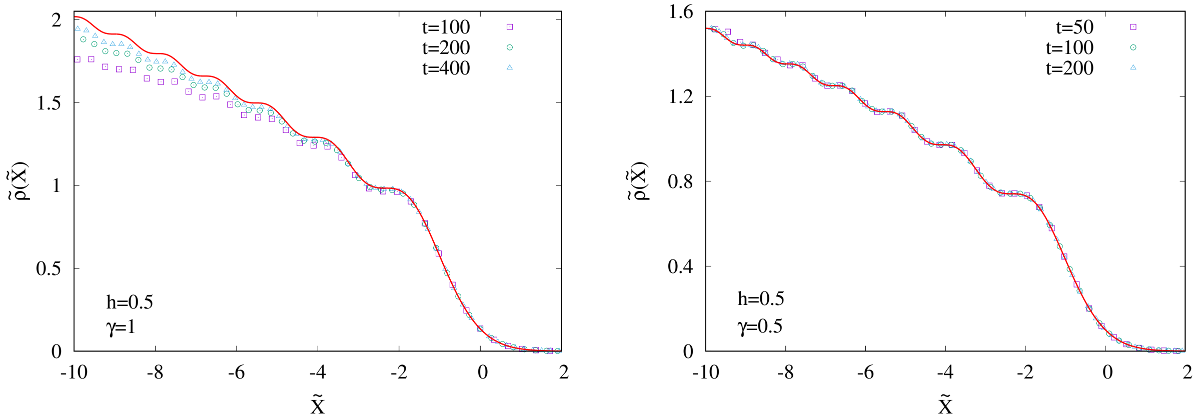

Figure III.B.3. Edge scaling (III.B.26) of the magnetization profiles after a spin-flip excitation for various h and γ. The red solid lines show the scaling function in (III.B.27).

III.B.3.4 Local quench

As a final example, we show here the results for the magnetization profile resulting from a local quench. That is, instead of applying a local excitation to the symmetry-broken ferromagnetic state, we rather prepare the two halves of our chain in oppositely magnetized ground states and join them together. Our goal is to check whether this protocol yields a similar result for the hydrodynamic profile as the one found for the single domain wall excitation.

The initial and time-evolved states are now given by

$$|\psi_0\rangle = |\Downarrow\rangle \otimes |\Uparrow\rangle \,, \qquad |\psi_t\rangle = \mathrm{e}^{-iHt}\,|\psi_0\rangle \,. \tag{III.B.28}$$

Since our initial state is not prepared as an excitation upon the bulk vacuum state, it is a nontrivial question how $|\psi_0\rangle$ can be written in the basis of the full Hamiltonian H. Thus we shall only perform numerical (MPS and Pfaffian based) calculations for the quench. The results, shown in Fig. III.B.4, turn out to be rather surprising. Namely, we find that in the TI limit ($\gamma = 1$) the profiles after the local quench (full symbols) almost exactly coincide with the ones for the domain wall excitation (empty symbols). The only deviations visible at the scale of the figure are around the front edges. In sharp contrast, for $\gamma = 0.5$ one has a huge deviation between the profiles for all the values of h we considered. This signals that in the latter case the factorized initial state is not well approximated by a single-particle excitation in the fermionic basis. We observe that the mismatch between the profiles gradually increases as one moves away from the TI limit. However, we have no clear explanation of this phenomenon which needs further studies.

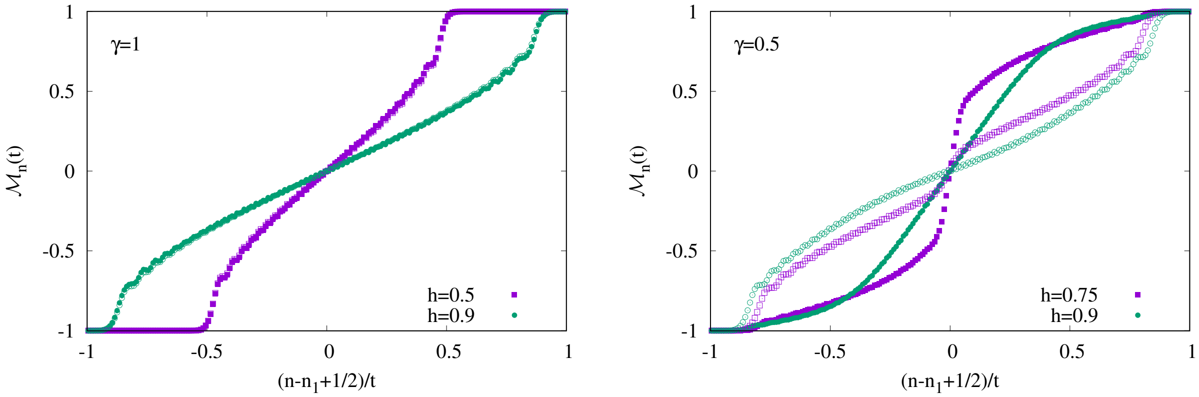

Figure III.B.4. Magnetization profiles after the local quench (full symbols) vs. single domain wall excitation (empty symbols), for various h and γ. The parameters are $N = 400$, $n_1 = 201$ and $t = 100$.

III.B.4 Correlation functions

The form-factor approach is not restricted to the study of the magnetization profile. The next simplest physically interesting observable is the correlation function between the spins. Here we shall restrict ourselves to equal-time correlations between the x-components of the spin, which have already been addressed briefly in[173]. It is useful to work with the normalized correlation functions

$$\mathcal{C}_{m,n}(t) = {}_{\mathrm{NS}}\langle\psi_t|\hat{\mathcal{M}}_m\hat{\mathcal{M}}_n\,|\psi_t\rangle_{\mathrm{NS}} \,, \tag{III.B.29}$$

where the expectation value is now taken between the NS components only, since the operator $\sigma^x_m\sigma^x_n$ does not change the parity. Note that we use here that the corresponding expectation value between the R components is equal to (III.B.29) in the thermodynamic limit.

In order to get a form-factor expansion of (III.B.29), we shall insert the resolution of the identity

$$\mathbb{1} = |0\rangle\,\langle 0| + \sum_p |p\rangle\langle p| + \sum_{p_1,p_2} |p_1,p_2\rangle\langle p_1,p_2| + \sum_{p_1,p_2,p_3} |p_1,p_2,p_3\rangle\langle p_1,p_2,p_3| + \ldots \tag{III.B.30}$$

Note that the resolution must be taken within the R sector, but we omit here the subscripts for notational simplicity. The form-factor expansion can be obtained by inserting the expression of $|\psi_t\rangle_{\mathrm{NS}}$ in terms of the fermionic basis. We focus here on the case of a single domain wall, since the calculations become rather cumbersome for more complicated excitations. In this case $|\psi_t\rangle_{\mathrm{NS}}$ is a superposition of single-particle states only and it is reasonable to assume that, for distances much larger than the correlation length $|n-m| \gg \xi$, the dominant contribution to the correlations comes from the single-particle terms in (III.B.30) as well. To lowest order in the form-factor expansion we thus arrive at the result

$$\begin{aligned} \mathcal{C}_{m,n}(t) \simeq & \int \frac{\mathrm{d}q_1}{2\pi} \int \frac{\mathrm{d}q_2}{2\pi} \mathrm{e}^{-i(\theta_{q_1}-\theta_{q_2})/2} \mathrm{e}^{i(\epsilon_{q_1}-\epsilon_{q_2})t} \\ & \times \int \frac{\mathrm{d}p}{2\pi} \frac{\epsilon_p+\epsilon_{q_1}}{2\sqrt{\epsilon_p \epsilon_{q_1}}} \frac{\epsilon_p+\epsilon_{q_2}}{2\sqrt{\epsilon_p \epsilon_{q_2}}} \frac{\mathrm{e}^{-i(m-n_1+1/2)(q_1-p)}}{\sin \frac{q_1-p}{2}} \frac{\mathrm{e}^{i(n-n_1+1/2)(q_2-p)}}{\sin \frac{q_2-p}{2}} \,. \end{aligned} \tag{III.B.31}$$

The hydrodynamic limit of (III.B.31) can be obtained in a similar fashion as was done for the magnetization profile. Expanding around the poles of the integrand and using the properties of the Θ function (see Appendix III.B.7.3 for details) one obtains

$$\mathcal{C}_{m,n}(t) \simeq 1 - 2 \int_{-\pi}^{\pi} \frac{\mathrm{d}P}{2\pi} \Theta(v_P - \mu)\Theta(\nu - v_P) \,, \tag{III.B.32}$$

where the ray variables

$$\mu = \frac{m-n_1+1/2}{t} \,, \qquad \nu = \frac{n-n_1+1/2}{t} \tag{III.B.33}$$

are measured from the initial domain wall location and the expression has a very simple interpretation. Let us assume $\nu > \mu$ and consider the contribution of a single quasi-particle traveling at speed v_P. Now, for short times $v_P < \mu$ the excitation has not yet reached the first spin and thus the correlations are ferromagnetic. Once $\mu < v_P < \nu$, the first spin has been flipped while the second one is still untouched, hence the correlation is antiferromagnetic. Finally, after the excitation has traveled through, $v_P > \nu$, the second spin is also flipped and the correlation becomes ferromagnetic again.

It turns out that, instead of approximating the integrals in (III.B.31), there is a way to directly relate $\mathcal{C}_{m,n}(t)$ to the profile $\mathcal{M}_n(t)$. Indeed, by turning the integral over p into a contour integral and applying the residue theorem, one obtains the formula (III.B.80) reported in Appendix III.B.7.3, which is an exact relation at the level of one-particle form factors. However it is easy to see that, similarly to the hydrodynamic approximation in (III.B.32), it yields perfect ferromagnetic correlations $\mathcal{C}_{m,n}(t) \simeq 1$ when both spins are outside the front region. Indeed, it can be shown that the many-particle form factors are the ones responsible for the exponentially decaying correlations $\mathcal{C}^0_{m,n}$ in the ground state[194]. One can thus reincorporate these correlations into the approximation as

$$\mathcal{C}_{m,n}(t) \simeq \mathcal{C}^0_{m,n} + \mathcal{M}_m(t) - \mathcal{M}_n(t) \,. \tag{III.B.34}$$

The relation in (III.B.34) is tested against exact numerical calculations for the TI chain in Fig. III.B.5. We have calculated the correlations along the front region while keeping the distance d between the spins fixed. One can see that, for $d = 1$, there is still a slight deviation from (III.B.34) which, however, decreases with increasing d. For $d = 10$ one has already an excellent agreement with no visible deviations. In fact, for $|n-m| \gg \xi$ one has $\mathcal{C}^0_{m,n} \to 1$, and one recovers the one-particle result (III.B.80) which should become exact. Note, however, that calculating the corrections to (III.B.34) would require to evaluate multiple integrals with higher-order offdiagonal form factors and is thus a difficult task. Nevertheless, a closer investigation of the form-factor structure in (III.B.48) confirms, that the dominant pole contribution is suppressed and thus one indeed obtains subleading terms.

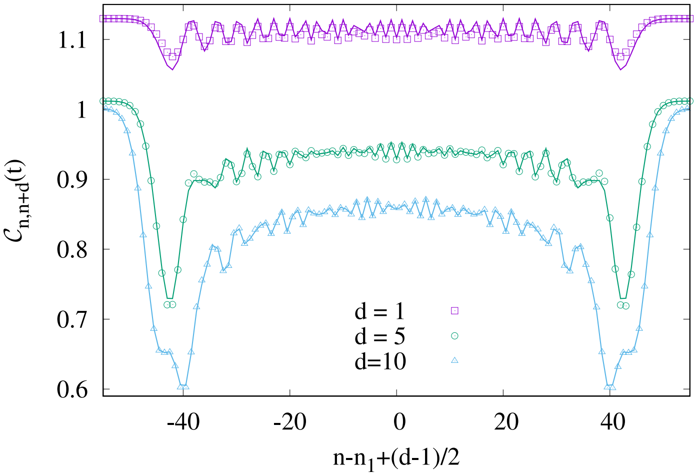

Figure III.B.5. Equal-time correlation functions at $t = 50$ for the TI model at $h = 0.9$, for various distances d between the spins. The solid lines show the approximation in (III.B.34).

III.B.5 Entanglement dynamics

So far we have studied the simplest observables. One can, however, gather important information about the time-evolved state by looking at the entanglement dynamics. In particular, we are interested in the entanglement profiles along the front region, considering a bipartition into two disjoint segments $A = [1, N/2 + r]$ and its complement B, and calculating the resulting von Neumann entropy. Entanglement profiles for domain-wall type initial conditions have been studied extensively for time evolution under critical Hamiltonians[177,230,232,233,238,247–250], and even a description in terms of CFT has been given[204,251]. However, much less is known about the non-critical case, such as the one at hand.

The calculation of the entanglement profile is straightforward in MPS calculations, however, extracting the entropy via covariance-matrix techniques for Gaussian states[210,211] requires some extra considerations. Indeed, the problem lies in the nature of the initial state, since the excitations are created upon the symmetry-broken ground state, which is inherently non-Gaussian[212]. Nevertheless, this difficulty can be overcome by relating the problem to the one where the very same excitations are created upon the Gaussian, non-magnetized ground states in (III.B.8). The method has already been outlined in[173] but we expand here the arguments for completeness.

Let us consider initial states corresponding to the two symmetry-broken ground states of the system. Using (III.B.8), the density matrices are given by

$$|\Uparrow\rangle\langle\Uparrow| = \rho_e + \rho_o\,, \qquad |\Downarrow\rangle\langle\Downarrow| = \rho_e - \rho_o\,, \tag{III.B.35}$$

where the even and odd parity components, satisfying $[\mathcal{P}, \rho_e] = 0$ and $\{\mathcal{P}, \rho_o\} = 0$, respectively, are defined as

$$\rho_e = \frac{1}{2}\big(\,|0\rangle_{\mathrm{NS}\ \mathrm{NS}}\langle 0| + |0\rangle_{\mathrm{R}\ \mathrm{R}}\langle 0|\big)\,, \qquad \rho_o = \frac{1}{2}\big(|0\rangle_{\mathrm{NS}\ \mathrm{R}}\langle 0| + |0\rangle_{\mathrm{R}\ \mathrm{NS}}\langle 0|\big)\,. \tag{III.B.36}$$

Clearly, the problem is with the odd component ρ_o, since a Gaussian density operator is by definition even. One can, however, eliminate ρ_o by considering an equal-weight convex combination of the density matrices in (III.B.35). The resulting density matrix ρ_e is itself still a convex combination of two Gaussian states from the NS and R sectors. However, working in the thermodynamic limit, these two states become indistinguishable[212], and one concludes that ρ_e is equivalent to a proper Gaussian state.

Furthermore, as shown in Ref.[213], excitations that can be written as a product of Majorana fermions

$$D_J = \prod_{j\in J} a_j\,, \tag{III.B.37}$$

where J is an arbitrary index set, preserve Gaussianity. So does unitary time evolution governed by a quadratic Hamiltonian. Hence, introducing the notation

$$\rho_A^{\Uparrow} = \mathrm{Tr}_B \left[\mathrm{e}^{-iHt} D_J \left|\Uparrow\right\rangle \left\langle\Uparrow\right| D_J^{\dagger} \mathrm{e}^{iHt} \right], \qquad \rho_A^{\Downarrow} = \mathrm{Tr}_B \left[\mathrm{e}^{-iHt} D_J \left|\Downarrow\right\rangle \left\langle\Downarrow\right| D_J^{\dagger} \mathrm{e}^{iHt} \right], \tag{III.B.38}$$

for the *reduced* density matrices of a given bipartition, after exciting and time evolving the initial states in (III.B.35), we finally come to the conclusion that

$$\rho_A = \frac{\rho_A^{\Uparrow} + \rho_A^{\Downarrow}}{2} \tag{III.B.39}$$

is a well-defined Gaussian state living on the Hilbert space of segment A.

Our goal is now to relate the entropy $S(\rho_A^{\Uparrow}) = -\mathrm{Tr}\, \rho_A^{\Uparrow} \ln \rho_A^{\Uparrow}$ of our target state to that $S(\rho_A)$ of the Gaussian state in (III.B.39). To this end we use the inequality for convex combinations of density matrices[214,215]

$$S(\sum_i \lambda_i \rho_i) \leq \sum_i \lambda_i S(\rho_i) - \sum_i \lambda_i \ln \lambda_i \, . \tag{III.B.40}$$

First, we note that from trivial symmetry arguments one has $S(\rho_A^{\Downarrow}) = S(\rho_A^{\Uparrow})$. Furthermore, it is also known[215] that the inequality (III.B.40) is saturated if the ranges of ρ_i are pairwise orthogonal, which is again clearly satisfied in our case due to $\langle \Uparrow \mid \Downarrow | \Uparrow \mid \Downarrow \rangle = 0$. Hence one finds

$$S(\rho_A^{\Uparrow}) = S(\rho_A) - \ln 2 \, . \tag{III.B.41}$$

Finally, it remains to calculate the covariance matrix Γ_A corresponding to ρ_A, from which the calculation of the entropy $S(\rho_A)$ follows standard procedure[210,211]. Since ρ_A is the reduced density matrix of the time-evolved and excited ground state $|\psi_t\rangle_{\mathrm{NS}}$, Γ_A is just the reduction of the full covariance matrix with elements $\Gamma_{k,l} = {}_{\mathrm{NS}}\langle\psi_t| \, [a_k, a_l] \, |\psi_t\rangle_{\mathrm{NS}} /2$. This can be obtained by working in the Heisenberg picture. Since D_J is unitary, $D_J D_J^{\dagger} = \mathbb{1}$, the effect of the excitation can be absorbed by a change of the Majorana basis[213]

$$a_k' = D_J^{\dagger} a_k \, D_J = \sum_{l=1}^{2N} Q_{k,l} a_l \, . \tag{III.B.42}$$

The orthogonal transformation Q has a simple diagonal matrix form

$$Q_{kl} = \delta_{k,l} \prod_{j \in J} (2\delta_{k,j} - 1) \, , \tag{III.B.43}$$

with entries ± 1, depending on whether the corresponding column is part of the index set J or not. In complete analogy, the unitary time evolution corresponds to the basis rotation

$$a_k'(t) = \mathrm{e}^{iHt} a_k' \mathrm{e}^{-iHt} = \sum_{l=1}^{2N} R_{k,l} a_l' \, , \tag{III.B.44}$$

where the explicit form of the orthogonal matrix R was reported in Ref.[178]. Putting everything together, one finds that

$$\Gamma = R \, Q \, \Gamma_0 \, Q^T R^T, \tag{III.B.45}$$

where Γ_0 is the ground-state covariance matrix with elements $(\Gamma_0)_{k,l} = {}_{\mathrm{NS}}\langle 0| \, [a_k, a_l] \, |0\rangle_{\mathrm{NS}} /2$.

We are now ready to discuss the entanglement dynamics for the simple excitations introduced in Sec. III.B.3. In each case we have verified that the entropy obtained by the procedure outlined above agrees perfectly with the results of our MPS calculations.

III.B.5.1 Single domain wall

The entropy profiles for the single domain wall, located initially in the center ($r = 0$) of the chain, have already been considered in[173] and are shown in the left of Fig. III.B.6 for $\gamma = 0.5$ and several values of h. The profile $\Delta S(r) = S(\rho_A^{\Uparrow}) - S_0$ is always measured from the initial entropy S_0 of the bulk ferromagnetic state, and is plotted against the rescaled distance $\zeta = r/t$ from the center of the chain. The main feature to be seen is the emergence of a kink in the profile for $h < h_c$, at the value ζ_* that equals the local maximum of the quasiparticle velocity, in complete analogy to the case of the magnetization.

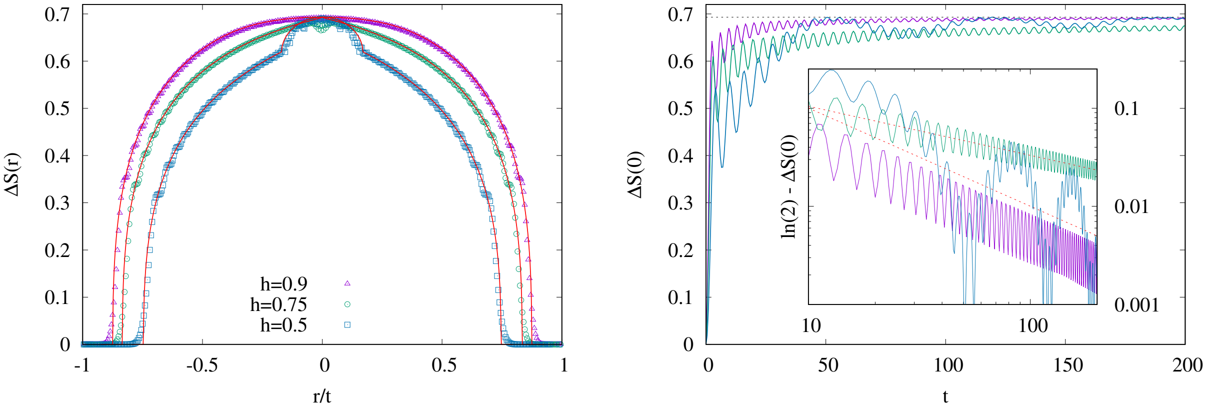

Figure III.B.6. Left: entanglement profiles for the single domain wall, for various h and $\gamma = 0.5$. The parameters are $N = 400$, $n_1 = 201$ and $t = 200$. The solid red lines show the ansatz (III.B.46). Right: half-chain entanglement as a function of time. The horizontal dotted line indicates the value $\ln 2$. The inset shows the deviation from $\ln 2$ on a logarithmic scale. The red dashed lines with slopes $-1/2$ and -1, respectively, are guides to the eye.

Due to the similar features observed in the entropy and magnetization profiles, one is naturally led to the question whether there is a simple relation between the two of them. We are also motivated by recent results of Refs.[240,241], where the entanglement content of particle excitations in $1 + 1$-dimensional massive quantum field theories was studied, with a surprisingly simple result. Namely, it has been found that the entropy difference (relative to the ground state) of a single-mode excitation is independent of the wavenumber and given by the binary entropy formula involving the ratio of the subsystem and full system lengths[240,241]. This ratio is just the density fraction of the single-mode excitation that is contained within the subsystem.

Inspired by these findings, we put forward the following ansatz

$$\Delta S(\zeta) = -\mathcal{N} \ln \mathcal{N} - (1 - \mathcal{N}) \ln (1 - \mathcal{N}) \, , \qquad \mathcal{N}(\zeta) = \int_{-\pi}^{\pi} \frac{\mathrm{d}P}{2\pi} \Theta(v_P - \zeta) \, . \tag{III.B.46}$$

In other words, we assume that the static results of[240,241] would generalize to our dynamical scenario, and the entropy difference for bipartitions along the ray ζ is just given by the same binary formula, with the density ratio $\mathcal{N}(\zeta)$ being the fraction of the quasiparticles that have reached the entangling point. Surprisingly, we find that the simple-minded ansatz (III.B.46), shown by the red solid lines in the left of Fig. III.B.6, gives a very good description of the entropy profiles. Via the density fraction $\mathcal{N}(\zeta)$, the entropy profiles are thus directly related to those of the magnetization (III.B.15).

In case $h < h_c$, one observes some deviations from the ansatz (III.B.46), which are only visible in the regime $\zeta < \zeta_*$ and are assumed to be finite-time effects. In order to better understand the convergence, on the right of Fig. III.B.6 we also studied the time evolution of the half-chain entropy $\Delta S(0)$, for the same parameter values. Although each of them can be seen to converge towards the asymptotic value $\ln 2$, their approach is rather different. For $h > h_c$ the convergence is fast and steady, with rapid oscillations only, whereas for $h < h_c$ there is a smaller frequency appearing with a larger amplitude, and the curve bounces back from its asymptotical value repeatedly. Interestingly, at the critical point $h = h_c = 0.75$ one can see a slowing down in the convergence, which becomes most evident on a logarithmic scale as shown on the inset of the figure. Indeed, the approach seems to be a power law $t^{-1/2}$, as opposed to t^{-1} in the $h \neq h_c$ case. This critical slowing down is responsible for the dip around $\zeta = 0$ in the profile for $h = h_c$ on the left of Fig. III.B.6.

One should stress the marked difference of the entropy profiles as compared to domain-wall evolution in critical systems, such as the XX chain. Indeed, in the latter case the entropy was found to grow logarithmically in time in the entire front region[248,251], whereas here the profiles converge to the scaling function (III.B.46) when plotted against $\zeta = r/t$. In particular, the result $\Delta S(0) = \ln 2$ for $\zeta = 0$ implies that the entropy converges towards the value attained in the ground state $|0\rangle_{\mathrm{NS}}$, which has been studied in[252,253]. Indeed, applying the relation (III.B.41) at $t = 0$, one finds that the entropy S_0 in the initial symmetry-broken ground state is exactly $\ln 2$ less than that of the NS ground state. This strongly suggests that the steady state is nothing but the ground state with its symmetry restored.

III.B.5.2 Double domain wall

The profiles for the double domain wall are shown in Fig. III.B.8 for various times and two different model parameters. In both cases, the profiles resemble those of two separate single domain walls for short times, while for large times the main feature is the emergence of an additional plateau in the overlap region. This strongly suggests the relation

$$\Delta S_{n_1,n_2}(r) = \Delta S_{n_1}(r) + \Delta S_{n_2}(r)\,, \tag{III.B.47}$$

where $\Delta S_{n_1,n_2}(r)$ and $\Delta S_{n_i}(r)$ denote the entropy differences for double and single domain walls, respectively, with the indices referring to the initial locations of the excitations. In other words, one expects the entropy differences to be additive, which is indeed perfectly confirmed by the numerics.

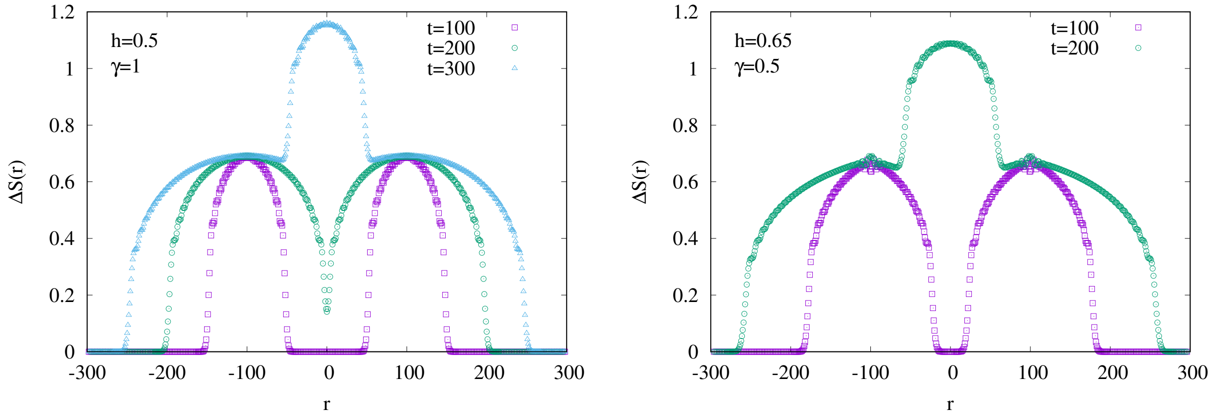

Figure III.B.7. Entanglement profiles after the double domain wall excitation for different h and γ. The parameters are the same as in Fig. III.B.1.

III.B.5.3 Single spin-flip

Finally, we consider the entropy profiles for the spin-flip excitation, with the results shown in Fig. III.B.8, for the same choice of parameters as for the magnetization profiles in Fig. III.B.2. When plotted against the scaling variable ζ, the profiles show a different behaviour as compared to those of the single domain wall excitation in Fig. III.B.6. In particular, the additivity (III.B.47) is not satisfied, analogously to the corresponding result (III.B.25) for the magnetization, which does not have a factorized form. Indeed, as explained under Sec. III.B.3.3, this has to do with an interference effect in the dynamics, where an incoming momentum of the first excitation can travel forward as an outgoing momentum of the second one. Clearly, such a process creates entanglement between the quasiparticles building up the two domain-wall excitations, which spoils the additivity and reduces the overall entropy of the state. Unfortunately, despite the qualitative understanding of the origin of the nontrivial entropy behaviour, we have not been able to find an ansatz analogous to (III.B.46) that captures the profiles quantitatively.

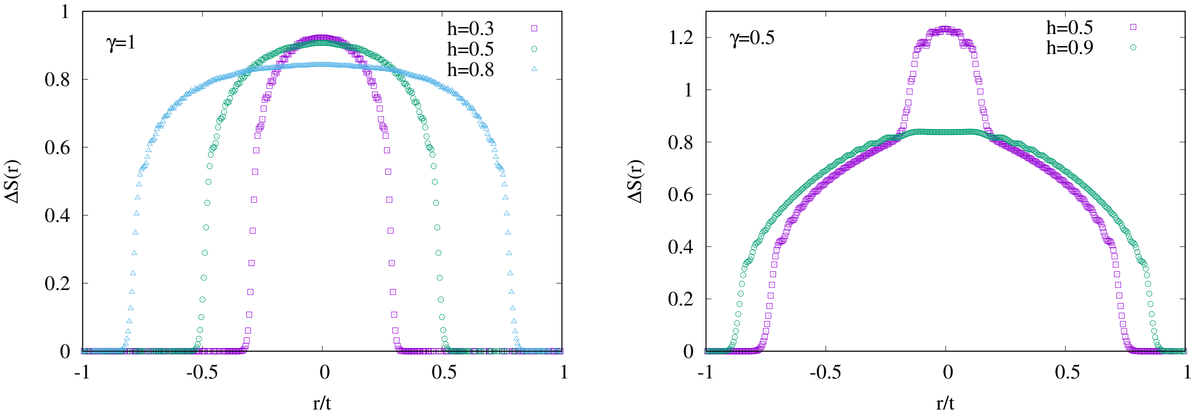

Figure III.B.8. Entanglement profiles after a spin-flip excitation. The parameters are the same as in Fig. III.B.2.

III.B.6 Discussion

We studied the time evolution of the magnetization and entanglement profiles in the XY chain for simple initial states that can be written as a product of one or two local fermionic excitations. The former corresponds to a single domain wall in the spin-picture and the magnetization profile has a simple hydrodynamic limit (III.B.15), corresponding to the motion of independent quasiparticles. Furthermore, in the very same limit we find that the entropy is given by the simple ansatz (III.B.46) and is thus directly related to the magnetization profile. The correlation function is also found to be related via (III.B.29) to the magnetization, which gives a very good approximation even for finite times and distances.

For double domain walls, excited by the product of two fermions separated by a large distance, we simply find the factorized form (III.B.22) for the magnetization, as well as the additivity (III.B.47) of the entropy differences. For a single spin-flip, however, the fermions are located on neighbouring sites and the excitation cannot be considered strictly local any more. As a consequence, we find an interference term in the magnetization profile (III.B.25). Furthermore, the additivity of the entropy is lost, and we find convergence towards a nontrivial profile

We have also compared the profiles for the single domain wall to the ones obtained via a local cut and glue quench, where the two ferromagnetic ground states are prepared on half-chains and joined together. Rather surprisingly we found that, while for the TI chain the respective profiles almost coincide, for the generic XY case they become completely different (see Fig. III.B.4), with the discrepancy growing with the distance from the TI limit. Apparently the local quench is well approximated by a single fermionic excitation for the TI but not any more for the XY case. The precise origin of this phenomenon is unclear to us and requires further studies.

It would be also interesting to see if a QFT treatment of the entropy increase could be given. Even though our ansatz (III.B.46) was inspired by QFT results[240,241] on the entanglement content of particle excitations, those particles are single wave modes and there is no dynamics involved. On the other hand, for the case of critical Hamiltonians there exists a CFT framework for calculating the time evolution of entropy after spatially local excitations[223]. Whether this approach could be generalized to a massive QFT to predict the asymptotic entropy increase after the excitations considered in this paper is a puzzling question to be addressed.

One could also think about extending the studies to excitations composed of a product of more than two fermions. While being a straightforward generalization, the form-factor calculations are likely to be very cumbersome, due to the increasing number of the pole contributions one has to account for. Finally, it is natural to ask how the setup could be extended to interacting integrable systems, and if the treatment of such composite but still essentially local excitations could be incorporated into the theory of GHD.

Acknowledgements

We thank H. G. Evertz for discussions and collaboration on a related previous project.

Funding information The authors acknowledge funding from the Austrian Science Fund (FWF) through Project No. P30616-N36, and through SFB ViCoM F41 (Project P04).

III.B.7 Appendix

III.B.7.1 Form factors for the TI and XY chains

Here we present the form factors used in the calculations of the main text. Although for our simple excitations we required only few-particle form factors, the general expression is reported for completeness. The formula is rather involved even after taking the thermodynamic limit $N \to \infty$, and for the TI chain ($\gamma = 1$) it reads[242]

$$\frac{{}_{\mathrm{R}}\langle p_1, \dots, p_L | \sigma_n^x | q_1, \dots, q_K \rangle_{\mathrm{NS}}}{{}_{\mathrm{R}}\langle 0 | \sigma_n^x | 0 \rangle_{\mathrm{NS}}} = i^{-(K+L)/2} \, (-1)^{L(L-1)/2} \, h^{(K-L)^2/4} \, \mathrm{e}^{in(\sum_{k=1}^{K} q_k - \sum_{l=1}^{L} p_l)}$$
$$\times \prod_{k=1}^{K} \frac{1}{\sqrt{N \epsilon_{q_k}}} \prod_{l=1}^{L} \frac{1}{\sqrt{N \epsilon_{p_l}}} \prod_{k<k'=1}^{K} \frac{\sin \frac{q_k - q_{k'}}{2}}{\frac{\epsilon_{q_k} + \epsilon_{q_{k'}}}{2}} \prod_{l<l'=1}^{L} \frac{\sin \frac{p_l - p_{l'}}{2}}{\frac{\epsilon_{p_l} + \epsilon_{p_{l'}}}{2}} \prod_{k=1}^{K} \prod_{l=1}^{L} \frac{\frac{\epsilon_{q_k} + \epsilon_{p_l}}{2}}{\sin \frac{q_k - p_l}{2}} \, . \tag{III.B.48}$$

We have assumed here that the number of momenta K and L on the right and left hand side have the same parity, otherwise the form factor vanishes. Note that we have normalized with the vacuum form factor, i.e. with the expectation value of the ground-state magnetization. For $K = L$ the form factors (III.B.48) depend only on the dispersion relation ϵ_q, given in Eq. (III.B.6), and the values of the momenta.

For the generic case of the XY chain, the expressions become even more complicated. In the limit $N \to \infty$ they can be written as[194,195]

$$\frac{{}_{\mathrm{R}}\langle p_1, \dots, p_L | \sigma_n^x | q_1, \dots, q_K \rangle_{\mathrm{NS}}}{{}_{\mathrm{R}}\langle 0 | \sigma_n^x | 0 \rangle_{\mathrm{NS}}} = i^{-(K+L)/2} \, (-1)^{L(L-1)/2} \, g^{(K-L)^2/4} \, \mathrm{e}^{in(\sum_{k=1}^{K} q_k - \sum_{l=1}^{L} p_l)}$$
$$\times \cosh \frac{\sum_{k=1}^{K} \Delta_{q_k} - \sum_{l=1}^{L} \Delta_{p_l}}{2} \prod_{k=1}^{K} \frac{1}{\sqrt{N \sinh \Delta_{q_k}}} \prod_{l=1}^{L} \frac{1}{\sqrt{N \sinh \Delta_{p_l}}}$$
$$\times \prod_{k<k'=1}^{K} \frac{\sin \frac{q_k - q_{k'}}{2}}{\sinh \frac{\Delta_{q_k} + \Delta_{q_{k'}}}{2}} \prod_{l<l'=1}^{L} \frac{\sin \frac{p_l - p_{l'}}{2}}{\sinh \frac{\Delta_{p_l} + \Delta_{p_{l'}}}{2}} \prod_{k=1}^{K} \prod_{l=1}^{L} \frac{\sinh \frac{\Delta_{q_k} + \Delta_{p_l}}{2}}{\sin \frac{q_k - p_l}{2}} \, , \tag{III.B.49}$$

where we have defined

$$\sinh \Delta_q = \frac{\sqrt{1 - \gamma^2}}{\gamma \sqrt{\gamma^2 + h^2 - 1}} \epsilon_q \, , \qquad g = \frac{1 - \gamma^2}{\gamma \sqrt{\gamma^2 + h^2 - 1}} \, . \tag{III.B.50}$$

The above definition is valid in the parameter regime $\sqrt{1 - \gamma^2} < h < 1$, i.e. in the non-oscillatory ferromagnetic phase. In the oscillatory phase $0 < h < \sqrt{1 - \gamma^2}$ the corresponding expressions can be obtained by analytic continuation[194]. One can also check that, in the singular TI limit $\gamma \to 1$, the expression (III.B.49) goes over to the one in (III.B.48). While in general they differ in the details, these will turn out to be irrelevant for the hydrodynamic limit, since their pole structure is exactly the same.

We now discuss the form factors needed in the main text. The simplest is the one-particle form factor ($K = L = 1$), where using some hyperbolic identities in (III.B.49), one can show that the TI and XY cases yield the same expression

$$\frac{{}_{\mathrm{R}}\langle p|\sigma^x_n|q\rangle_{\mathrm{NS}}}{{}_{\mathrm{R}}\langle 0|\sigma^x_n|0\rangle_{\mathrm{NS}}} = -\frac{i}{N}\frac{\epsilon_p+\epsilon_q}{2\sqrt{\epsilon_p\epsilon_q}}\frac{\mathrm{e}^{in(q-p)}}{\sin\frac{q-p}{2}}\,. \tag{III.B.51}$$

Thus the formula (III.B.14) for the single domain wall excitation is valid for arbitrary parameter values of the XY chain. In general, no such simplification occurs and in the following we restrict ourselves to the TI case for the sake of simplicity. For the spin-flip excitation one needs the off-diagonal form factor with $K = 2$ and $L = 0$ which reads

$$\frac{{}_{\mathrm{R}}\langle 0|\sigma^x_n|q_1,q_2\rangle_{\mathrm{NS}}}{{}_{\mathrm{R}}\langle 0|\sigma^x_n|0\rangle_{\mathrm{NS}}} = -\frac{i}{N}\frac{h}{\sqrt{\epsilon_{q_1}\epsilon_{q_2}}}\mathrm{e}^{in(q_1+q_2)}\frac{2\sin\frac{q_1-q_2}{2}}{\epsilon_{q_1}+\epsilon_{q_2}}\,. \tag{III.B.52}$$

One can see immediately, that this form factor does not have any poles which implies that it will only give a subleading contribution. The diagonal two-particle form factor ($K = L = 2$), on the other hand, has the form

$$\begin{aligned}\frac{{}_{\mathrm{R}}\langle p_1,p_2|\sigma^x_n|q_1,q_2\rangle_{\mathrm{NS}}}{{}_{\mathrm{R}}\langle 0|\sigma^x_n|0\rangle_{\mathrm{NS}}} &= \frac{1}{N^2}\frac{\mathrm{e}^{in(q_1+q_2-p_1-p_2)}}{\sqrt{\epsilon_{p_1}\epsilon_{p_2}\epsilon_{q_1}\epsilon_{q_2}}}\frac{2\sin\frac{p_1-p_2}{2}}{\epsilon_{p_1}+\epsilon_{p_2}}\frac{2\sin\frac{q_1-q_2}{2}}{\epsilon_{q_1}+\epsilon_{q_2}}\\ &\times\frac{\epsilon_{q_1}+\epsilon_{p_1}}{2\sin\frac{q_1-p_1}{2}}\frac{\epsilon_{q_1}+\epsilon_{p_2}}{2\sin\frac{q_1-p_2}{2}}\frac{\epsilon_{q_2}+\epsilon_{p_1}}{2\sin\frac{q_2-p_1}{2}}\frac{\epsilon_{q_2}+\epsilon_{p_2}}{2\sin\frac{q_2-p_2}{2}}\,,\end{aligned} \tag{III.B.53}$$

with two possible poles for $q_1 = p_1$ and $q_2 = p_2$, or with an exchange of momenta for $q_1 = p_2$ and $q_2 = p_1$. It should be noted that, for the generic diagonal K-particle form factors in (III.B.48), an arbitrary permutation between the incoming and outgoing momenta yields a pole, which makes the analysis of the contributions increasingly complicated.

III.B.7.2 Stationary phase calculations for the profile

In this appendix we summarize the calculations leading to the approximations of the magnetization profile in the hydrodynamic regime. The simplest case is the single domain wall, where $\mathcal{M}_n(t)$ is given by a double integral (III.B.14). The integrand has a pole due to the form factor, which can be regularized as

$$\mathcal{M}_n(t) = 1 + \int_{-\pi}^{\pi}\frac{\mathrm{d}p}{2\pi}\int_{-\pi}^{\pi}\frac{\mathrm{d}q}{2\pi}\frac{\epsilon_p+\epsilon_q}{2\sqrt{\epsilon_p\epsilon_q}}\frac{\mathrm{e}^{i(n-n_1+1/2)(q-p)}}{i\sin\left(\frac{q-p+i\varepsilon}{2}\right)}\mathrm{e}^{i(\theta_q-\theta_p)/2}\mathrm{e}^{-i(\epsilon_q-\epsilon_p)t}\,, \tag{III.B.54}$$

by introducing the infinitesimal shift $\varepsilon > 0$. The integrand of (III.B.54) is highly oscillatory for $|n - n_1| \gg 1$ and $t \gg 1$, and the location of the pole at $q = p$ suggests the change of variables $Q = q-p$ and $P = (q+p)/2$. The phase factors become stationary at $Q = 0$, thus the integrand should be expanded around this value. Keeping only the most singular term one has

$$1 + 2\int_{-\pi}^{\pi}\frac{\mathrm{d}P}{2\pi}\int_{-\infty}^{\infty}\frac{\mathrm{d}Q}{2\pi i}\frac{\mathrm{e}^{i(n-n_1+1/2+\theta'_P-v_Pt)Q}}{Q+i\varepsilon}\,, \tag{III.B.55}$$

where we have extended the integration in the relative momentum up to infinity. Thanks to the definition (III.B.6), the function θ'_P varies smoothly and one can neglect it in the hydrodynamic regime. Then using the integral representation of the Heaviside theta function

$$\Theta(x) = -\lim_{\varepsilon\to 0}\int_{-\infty}^{\infty}\frac{\mathrm{d}Q}{2\pi i}\frac{\mathrm{e}^{-iQx}}{Q+i\varepsilon}\,, \tag{III.B.56}$$

and introducing the ray variable $\nu = (n - n_1 + 1/2)/t$ brings us to the result (III.B.15) in the main text.

The bulk hydrodynamic profile is thus recovered by solving the equation $v_q = \nu$. Special attention is needed around the maximum $v_{q_*} = v_{max}$ of the velocities, where the solutions coalesce at momentum q_*. To get the fine structure of the front edge, one has to expand the dispersion around q_* as

$$\epsilon_q \approx \epsilon_{q_*} + v_{q_*}(q-q_*) + \frac{\epsilon'''_{q_*}}{6}(q-q_*)^3 . \tag{III.B.57}$$

Furthermore, one can introduce the following rescaled variables

$$\begin{gathered} X = \left(\frac{-2}{\epsilon'''_{q_*} t}\right)^{1/3} (n - n_1 + 1/2 + \theta'_{q_*}/2 - v_{q_*} t), \\ Q = \left(\frac{-2}{\epsilon'''_{q_*} t}\right)^{-1/3} (q-q_*), \quad P = \left(\frac{-2}{\epsilon'''_{q_*} t}\right)^{-1/3} (p-q_*). \end{gathered} \tag{III.B.58}$$

Substituting (III.B.57) and (III.B.58) into (III.B.54), one arrives at the following integral

$$1 + 2\left(\frac{-2}{\epsilon'''_{q_*} t}\right)^{1/3} \int \frac{\mathrm{d}P}{2\pi} \int \frac{\mathrm{d}Q}{2\pi} \frac{\mathrm{e}^{iX(Q-P)}\mathrm{e}^{i(Q^3-P^3)/3}}{i(Q-P+i\varepsilon)} . \tag{III.B.59}$$

Using the integral representation of the Airy kernel[208]

$$\mathcal{K}_{Ai}(X,Y) = \lim_{\varepsilon\to 0} \int \frac{\mathrm{d}P}{2\pi} \int \frac{\mathrm{d}Q}{2\pi} \frac{\mathrm{e}^{-iXP}\mathrm{e}^{-iP^3/3}\mathrm{e}^{iYQ}\mathrm{e}^{iQ^3/3}}{i(P-Q-i\varepsilon)} = \frac{\mathrm{Ai}(X)\mathrm{Ai}'(Y) - \mathrm{Ai}'(X)\mathrm{Ai}(Y)}{X-Y}, \tag{III.B.60}$$

one recovers (III.B.16) of the main text, with $\rho(X) = \lim_{Y\to X} \mathcal{K}_{Ai}(X,Y)$ given by the diagonal terms of the Airy kernel.

The hydrodynamic limit (III.B.22) for the double domain wall can be obtained in a similar fashion, however, one has now a quadruple integral to start with. The poles are contained in the two-particle form factor (III.B.53). First, we consider the pole with $q_1 = p_1$ and $q_2 = p_2$. Changing variables as

$$Q_i = q_i - p_i, \qquad P_i = \frac{q_i + p_i}{2}, \tag{III.B.61}$$

and expanding the phases around the stationary points $Q_i = 0$, one has

$$\mathcal{I}_1 = 4 \int \frac{\mathrm{d}P_1}{2\pi} \int \frac{\mathrm{d}P_2}{2\pi} f(P_1,P_2,Q_1,Q_2) \int \frac{\mathrm{d}Q_1}{2\pi} \frac{\mathrm{e}^{-ix_1Q_1}}{Q_1} \int \frac{\mathrm{d}Q_2}{2\pi} \frac{\mathrm{e}^{-ix_2Q_2}}{Q_2} , \tag{III.B.62}$$

where we defined

$$x_i = v_{P_i} t - (-1)^i \theta'_{P_i} - (n - n_i + 1/2) . \tag{III.B.63}$$

The function f in (III.B.62) describes the slowly varying part of the form factor in (III.B.53). It is easy to see, that the terms containing the dispersion ϵ_{q_i} and ϵ_{p_i} can be approximated by 1 to leading order. It remains to analyze the contribution of the trigonometric factors that do not contain the poles, which can be rewritten as

$$f(P_1,P_2,Q_1,Q_2) \approx -\frac{\cos\left(\frac{Q_1-Q_2}{2}\right) - \cos(P_1-P_2)}{\cos\left(\frac{Q_1+Q_2}{2}\right) - \cos(P_1-P_2)} . \tag{III.B.64}$$

Thus, again to leading order around $Q_i = 0$, one has $f(P_1,P_2,Q_1,Q_2) \approx -1 + \mathcal{O}(Q_1Q_2)$, meaning that the first correction would already remove the singularity in the integral (III.B.62), and can be neglected. Setting $f = -1$, one recovers immediately the factorized result (III.B.22).

The second pole of the form factor (III.B.53) is given by $q_1 = p_2$ and $q_2 = p_1$ and corresponds to an exchange of the outgoing momenta. The form factor itself transforms trivially under this exchange, acquiring only a sign. The time-evolved state (III.B.20), however, has phase factors attached to the locations of the domain walls and thus transforms nontrivially under exchange of the momenta. Indeed, introducing the variables

$$Q_1' = q_1 - p_2, \qquad Q_2' = q_2 - p_1, \qquad P_1' = \frac{q_1 + p_2}{2}, \qquad P_2' = \frac{q_2 + p_1}{2}, \tag{III.B.65}$$

this phase factor can now be rewritten as

$$\mathrm{e}^{-i(Q_1'+Q_2')(n_1+n_2)/2}\,\mathrm{e}^{i(P_1'-P_2')(n_2-n_1)}. \tag{III.B.66}$$

The second term contains the center of mass momenta and becomes highly oscillatory for $|n_2 - n_1| \gg 1$. This phase, however, cannot be made stationary, since the time-dependent part of the phase in (III.B.20) is symmetric under the exchange of the momenta. One thus concludes that, for large separations of the domain walls, the second pole gives a negligible contribution.

The situation for the spin-flip excitation is different. As discussed in the main text, except for a sign change of the Bogoliubov angles, the state (III.B.23) is a double domain wall with $n_2 = n_1 + 1$. The first pole thus yields the very same factorized result as in (III.B.62), with the corresponding changes in x_i. In the hydrodynamic limit, however, it is more natural to measure distances from the spin-flip location n_1 (instead of $n_1 \pm 1/2$) and use the ray variable $\tilde{\nu} = \frac{n-n_1}{t}$, which gives the second term in (III.B.25). The second pole, however, has also a significant contribution, since $n_2 - n_1 = 1$ and the phase factor in (III.B.66) now varies slowly. Expanding around $Q_i' = 0$, one finds

$$\mathcal{I}_2 = 4\int \frac{\mathrm{d}P_1'}{2\pi} \int \frac{\mathrm{d}P_2'}{2\pi} \mathrm{e}^{iP_1'}\mathrm{e}^{i\theta_{P_1'}}\mathrm{e}^{-iP_2'}\mathrm{e}^{-i\theta_{P_2'}} \int \frac{\mathrm{d}Q_1'}{2\pi} \frac{\mathrm{e}^{-ix_1'Q_1'}}{Q_1'} \int \frac{\mathrm{d}Q_2'}{2\pi} \frac{\mathrm{e}^{-ix_2'Q_2'}}{Q_2'}\,, \tag{III.B.67}$$

where $x_i' = v_{P_i'}t - (n - n_1)$ and the sign change in the form factor has been taken into account. It is easy to see that

$$\mathcal{I}_2 = -\left| 2\int \frac{\mathrm{d}P'}{2\pi}\mathrm{e}^{iP'}\mathrm{e}^{i\theta_{P'}} \int \frac{\mathrm{d}Q'}{2\pi i}\frac{\mathrm{e}^{-ix'Q'}}{Q'} \right|^2 . \tag{III.B.68}$$

Regularizing the pole via the identity $Q'^{-1} = i\pi\delta(Q') + \lim_{\varepsilon\to 0}(Q' + i\varepsilon)^{-1}$, using (III.B.56) and the expression of the transverse magnetization in (III.B.24), the third term of (III.B.25) follows.

It remains to investigate the edge scaling regime for the spin-flip excitation. The second term of (III.B.25) is simply the square of the profile for a single domain wall, where the edge scaling is given by (III.B.16). To leading order, this just yields a factor 2. The situation is similar for the third term in (III.B.25) where, additionally, the phase factors in the integral must be evaluated at the momentum q_* where the velocity has its maximum, $v_{q_*} = v_{max}$. Collecting the terms, one obtains the prefactor in (III.B.27).

Finally it should be noted that, although the calculation above has been carried out using the form factors for the TI chain, the result generalizes to the XY case. Indeed, the pole structure of the form factors is exactly the same, whereas the differences in the slowly varying part are irrelevant in the hydrodynamic limit, since they have the same trivial limit after expanding around the pole.

III.B.7.3 Calculation of correlation functions

At one-particle level of the form-factor expansion, the normalized correlation function is given by the triple integral

$$\begin{aligned} \mathcal{C}_{m,n}(t) \simeq & \int \frac{\mathrm{d}q_1}{2\pi} \int \frac{\mathrm{d}q_2}{2\pi} \mathrm{e}^{-i(\theta_{q_1}-\theta_{q_2})/2}\mathrm{e}^{i(\epsilon_{q_1}-\epsilon_{q_2})t} \\ & \times \int \frac{\mathrm{d}p}{2\pi} \frac{\epsilon_p + \epsilon_{q_1}}{2\sqrt{\epsilon_p\epsilon_{q_1}}} \frac{\epsilon_p + \epsilon_{q_2}}{2\sqrt{\epsilon_p\epsilon_{q_2}}} \frac{\mathrm{e}^{-i(m-n_1+1/2)(q_1-p)}}{\sin\frac{q_1-p}{2}} \frac{\mathrm{e}^{i(n-n_1+1/2)(q_2-p)}}{\sin\frac{q_2-p}{2}}\,. \end{aligned} \tag{III.B.69}$$

The stationary phase approximation of this integral is very similar to that of the magnetization profile. Introducing the new set of variables

$$Q_1 = q_1 - p, \qquad Q_2 = q_2 - p, \qquad P = \frac{q_1 + p}{2}, \tag{III.B.70}$$

and expanding around the poles $Q_1 = 0$ and $Q_2 = 0$, one obtains

$$\mathcal{C}_{m,n}(t) \simeq 4 \int \frac{\mathrm{d}P}{2\pi} \int \frac{\mathrm{d}Q_1}{2\pi} \frac{\mathrm{e}^{-i(m-n_1+1/2+\theta'_P - v_P t)Q_1}}{Q_1} \int \frac{\mathrm{d}Q_2}{2\pi} \frac{\mathrm{e}^{i(n-n_1+1/2+\theta'_P - v_P t)Q_2}}{Q_2}. \tag{III.B.71}$$

Applying (III.B.56) in both the Q_1 and Q_2 integrals, the result can again be written with the help of step functions

$$\mathcal{C}_{m,n}(t) \simeq 1 - 2 \int_{-\pi}^{\pi} \frac{\mathrm{d}P}{2\pi} \left[\Theta(v_P - \mu) + \Theta(v_P - \nu) - 2\Theta(v_P - \mu)\Theta(v_P - \nu)\right], \tag{III.B.72}$$

where the scaling variable $\mu = (m - n_1 + 1/2)/t$ is introduced analogously to ν. Assuming $\mu < \nu$ and using the identities for the step function

$$\Theta(v_P - \nu) = 1 - \Theta(\nu - v_P)\,, \qquad \Theta(v_P - \mu) - \Theta(v_P - \nu) = \Theta(v_P - \mu)\Theta(\nu - v_P)\,, \tag{III.B.73}$$

the result (III.B.32) of the main text follows immediately.

Instead of applying the stationary phase argument, one can also do a more precise analysis. Indeed, it turns out that the integral over p in (III.B.69) can be carried out explicitly. We first regularize the factor containing the pole as

$$\frac{1}{\sin\left(\frac{q_1-p}{2}\right)\sin\left(\frac{q_2-p}{2}\right)} = \left[2\pi\delta(p-q_1) + \frac{1}{i\sin\left(\frac{q_1-p+i\varepsilon}{2}\right)}\right]\left[2\pi\delta(p-q_2) + \frac{1}{i\sin\left(\frac{p-q_2+i\varepsilon}{2}\right)}\right]. \tag{III.B.74}$$

Multiplying out this expression, the terms containing the delta functions can be plugged back into (III.B.69) and integrated over. Comparing to (III.B.54), one can identify the resulting double integrals as $\mathcal{M}_m(t) - 1$ and $\mathcal{M}_n(t) - 1$, respectively, while the product of the delta functions trivially yields one. The remaining factor from (III.B.74) can be rewritten as

$$\frac{1}{\sin\left(\frac{q_1-p+i\varepsilon}{2}\right)\sin\left(\frac{p-q_2+i\varepsilon}{2}\right)} = \frac{2}{\cos\left(\frac{q_1+q_2}{2} - p\right) - \cos\left(\frac{q_1-q_2}{2} + i\varepsilon\right)}\,. \tag{III.B.75}$$

Introducing new variables

$$z = \mathrm{e}^{i[p-(q_1+q_2)/2]}\,, \qquad z_0 = \mathrm{e}^{i[(q_1-q_2)/2+i\varepsilon]}\,, \tag{III.B.76}$$

the integral over p is transformed into the contour integral

$$\mathcal{I} = \oint \frac{\mathrm{d}z}{2\pi i z} f(z) \frac{4}{z + z^{-1} - (z_0 + z_0^{-1})}, \tag{III.B.77}$$

where $f(z)$ is the slowly varying regular part of the integrand in (III.B.69), and the contour is the unit circle. Now the two poles are located at $z = z_0$ and $z = z_0^{-1}$. However, for $\varepsilon > 0$, only $z = z_0$ lies inside the contour and contributes to the integral. We have thus to obtain the residue around this pole. Rewriting

$$\frac{4}{z^2 + 1 - z(z_0 + z_0^{-1})} = \frac{4}{z_0 - z_0^{-1}} \left(\frac{1}{z - z_0} - \frac{1}{z - z_0^{-1}}\right), \tag{III.B.78}$$

and the two poles correspond to $p = q_1$ and $p = q_2$, respectively. Hence the result of the contour integral is

$$\mathcal{I} = \frac{2f(q_1)}{i\sin\left(\frac{q_1-q_2}{2} + i\varepsilon\right)}\,. \tag{III.B.79}$$

Finally, noting that $\mathcal{I}$ enters with a minus sign (see (III.B.74)), and inserting the result back into (III.B.69), one can easily identify the contribution as $-2(\mathcal{M}_n(t)-1)$. Collecting all the terms, one arrives at the result

$$\mathcal{C}_{m,n}(t) \simeq 1 + \mathcal{M}_m(t) - \mathcal{M}_n(t)\,. \tag{III.B.80}$$

As a closing remark, we give a simple argument why the many-particle contributions in the form-factor expansion of the correlation functions can be neglected. In the one-particle expression (III.B.69), the dominant contribution is obtained from momenta satisfying $q_1 = p = q_2$, where the stationary phase conditions match the poles of the integrand. The next nonvanishing term in the expansion involves three intermediate particles, where the phase factor could be made stationary for $q_1 = p_1 = q_2$ and $p_2 = -p_3$. However, from (III.B.48) one can see that there is no pole in the form factor at $p_2 = -p_3$, and thus the contribution is subleading.

IV Summary

We developed a solver for non-equilibrium Dynamical Mean Field Theory (DMFT) that works directly at zero temperature and with correlated initial states, does not have a sign problem, and does not need an analytic continuation of the Green function. One of the main ideas is to use two real time axes instead of the usually L-shaped contour on which non-equilibrium DMFT is usually done. When the quantum state is time-evolved with respect to *equilibrium time*, the Hamiltonian stays constant. Green functions for DMFT of the initial state can be calculated on the first axis, the *equilibrium time* axis. The second axis is the *non-equilibrium time* axis, where the Hamiltonian is time-dependent. The real time solver employed on these axes uses Matrix Product States (MPS), which represents quantum states as a product of matrices.

In contrast to existing non-equilibrium solvers, the new solver has a number of advantages. It is a controlled approximation, is formulated directly at zero temperature, and is flexible in what parameter regions can be simulated, meaning that a wide range of Hamiltonian parameters can be simulated as long as the entanglement entropy stays small enough. Limitations are that a large entanglement entropy may prohibit long simulation times, and that several DMFT loops have to be done for every time step, which may be slow in comparison to solvers which can do one DMFT loop for all time steps at once.

To test the new solver we replicated and extended the results of Ref. 52, where an interaction quench in the Hubbard model at zero temperature was investigated with DMFT, and CTQMC as the solver. We found that our results are in good agreement with the results of Ref. 52 and can reach longer simulation times than Ref. 52 if there is a quench to high interaction strengths. Furthermore, we are able to investigate interacting initial states, which was not possible at zero temperature before, where we find that the critical interaction strength increases with increasing initial interaction strength.

With the new solver many possible simulation setups can be investigated right away, such as slow, instead of sudden quenches, quenches with isolating initial states, initial states away from half-filling, quenches in the chemical potential, and more. A possible avenue for future extension is the combination of the Fork Tensor Product State ansatz (see Ref. 41) with our solver in order to perform non-equilibrium DMFT with multiple orbitals. There is room for improvement with regards to the computation of G_k on the contour of our new solver, since the quality of the results depends on the extrapolation to infinite equilibrium time.

In the second part of the thesis, we investigated impact ionization in a strongly correlated model system. We calculated the time-evolution of a 4×3 Hubbard model under the influence of a short electric field pulse and confirmed the presence of impact ionization, which is the generation of multiple charge excitations from a single photon, even while spatial correlations are present. We also observed multiple photon absorption and Auger recombination. This was made possible with Gaussian filtering of states and the computation of the eigenstate spectrum with the Loschmidt amplitude, a tool that was independently developed both for this thesis and by other groups in Ref. 114 and 167. Interestingly, the occurrence of impact ionization and Auger recombination align very well with expectations based on the density of states and the quasi-particle picture. Most of the charge carriers are produced during the laser pulse. Impact ionization, with a moderate further increase in the number of carriers after the pulse, occurs if the energy of the photon is in the right energy window which one expects from the quasi-particle picture. The results can also be viewed from the perspective of the Eigenstate Thermalization Hypothesis (ETH), showing that the long-time behavior of the system is almost entirely dependent on the absorbed energy alone.

In the third part of the thesis we used MPS for their more traditional application of simulating one dimensional spin chains where we computed the expectation values of observables and the entanglement entropy, checking and verifying the results of other methods. The model of interest is the XY model, where the symmetry broken ground state is manipulated with different operators at time zero and the magnetization profile of the resulting steady state is investigated. We found that there is a "hydrodynamical" phase transition in the magnetization profile and entanglement entropy profile in the case of an initial Jordan-Wigner excitation, where there shape qualitatively depends on whether the magnetic field strength is above or below a critical field strength. In the case of two initial domain walls we found that the magnetization profile factorizes into a product of the magnetization profiles of two single domain walls. We also observed an interesting connection between the domain wall excitation of the Transverse Field Ising model and two combined chains with differently symmetry broken ground states. In these two cases the magnetization profiles almost are almost identical, which will be an interesting topic for future research.

V Danksagung

Ich möchte mich bei allen bedanken, die mich in meiner Studienzeit unterstützt haben, insbesondere bei meiner lieben Freundin Adenike, meinen Eltern, meinen Geschwistern, all meinen anderen Familienmitgliedern, und bei der Familie meiner Freundin. Ich bedanke mich bei allen Freunden und Kollegen vom Institut, die mir eine unvergessliche Studienzeit beschert haben. Ohne euch wär die Uni nur ein fades Gebäude in der Petersgasse gewesen. An dieser Stelle möchte ich noch extra meinen Betreuer Hans Gerd und meine Sitznachbarn den Dani und den Matthias dankend erwähnen. Wir haben über die Jahre viel Zeit miteinander verbracht, und ich werde die netten Diskussions- und Philosophierunden sehr vermissen. Weiters möchte ich mich bei Martin Eckstein und Marcus Kollar für die gute Beratung und das Zusenden von Simulationsergebnissen bedanken. Zu guter Letzt bedanke ich mich bei allen die diese Arbeit gelesen haben, und bei allen die sich für mich freuen.

VI Appendix

VI.1 Fourier Transform of Green Function

The Fourier transform of the components with at least on equilibrium time argument can be easily calculated in the eigenbasis with $\int_{-\infty}^{\infty} e^{ixp}\,\mathrm{d}p = 2\pi\,\delta(x)$ (see Ref. 97).

Greater Equilibrium Component

$$\begin{aligned}
G^{>E}(t_E, t'_E) &= -i\,\left\langle \psi \middle| c(t_E)\, c^\dagger(t'_E) \middle| \psi \right\rangle && \text{(VI.1)}\\
&= -i \sum_n \langle \psi \,|\, c \,|\, n\rangle\, \left\langle n \middle| c^\dagger \middle| \psi \right\rangle\, e^{i(t_E - t'_E)(E_0 - E_n)} && \text{(VI.2)}\\
G^{>E}(\omega) &= \int_{-\infty}^{\infty} G^{>E}(t_E, t'_E)\, e^{i\omega(t_E - t'_E)}\, \mathrm{d}(t_E - t'_E) && \text{(VI.3)}\\
&= -i\,2\pi \sum_n \langle \psi \,|\, c \,|\, n\rangle\, \left\langle n \middle| c^\dagger \middle| \psi \right\rangle\, \delta\left(\omega - (E_n - E_0)\right) && \text{(VI.4)}
\end{aligned}$$

Lesser Equilibrium Component

$$\begin{aligned}
G^{<E}(t_E, t'_E) &= i\,\left\langle \psi \middle| c^\dagger(t'_E)\, c(t_E) \middle| \psi \right\rangle && \text{(VI.5)}\\
&= i \sum_n \left\langle \psi \middle| c^\dagger \middle| n \right\rangle\, \langle n \,|\, c \,|\, \psi\rangle\, e^{i(t_E - t'_E)(E_n - E_0)} && \text{(VI.6)}\\
G^{<E}(\omega) &= \int_{-\infty}^{\infty} G^{<E}(t_E, t'_E)\, e^{i\omega(t_E - t'_E)}\, \mathrm{d}(t_E - t'_E) && \text{(VI.7)}\\
&= i\,2\pi \sum_n \left\langle \psi \middle| c^\dagger \middle| n \right\rangle\, \langle n \,|\, c \,|\, \psi\rangle\, \delta\left(\omega - (E_0 - E_n)\right) && \text{(VI.8)}
\end{aligned}$$

Right-Mixing Equilibrium Component

$$G^{\ulcorner}(t_E, t_N) = -i\, \langle \psi \,|\, c(t_E)\, c^\dagger(t_N) \,|\, \psi \rangle \tag{VI.9}$$

$$= -i \sum_n \langle \psi \,|\, c \,|\, n \rangle\, \langle n \,|\, c^\dagger(t_N) \,|\, \psi \rangle\; e^{i t_E (E_0 - E_n)} \tag{VI.10}$$

$$G^{\ulcorner}(\omega, t_N) = \int_{-\infty}^{\infty} G^{\ulcorner}(t_E, t_N)\, e^{i\omega t_E}\, \mathrm{d}t_E \tag{VI.11}$$

$$= -i\, 2\pi \sum_n \langle \psi \,|\, c \,|\, n \rangle\, \langle n \,|\, c^\dagger(t_N) \,|\, \psi \rangle\; \delta\left(\omega - (E_n - E_0)\right) \tag{VI.12}$$

Left-Mixing Equilibrium Component

$$G^{\urcorner}(t_N, t_E) = i\, \langle \psi \,|\, c^\dagger(t_E)\, c(t_N) \,|\, \psi \rangle \tag{VI.13}$$

$$= i \sum_n \langle \psi \,|\, c^\dagger \,|\, n \rangle\, \langle n \,|\, c(t_N) \,|\, \psi \rangle\; e^{i t_E (E_0 - E_n)} \tag{VI.14}$$

$$G^{\urcorner}(t_N, \omega) = \int_{-\infty}^{\infty} G^{\urcorner}(t_N, t_E)\, e^{i\omega t_E}\, \mathrm{d}t_E \tag{VI.15}$$

$$= i\, 2\pi \sum_n \langle \psi \,|\, c^\dagger \,|\, n \rangle\, \langle n \,|\, c(t_N) \,|\, \psi \rangle\; \delta\left(\omega - (E_n - E_0)\right) \tag{VI.16}$$

Pre-Right-Mixing Equilibrium Component

$$G^{\llcorner}(t_E, t_N) = i\, \langle \psi \,|\, c^\dagger(t_N)\, c(t_E) \,|\, \psi \rangle \tag{VI.17}$$

$$= i \sum_n \langle \psi \,|\, c^\dagger(t_N) \,|\, n \rangle\, \langle n \,|\, c \,|\, \psi \rangle\; e^{i t_E (E_n - E_0)} \tag{VI.18}$$

$$G^{\llcorner}(\omega, t_N) = \int_{-\infty}^{\infty} G^{\llcorner}(t_E, t_N)\, e^{i\omega t_E}\, \mathrm{d}t_E \tag{VI.19}$$

$$= i\, 2\pi \sum_n \langle \psi \,|\, c^\dagger(t_N) \,|\, n \rangle\, \langle n \,|\, c \,|\, \psi \rangle\; \delta\left(\omega - (E_0 - E_n)\right) \tag{VI.20}$$

Pre-Left-Mixing Equilibrium Component

$$G^{\lrcorner}(t_N, t_E) = -i \, \langle \psi \,|\, c(t_N) \, c^\dagger(t_E) \,|\, \psi \rangle \tag{VI.21}$$

$$= -i \sum_n \langle \psi \,|\, c(t_N) \,|\, n \rangle \, \langle n \,|\, c^\dagger \,|\, \psi \rangle \; e^{i t_E (E_n - E_0)} \tag{VI.22}$$

$$G^{\lrcorner}(t_N, \omega) = \int_{-\infty}^{\infty} G^{\lrcorner}(t_N, t_E) \, e^{i\omega t_E} \; \mathrm{d}t_E \tag{VI.23}$$

$$= -i \, 2\pi \sum_n \langle \psi \,|\, c(t_N) \,|\, n \rangle \, \langle n \,|\, c^\dagger \,|\, \psi \rangle \; \delta \left(\omega - (E_0 - E_n) \right) \tag{VI.24}$$

VI.2 Linear Prediction

In many situations, growing matrix dimensions in the MPS formalism prohibit reaching very long simulations times. When one is primarily interested in e.g. the Fourier transform of the Green function, it is possible to so-called use linear prediction to estimate the Green function for times longer than the maximum simulation time[68,98,99]. For linear prediction it is assumed that the Green function is a linear combination of Lorentz peaks in ω-space. In the time domain, this implies that $G(t)$ is a linear combination of earlier time steps:

$$G(t) = \sum_{i=1}^{N} a_i G(t - i\Delta t_{LP}) \tag{VI.25}$$

Here Δt_{LP} can be the time step used with the time-evolution or a multiple of it. When doing linear prediction, the a_i are fitted so that the least squares error between the actual Green function and the prediction based on the earlier values is minimized. In this thesis, linear prediction is used to predict the right-, left-, pre-right, and pre-left-mixing components of the Green function and and of the hybridization function with respect to the equilibrium time t_E.

VI.3 Integrals

VI.3.1 I_1

In this subsection we analyze the order of limits and the influence of the regularization of the following integral. More specifically, we are interested in the product $0^+ t_E$.

$$I_1 = \lim_{R_1\to\infty} \lim_{R_2\to\infty} \int_{-R_1}^{R_1} e^{i\omega t_E} \int_{t_E}^{-R_2} f(\bar{t}_E)\, g(\bar{t}_E)\ \mathrm{d}\bar{t}_E\ \mathrm{d}t_E \tag{VI.26}$$

$$= \frac{1}{4\pi^2} \lim_{R_1\to\infty} \lim_{R_2\to\infty} \lim_{R_3\to\infty} \int_{-R_1}^{R_1} \iint_{-R_3}^{R_3} \int_{t_E}^{-R_2} \tag{VI.27}$$

$$f(\omega')\, g(\omega'')\, e^{-i(-\omega+\omega'+\omega'')\bar{t}_E}\ \mathrm{d}\bar{t}_E\ \mathrm{d}\omega'\ \mathrm{d}\omega''\ \mathrm{d}t_E$$

$$= \frac{i}{4\pi^2} \lim_{R_1\to\infty} \lim_{\eta\to 0^+} \lim_{R_2\to\infty} \lim_{R_3\to\infty} \int_{-R_1}^{R_1} e^{i\omega t_E} \iint_{-R_3}^{R_3} \tag{VI.28}$$

$$f(\omega')\, g(\omega'')\, \frac{e^{i(\omega'+\omega''+i\eta)R_2} - e^{-i(\omega'+\omega''+i\eta)t_E}}{\omega'+\omega''+i\eta}\ \mathrm{d}\omega'\ \mathrm{d}\omega''\ \mathrm{d}t_E$$

$$= -\frac{i}{4\pi^2} \lim_{R_1\to\infty} \lim_{\eta\to 0^+} \lim_{R_3\to\infty} \int_{-R_1}^{R_1} \iint_{-R_3}^{R_3} f(\omega')\, g(\omega'')\, \frac{e^{-i(-\omega+\omega'+\omega''+i\eta)t_E}}{\omega'+\omega''+i\eta}\ \mathrm{d}\omega'\ \mathrm{d}\omega''\ \mathrm{d}t_E \tag{VI.29}$$

Because we do the limit $\eta \to 0^+$ before $R_1 \to \infty$ the product ηt_E tends to zero and the integral simplifies to:

$$I_1 = -\frac{i}{4\pi^2} \iiint_{-\infty}^{+\infty} f(\omega')\, g(\omega'')\, \frac{e^{-i(-\omega+\omega'+\omega'')t_E}}{\omega'+\omega''+i0^+}\ \mathrm{d}\omega'\ \mathrm{d}\omega''\ \mathrm{d}t_E \tag{VI.30}$$

We assume here, that $f(\omega')$ and $g(\omega'')$ are well behaved, so that the other limits can be exchanged freely. To summarize, we can ignore the product of t_E and the regularization parameter 0^+.

VI.3.2 I_2

We want to solve the integral I_2 below, where we assume the following properties for the function f:

$$f(\omega,\omega') = \begin{cases} 0 & \text{if } \omega < 0 \\ 0 & \text{if } \omega' > 0 \\ \text{finite} & \text{if } \omega = 0 \wedge \omega' = 0 \\ \text{arbitrary} & \text{otherwise} \end{cases} \tag{VI.31}$$

Furthermore, we will use this representation of the dirac delta[97]:

$$\lim_{\eta\to 0^+} \frac{\eta}{x^2+\eta^2} = \pi\,\delta(x) \tag{VI.32}$$

$$\begin{aligned}
I_2 &= \frac{i}{2\pi}\int_{-\infty}^{\infty} f(\omega,\omega')\,\frac{1}{\omega-\omega'\pm i0^+}\,\mathrm{d}\omega' && \text{(VI.33)}\\
&= \frac{i}{2\pi}\lim_{\eta\to 0^+}\int_{-\infty}^{\infty} f(\omega,\omega')\,\frac{1}{\omega-\omega'\pm i\eta}\,\mathrm{d}\omega' && \text{(VI.34)}\\
&= \frac{i}{2\pi}\lim_{\eta\to 0^+}\int_{-\infty}^{\infty} f(\omega,\omega')\,\frac{1}{\omega-\omega'\pm i\eta}\,\frac{\omega-\omega'\mp i\eta}{\omega-\omega'\mp i\eta}\,\mathrm{d}\omega' && \text{(VI.35)}\\
&= \frac{i}{2\pi}\lim_{\eta\to 0^+}\int_{-\infty}^{\infty} f(\omega,\omega')\left(\frac{\omega-\omega'}{(\omega-\omega')^2+\eta^2}\mp i\frac{\eta}{(\omega-\omega')^2+\eta^2}\right)\mathrm{d}\omega' && \text{(VI.36)}\\
&= \frac{i}{2\pi}\lim_{\eta\to 0^+}\int_{-\infty}^{\infty} f(\omega,\omega')\,\frac{\omega-\omega'}{(\omega-\omega')^2+\eta^2}\,\mathrm{d}\omega' \pm \frac{1}{2}\int_{-\infty}^{\infty} f(\omega,\omega')\,\delta(\omega-\omega')\,\mathrm{d}\omega' && \text{(VI.37)}
\end{aligned}$$

Because of the assumed properties of $f(\omega,\omega')$, the difference $\omega-\omega'$ will always be non-negative within the integral, and we can simplify the first term:

$$I_2 = \frac{i}{2\pi}\int_{-\infty}^{\infty} f(\omega,\omega')\,\frac{1}{\omega-\omega'+0^+}\,\mathrm{d}\omega' \pm \frac{1}{2}\,f(\omega,\omega) \tag{VI.38}$$

VI.4 Full Comparison After Convolution

As a reminder, we want to that relations Eqs. (VI.41) to (VI.45) are true. The proofs will be kept rather short, as they are all very similar. For a more in depth calculation for the right-mixing component see Sec. I.B.1.3.

$$C = A * B \qquad \text{(...on the contour with two real time axes)} \tag{VI.39}$$

$$C_L = A_L * B_L \qquad \text{(...on the L-shaped contour)} \tag{VI.40}$$

$$C_L^{\ulcorner}(\tau, t_N) \overset{?}{=} \frac{1}{2\pi} \int_{-\infty}^{\infty} e^{-\tau\omega} \; \left(C^{\ulcorner}(\omega, t_N)\, \theta(\tau) + C^{\llcorner}(\omega, t_N)\, \theta(-\tau)\right) \, \mathrm{d}\omega \tag{VI.41}$$

$$C_L^{\urcorner}(\tau, t_N) \overset{?}{=} \frac{1}{2\pi} \int_{-\infty}^{\infty} e^{-\tau\omega} \; \left(C^{\urcorner}(\omega, t_N)\, \theta(\tau) + C^{\lrcorner}(\omega, t_N)\, \theta(-\tau)\right) \, \mathrm{d}\omega \tag{VI.42}$$

$$C_L^{M}(\tau, \tau') \overset{?}{=} \frac{1}{i\, 2\pi} \int_{-\infty}^{\infty} e^{-(\tau-\tau')\omega} \; \left(C^{>E}(\omega, t_N)\, \theta(\tau-\tau') + C^{<E}(\omega, t_N)\, \theta(\tau'-\tau)\right) \, \mathrm{d}\omega \tag{VI.43}$$

$$C_L^{>N}(t_N, t'_N) \overset{?}{=} C^{>N}(t_N, t'_N) \tag{VI.44}$$

$$C_L^{<N}(t_N, t'_N) \overset{?}{=} C^{<N}(t_N, t'_N) \tag{VI.45}$$

VI.4.1 Right-Mixing Component, $\tau \geq 0$

Definition on L-shaped contour:

$$\begin{aligned} C_L^{\ulcorner}(\tau, t_N) &= \int_0^{t_N} A_L^{\ulcorner}(\tau, \bar{t}_N)\, B_L^{<N}(\bar{t}_N, t_N) \, \mathrm{d}\bar{t}_N \\ &\quad + \int_{t_N}^{0} A_L^{\ulcorner}(\tau, \bar{t}_N)\, B_L^{>N}(\bar{t}_N, t_N) \, \mathrm{d}\bar{t}_N \\ &\quad + \int_{-\infty}^{\infty} A_L^{M}(\tau-\bar{\tau})\, B_L^{\ulcorner}(\bar{\tau}, t_N) \, \mathrm{d}\bar{\tau} \\ &= \int_0^{\infty} A_L^{\ulcorner}(\tau, \bar{t})\, B_L^{AN}(\bar{t}, t_N) \, \mathrm{d}\bar{t} \\ &\quad + \int_{-\infty}^{\infty} A_L^{M}(\tau-\bar{\tau})\, B_L^{\ulcorner}(\bar{\tau}, t_N) \, \mathrm{d}\bar{\tau} \end{aligned} \tag{VI.46}$$

With integration limits:

$$\begin{aligned} C^{\ulcorner}_L(\tau, t_N) = \int_0^{\infty} & A^{\ulcorner}_L(\tau, \bar{t}_N)\, B^{AN}_L(\bar{t}_N, t_N)\ \mathrm{d}\bar{t}_N \\ & + \int_{-\infty}^{0} A^M_L(\tau - \bar{\tau})\, B^{\ulcorner}_L(\bar{\tau}, t_N)\ \mathrm{d}\bar{\tau} \\ & + \int_0^{\tau} A^M_L(\tau - \bar{\tau})\, B^{\ulcorner}_L(\bar{\tau}, t_N)\ \mathrm{d}\bar{\tau} \\ & + \int_{\tau}^{\infty} A^M_L(\tau - \bar{\tau})\, B^{\ulcorner}_L(\bar{\tau}, t_N)\ \mathrm{d}\bar{\tau} \end{aligned} \tag{VI.47}$$

Replace components:

$$\begin{aligned} C^{\ulcorner}_L(\tau, t_N) = & \frac{1}{2\pi} \int_{-\infty}^{\infty} \int_0^{\infty} A^{\ulcorner}(\omega', \bar{t}_N)\, B^{AN}(\bar{t}_N, t_N)\, e^{-\tau\omega'}\ \mathrm{d}\bar{t}_N\, \mathrm{d}\omega' \\ & - \frac{i}{4\pi^2} \int_{-\infty}^{\infty} \int_{-\infty}^{\infty} \int_{-\infty}^{0} A^{>E}(\omega')\, e^{-(\tau-\bar{\tau})\omega'}\, B^{\llcorner}(\omega'', t_N)\, e^{-\bar{\tau}\omega''}\ \mathrm{d}\bar{\tau}\, \mathrm{d}\omega'\ \mathrm{d}\omega'' \\ & - \frac{i}{4\pi^2} \int_{-\infty}^{\infty} \int_{-\infty}^{\infty} \int_{0}^{\tau} A^{>E}(\omega')\, e^{-(\tau-\bar{\tau})\omega'}\, B^{\ulcorner}(\omega'', t_N)\, e^{-\bar{\tau}\omega''}\ \mathrm{d}\bar{\tau}\, \mathrm{d}\omega'\ \mathrm{d}\omega'' \\ & - \frac{i}{4\pi^2} \int_{-\infty}^{\infty} \int_{-\infty}^{\infty} \int_{\tau}^{\infty} A^{<E}(\omega')\, e^{-(\tau-\bar{\tau})\omega'}\, B^{\ulcorner}(\omega'', t_N)\, e^{-\bar{\tau}\omega''}\ \mathrm{d}\bar{\tau}\, \mathrm{d}\omega'\ \mathrm{d}\omega'' \end{aligned} \tag{VI.48}$$

$$\begin{aligned} = & \frac{1}{2\pi} \int_{-\infty}^{\infty} \int_0^{\infty} A^{\ulcorner}(\omega', \bar{t}_N)\, B^{AN}(\bar{t}_N, t_N)\, e^{-\tau\omega'}\ \mathrm{d}\bar{t}_N\, \mathrm{d}\omega' \\ & - \frac{i}{4\pi^2} \int_{-\infty}^{\infty} \int_{-\infty}^{\infty} A^{>E}(\omega')\, B^{\llcorner}(\omega'', t_N)\, \frac{e^{-\tau\omega'}}{\omega' - \omega'' + 0^+}\ \mathrm{d}\omega'\ \mathrm{d}\omega'' \\ & - \frac{i}{4\pi^2} \int_{-\infty}^{\infty} \int_{-\infty}^{\infty} A^{>E}(\omega')\, B^{\ulcorner}(\omega'', t_N)\, \frac{e^{-\tau\omega''} - e^{-\tau\omega'}}{\omega' - \omega''}\ \mathrm{d}\omega'\ \mathrm{d}\omega'' \\ & + \frac{i}{4\pi^2} \int_{-\infty}^{\infty} \int_{-\infty}^{\infty} A^{<E}(\omega')\, B^{\ulcorner}(\omega'', t_N)\, \frac{e^{-\tau\omega''}}{\omega' - \omega'' - 0^+}\ \mathrm{d}\omega'\ \mathrm{d}\omega'' \end{aligned} \tag{VI.49}$$

Definition on the contour with two real time axes:

$$\begin{aligned}
C^{\ulcorner}(t_E, t_N) = &\int_{-\infty}^{0} A^{>E}(t_E, \bar{t}_E)\, B^{\llcorner}(\bar{t}_E, t_N)\ \mathrm{d}\bar{t}_E \\
&+ \int_{0}^{t_N} A^{\ulcorner}(t_E, \bar{t}_N)\, B^{<N}(\bar{t}_N, t_N)\ \mathrm{d}\bar{t}_N \\
&+ \int_{t_N}^{0} A^{\ulcorner}(t_E, \bar{t}_N)\, B^{>N}(\bar{t}_N, t_N)\ \mathrm{d}\bar{t}_N \\
&+ \int_{0}^{t_E} A^{>E}(t_E, \bar{t}_E)\, B^{\ulcorner}(\bar{t}_E, t_N)\ \mathrm{d}\bar{t}_E \\
&+ \int_{t_E}^{-\infty} A^{<E}(t_E, \bar{t}_E)\, B^{\ulcorner}(\bar{t}_E, t_N)\ \mathrm{d}\bar{t}_E
\end{aligned} \tag{VI.50}$$

Go to Fourier space inside of integrals and integrate over $\bar{t}_E$:

$$C^{\ulcorner}(t_E, t_N) = \frac{1}{4\pi^2} \int_{-\infty}^{\infty}\int_{-\infty}^{\infty}\int_{-\infty}^{0} A^{>E}(\omega')\, B^{\llcorner}(\omega'', t_N)\, e^{-i\omega'(t_E - \bar{t}_E)}\, e^{-i\omega''\bar{t}_E}\ \mathrm{d}\bar{t}_E\ \mathrm{d}\omega'\ \mathrm{d}\omega'' \tag{VI.51}$$

$$\begin{aligned}
&+ \int_{0}^{\infty} A^{\ulcorner}(t_E, \bar{t}_N)\, B^{AN}(\bar{t}_N, t_N)\ \mathrm{d}\bar{t}_N \\
&+ \frac{1}{4\pi^2} \int_{-\infty}^{\infty}\int_{-\infty}^{\infty}\int_{0}^{t_E} A^{>E}(\omega')\, B^{\ulcorner}(\omega'', t_N)\, e^{-i\omega'(t_E - \bar{t}_E)}\, e^{-i\omega''\bar{t}_E}\ \mathrm{d}\bar{t}_E\ \mathrm{d}\omega'\ \mathrm{d}\omega'' \\
&+ \frac{1}{4\pi^2} \int_{-\infty}^{\infty}\int_{-\infty}^{\infty}\int_{t_E}^{-\infty} A^{<E}(\omega')\, B^{\ulcorner}(\omega'', t_N)\, e^{-i\omega'(t_E - \bar{t}_E)}\, e^{-i\omega''\bar{t}_E}\ \mathrm{d}\bar{t}_E\ \mathrm{d}\omega'\ \mathrm{d}\omega''
\end{aligned}$$

$$\begin{aligned}
= &-\frac{i}{4\pi^2} \int_{-\infty}^{\infty}\int_{-\infty}^{\infty} A^{>E}(\omega')\, B^{\llcorner}(\omega'', t_N)\, \frac{e^{-it_E\omega'}}{\omega' - \omega'' - i0^+}\ \mathrm{d}\omega'\ \mathrm{d}\omega'' \\
&+ \int_{0}^{\infty} A^{\ulcorner}(t_E, \bar{t}_N)\, B^{AN}(\bar{t}_N, t_N)\ \mathrm{d}\bar{t}_N \\
&- \frac{i}{4\pi^2} \int_{-\infty}^{\infty}\int_{-\infty}^{\infty} A^{>E}(\omega')\, B^{\ulcorner}(\omega'', t_N)\, \frac{e^{-i\omega'' t_E} - e^{-i\omega' t_E}}{\omega' - \omega''}\ \mathrm{d}\omega'\ \mathrm{d}\omega'' \\
&+ \frac{i}{4\pi^2} \int_{-\infty}^{\infty}\int_{-\infty}^{\infty} A^{<E}(\omega')\, B^{\ulcorner}(\omega'', t_N)\, \frac{e^{-it_E\omega''}}{\omega' - \omega'' - i0^+}\ \mathrm{d}\omega'\ \mathrm{d}\omega''
\end{aligned} \tag{VI.52}$$

Go to Fourier space outside of integrals:

$$\begin{aligned}
C^{\ulcorner}(\omega, t_N) = -\frac{i}{2\pi} \int_{-\infty}^{\infty} & A^{>E}(\omega)\, B^{\llcorner}(\omega'', t_N)\, \frac{1}{\omega - \omega'' - i0^+}\ \mathrm{d}\omega'' \\
&+ \int_{0}^{\infty} A^{\ulcorner}(\omega, \bar{t})\, B^{AN}(\bar{t}, t_N)\ \mathrm{d}\bar{t} \\
&- \frac{i}{2\pi} \int_{-\infty}^{\infty} A^{>E}(\omega')\, B^{\ulcorner}(\omega, t_N)\, \frac{1}{\omega' - \omega}\ \mathrm{d}\omega' \\
&+ \frac{i}{2\pi} \int_{-\infty}^{\infty} A^{>E}(\omega)\, B^{\ulcorner}(\omega'', t_N)\, \frac{1}{\omega - \omega''}\ \mathrm{d}\omega'' \\
&+ \frac{i}{2\pi} \int_{-\infty}^{\infty} A^{<E}(\omega')\, B^{\ulcorner}(\omega, t_N)\, \frac{1}{\omega' - \omega - i0^+}\ \mathrm{d}\omega'
\end{aligned} \tag{VI.53}$$

Use Sec. VI.3.2:

$$\begin{aligned}
C^{\ulcorner}(\omega, t_N) = -\frac{i}{2\pi} \int_{-\infty}^{\infty} & A^{>E}(\omega)\, B^{\llcorner}(\omega'', t_N)\, \frac{1}{\omega - \omega'' + 0^+}\ \mathrm{d}\omega'' \\
&+ \int_{0}^{\infty} A^{\ulcorner}(\omega, \bar{t})\, B^{AN}(\bar{t}, t_N)\ \mathrm{d}\bar{t} \\
&- \frac{i}{2\pi} \int_{-\infty}^{\infty} A^{>E}(\omega')\, B^{\ulcorner}(\omega, t_N)\, \frac{1}{\omega' - \omega}\ \mathrm{d}\omega' \\
&+ \frac{i}{2\pi} \int_{-\infty}^{\infty} A^{>E}(\omega)\, B^{\ulcorner}(\omega'', t_N)\, \frac{1}{\omega - \omega''}\ \mathrm{d}\omega'' \\
&+ \frac{i}{2\pi} \int_{-\infty}^{\infty} A^{<E}(\omega')\, B^{\ulcorner}(\omega, t_N)\, \frac{1}{\omega' - \omega - 0^+}\ \mathrm{d}\omega' \\
&+ \frac{1}{2} \left(A^{>E}(\omega)\, B^{\llcorner}(\omega, t_N) - A^{<E}(\omega)\, B^{\ulcorner}(\omega, t_N) \right)
\end{aligned} \tag{VI.54}$$

Integrate over ω:

$$\begin{aligned}
\frac{1}{2\pi}\int_{-\infty}^{\infty} C^{\ulcorner}(\omega,t_N)\,e^{-\tau\omega}\;\mathrm{d}\omega = &-\frac{i}{4\pi^2}\int_{-\infty}^{\infty}\int_{-\infty}^{\infty} A^{>E}(\omega')\,B^{\llcorner}(\omega'',t_N)\,\frac{e^{-\tau\omega'}}{\omega'-\omega''+0^+}\;\mathrm{d}\omega'\;\mathrm{d}\omega'' \qquad \text{(VI.55)}\\
&+\frac{1}{2\pi}\int_{-\infty}^{\infty}\int_{0}^{\infty} A^{\ulcorner}(\omega',\bar{t})\,B^{AN}(\bar{t},t_N)\,e^{-\tau\omega'}\;\mathrm{d}\bar{t}\;\mathrm{d}\omega'\\
&-\frac{i}{4\pi^2}\int_{-\infty}^{\infty}\int_{-\infty}^{\infty} A^{>E}(\omega')\,B^{\ulcorner}(\omega'',t_N)\,\frac{e^{-\tau\omega''}}{\omega'-\omega''}\;\mathrm{d}\omega'\;\mathrm{d}\omega''\\
&+\frac{i}{4\pi^2}\int_{-\infty}^{\infty}\int_{-\infty}^{\infty} A^{>E}(\omega')\,B^{\ulcorner}(\omega'',t_N)\,\frac{e^{-\tau\omega'}}{\omega'-\omega''}\;\mathrm{d}\omega'\;\mathrm{d}\omega''\\
&+\frac{i}{4\pi^2}\int_{-\infty}^{\infty}\int_{-\infty}^{\infty} A^{<E}(\omega')\,B^{\ulcorner}(\omega'',t_N)\,\frac{e^{-\tau\omega''}}{\omega'-\omega''-0^+}\;\mathrm{d}\omega'\;\mathrm{d}\omega''
\end{aligned}$$

Compare Eq. (VI.49) and Eq. (VI.55). They are the same.

VI.4.2 Right-Mixing Component, $\tau < 0$

Definition on L-shaped contour:

$$\begin{aligned}
C^{\ulcorner}_L(\tau,t_N) &= \int_0^{t_N} A^{\ulcorner}_L(\tau,\bar{t}_N)\,B^{<N}_L(\bar{t}_N,t_N)\;\mathrm{d}\bar{t}_N \qquad \text{(VI.56)}\\
&\quad+\int_{t_N}^{0} A^{\ulcorner}_L(\tau,\bar{t}_N)\,B^{>N}_L(\bar{t}_N,t_N)\;\mathrm{d}\bar{t}_N\\
&\quad+\int_{-\infty}^{\infty} A^{M}_L(\tau-\bar{\tau})\,B^{\ulcorner}_L(\bar{\tau},t_N)\;\mathrm{d}\bar{\tau}\\
&=\int_0^{\infty} A^{\ulcorner}_L(\tau,\bar{t})\,B^{AN}_L(\bar{t},t_N)\;\mathrm{d}\bar{t}\\
&\quad+\int_{-\infty}^{\infty} A^{M}_L(\tau-\bar{\tau})\,B^{\ulcorner}_L(\bar{\tau},t_N)\;\mathrm{d}\bar{\tau}
\end{aligned}$$

With integration limits:

$$\begin{aligned}
C_L^{\ulcorner}(\tau, t_N) = \int_0^{\infty} & A_L^{\ulcorner}(\tau, \bar{t}_N)\, B_L^{AN}(\bar{t}_N, t_N)\ \mathrm{d}\bar{t}_N \\
& + \int_{-\infty}^{\tau} A_L^{M}(\tau - \bar{\tau})\, B_L^{\ulcorner}(\bar{\tau}, t_N)\ \mathrm{d}\bar{\tau} \\
& + \int_{\tau}^{0} A_L^{M}(\tau - \bar{\tau})\, B_L^{\ulcorner}(\bar{\tau}, t_N)\ \mathrm{d}\bar{\tau} \\
& + \int_{0}^{\infty} A_L^{M}(\tau - \bar{\tau})\, B_L^{\ulcorner}(\bar{\tau}, t_N)\ \mathrm{d}\bar{\tau}
\end{aligned} \tag{VI.57}$$

Replace components:

$$\begin{aligned}
C_L^{\ulcorner}(\tau, t_N) = & \frac{1}{2\pi} \int_{-\infty}^{\infty} \int_0^{\infty} A^{\llcorner}(\omega', \bar{t})\, B^{AN}(\bar{t}, t_N)\, e^{-\tau\omega'}\ \mathrm{d}\bar{t}\ \mathrm{d}\omega' \\
& - \frac{i}{4\pi^2} \int_{-\infty}^{\infty} \int_{-\infty}^{\infty} \int_{-\infty}^{\tau} A^{>E}(\omega')\, e^{-(\tau-\bar{\tau})\omega'}\, B^{\llcorner}(\omega'', t_N)\, e^{-\bar{\tau}\omega''}\ \mathrm{d}\bar{\tau}\, \mathrm{d}\omega'\ \mathrm{d}\omega'' \\
& - \frac{i}{4\pi^2} \int_{-\infty}^{\infty} \int_{-\infty}^{\infty} \int_{\tau}^{0} A^{<E}(\omega')\, e^{-(\tau-\bar{\tau})\omega'}\, B^{\llcorner}(\omega'', t_N)\, e^{-\bar{\tau}\omega''}\ \mathrm{d}\bar{\tau}\, \mathrm{d}\omega'\ \mathrm{d}\omega'' \\
& - \frac{i}{4\pi^2} \int_{-\infty}^{\infty} \int_{-\infty}^{\infty} \int_{0}^{\infty} A^{<E}(\omega')\, e^{-(\tau-\bar{\tau})\omega'}\, B^{\ulcorner}(\omega'', t_N)\, e^{-\bar{\tau}\omega''}\ \mathrm{d}\bar{\tau}\, \mathrm{d}\omega'\ \mathrm{d}\omega''
\end{aligned} \tag{VI.58}$$

$$\begin{aligned}
= & \frac{1}{2\pi} \int_{-\infty}^{\infty} \int_0^{\infty} A^{\llcorner}(\omega', \bar{t})\, B^{AN}(\bar{t}, t_N)\, e^{-\tau\omega'}\ \mathrm{d}\bar{t}\ \mathrm{d}\omega' \\
& - \frac{i}{4\pi^2} \int_{-\infty}^{\infty} \int_{-\infty}^{\infty} A^{>E}(\omega')\, B^{\llcorner}(\omega'', t_N)\, \frac{e^{-\tau\omega''}}{\omega' - \omega'' + 0^+}\ \mathrm{d}\omega'\ \mathrm{d}\omega'' \\
& - \frac{i}{4\pi^2} \int_{-\infty}^{\infty} \int_{-\infty}^{\infty} A^{<E}(\omega')\, B^{\llcorner}(\omega'', t_N)\, \frac{e^{-\tau\omega'} - e^{-\tau\omega''}}{\omega' - \omega''}\ \mathrm{d}\omega'\ \mathrm{d}\omega'' \\
& + \frac{i}{4\pi^2} \int_{-\infty}^{\infty} \int_{-\infty}^{\infty} A^{<E}(\omega')\, B^{\ulcorner}(\omega'', t_N)\, \frac{e^{-\tau\omega'}}{\omega' - \omega'' - 0^+}\ \mathrm{d}\omega'\ \mathrm{d}\omega''
\end{aligned} \tag{VI.59}$$

Definition on the contour with two real time axes:

$$\begin{aligned}
C^{\llcorner}(t_E, t_N) = &\int_{-\infty}^{t_E} A^{>E}(t_E, \bar{t}_E)\, B^{\llcorner}(\bar{t}_E, t_N)\ \mathrm{d}\bar{t}_E \\
&+ \int_{t_E}^{0} A^{<E}(t_E, \bar{t}_E)\, B^{\llcorner}(\bar{t}_E, t_N)\ \mathrm{d}\bar{t}_E \\
&+ \int_{0}^{\infty} A^{\llcorner}(t_E, \bar{t}_N)\, B^{AN}(\bar{t}_N, t_N)\ \mathrm{d}\bar{t}_N \\
&+ \int_{0}^{-\infty} A^{<E}(t_E, \bar{t}_E)\, B^{\ulcorner}(\bar{t}_E, t_N)\ \mathrm{d}\bar{t}_E
\end{aligned} \tag{VI.60}$$

Go to Fourier space inside of integrals and integrate over $\bar{t}_E$:

$$C^{\llcorner}(t_E, t_N) = \frac{1}{4\pi^2} \int_{-\infty}^{\infty} \int_{-\infty}^{\infty} \int_{-\infty}^{t_E} A^{>E}(\omega')\, e^{-i\omega'(t_E - \bar{t}_E)}\, B^{\llcorner}(\omega'', t_N)\, e^{-i\omega''\bar{t}_E}\ \mathrm{d}\bar{t}_E\ \mathrm{d}\omega'\ \mathrm{d}\omega'' \tag{VI.61}$$

$$\begin{aligned}
&+ \frac{1}{4\pi^2} \int_{-\infty}^{\infty} \int_{-\infty}^{\infty} \int_{t_E}^{0} A^{<E}(\omega')\, e^{-i\omega'(t_E - \bar{t}_E)}\, B^{\llcorner}(\omega'', t_N)\, e^{-i\omega''\bar{t}_E}\ \mathrm{d}\bar{t}_E\ \mathrm{d}\omega'\ \mathrm{d}\omega'' \\
&+ \int_{0}^{\infty} A^{\llcorner}(t_E, \bar{t}_N)\, B^{AN}(\bar{t}_N, t_N)\ \mathrm{d}\bar{t}_N \\
&+ \frac{1}{4\pi^2} \int_{-\infty}^{\infty} \int_{-\infty}^{\infty} \int_{0}^{-\infty} A^{<E}(\omega')\, e^{-i\omega'(t_E - \bar{t}_E)}\, B^{\ulcorner}(\omega'', t_N)\, e^{-i\omega''\bar{t}_E}\ \mathrm{d}\bar{t}_E\ \mathrm{d}\omega'\ \mathrm{d}\omega''
\end{aligned}$$

$$\begin{aligned}
= &-\frac{i}{4\pi^2} \int_{-\infty}^{\infty} \int_{-\infty}^{\infty} A^{>E}(\omega')\, B^{\llcorner}(\omega'', t_N)\, \frac{e^{-it_E\omega''}}{\omega' - \omega'' - i0^+}\ \mathrm{d}\omega'\ \mathrm{d}\omega'' \\
&- \frac{i}{4\pi^2} \int_{-\infty}^{\infty} \int_{-\infty}^{\infty} A^{<E}(\omega')\, B^{\llcorner}(\omega'', t_N)\, \frac{e^{-it_E\omega'} - e^{-i\omega'' t_E}}{\omega' - \omega''}\ \mathrm{d}\omega'\ \mathrm{d}\omega'' \\
&+ \int_{0}^{\infty} A^{\llcorner}(t_E, \bar{t}_N)\, B^{AN}(\bar{t}_N, t_N)\ \mathrm{d}\bar{t}_N \\
&+ \frac{i}{4\pi^2} \int_{-\infty}^{\infty} \int_{-\infty}^{\infty} A^{<E}(\omega')\, B^{\ulcorner}(\omega'', t_N)\, \frac{e^{-i\omega' t_E}}{\omega' - \omega'' - i0^+}\ \mathrm{d}\omega'\ \mathrm{d}\omega''
\end{aligned} \tag{VI.62}$$

Go to Fourier space outside of integrals:

$$\begin{aligned} C^{\llcorner}(\omega, t_N) = &-\frac{i}{2\pi}\int_{-\infty}^{\infty} A^{>E}(\omega')\, B^{\llcorner}(\omega, t_N)\, \frac{1}{\omega' - \omega - i0^+}\ \mathrm{d}\omega' \\ &-\frac{i}{2\pi}\int_{-\infty}^{\infty} A^{<E}(\omega)\, B^{\llcorner}(\omega'', t_N)\, \frac{1}{\omega - \omega''}\ \mathrm{d}\omega'' \\ &+\frac{i}{2\pi}\int_{-\infty}^{\infty} A^{<E}(\omega')\, B^{\llcorner}(\omega, t_N)\, \frac{1}{\omega' - \omega}\ \mathrm{d}\omega' \\ &+\int_{0}^{\infty} A^{\llcorner}(\omega, \bar{t})\, B^{AN}(\bar{t}, t_N)\ \mathrm{d}\bar{t} \\ &+\frac{i}{2\pi}\int_{-\infty}^{\infty} A^{<E}(\omega)\, B^{\ulcorner}(\omega'', t_N)\, \frac{1}{\omega - \omega'' - i0^+}\ \mathrm{d}\omega'' \end{aligned} \tag{VI.63}$$

Use Sec. VI.3.2:

$$\begin{aligned} C^{\llcorner}(\omega, t_N) = &-\frac{i}{2\pi}\int_{-\infty}^{\infty} A^{>E}(\omega')\, B^{\llcorner}(\omega, t_N)\, \frac{1}{\omega' - \omega + 0^+}\ \mathrm{d}\omega' \\ &-\frac{i}{2\pi}\int_{-\infty}^{\infty} A^{<E}(\omega)\, B^{\llcorner}(\omega'', t_N)\, \frac{1}{\omega - \omega''}\ \mathrm{d}\omega'' \\ &+\frac{i}{2\pi}\int_{-\infty}^{\infty} A^{<E}(\omega')\, B^{\llcorner}(\omega, t_N)\, \frac{1}{\omega' - \omega}\ \mathrm{d}\omega' \\ &+\int_{0}^{\infty} A^{\llcorner}(\omega, \bar{t})\, B^{AN}(\bar{t}, t_N)\ \mathrm{d}\bar{t} \\ &+\frac{i}{2\pi}\int_{-\infty}^{\infty} A^{<E}(\omega)\, B^{\ulcorner}(\omega'', t_N)\, \frac{1}{\omega - \omega'' - 0^+}\ \mathrm{d}\omega'' \\ &+\frac{1}{2}\left(A^{>E}(\omega)\, B^{\llcorner}(\omega, t_N) - A^{<E}(\omega)\, B^{\ulcorner}(\omega, t_N)\right) \end{aligned} \tag{VI.64}$$

Integrate over ω:

$$\begin{aligned}
\frac{1}{2\pi}\int_{-\infty}^{\infty} C^{\llcorner}(\omega, t_N)\, e^{-\tau\omega}\ \mathrm{d}\omega = &-\frac{i}{4\pi^2}\int_{-\infty}^{\infty}\int_{-\infty}^{\infty} A^{>E}(\omega')\, B^{\llcorner}(\omega'', t_N)\, \frac{e^{-\tau\omega''}}{\omega' - \omega'' + 0^+}\ \mathrm{d}\omega'\ \mathrm{d}\omega'' \\
&-\frac{i}{4\pi^2}\int_{-\infty}^{\infty}\int_{-\infty}^{\infty} A^{<E}(\omega')\, B^{\llcorner}(\omega'', t_N)\, \frac{e^{-\tau\omega'}}{\omega' - \omega''}\ \mathrm{d}\omega'\ \mathrm{d}\omega'' \\
&+\frac{i}{4\pi^2}\int_{-\infty}^{\infty}\int_{-\infty}^{\infty} A^{<E}(\omega')\, B^{\llcorner}(\omega'', t_N)\, \frac{e^{-\tau\omega''}}{\omega' - \omega''}\ \mathrm{d}\omega'\ \mathrm{d}\omega'' \\
&+\frac{1}{2\pi}\int_{-\infty}^{\infty}\int_{0}^{\infty} A^{\llcorner}(\omega', \bar{t})\, B^{AN}(\bar{t}, t_N)\, e^{-\tau\omega'}\ \mathrm{d}\bar{t}\ \mathrm{d}\omega' \\
&+\frac{i}{4\pi^2}\int_{-\infty}^{\infty}\int_{-\infty}^{\infty} A^{<E}(\omega')\, B^{\ulcorner}(\omega'', t_N)\, \frac{e^{-\tau\omega'}}{\omega' - \omega'' - 0^+}\ \mathrm{d}\omega'\ \mathrm{d}\omega''
\end{aligned} \tag{VI.65}$$

Compare Eq. (VI.59) and Eq. (VI.65). They are the same.

VI.4.3 Left-Mixing Component, $\tau \geq 0$

Definition on L-shaped contour:

$$\begin{aligned}
C_L^{\urcorner}(t_N, \tau) = &\int_0^{t_N} A^{>}(t_N, \bar{t}_N)\, B_L^{\urcorner}(\bar{t}_N, \tau)\ \mathrm{d}\bar{t}_N \\
&+\int_{t_N}^{0} A^{<}(t_N, \bar{t}_N)\, B_L^{\urcorner}(\bar{t}_N, \tau)\ \mathrm{d}\bar{t}_N \\
&+\int_{-\infty}^{\infty} A_L^{\urcorner}(t_N, \bar{\tau})\, B_L^{M}(\bar{\tau} - \tau)\ \mathrm{d}\bar{\tau}
\end{aligned} \tag{VI.66}$$

With integration limits:

$$\begin{aligned}
C_L^{\urcorner}(t_N, \tau) = &\int_0^{\infty} A^{RN}(t_N, \bar{t}_N)\, B_L^{\urcorner}(\bar{t}, \tau)\ \mathrm{d}\bar{t}_N \\
&+\int_{-\infty}^{0} A_L^{\urcorner}(t_N, \bar{\tau})\, B_L^{M}(\bar{\tau} - \tau)\ \mathrm{d}\bar{\tau} \\
&+\int_{0}^{\tau} A_L^{\urcorner}(t_N, \bar{\tau})\, B_L^{M}(\bar{\tau} - \tau)\ \mathrm{d}\bar{\tau} \\
&+\int_{\tau}^{\infty} A_L^{\urcorner}(t_N, \bar{\tau})\, B_L^{M}(\bar{\tau} - \tau)\ \mathrm{d}\bar{\tau}
\end{aligned} \tag{VI.67}$$

Replace components:

$$\begin{aligned}
C^{\neg}_{L}(t_N, \tau) = \frac{1}{2\pi} \int_{-\infty}^{\infty} \int_{0}^{\infty} \; & A^{RN}(t_N, \bar{t}_N)\, B^{\neg}(\bar{t}_N, \omega'')\, e^{-\tau\omega''} \;\mathrm{d}\bar{t}_N \;\mathrm{d}\omega'' \qquad \text{(VI.68)} \\
& - \frac{i}{4\pi^2} \int_{-\infty}^{\infty} \int_{-\infty}^{\infty} \int_{-\infty}^{0} \; A^{\lrcorner}(t_N, \omega')\, e^{-\bar{\tau}\omega'}\; B^{<E}(\omega'')\, e^{-(\bar{\tau}-\tau)\omega''} \;\mathrm{d}\bar{\tau}\;\mathrm{d}\omega' \;\mathrm{d}\omega'' \\
& - \frac{i}{4\pi^2} \int_{-\infty}^{\infty} \int_{-\infty}^{\infty} \int_{0}^{\tau} \; A^{\neg}(t_N, \omega')\, e^{-\bar{\tau}\omega'}\; B^{<E}(\omega'')\, e^{-(\bar{\tau}-\tau)\omega''} \;\mathrm{d}\bar{\tau}\;\mathrm{d}\omega' \;\mathrm{d}\omega'' \\
& - \frac{i}{4\pi^2} \int_{-\infty}^{\infty} \int_{-\infty}^{\infty} \int_{\tau}^{\infty} \; A^{\neg}(t_N, \omega')\, e^{-\bar{\tau}\omega'}\; B^{>E}(\omega'')\, e^{-(\bar{\tau}-\tau)\omega''} \;\mathrm{d}\bar{\tau}\;\mathrm{d}\omega' \;\mathrm{d}\omega''
\end{aligned}$$

$$\begin{aligned}
= \frac{1}{2\pi} \int_{-\infty}^{\infty} \int_{0}^{\infty} \; & A^{RN}(t_N, \bar{t}_N)\, B^{\neg}(\bar{t}_N, \omega'')\, e^{-\tau\omega''} \;\mathrm{d}\bar{t}_N \;\mathrm{d}\omega'' \qquad \text{(VI.69)} \\
& + \frac{i}{4\pi^2} \int_{-\infty}^{\infty} \int_{-\infty}^{\infty} A^{\lrcorner}(t_N, \omega')\, B^{<E}(\omega'')\, \frac{e^{\tau\omega''}}{\omega' + \omega'' - 0^{+}} \;\mathrm{d}\omega' \;\mathrm{d}\omega'' \\
& + \frac{i}{4\pi^2} \int_{-\infty}^{\infty} \int_{-\infty}^{\infty} A^{\neg}(t_N, \omega')\, B^{<E}(\omega'')\, \frac{e^{-\tau\omega'} - e^{\tau\omega''}}{\omega' + \omega''} \;\mathrm{d}\omega' \;\mathrm{d}\omega'' \\
& - \frac{i}{4\pi^2} \int_{-\infty}^{\infty} \int_{-\infty}^{\infty} A^{\neg}(t_N, \omega')\, B^{>E}(\omega'')\, \frac{e^{-\tau\omega'}}{\omega' + \omega'' + 0^{+}} \;\mathrm{d}\omega' \;\mathrm{d}\omega''
\end{aligned}$$

Definition on the contour with two real time axes:

$$\begin{aligned}
C^{\neg}(t_N, t_E) = & \int_{-\infty}^{0} A^{\lrcorner}(t_N, \bar{t}_E)\, B^{<E}(\bar{t}_E, t_E) \;\mathrm{d}\bar{t}_E \qquad \text{(VI.70)} \\
& + \int_{0}^{t_N} A^{>}(t_N, \bar{t}_N)\, B^{\neg}(\bar{t}_N, t_E) \;\mathrm{d}\bar{t}_N \\
& + \int_{t_N}^{0} A^{<}(t_N, \bar{t}_N)\, B^{\neg}(\bar{t}_N, t_E) \;\mathrm{d}\bar{t}_N \\
& + \int_{0}^{t_E} A^{\neg}(t_N, \bar{t}_E)\, B^{<E}(\bar{t}_E, t_E) \;\mathrm{d}\bar{t}_E \\
& + \int_{t_E}^{-\infty} A^{\neg}(t_N, \bar{t}_E)\, B^{>E}(\bar{t}_E, t_E) \;\mathrm{d}\bar{t}_E
\end{aligned}$$

(VI.71)

Go to Fourier space inside of integrals and integrate over $\bar{t}_E$:

$$
C^{\neg}(t_N, t_E) = \frac{1}{4\pi^2} \int_{-\infty}^{\infty} \int_{-\infty}^{\infty} \int_{-\infty}^{0} A^{\urcorner}(t_N, \omega')\, B^{<E}(\omega'')\, e^{-i\omega' \bar{t}_E}\, e^{-i\omega''(\bar{t}_E - t_E)}\, \mathrm{d}\bar{t}_E\, \mathrm{d}\omega'\, \mathrm{d}\omega'' \tag{VI.72}
$$

$$
\begin{aligned}
&+ \int_{0}^{\infty} A^{RN}(t_N, \bar{t}_N)\, B^{\neg}(\bar{t}_N, t_E)\, \mathrm{d}\bar{t}_N \\
&+ \frac{1}{4\pi^2} \int_{-\infty}^{\infty} \int_{-\infty}^{\infty} \int_{0}^{t_E} A^{\neg}(t_N, \omega')\, B^{<E}(\omega'')\, e^{-i\omega' \bar{t}_E}\, e^{-i\omega''(\bar{t}_E - t_E)}\, \mathrm{d}\bar{t}_E\, \mathrm{d}\omega'\, \mathrm{d}\omega'' \\
&+ \frac{1}{4\pi^2} \int_{-\infty}^{\infty} \int_{-\infty}^{\infty} \int_{t_E}^{-\infty} A^{\neg}(t_N, \omega')\, B^{>E}(\omega'')\, e^{-i\omega' \bar{t}_E}\, e^{-i\omega''(\bar{t}_E - t_E)}\, \mathrm{d}\bar{t}_E\, \mathrm{d}\omega'\, \mathrm{d}\omega''
\end{aligned}
$$

$$
= \frac{i}{4\pi^2} \int_{-\infty}^{\infty} \int_{-\infty}^{\infty} A^{\urcorner}(t_N, \omega')\, B^{<E}(\omega'')\, \frac{e^{i\omega'' t_E}}{\omega' + \omega'' + i0^+}\, \mathrm{d}\omega'\, \mathrm{d}\omega'' \tag{VI.73}
$$

$$
\begin{aligned}
&+ \int_{0}^{\infty} A^{RN}(t_N, \bar{t}_N)\, B^{\neg}(\bar{t}_N, t_E)\, \mathrm{d}\bar{t}_N \\
&+ \frac{i}{4\pi^2} \int_{-\infty}^{\infty} \int_{-\infty}^{\infty} A^{\neg}(t_N, \omega')\, B^{<E}(\omega'')\, \frac{e^{-i\omega' t_E} - e^{i\omega'' t_E}}{\omega' + \omega''}\, \mathrm{d}\omega'\, \mathrm{d}\omega'' \\
&- \frac{i}{4\pi^2} \int_{-\infty}^{\infty} \int_{-\infty}^{\infty} A^{\neg}(t_N, \omega')\, B^{>E}(\omega'')\, \frac{e^{-i\omega' t_E}}{\omega' + \omega'' + i0^+}\, \mathrm{d}\omega'\, \mathrm{d}\omega''
\end{aligned}
$$

Go to Fourier space outside of integrals:

$$
\begin{aligned}
C^{\neg}(t_N, \omega) = {} & \frac{i}{2\pi} \int_{-\infty}^{\infty} A^{\urcorner}(t_N, \omega')\, B^{<E}(-\omega)\, \frac{1}{\omega' - \omega + i0^+}\, \mathrm{d}\omega' \\
&+ \int_{0}^{\infty} A^{RN}(t_N, \bar{t}_E)\, B^{\neg}(\bar{t}_E, \omega)\, \mathrm{d}\bar{t}_E \\
&+ \frac{i}{2\pi} \int_{-\infty}^{\infty} A^{\neg}(t_N, \omega)\, B^{<E}(\omega'')\, \frac{1}{\omega + \omega''}\, \mathrm{d}\omega'' \\
&- \frac{i}{2\pi} \int_{-\infty}^{\infty} A^{\neg}(t_N, \omega')\, B^{<E}(-\omega)\, \frac{1}{\omega' - \omega}\, \mathrm{d}\omega' \\
&- \frac{i}{2\pi} \int_{-\infty}^{\infty} A^{\neg}(t_N, \omega)\, B^{>E}(\omega'')\, \frac{1}{\omega + \omega'' + i0^+}\, \mathrm{d}\omega''
\end{aligned} \tag{VI.74}
$$

Use Sec. VI.3.2:

$$
\begin{aligned}
C^{\neg}(t_N, \omega) &= \frac{i}{2\pi} \int_{-\infty}^{\infty} A^{\lrcorner}(t_N, \omega')\, B^{<E}(-\omega)\, \frac{1}{\omega' - \omega - 0^+}\ \mathrm{d}\omega' \\
&+ \int_{0}^{\infty} A^{RN}(t_N, \bar{t}_E)\, B^{\neg}(\bar{t}_E, \omega)\ \mathrm{d}\bar{t}_E \\
&+ \frac{i}{2\pi} \int_{-\infty}^{\infty} A^{\neg}(t_N, \omega)\, B^{<E}(\omega'')\, \frac{1}{\omega + \omega''}\ \mathrm{d}\omega'' \\
&- \frac{i}{2\pi} \int_{-\infty}^{\infty} A^{\neg}(t_N, \omega')\, B^{<E}(-\omega)\, \frac{1}{\omega' - \omega}\ \mathrm{d}\omega' \\
&- \frac{i}{2\pi} \int_{-\infty}^{\infty} A^{\neg}(t_N, \omega)\, B^{>E}(\omega'')\, \frac{1}{\omega + \omega'' + 0^+}\ \mathrm{d}\omega'' \\
&+ \frac{1}{2} \left(A^{\lrcorner}(t_N, \omega)\, B^{<E}(-\omega) - A^{\neg}(t_N, \omega)\, B^{>E}(-\omega) \right)
\end{aligned}
\tag{VI.75}
$$

Integrate over ω:

$$
\begin{aligned}
\frac{1}{2\pi} \int_{-\infty}^{\infty} C^{\neg}(t_N, \omega)\, e^{-\tau\omega}\, \mathrm{d}\omega &= \frac{i}{4\pi^2} \int_{-\infty}^{\infty} \int_{-\infty}^{\infty} A^{\lrcorner}(t_N, \omega')\, B^{<E}(-\omega'')\, \frac{e^{-\tau\omega''}}{\omega' - \omega'' - 0^+}\ \mathrm{d}\omega'\ \mathrm{d}\omega'' \\
&+ \frac{1}{2\pi^2} \int_{-\infty}^{\infty} \int_{0}^{\infty} A^{RN}(t_N, \bar{t}_E)\, B^{\neg}(\bar{t}_E, \omega'')\, e^{-\tau\omega''}\ \mathrm{d}\bar{t}_E\ \mathrm{d}\omega'' \\
&+ \frac{i}{4\pi^2} \int_{-\infty}^{\infty} \int_{-\infty}^{\infty} A^{\neg}(t_N, \omega')\, B^{<E}(\omega'')\, \frac{e^{-\tau\omega'}}{\omega' + \omega''}\ \mathrm{d}\omega'\ \mathrm{d}\omega'' \\
&- \frac{i}{4\pi^2} \int_{-\infty}^{\infty} \int_{-\infty}^{\infty} A^{\neg}(t_N, \omega')\, B^{<E}(-\omega'')\, \frac{e^{-\tau\omega''}}{\omega' - \omega''}\ \mathrm{d}\omega'\ \mathrm{d}\omega'' \\
&- \frac{i}{4\pi^2} \int_{-\infty}^{\infty} \int_{-\infty}^{\infty} A^{\neg}(t_N, \omega')\, B^{>E}(\omega'')\, \frac{e^{-\tau\omega'}}{\omega' + \omega'' + 0^+}\ \mathrm{d}\omega'\ \mathrm{d}\omega''
\end{aligned}
\tag{VI.76}
$$

Substitute negative ω' and ω'':

$$\frac{1}{2\pi}\int_{-\infty}^{\infty} C^{\neg}(t_N,\omega)\, e^{-\tau\omega}\,\mathrm{d}\omega = \frac{i}{4\pi^2}\int_{-\infty}^{\infty}\int_{-\infty}^{\infty} A^{\lrcorner}(t_N,\omega')\, B^{<E}(\omega'')\,\frac{e^{\tau\omega''}}{\omega'+\omega''-0^+}\;\mathrm{d}\omega'\;\mathrm{d}\omega'' \tag{VI.77}$$

$$+\frac{1}{2\pi}\int_{-\infty}^{\infty}\int_{0}^{\infty} A^{RN}(t_N,\bar{t}_E)\, B^{\neg}(\bar{t}_E,\omega'')\, e^{-\tau\omega''}\;\mathrm{d}\bar{t}_E\;\mathrm{d}\omega''$$

$$+\frac{i}{4\pi^2}\int_{-\infty}^{\infty}\int_{-\infty}^{\infty} A^{\neg}(t_N,\omega')\, B^{<E}(\omega'')\,\frac{e^{-\tau\omega'}}{\omega'+\omega''}\;\mathrm{d}\omega'\;\mathrm{d}\omega''$$

$$-\frac{i}{4\pi^2}\int_{-\infty}^{\infty}\int_{-\infty}^{\infty} A^{\neg}(t_N,\omega')\, B^{<E}(\omega'')\,\frac{e^{\tau\omega''}}{\omega'+\omega''}\;\mathrm{d}\omega'\;\mathrm{d}\omega''$$

$$-\frac{i}{4\pi^2}\int_{-\infty}^{\infty}\int_{-\infty}^{\infty} A^{\neg}(t_N,\omega')\, B^{>E}(\omega'')\,\frac{e^{-\tau\omega'}}{\omega'+\omega''+0^+}\;\mathrm{d}\omega'\;\mathrm{d}\omega''$$

Compare Eq. (VI.69) and Eq. (VI.77). They are the same.

VI.4.4 Left-Mixing Component, $\tau < 0$

Definition on L-shaped contour:

$$C_L^{\neg}(t_N,\tau) = \int_{0}^{t_N} A_L^{>N}(t_N,\bar{t}_N)\, B_L^{\neg}(\bar{t}_N,\tau)\;\mathrm{d}\bar{t}_N \tag{VI.78}$$

$$+\int_{t_N}^{0} A_L^{<N}(t_N,\bar{t}_N)\, B_L^{\neg}(\bar{t}_N,\tau)\;\mathrm{d}\bar{t}_N$$

$$+\int_{-\infty}^{\infty} A_L^{\neg}(t_N,\bar{\tau})\, B_L^{M}(\bar{\tau}-\tau)\;\mathrm{d}\bar{\tau}$$

With integration limits:

$$C_L^{\neg}(t_N,\tau) = \int_{0}^{\infty} A_L^{RN}(t_N,\bar{t}_N)\, B_L^{\neg}(\bar{t}_N,\tau)\;\mathrm{d}\bar{t}_N \tag{VI.79}$$

$$+\int_{-\infty}^{\tau} A_L^{\neg}(t_N,\bar{\tau})\, B_L^{M}(\bar{\tau}-\tau)\;\mathrm{d}\bar{\tau}$$

$$+\int_{\tau}^{0} A_L^{\neg}(t_N,\bar{\tau})\, B_L^{M}(\bar{\tau}-\tau)\;\mathrm{d}\bar{\tau}$$

$$+\int_{0}^{\infty} A_L^{\neg}(t_N,\bar{\tau})\, B_L^{M}(\bar{\tau}-\tau)\;\mathrm{d}\bar{\tau}$$

Replace components:

$$\begin{aligned}
C_L^{\neg}(t_N, \tau) = \frac{1}{2\pi} \int_{-\infty}^{\infty} \int_{0}^{\infty} \; A^{RN}(t_N, \bar{t}_N)\, B^{\lrcorner}(\bar{t}_N, \omega'')\, e^{-\tau\omega''} \;\, \mathrm{d}\bar{t}_N \;\mathrm{d}\omega'' \qquad \text{(VI.80)} \\
- \frac{i}{4\pi^2} \int_{-\infty}^{\infty} \int_{-\infty}^{\infty} \int_{-\infty}^{\tau} \; A^{\lrcorner}(t_N, \omega')\, e^{-\bar{\tau}\omega'} \; B^{<E}(\omega'')\, e^{-(\bar{\tau}-\tau)\omega''} \;\, \mathrm{d}\bar{\tau}\, \mathrm{d}\omega' \;\mathrm{d}\omega'' \\
- \frac{i}{4\pi^2} \int_{-\infty}^{\infty} \int_{-\infty}^{\infty} \int_{\tau}^{0} \; A^{\lrcorner}(t_N, \omega')\, e^{-\bar{\tau}\omega'} \; B^{>E}(\omega'')\, e^{-(\bar{\tau}-\tau)\omega''} \;\, \mathrm{d}\bar{\tau}\, \mathrm{d}\omega' \;\mathrm{d}\omega'' \\
- \frac{i}{4\pi^2} \int_{-\infty}^{\infty} \int_{-\infty}^{\infty} \int_{0}^{\infty} \; A^{\neg}(t_N, \omega')\, e^{-\bar{\tau}\omega'} \; B^{>E}(\omega'')\, e^{-(\bar{\tau}-\tau)\omega''} \;\, \mathrm{d}\bar{\tau}\, \mathrm{d}\omega' \;\mathrm{d}\omega'' \\
= \frac{1}{2\pi} \int_{-\infty}^{\infty} \int_{0}^{\infty} \; A^{RN}(t_N, \bar{t}_N)\, B^{\lrcorner}(\bar{t}_N, \omega'')\, e^{-\tau\omega''} \;\, \mathrm{d}\bar{t}_N \;\mathrm{d}\omega'' \qquad \text{(VI.81)} \\
+ \frac{i}{4\pi^2} \int_{-\infty}^{\infty} \int_{-\infty}^{\infty} \; A^{\lrcorner}(t_N, \omega')\, B^{<E}(\omega'')\, \frac{e^{-\tau\omega'}}{\omega' + \omega'' - 0^+} \;\, \mathrm{d}\omega' \;\mathrm{d}\omega'' \\
+ \frac{i}{4\pi^2} \int_{-\infty}^{\infty} \int_{-\infty}^{\infty} \; A^{\lrcorner}(t_N, \omega')\, B^{>E}(\omega'')\, \frac{e^{\tau\omega''} - e^{-\tau\omega'}}{\omega' + \omega''} \;\, \mathrm{d}\omega' \;\mathrm{d}\omega'' \\
- \frac{i}{4\pi^2} \int_{-\infty}^{\infty} \int_{-\infty}^{\infty} \; A^{\neg}(t_N, \omega')\, B^{>E}(\omega'')\, \frac{e^{\tau\omega''}}{\omega' + \omega'' + 0^+} \;\, \mathrm{d}\omega' \;\mathrm{d}\omega''
\end{aligned}$$

Definition on the contour with two real time axes:

$$\begin{aligned}
C^{\lrcorner}(t_N, t_E) = \int_{-\infty}^{t_E} \; A^{\lrcorner}(t_N, \bar{t}_E)\, B^{<E}(\bar{t}_E, t_E) \;\, \mathrm{d}\bar{t}_E \qquad \text{(VI.82)} \\
+ \int_{t_E}^{0} \; A^{\lrcorner}(t_N, \bar{t}_E)\, B^{>E}(\bar{t}_E, t_E) \;\, \mathrm{d}\bar{t}_E \\
+ \int_{0}^{t_N} \; A^{>N}(t_N, \bar{t}_N)\, B^{\lrcorner}(\bar{t}_N, t_E) \;\, \mathrm{d}\bar{t}_N \\
+ \int_{t_N}^{0} \; A^{<N}(t_N, \bar{t}_N)\, B^{\lrcorner}(\bar{t}_N, t_E) \;\, \mathrm{d}\bar{t}_N \\
+ \int_{0}^{-\infty} \; A^{\neg}(t_N, \bar{t}_E)\, B^{>E}(\bar{t}_E, t_E) \;\, \mathrm{d}\bar{t}_E
\end{aligned}$$

Go to Fourier space inside of integrals and integrate over $\bar{t}_E$:

$$C^{\lrcorner}(t_N, t_E) = \frac{1}{4\pi^2} \int_{-\infty}^{\infty} \int_{-\infty}^{\infty} \int_{-\infty}^{t_E} A^{\lrcorner}(t_N, \omega')\, e^{-i\omega' \bar{t}_E}\, B^{<E}(\omega'')\, e^{-i\omega''(\bar{t}_E - t_E)}\ \mathrm{d}\bar{t}_E\ \mathrm{d}\omega'\ \mathrm{d}\omega'' \tag{VI.83}$$

$$\begin{aligned}
&+ \frac{1}{4\pi^2} \int_{-\infty}^{\infty} \int_{-\infty}^{\infty} \int_{t_E}^{0} A^{\lrcorner}(t_N, \omega')\, e^{-i\omega' \bar{t}_E}\, B^{>E}(\omega'')\, e^{-i\omega''(\bar{t}_E - t_E)}\ \mathrm{d}\bar{t}_E\ \mathrm{d}\omega'\ \mathrm{d}\omega'' \\
&+ \int_{0}^{\infty} A^{RN}(t_N, \bar{t}_N)\, B^{\lrcorner}(\bar{t}_N, t_E)\ \mathrm{d}\bar{t}_N \\
&+ \frac{1}{4\pi^2} \int_{-\infty}^{\infty} \int_{-\infty}^{\infty} \int_{0}^{-\infty} A^{\neg}(t_N, \omega')\, e^{-i\omega' \bar{t}_E}\, B^{>E}(\omega'')\, e^{-i\omega''(\bar{t}_E - t_E)}\ \mathrm{d}\bar{t}_E\ \mathrm{d}\omega'\ \mathrm{d}\omega''
\end{aligned}$$

$$\begin{aligned}
= &\frac{i}{4\pi^2} \int_{-\infty}^{\infty} \int_{-\infty}^{\infty} A^{\lrcorner}(t_N, \omega')\, B^{<E}(\omega'')\, \frac{e^{-i\omega' t_E}}{\omega' + \omega'' + i0^+}\ \mathrm{d}\omega'\ \mathrm{d}\omega'' \\
&+ \frac{i}{4\pi^2} \int_{-\infty}^{\infty} \int_{-\infty}^{\infty} A^{\lrcorner}(t_N, \omega')\, B^{>E}(\omega'')\, \frac{e^{i\omega'' t_E} - e^{-i\omega' t_E}}{\omega' + \omega''}\ \mathrm{d}\omega'\ \mathrm{d}\omega'' \\
&+ \int_{0}^{\infty} A^{RN}(t_N, \bar{t}_N)\, B^{\lrcorner}(\bar{t}_N, t_E)\ \mathrm{d}\bar{t}_N \\
&- \frac{i}{4\pi^2} \int_{-\infty}^{\infty} \int_{-\infty}^{\infty} A^{\neg}(t_N, \omega')\, B^{>E}(\omega'')\, \frac{e^{i\omega'' t_E}}{\omega' + \omega'' + i0^+}\ \mathrm{d}\omega'\ \mathrm{d}\omega''
\end{aligned} \tag{VI.84}$$

Go to Fourier space outside of integrals:

$$\begin{aligned}
C^{\lrcorner}(t_N, \omega) = &\frac{i}{2\pi} \int_{-\infty}^{\infty} A^{\lrcorner}(t_N, \omega)\, B^{<E}(\omega'')\, \frac{1}{\omega + \omega'' + i0^+}\ \mathrm{d}\omega'' \\
&+ \frac{i}{2\pi} \int_{-\infty}^{\infty} A^{\lrcorner}(t_N, \omega')\, B^{>E}(-\omega)\, \frac{1}{\omega' - \omega}\ \mathrm{d}\omega' \\
&- \frac{i}{2\pi} \int_{-\infty}^{\infty} A^{\lrcorner}(t_N, \omega)\, B^{>E}(\omega'')\, \frac{1}{\omega + \omega''}\ \mathrm{d}\omega'' \\
&+ \int_{0}^{\infty} A^{RN}(t_N, \bar{t}_N)\, B^{\lrcorner}(\bar{t}_N, \omega)\ \mathrm{d}\bar{t}_N \\
&- \frac{i}{2\pi} \int_{-\infty}^{\infty} A^{\neg}(t_N, \omega')\, B^{>E}(-\omega)\, \frac{1}{\omega' - \omega + i0^+}\ \mathrm{d}\omega'
\end{aligned}$$

Use Sec. VI.3.2:

$$\begin{aligned}
C^{\lrcorner}(t_N,\omega) = {} & \frac{i}{2\pi}\int_{-\infty}^{\infty} A^{\lrcorner}(t_N,\omega)\, B^{<E}(\omega'')\, \frac{1}{\omega+\omega''-0^+}\ \mathrm{d}\omega'' \\
& + \frac{i}{2\pi}\int_{-\infty}^{\infty} A^{\lrcorner}(t_N,\omega')\, B^{>E}(-\omega)\, \frac{1}{\omega'-\omega}\ \mathrm{d}\omega' \\
& - \frac{i}{2\pi}\int_{-\infty}^{\infty} A^{\lrcorner}(t_N,\omega)\, B^{>E}(\omega'')\, \frac{1}{\omega+\omega''}\ \mathrm{d}\omega'' \\
& + \int_{0}^{\infty} A^{RN}(t_N,\bar{t}_N)\, B^{\lrcorner}(\bar{t}_N,\omega)\ \mathrm{d}\bar{t}_N \\
& - \frac{i}{2\pi}\int_{-\infty}^{\infty} A^{\urcorner}(t_N,\omega')\, B^{>E}(-\omega)\, \frac{1}{\omega'-\omega+0^+}\ \mathrm{d}\omega' \\
& + \frac{1}{2}\left(A^{\lrcorner}(t_N,\omega)\, B^{<E}(-\omega) - A^{\urcorner}(t_N,\omega)\, B^{>E}(-\omega)\right)
\end{aligned} \tag{VI.85}$$

Integrate over ω:

$$\begin{aligned}
\frac{1}{2\pi}\int_{-\infty}^{\infty} C^{\lrcorner}(t_N,\omega)\, e^{-\tau\omega}\ \mathrm{d}\omega = {} & \frac{i}{4\pi^2}\int_{-\infty}^{\infty}\int_{-\infty}^{\infty} A^{\lrcorner}(t_N,\omega')\, B^{<E}(\omega'')\, \frac{e^{-\tau\omega'}}{\omega'+\omega''-0^+}\ \mathrm{d}\omega'\ \mathrm{d}\omega'' \\
& + \frac{i}{4\pi^2}\int_{-\infty}^{\infty}\int_{-\infty}^{\infty} A^{\lrcorner}(t_N,\omega')\, B^{>E}(-\omega'')\, \frac{e^{-\tau\omega''}}{\omega'-\omega''}\ \mathrm{d}\omega'\ \mathrm{d}\omega'' \\
& - \frac{i}{4\pi^2}\int_{-\infty}^{\infty}\int_{-\infty}^{\infty} A^{\lrcorner}(t_N,\omega')\, B^{>E}(\omega'')\, \frac{e^{-\tau\omega'}}{\omega'+\omega''}\ \mathrm{d}\omega'\ \mathrm{d}\omega'' \\
& + \frac{1}{2\pi}\int_{-\infty}^{\infty}\int_{0}^{\infty} A^{RN}(t_N,\bar{t}_N)\, B^{\lrcorner}(\bar{t}_N,\omega'')\, e^{-\tau\omega''}\ \mathrm{d}\bar{t}_N\ \mathrm{d}\omega'' \\
& - \frac{i}{4\pi^2}\int_{-\infty}^{\infty}\int_{-\infty}^{\infty} A^{\urcorner}(t_N,\omega')\, B^{>E}(-\omega'')\, \frac{e^{-\tau\omega''}}{\omega'-\omega''+0^+}\ \mathrm{d}\omega'\ \mathrm{d}\omega''
\end{aligned} \tag{VI.86}$$

Substitute negative ω' and ω'':

$$\frac{1}{2\pi}\int_{-\infty}^{\infty} C^{\lrcorner}(t_N,\omega)\, e^{-\tau\omega}\ \mathrm{d}\omega = \frac{i}{4\pi^2}\int_{-\infty}^{\infty}\int_{-\infty}^{\infty} A^{\lrcorner}(t_N,\omega')\, B^{<E}(\omega'')\, \frac{e^{-\tau\omega'}}{\omega'+\omega''-0^+}\ \mathrm{d}\omega'\ \mathrm{d}\omega'' \tag{VI.87}$$

$$\begin{aligned}
&+ \frac{i}{4\pi^2}\int_{-\infty}^{\infty}\int_{-\infty}^{\infty} A^{\lrcorner}(t_N,\omega')\, B^{>E}(\omega'')\, \frac{e^{\tau\omega''}}{\omega'+\omega''}\ \mathrm{d}\omega'\ \mathrm{d}\omega'' \\
&- \frac{i}{4\pi^2}\int_{-\infty}^{\infty}\int_{-\infty}^{\infty} A^{\lrcorner}(t_N,\omega')\, B^{>E}(\omega'')\, \frac{e^{-\tau\omega'}}{\omega'+\omega''}\ \mathrm{d}\omega'\ \mathrm{d}\omega'' \\
&+ \frac{1}{2\pi}\int_{-\infty}^{\infty}\int_{0}^{\infty} A^{RN}(t_N,\bar{t}_N)\, B^{\lrcorner}(\bar{t}_N,\omega'')\, e^{-\tau\omega''}\ \mathrm{d}\bar{t}_N\ \mathrm{d}\omega'' \\
&- \frac{i}{4\pi^2}\int_{-\infty}^{\infty}\int_{-\infty}^{\infty} A^{\urcorner}(t_N,\omega')\, B^{>E}(\omega'')\, \frac{e^{\tau\omega''}}{\omega'+\omega''+0^+}\ \mathrm{d}\omega'\ \mathrm{d}\omega''
\end{aligned}$$

Compare Eq. (VI.81) and Eq. (VI.87). They are the same.

VI.4.5 Matsubara Component, $\tau-\tau'\geq 0$

Definition on L-shaped contour:

$$C_L^M(\tau-\tau') = -i\, G_{L,33}(\tau-\tau') \tag{VI.88}$$

$$= \int_{-\infty}^{\infty} A_L^M(\tau-\bar{\tau})\, B_L^M(\bar{\tau}-\tau')\ \mathrm{d}\bar{\tau} \tag{VI.89}$$

$$\tag{VI.90}$$

With integration limits:

$$\begin{aligned}
C_L^M(\tau-\tau') &= \int_{-\infty}^{\tau'} A_L^M(\tau-\bar{\tau})\, B_L^M(\bar{\tau}-\tau')\ \mathrm{d}\bar{\tau} \qquad \text{(VI.91)} \\
&+ \int_{\tau'}^{\tau} A_L^M(\tau-\bar{\tau})\, B_L^M(\bar{\tau}-\tau')\ \mathrm{d}\bar{\tau} \\
&+ \int_{\tau}^{\infty} A_L^M(\tau-\bar{\tau})\, B_L^M(\bar{\tau}-\tau')\ \mathrm{d}\bar{\tau}
\end{aligned}$$

Replace components:

$$C_L^M(\tau-\tau') = -\frac{1}{4\pi^2}\int_{-\infty}^{\infty}\int_{-\infty}^{\infty}\int_{-\infty}^{\tau'} A^{>E}(\omega')\, e^{-(\tau-\bar{\tau})\omega'}\, B^{<E}(\omega'')\, e^{-(\bar{\tau}-\tau')\omega''}\ \mathrm{d}\bar{\tau}\,\mathrm{d}\omega'\ \mathrm{d}\omega'' \tag{VI.92}$$

$$-\frac{1}{4\pi^2}\int_{-\infty}^{\infty}\int_{-\infty}^{\infty}\int_{\tau'}^{\tau} A^{>E}(\omega')\, e^{-(\tau-\bar{\tau})\omega'}\, B^{>E}(\omega'')\, e^{-(\bar{\tau}-\tau')\omega''}\ \mathrm{d}\bar{\tau}\,\mathrm{d}\omega'\ \mathrm{d}\omega''$$

$$-\frac{1}{4\pi^2}\int_{-\infty}^{\infty}\int_{-\infty}^{\infty}\int_{\tau}^{\infty} A^{<E}(\omega')\, e^{-(\tau-\bar{\tau})\omega'}\, B^{>E}(\omega'')\, e^{-(\bar{\tau}-\tau')\omega''}\ \mathrm{d}\bar{\tau}\,\mathrm{d}\omega'\ \mathrm{d}\omega''$$

$$= -\frac{1}{4\pi^2}\int_{-\infty}^{\infty}\int_{-\infty}^{\infty} A^{>E}(\omega')\, B^{<E}(\omega'')\, \frac{e^{-(\tau-\tau')\omega'}}{\omega'-\omega''+0^+}\ \mathrm{d}\omega'\ \mathrm{d}\omega'' \tag{VI.93}$$

$$-\frac{1}{4\pi^2}\int_{-\infty}^{\infty}\int_{-\infty}^{\infty} A^{>E}(\omega')\, B^{>E}(\omega'') \frac{e^{-(\tau-\tau')\omega''}-e^{-(\tau-\tau')\omega'}}{\omega'-\omega''}\ \mathrm{d}\omega'\ \mathrm{d}\omega''$$

$$+\frac{1}{4\pi^2}\int_{-\infty}^{\infty}\int_{-\infty}^{\infty} A^{<E}(\omega')\, B^{>E}(\omega'')\, \frac{e^{-(\tau-\tau')\omega''}}{\omega'-\omega''-0^+}\ \mathrm{d}\omega'\ \mathrm{d}\omega''$$

Definition on the contour with two real time axes:

$$C^{>E}(t_E-t'_E) = \int_{-\infty}^{t'_E} A^{>E}(t_E-\bar{t})\, B^{<E}(\bar{t}-t'_E)\ \mathrm{d}\bar{t} \tag{VI.94}$$

$$+\int_{t'_E}^{t_E} A^{>E}(t_E-\bar{t})\, B^{>E}(\bar{t}-t'_E)\ \mathrm{d}\bar{t}$$

$$+\int_{t_E}^{-\infty} A^{<E}(t_E-\bar{t})\, B^{>E}(\bar{t}-t'_E)\ \mathrm{d}\bar{t}$$

Go to Fourier space inside of integrals and integrate over $\bar{t}_E$:

$$
\begin{aligned}
C^{>E}(t_E - t'_E) = \frac{1}{4\pi^2} \int_{-\infty}^{\infty} \int_{-\infty}^{\infty} \int_{-\infty}^{t'_E} A^{>E}(\omega')\, e^{-i\omega'(t_E-\bar{t})}\, B^{<E}(\omega'')\, e^{-i\omega''(\bar{t}-t'_E)}\ \mathrm{d}\bar{t}\ \mathrm{d}\omega'\ \mathrm{d}\omega'' \qquad \text{(VI.95)}
\end{aligned}
$$

$$
\begin{aligned}
&+ \frac{1}{4\pi^2} \int_{-\infty}^{\infty} \int_{-\infty}^{\infty} \int_{t'_E}^{t_E} A^{>E}(\omega')\, e^{-i\omega'(t_E-\bar{t})}\, B^{>E}(\omega'')\, e^{-i\omega''(\bar{t}-t'_E)}\ \mathrm{d}\bar{t}\ \mathrm{d}\omega'\ \mathrm{d}\omega'' \\
&+ \frac{1}{4\pi^2} \int_{-\infty}^{\infty} \int_{-\infty}^{\infty} \int_{t_E}^{-\infty} A^{<E}(\omega')\, e^{-i\omega'(t_E-\bar{t})}\, B^{>E}(\omega'')\, e^{-i\omega''(\bar{t}-t'_E)}\ \mathrm{d}\bar{t}\ \mathrm{d}\omega'\ \mathrm{d}\omega'' \\
&= -\frac{i}{4\pi^2} \int_{-\infty}^{\infty} \int_{-\infty}^{\infty} A^{>E}(\omega')\, B^{<E}(\omega'')\, \frac{e^{-i(t_E-t'_E)\omega'}}{\omega' - \omega'' - i0^+}\ \mathrm{d}\omega'\ \mathrm{d}\omega'' \qquad \text{(VI.96)} \\
&- \frac{i}{4\pi^2} \int_{-\infty}^{\infty} \int_{-\infty}^{\infty} A^{>E}(\omega')\, B^{>E}(\omega'')\, \frac{e^{-i(t_E-t'_E)\omega''} - e^{-i(t_E-t'_E)\omega'}}{\omega' - \omega''}\ \mathrm{d}\omega'\ \mathrm{d}\omega'' \\
&+ \frac{i}{4\pi^2} \int_{-\infty}^{\infty} \int_{-\infty}^{\infty} A^{<E}(\omega')\, B^{>E}(\omega'')\, \frac{e^{-i(t_E-t'_E)\omega''}}{\omega' - \omega'' - i0^+}\ \mathrm{d}\omega'\ \mathrm{d}\omega''
\end{aligned}
$$

Go to Fourier space outside of integrals:

$$
\begin{aligned}
C^{>E}(\omega) = &-\frac{i}{2\pi} \int_{-\infty}^{\infty} A^{>E}(\omega)\, B^{<E}(\omega'')\, \frac{1}{\omega - \omega'' - i0^+}\ \mathrm{d}\omega'' \qquad \text{(VI.97)} \\
&- \frac{i}{2\pi} \int_{-\infty}^{\infty} A^{>E}(\omega')\, B^{>E}(\omega)\, \frac{1}{\omega' - \omega}\ \mathrm{d}\omega' \\
&+ \frac{i}{2\pi} \int_{-\infty}^{\infty} A^{>E}(\omega)\, B^{>E}(\omega'')\, \frac{1}{\omega - \omega''}\ \mathrm{d}\omega'' \\
&+ \frac{i}{2\pi} \int_{-\infty}^{\infty} A^{<E}(\omega')\, B^{>E}(\omega)\, \frac{1}{\omega' - \omega - i0^+}\ \mathrm{d}\omega'
\end{aligned}
$$

Use Sec. VI.3.2:

$$\begin{aligned} C^{>E}(\omega) = &-\frac{i}{2\pi}\int_{-\infty}^{\infty} A^{>E}(\omega)\, B^{<E}(\omega'')\, \frac{1}{\omega-\omega''+0^+}\ \mathrm{d}\omega'' \\ &-\frac{i}{2\pi}\int_{-\infty}^{\infty} A^{>E}(\omega')\, B^{>E}(\omega)\, \frac{1}{\omega'-\omega}\ \mathrm{d}\omega' \\ &+\frac{i}{2\pi}\int_{-\infty}^{\infty} A^{>E}(\omega)\, B^{>E}(\omega'')\, \frac{1}{\omega-\omega''}\ \mathrm{d}\omega'' \\ &+\frac{i}{2\pi}\int_{-\infty}^{\infty} A^{<E}(\omega')\, B^{>E}(\omega)\, \frac{1}{\omega'-\omega-0^+}\ \mathrm{d}\omega' \\ &+\frac{1}{2}\left(A^{>E}(\omega)\, B^{<E}(\omega) - A^{<E}(\omega)\, B^{>E}(\omega)\right) \end{aligned} \tag{VI.98}$$

Integrate over ω:

$$\begin{aligned} \frac{1}{i\,2\pi}\int_{-\infty}^{\infty} C^{>E}(\omega)\, e^{-(\tau-\tau')\omega}\ \mathrm{d}\omega = &-\frac{1}{4\pi^2}\int_{-\infty}^{\infty} A^{>E}(\omega')\, B^{<E}(\omega'')\, \frac{e^{-(\tau-\tau')\omega'}}{\omega'-\omega''+0^+}\ \mathrm{d}\omega'\ \mathrm{d}\omega'' \\ &-\frac{1}{4\pi^2}\int_{-\infty}^{\infty} A^{>E}(\omega')\, B^{>E}(\omega'')\, \frac{e^{-(\tau-\tau')\omega''}}{\omega'-\omega''}\ \mathrm{d}\omega'\ \mathrm{d}\omega'' \\ &+\frac{1}{4\pi^2}\int_{-\infty}^{\infty} A^{>E}(\omega')\, B^{>E}(\omega'')\, \frac{e^{-(\tau-\tau')\omega'}}{\omega'-\omega''}\ \mathrm{d}\omega'\ \mathrm{d}\omega'' \\ &+\frac{1}{4\pi^2}\int_{-\infty}^{\infty} A^{<E}(\omega')\, B^{>E}(\omega'')\, \frac{e^{-(\tau-\tau')\omega''}}{\omega'-\omega''-0^+}\ \mathrm{d}\omega'\ \mathrm{d}\omega'' \end{aligned} \tag{VI.99}$$

Compare Eq. (VI.93) and Eq. (VI.99). They are the same.

VI.4.6 Matsubara Component, $\tau-\tau'<0$

Definition on L-shaped contour:

$$C_L^M(\tau-\tau') = -i\, G_{L,33}(\tau-\tau') \tag{VI.100}$$

$$= \int_{-\infty}^{\infty} A_L^M(\tau-\bar{\tau})\, B_L^M(\bar{\tau}-\tau')\ \mathrm{d}\bar{\tau} \tag{VI.101}$$

With integration limits:

$$
\begin{aligned}
&= \int_{-\infty}^{\tau} A_L^M(\tau-\bar{\tau})\, B_L^M(\bar{\tau}-\tau')\ \mathrm{d}\bar{\tau} \\
&\quad + \int_{\tau}^{\tau'} A_L^M(\tau-\bar{\tau})\, B_L^M(\bar{\tau}-\tau')\ \mathrm{d}\bar{\tau} \\
&\quad + \int_{\tau'}^{\infty} A_L^M(\tau-\bar{\tau})\, B_L^M(\bar{\tau}-\tau')\ \mathrm{d}\bar{\tau}
\end{aligned}
$$

Replace components:

$$
C_L^M(\tau-\tau') = -\frac{1}{4\pi^2}\int_{-\infty}^{\infty}\int_{-\infty}^{\infty}\int_{-\infty}^{\tau} A^{>E}(\omega')\, e^{-(\tau-\bar{\tau})\omega'}\, B^{<E}(\omega'')\, e^{-(\bar{\tau}-\tau')\omega''}\ \mathrm{d}\bar{\tau}\,\mathrm{d}\omega'\ \mathrm{d}\omega'' \tag{VI.102}
$$

$$
\begin{aligned}
&- \frac{1}{4\pi^2}\int_{-\infty}^{\infty}\int_{-\infty}^{\infty}\int_{\tau}^{\tau'} A^{<E}(\omega')\, e^{-(\tau-\bar{\tau})\omega'}\, B^{<E}(\omega'')\, e^{-(\bar{\tau}-\tau')\omega''}\ \mathrm{d}\bar{\tau}\,\mathrm{d}\omega'\ \mathrm{d}\omega'' \\
&- \frac{1}{4\pi^2}\int_{-\infty}^{\infty}\int_{-\infty}^{\infty}\int_{\tau'}^{\infty} A^{<E}(\omega')\, e^{-(\tau-\bar{\tau})\omega'}\, B^{>E}(\omega'')\, e^{-(\bar{\tau}-\tau')\omega''}\ \mathrm{d}\bar{\tau}\,\mathrm{d}\omega'\ \mathrm{d}\omega''
\end{aligned}
$$

$$
= -\frac{1}{4\pi^2}\int_{-\infty}^{\infty}\int_{-\infty}^{\infty} A^{>E}(\omega')\, B^{<E}(\omega'')\, \frac{e^{-(\tau-\tau')\omega''}}{\omega'-\omega''+0^+}\ \mathrm{d}\omega'\ \mathrm{d}\omega'' \tag{VI.103}
$$

$$
\begin{aligned}
&- \frac{1}{4\pi^2}\int_{-\infty}^{\infty}\int_{-\infty}^{\infty} A^{<E}(\omega')\, B^{<E}(\omega'')\frac{e^{-(\tau-\tau')\omega'} - e^{-(\tau-\tau')\omega''}}{\omega'-\omega''}\ \mathrm{d}\omega'\ \mathrm{d}\omega'' \\
&+ \frac{1}{4\pi^2}\int_{-\infty}^{\infty}\int_{-\infty}^{\infty} A^{<E}(\omega')\, B^{>E}(\omega'')\, \frac{e^{-(\tau-\tau')\omega'}}{\omega'-\omega''-0^+}\ \mathrm{d}\omega'\ \mathrm{d}\omega''
\end{aligned}
$$

Definition on the contour with two real time axes:

$$
\begin{aligned}
C^{<E}(t_E - t'_E) &= \int_{-\infty}^{t_E} A^{>E}(t_E-\bar{t})\, B^{<E}(\bar{t}-t'_E)\ \mathrm{d}\bar{t} \\
&\quad + \int_{t_E}^{t'_E} A^{<E}(t_E-\bar{t})\, B^{<E}(\bar{t}-t'_E)\ \mathrm{d}\bar{t} \\
&\quad + \int_{t'_E}^{-\infty} A^{<E}(t_E-\bar{t})\, B^{>E}(\bar{t}-t'_E)\ \mathrm{d}\bar{t}
\end{aligned} \tag{VI.104}
$$

Go to Fourier space inside of integrals and integrate over $\bar{t}_E$:

$$C^{<E}(t_E - t'_E) = \frac{1}{4\pi^2} \int_{-\infty}^{\infty} \int_{-\infty}^{\infty} \int_{-\infty}^{t_E} A^{>E}(\omega')\, e^{-i\omega'(t_E - \bar{t})}\, B^{<E}(\omega'')\, e^{-i\omega''(\bar{t} - t'_E)} \; \mathrm{d}\bar{t} \; \mathrm{d}\omega' \; \mathrm{d}\omega'' \tag{VI.105}$$

$$\begin{aligned}
&+ \frac{1}{4\pi^2} \int_{-\infty}^{\infty} \int_{-\infty}^{\infty} \int_{t_E}^{t'_E} A^{<E}(\omega')\, e^{-i\omega'(t_E - \bar{t})}\, B^{<E}(\omega'')\, e^{-i\omega''(\bar{t} - t'_E)} \; \mathrm{d}\bar{t} \; \mathrm{d}\omega' \; \mathrm{d}\omega'' \\
&+ \frac{1}{4\pi^2} \int_{-\infty}^{\infty} \int_{-\infty}^{\infty} \int_{t'_E}^{-\infty} A^{<E}(\omega')\, e^{-i\omega'(t_E - \bar{t})}\, B^{>E}(\omega'')\, e^{-i\omega''(\bar{t} - t'_E)} \; \mathrm{d}\bar{t} \; \mathrm{d}\omega' \; \mathrm{d}\omega''
\end{aligned}$$

$$\begin{aligned}
&= -\frac{i}{4\pi^2} \int_{-\infty}^{\infty} \int_{-\infty}^{\infty} A^{>E}(\omega')\, B^{<E}(\omega'')\, \frac{e^{-i(t_E - t'_E)\omega''}}{\omega' - \omega'' - i0^+} \; \mathrm{d}\omega' \; \mathrm{d}\omega'' \qquad \text{(VI.106)} \\
&\quad - \frac{i}{4\pi^2} \int_{-\infty}^{\infty} \int_{-\infty}^{\infty} A^{<E}(\omega')\, B^{<E}(\omega'')\, \frac{e^{-i(t_E - t'_E)\omega'} - e^{-i(t_E - t'_E)\omega''}}{\omega' - \omega''} \; \mathrm{d}\omega' \; \mathrm{d}\omega'' \\
&\quad + \frac{i}{4\pi^2} \int_{-\infty}^{\infty} \int_{-\infty}^{\infty} A^{<E}(\omega')\, B^{>E}(\omega'')\, \frac{e^{-i(t_E - t'_E)\omega'}}{\omega' - \omega'' - i0^+} \; \mathrm{d}\omega' \; \mathrm{d}\omega''
\end{aligned}$$

Go to Fourier space outside of integrals:

$$\begin{aligned}
C^{<E}(\omega) &= -\frac{i}{2\pi} \int_{-\infty}^{\infty} A^{>E}(\omega')\, B^{<E}(\omega)\, \frac{1}{\omega' - \omega - i0^+} \; \mathrm{d}\omega' \qquad \text{(VI.107)} \\
&\quad - \frac{i}{2\pi} \int_{-\infty}^{\infty} A^{<E}(\omega)\, B^{<E}(\omega'')\, \frac{1}{\omega - \omega''} \; \mathrm{d}\omega'' \\
&\quad + \frac{i}{2\pi} \int_{-\infty}^{\infty} A^{<E}(\omega')\, B^{<E}(\omega)\, \frac{1}{\omega' - \omega} \; \mathrm{d}\omega' \\
&\quad + \frac{i}{2\pi} \int_{-\infty}^{\infty} A^{<E}(\omega)\, B^{>E}(\omega'')\, \frac{1}{\omega - \omega'' - i0^+} \; \mathrm{d}\omega''
\end{aligned}$$

Use Sec. VI.3.2:

$$\begin{aligned}C^{<E}(\omega) = &-\frac{i}{2\pi}\int_{-\infty}^{\infty} A^{>E}(\omega')\, B^{<E}(\omega)\, \frac{1}{\omega'-\omega+0^+}\ \mathrm{d}\omega' \\ &- \frac{i}{2\pi}\int_{-\infty}^{\infty} A^{<E}(\omega)\, B^{<E}(\omega'')\, \frac{1}{\omega-\omega''}\ \mathrm{d}\omega'' \\ &+ \frac{i}{2\pi}\int_{-\infty}^{\infty} A^{<E}(\omega')\, B^{<E}(\omega)\, \frac{1}{\omega'-\omega}\ \mathrm{d}\omega' \\ &+ \frac{i}{2\pi}\int_{-\infty}^{\infty} A^{<E}(\omega)\, B^{>E}(\omega'')\, \frac{1}{\omega-\omega''-0^+}\ \mathrm{d}\omega'' \\ &+ \frac{1}{2}\left(A^{>E}(\omega)\, B^{<E}(\omega) - A^{<E}(\omega)\, B^{>E}(\omega)\right)\end{aligned} \tag{VI.108}$$

Integrate over ω:

$$\begin{aligned}&\frac{1}{i\,2\pi}\int_{-\infty}^{\infty} C^{<E}(\omega)\, e^{-(\tau-\tau')\omega}\ \mathrm{d}\omega = \\ &= -\frac{1}{4\pi^2}\int_{-\infty}^{\infty}\int_{-\infty}^{\infty} A^{>E}(\omega')\, B^{<E}(\omega'')\, \frac{e^{-(\tau-\tau')\omega''}}{\omega'-\omega''+0^+}\ \mathrm{d}\omega'\ \mathrm{d}\omega'' \\ &\quad - \frac{1}{4\pi^2}\int_{-\infty}^{\infty}\int_{-\infty}^{\infty} A^{<E}(\omega')\, B^{<E}(\omega'')\, \frac{e^{-(\tau-\tau')\omega'}}{\omega'-\omega''}\ \mathrm{d}\omega'\ \mathrm{d}\omega'' \\ &\quad + \frac{1}{4\pi^2}\int_{-\infty}^{\infty}\int_{-\infty}^{\infty} A^{<E}(\omega')\, B^{<E}(\omega'')\, \frac{e^{-(\tau-\tau')\omega''}}{\omega'-\omega''}\ \mathrm{d}\omega'\ \mathrm{d}\omega'' \\ &\quad + \frac{1}{4\pi^2}\int_{-\infty}^{\infty}\int_{-\infty}^{\infty} A^{<E}(\omega')\, B^{>E}(\omega'')\, \frac{e^{-(\tau-\tau')\omega'}}{\omega'-\omega''-0^+}\ \mathrm{d}\omega'\ \mathrm{d}\omega''\end{aligned} \tag{VI.109}$$

Compare Eq. (VI.103) and Eq. (VI.109). They are the same.

VI.4.7 Greater and Lesser Non-Equilibrium Component

Definition of greater component on L-shaped contour:

$$\begin{aligned}
C_L^{>N}(t_N,t_N') = &\int_0^{t_N'} A_L^{>N}(t_N,\bar t_N)\, B_L^{<N}(\bar t_N,t_N')\;\mathrm{d}\bar t_N \\
&+ \int_{t_N'}^{t_N} A_L^{>N}(t_N,\bar t_N)\, B_L^{>N}(\bar t_N,t_N')\;\mathrm{d}\bar t_N \\
&+ \int_{t_N}^{0} A_L^{<N}(t_N,\bar t_N)\, B_L^{>N}(\bar t_N,t_N')\;\mathrm{d}\bar t_N \\
&- i\int_{-\infty}^{\infty} A_L^{\urcorner}(t_N,\bar\tau)\, B_L^{\ulcorner}(\bar\tau,t_N')\;\mathrm{d}\bar\tau
\end{aligned} \tag{VI.110}$$

Definition of lesser component on L-shaped contour:

$$\begin{aligned}
C_L^{<N}(t_N,t_N') = &\int_0^{t_N} A_L^{>N}(t_N,\bar t_N)\, B_L^{<N}(\bar t_N,t_N')\;\mathrm{d}\bar t_N \\
&+ \int_{t_N}^{t_N'} A_L^{<N}(t_N,\bar t_N)\, B_L^{<N}(\bar t_N,t_N')\;\mathrm{d}\bar t_N \\
&+ \int_{t_N'}^{0} A_L^{<N}(t_N,\bar t_N)\, B_L^{>N}(\bar t_N,t_N')\;\mathrm{d}\bar t_N \\
&- i\int_{-\infty}^{\infty} A_L^{\urcorner}(t_N,\bar\tau)\, B_L^{\ulcorner}(\bar\tau,t_N')\;\mathrm{d}\bar\tau
\end{aligned} \tag{VI.111}$$

Definition of greater component on the contour with two real time axes:

$$\begin{aligned}
C^{>N}(t_N,t_N') = &\int_{-\infty}^{0} A^{\lrcorner}(t_N,\bar t_E)\, B^{\llcorner}(\bar t_E,t_N')\;\mathrm{d}\bar t_E \\
&+ \int_0^{t_N'} A^{>N}(t_N,\bar t_N)\, B^{<N}(\bar t_N,t_N')\;\mathrm{d}\bar t_N \\
&+ \int_{t_N'}^{t_N} A^{>N}(t_N,\bar t_N)\, B^{>N}(\bar t_N,t_N')\;\mathrm{d}\bar t_N \\
&+ \int_{t_N}^{0} A^{<N}(t_N,\bar t_N)\, B^{>N}(\bar t_N,t_N')\;\mathrm{d}\bar t_N \\
&+ \int_0^{-\infty} A^{\urcorner}(t_N,\bar t_E)\, B^{\ulcorner}(\bar t_E,t_N')\;\mathrm{d}\bar t_E
\end{aligned} \tag{VI.112}$$

Definition of lesser component on the contour with two real time axes:

$$\begin{align}
C^{<N}(t_N, t'_N) = &\int_{-\infty}^{0} A^{\lrcorner}(t_N, \bar{t}_E)\, B^{\llcorner}(\bar{t}_E, t'_N)\ \mathrm{d}\bar{t}_E \tag{VI.113}\\
&+ \int_{0}^{t_N} A^{>N}(t_N, \bar{t}_N)\, B^{<N}(\bar{t}_N, t'_N)\ \mathrm{d}\bar{t}_N \tag{VI.114}\\
&+ \int_{t_N}^{t'_N} A^{<N}(t_N, \bar{t}_N)\, B^{<N}(\bar{t}_N, t'_N)\ \mathrm{d}\bar{t}_N \notag\\
&+ \int_{t'_N}^{0} A^{<N}(t_N, \bar{t}_N)\, B^{>N}(\bar{t}_N, t'_N)\ \mathrm{d}\bar{t}_N \notag\\
&+ \int_{0}^{-\infty} A^{\urcorner}(t_N, \bar{t}_E)\, B^{\ulcorner}(\bar{t}_E, t'_N)\ \mathrm{d}\bar{t}_E \notag
\end{align}$$

As we assumed $A_L^{>N} = A^{>N}$, $B_L^{>N} = B^{>N}$, $A_L^{<N} = A^{<N}$, and $B_L^{<N} = B^{<N}$, we only need to show:

$$\begin{align}
-i \int_{-\infty}^{\infty} A_L^{\urcorner}(t_N, \bar{\tau})\, B_L^{\ulcorner}(\bar{\tau}, t'_N)\ \mathrm{d}\bar{\tau} \overset{?}{=} &\int_{-\infty}^{0} A^{\lrcorner}(t_N, \bar{t}_E)\, B^{\llcorner}(\bar{t}_E, t'_N)\ \mathrm{d}\bar{t}_E \tag{VI.115}\\
&+ \int_{0}^{-\infty} A^{\urcorner}(t_N, \bar{t}_E)\, B^{\ulcorner}(\bar{t}_E, t'_N)\ \mathrm{d}\bar{t}_E \notag
\end{align}$$

Replace integration limits of left hand side of Eq. (VI.115):

$$\begin{aligned}
-i \int_{-\infty}^{\infty} A_L^{\urcorner}(t_N, \bar{\tau})\, B_L^{\ulcorner}(\bar{\tau}, t'_N)\ \mathrm{d}\bar{\tau} = &-i \int_{-\infty}^{0} A_L^{\urcorner}(t_N, \bar{\tau})\, B_L^{\ulcorner}(\bar{\tau}, t'_N)\ \mathrm{d}\bar{\tau}\\
&- i \int_{0}^{\infty} A_L^{\urcorner}(t_N, \bar{\tau})\, B_L^{\ulcorner}(\bar{\tau}, t'_N)\ \mathrm{d}\bar{\tau}
\end{aligned}$$

Replace components:

$$
\begin{aligned}
&-i\int_{-\infty}^{\infty} A^{\urcorner}_{L}(t_N,\bar{\tau})\, B^{\ulcorner}_{L}(\bar{\tau},t'_N)\ \mathrm{d}\bar{\tau} = \qquad \text{(VI.116)}\\
&\quad = -\frac{i}{4\pi^2}\int_{-\infty}^{\infty}\int_{-\infty}^{\infty}\int_{-\infty}^{0} A^{\lrcorner}(t_N,\omega')\, e^{-\bar{\tau}\omega'}\ B^{\llcorner}(\omega'',t'_N)\, e^{-\bar{\tau}\omega''}\ \mathrm{d}\bar{\tau}\,\mathrm{d}\omega'\ \mathrm{d}\omega''\\
&\qquad - \frac{i}{4\pi^2}\int_{-\infty}^{\infty}\int_{-\infty}^{\infty}\int_{0}^{\infty} A^{\urcorner}(t_N,\omega')\, e^{-\bar{\tau}\omega'}\ B^{\ulcorner}(\omega'',t'_N)\, e^{-\bar{\tau}\omega''}\ \mathrm{d}\bar{\tau}\,\mathrm{d}\omega'\ \mathrm{d}\omega''\\
&\quad = \frac{i}{4\pi^2}\int_{-\infty}^{\infty}\int_{-\infty}^{\infty} A^{\lrcorner}(t_N,\omega')\, B^{\llcorner}(\omega'',t'_N)\,\frac{1}{\omega'+\omega''-0^+}\ \mathrm{d}\omega'\ \mathrm{d}\omega'' \qquad \text{(VI.117)}\\
&\qquad - \frac{i}{4\pi^2}\int_{-\infty}^{\infty}\int_{-\infty}^{\infty} A^{\urcorner}(t_N,\omega')\, B^{\ulcorner}(\omega'',t'_N)\,\frac{1}{\omega'+\omega''+0^+}\ \mathrm{d}\omega'\ \mathrm{d}\omega''
\end{aligned}
$$

Right hand side of Eq. (VI.115), go to Fourier space inside of integrals and integrate over $\bar{t}_E$:

$$
\begin{aligned}
&\int_{-\infty}^{0} A^{\lrcorner}(t_N,\bar{t}_E)\, B^{\llcorner}(\bar{t}_E,t'_N)\ \mathrm{d}\bar{t}_E + \int_{0}^{-\infty} A^{\urcorner}(t_N,\bar{t}_E)\, B^{\ulcorner}(\bar{t}_E,t'_N)\ \mathrm{d}\bar{t}_E = \qquad \text{(VI.118)}\\
&\quad = +\frac{1}{4\pi^2}\int_{-\infty}^{\infty}\int_{-\infty}^{\infty}\int_{-\infty}^{0} A^{\lrcorner}(t_N,\omega')\, e^{-i\omega'\bar{t}_E}\, B^{\llcorner}(\omega'',t'_N)\, e^{-i\omega''\bar{t}_E}\ \mathrm{d}\bar{t}_E\ \mathrm{d}\omega'\ \mathrm{d}\omega''\\
&\qquad + \frac{1}{4\pi^2}\int_{-\infty}^{\infty}\int_{-\infty}^{\infty}\int_{0}^{-\infty} A^{\urcorner}(t_N,\omega')\, e^{-i\omega'\bar{t}_E}\, B^{\ulcorner}(\omega'',t'_N)\, e^{-i\omega''\bar{t}_E}\ \mathrm{d}\bar{t}_E\ \mathrm{d}\omega'\ \mathrm{d}\omega''\\
&\quad = \frac{i}{4\pi^2}\int_{-\infty}^{\infty}\int_{-\infty}^{\infty} A^{\lrcorner}(t_N,\omega')\, B^{\llcorner}(\omega'',t'_N)\,\frac{1}{\omega'+\omega''+i0^+}\ \mathrm{d}\omega'\ \mathrm{d}\omega'' \qquad \text{(VI.119)}\\
&\qquad - \frac{i}{4\pi^2}\int_{-\infty}^{\infty}\int_{-\infty}^{\infty} A^{\urcorner}(t_N,\omega')\, B^{\ulcorner}(\omega'',t'_N)\,\frac{1}{\omega'+\omega''+i0^+}\ \mathrm{d}\omega'\ \mathrm{d}\omega''
\end{aligned}
$$

Use Sec. VI.3.2:

$$
\begin{aligned}
&\int_{-\infty}^{0} A^{\lrcorner}(t_N,\bar{t}_E)\, B^{\llcorner}(\bar{t}_E,t'_N)\ \mathrm{d}\bar{t}_E + \int_{0}^{-\infty} A^{\urcorner}(t_N,\bar{t}_E)\, B^{\ulcorner}(\bar{t}_E,t'_N)\ \mathrm{d}\bar{t}_E = \qquad \text{(VI.120)}\\
&\quad = \frac{i}{4\pi^2}\int_{-\infty}^{\infty}\int_{-\infty}^{\infty} A^{\lrcorner}(t_N,\omega')\, B^{\llcorner}(\omega'',t'_N)\,\frac{1}{\omega'+\omega''-0^+}\ \mathrm{d}\omega'\ \mathrm{d}\omega''\\
&\qquad - \frac{i}{4\pi^2}\int_{-\infty}^{\infty}\int_{-\infty}^{\infty} A^{\urcorner}(t_N,\omega')\, B^{\ulcorner}(\omega'',t'_N)\,\frac{1}{\omega'+\omega''+0^+}\ \mathrm{d}\omega'\ \mathrm{d}\omega''\\
&\qquad + \underbrace{\frac{1}{4}\int_{-\infty}^{\infty}\left(A^{\lrcorner}(t_N,\omega')\, B^{\llcorner}(-\omega',t'_N) - A^{\urcorner}(t_N,\omega')\, B^{\ulcorner}(-\omega',t'_N)\right)\mathrm{d}\omega'}_{=0,\text{by assumption}}
\end{aligned}
$$

Compare Eq. (VI.117) and Eq. (VI.120). They are the same.

VII References

[1] R. O. Jones, "Density functional theory: Its origins, rise to prominence, and future," Reviews of Modern Physics **87**, 897–923 (2015).

[2] R. Pariser and R. G. Parr, "A semi-empirical theory of the electronic spectra and electronic structure of complex unsaturated molecules. i." The Journal of Chemical Physics **21**, 466–471 (1953).

[3] R. Pariser and R. G. Parr, "A semi-empirical theory of the electronic spectra and electronic structure of complex unsaturated molecules. II," The Journal of Chemical Physics **21**, 767–776 (1953).

[4] J. Hubbard, "Electron correlations in narrow energy bands," Proceedings of the Royal Society of London. Series A. Mathematical and Physical Sciences **276**, 238–257 (1963).

[5] A. Georges, "Strongly correlated electron materials: Dynamical mean-field theory and electronic structure," in *AIP Conference Proceedings* (AIP, 2004) pp. 3–74.

[6] D. Vollhardt, K. Byczuk, and M. Kollar, "Dynamical mean-field theory," in *Springer Series in Solid-State Sciences* (Springer Berlin Heidelberg, 2011) pp. 203–236.

[7] H. Park, A. J. Millis, and C. A. Marianetti, "Computing total energies in complex materials using charge self-consistent DFT + DMFT," Physical Review B **90**, 235103 (2014).

[8] A. Paul and T. Birol, "Applications of DFT + DMFT in materials science," Annual Review of Materials Research **49**, 31–52 (2019).

[9] H. Tasaki, "The hubbard model - an introduction and selected rigorous results," Journal of Physics: Condensed Matter **10**, 4353–4378 (1998).

[10] B. Keimer, S. A. S. A. Kivelson, M. R. Norman, S. Uchida, and J. Zaanen, "From quantum matter to high-temperature superconductivity in copper oxides," Nature **518**, 179–186 (2015).

[11] N. F. Mott, "Review lecture: Metal–insulator transitions," Proceedings of the Royal Society of London. A. Mathematical and Physical Sciences **382**, 1–24 (1982).

[12] E. H. Lieb and F. Y. Wu, "Absence of mott transition in an exact solution of the short-range, one-band model in one dimension," Physical Review Letters **20**, 1445–1448 (1968).

[13] E. H. Lieb and F. Y. Wu, "Absence of mott transition in an exact solution of the short-range, one-band model in one dimension," Physical Review Letters **21**, 192–192 (1968).

[14] R. D. Mattuck, *A Guide to Feynman Diagrams in the Many-Body Problem: Second Edition* (Dover Publications, 1992).

[15] C. Caroli, D. Lederer-Rozenblatt, B. Roulet, and D. Saint-James, "Inelastic effects in photoemission: Microscopic formulation and qualitative discussion," Physical Review B **8**, 4552–4569 (1973).

[16] P. J. Feibelman and D. E. Eastman, "Photoemission spectroscopy—correspondence between quantum theory and experimental phenomenology," Physical Review B **10**, 4932–4947 (1974).

[17] C. A. Ashley and S. Doniach, "Theory of extended x-ray absorption edge fine structure (EXAFS) in crystalline solids," Physical Review B **11**, 1279–1288 (1975).

[18] C. Kittel, *Introduction to Solid State Physics.* (John Wiley & Sons, 1966).

[19] J. W. Negele and H. Orland, *Quantum Many-particle Systems* (CRC Press, 1998).

[20] S. Pairault, D. Sénéchal, and A.-M. S. Tremblay, "Strong-coupling perturbation theory of the hubbard model," The European Physical Journal B **16**, 85–105 (2000).

[21] L. Bartosch, M. Kollar, and P. Kopietz, "Ferromagnetic luttinger liquids," Physical Review B **67**, 092403 (2003).

[22] M. Kollar, F. A. Wolf, and M. Eckstein, "Generalized gibbs ensemble prediction of prethermalization plateaus and their relation to nonthermal steady states in integrable systems," Physical Review B **84**, 054304 (2011).

[23] A. J. Cohen, P. Mori-Sánchez, and W. Yang, "Challenges for density functional theory," Chemical Reviews **112**, 289–320 (2011).

[24] C. Lanczos, "An iteration method for the solution of the eigenvalue problem of linear differential and integral operators," Journal of Research of the National Bureau of Standards **45**, 255 (1950).

[25] W. M. C. Foulkes, L. Mitas, R. J. Needs, and G. Rajagopal, "Quantum monte carlo simulations of solids," Reviews of Modern Physics **73**, 33–83 (2001).

[26] S. R. White, "Density matrix formulation for quantum renormalization groups," Physical Review Letters **69**, 2863–2866 (1992).

[27] G. Vidal, "Efficient simulation of one-dimensional quantum many-body systems," Physical Review Letters **93**, 040502 (2004).

[28] S. R. Manmana, A. Muramatsu, and R. M. Noack, "Time evolution of one-dimensional quantum many body systems," in *AIP Conference Proceedings* (AIP, 2005) pp. 269–278.

[29] S. Paeckel, T. Köhler, A. Swoboda, S. R. Manmana, U. Schollwöck, and C. Hubig, "Time-evolution methods for matrix-product states," Annals of Physics **411**, 167998 (2019).

[30] U. Schollwöck, "The density-matrix renormalization group in the age of matrix product states," Annals of Physics **326**, 96–192 (2011).

[31] J. Haegeman, C. Lubich, I. Oseledets, B. Vandereycken, and F. Verstraete, "Unifying time evolution and optimization with matrix product states," Physical Review B **94**, 165116 (2016).

[32] W. Metzner and D. Vollhardt, "Correlated lattice fermions in $d{=}\infty$ dimensions," Physical Review Letters **62**, 324–327 (1989).

[33] A. Georges and G. Kotliar, "Hubbard model in infinite dimensions," Physical Review B **45**, 6479–6483 (1992).

[34] G. Kotliar, S. Y. Savrasov, K. Haule, V. S. Oudovenko, O. Parcollet, and C. A. Marianetti, "Electronic structure calculations with dynamical mean-field theory," Reviews of Modern Physics **78**, 865–951 (2006).

[35] O. Parcollet, M. Ferrero, T. Ayral, H. Hafermann, I. Krivenko, L. Messio, and P. Seth, "TRIQS: A toolbox for research on interacting quantum systems," Computer Physics Communications **196**, 398–415 (2015).

[36] I. A. Nekrasov, K. Held, G. Keller, D. E. Kondakov, Th. Pruschke, M. Kollar, O. K. Andersen, V. I. Anisimov, and D. Vollhardt, "Momentum-resolved spectral functions of SrVO3 calculated by LDA+DMFT," Physical Review B **73**, 115131 (2006).

[37] X. Ren, I. Leonov, G. Keller, M. Kollar, I. Nekrasov, and D. Vollhardt, "LDA+DMFT computation of the electronic spectrum of NiO," Physical Review B **74**, 195114 (2006).

[38] M. Zingl, E. Assmann, P. Seth, I. Krivenko, and M. Aichhorn, "Importance of effective dimensionality in manganese pnictides," Physical Review B **94**, 045130 (2016).

[39] E. Gull, A. J. Millis, A. I. Lichtenstein, A. N. Rubtsov, M. Troyer, and P. Werner, "Continuous-time monte carlo methods for quantum impurity models," Reviews of Modern Physics **83**, 349–404 (2011).

[40] R. Bulla, T. A. Costi, and T. Pruschke, "Numerical renormalization group method for quantum impurity systems," Reviews of Modern Physics **80**, 395–450 (2008).

[41] D. Bauernfeind, M. Zingl, R. Triebl, M. Aichhorn, and H. G. Evertz, "Fork tensor-product states: Efficient multiorbital real-time DMFT solver," Physical Review X **7**, 031013 (2017).

[42] H. Aoki, N. Tsuji, M. Eckstein, M. Kollar, T. Oka, and P. Werner, "Nonequilibrium dynamical mean-field theory and its applications," Reviews of Modern Physics **86**, 779–837 (2014).

[43] R. Peierls, "Zur theorie des diamagnetismus von leitungselektronen," Zeitschrift für Physik **80**, 763–791 (1933).

[44] M. Troyer and U.-J. Wiese, "Computational complexity and fundamental limitations to fermionic quantum monte carlo simulations," Physical Review Letters **94**, 170201 (2005).

[45] G. Cohen, E. Gull, D. R. Reichman, and A. J. Millis, "Taming the dynamical sign problem in real-time evolution of quantum

many-body problems," Physical Review Letters **115**, 266802 (2015).

[46] M. Eckstein and P. Werner, "Nonequilibrium dynamical mean-field calculations based on the noncrossing approximation and its generalizations," Physical Review B **82**, 115115 (2010).

[47] C. Lin and A. A. Demkov, "Quench dynamics of anderson impurity model using configuration interaction method," Physical Review B **92**, 155135 (2015).

[48] A. Dorda, M. Nuss, W. von der Linden, and E. Arrigoni, "Auxiliary master equation approach to nonequilibrium correlated impurities," Physical Review B **89**, 165105 (2014).

[49] C. Gramsch, K. Balzer, M. Eckstein, and M. Kollar, "Hamiltonian-based impurity solver for nonequilibrium dynamical mean-field theory," Physical Review B **88**, 235106 (2013).

[50] M. Eckstein, *Nonequilibrium dynamical mean-field theory*, Ph.D. thesis, Universität Augsburg (2009).

[51] F. A. Wolf, I. P. McCulloch, and U. Schollwöck, "Solving nonequilibrium dynamical mean-field theory using matrix product states," Physical Review B **90**, 235131 (2014).

[52] M. Eckstein, M. Kollar, and P. Werner, "Thermalization after an interaction quench in the hubbard model," Physical Review Letters **103**, 056403 (2009).

[53] M. Eckstein, M. Kollar, and P. Werner, "Interaction quench in the hubbard model: Relaxation of the spectral function and the optical conductivity," Physical Review B **81**, 115131 (2010).

[54] P. Wissgott, J. Kuneš, A. Toschi, and K. Held, "Dipole matrix element approach versus peierls approximation for optical conductivity," Physical Review B **85**, 205133 (2012).

[55] P. Werner, K. Held, and M. Eckstein, "Role of impact ionization in the thermalization of photoexcited mott insulators," Physical Review B **90**, 235102 (2014).

[56] H. Hashimoto and S. Ishihara, "Photoinduced correlated electron dynamics in a two-leg ladder hubbard system," Physical Review B **93**, 165133 (2016).

[57] M. Innerberger, P. Worm, P. Prauhardt, and A. Kauch, "Electron-light interaction in nonequilibrium–exact diagonalization for time dependent hubbard hamiltonians," arXiv preprint arXiv:2005.13498 (2020).

[58] A. Kauch, P. Worm, P. Prauhart, M. Innerberger, C. Watzenböck, and K. Held, "Enhancement of impact ionization in hubbard clusters by disorder and next-nearest-neighbor hopping," (2020), in preparation.

[59] W. Shockley and H. J. Queisser, "Detailed balance limit of efficiency of p-n junction solar cells," Journal of Applied Physics **32**, 510–519 (1961).

[60] P. T. Landsberg, H. Nussbaumer, and G. Willeke, "Band-band impact ionization and solar cell efficiency," Journal of Applied Physics **74**, 1451–1452 (1993).

[61] M. E. Sorantin, A. Dorda, K. Held, and E. Arrigoni, "Impact ionization processes in the steady state of a driven mott-insulating layer coupled to metallic leads," Physical Review B **97**, 115113 (2018).

[62] F. Petocchi, S. Beck, C. Ederer, and P. Werner, "Hund excitations and the efficiency of mott solar cells," Physical Review B **100**, 075147 (2019).

[63] M. Wais, M. Eckstein, R. Fischer, P. Werner, M. Battiato, and K. Held, "Quantum boltzmann equation for strongly correlated systems: Comparison to dynamical mean field theory," Physical Review B **98**, 134312 (2018).

[64] A. Georges, G. Kotliar, W. Krauth, and M. J. Rozenberg, "Dynamical mean-field theory of strongly correlated fermion systems and the limit of infinite dimensions," Reviews of Modern Physics **68**, 13–125 (1996).

[65] E. Manousakis, "Photovoltaic effect for narrow-gap mott insulators," Physical Review B **82**, 125109 (2010).

[66] P. Calabrese, F. H. L. Essler, and G. Mussardo, "Introduction to 'quantum integrability in out of equilibrium systems'," Journal of Statistical Mechanics: Theory and Experiment **2016**, 064001 (2016).

[67] F. J. Ohkawa, "Electron correlation in the hubbard modelind$=\infty$ dimension," Journal of the Physical Society of Japan **60**, 3218–3221 (1991).

[68] M. Ganahl, P. Thunström, F. Verstraete, K. Held, and H. G. Evertz, "Chebyshev expansion for impurity models using matrix product states," Physical Review B **90**, 045144 (2014).

[69] M. Ganahl, M. Aichhorn, H. G. Evertz, P. Thunström, K. Held, and F. Verstraete, "Efficient DMFT impurity solver using real-time dynamics with matrix product states," Physical Review B **92**, 155132 (2015).

[70] F. A. Wolf, I. P. McCulloch, O. Parcollet, and U. Schollwöck, "Chebyshev matrix product state impurity solver for dynamical mean-field theory," Physical Review B **90**, 115124 (2014).

[71] D. Bauernfeind, R. Triebl, M. Zingl, M. Aichhorn, and H. G. Evertz, "Dynamical mean-field theory on the real-frequency axis: p-d hybridization and atomic physics in SrMnO3," Physical Review B **97**, 115156 (2018).

[72] Stoudenmirem E. M. and S. R. White, "Minimally entangled typical thermal state algorithms," New Journal of Physics **12**, 055026 (2010).

[73] M. Suzuki, "Fractal decomposition of exponential operators with applications to many-body theories and monte carlo simulations," Physics Letters A **146**, 319–323 (1990).

[74] J. K. Freericks, V. M. Turkowski, and V. Zlatić, "Nonequilibrium dynamical mean-field theory," Physical Review Letters **97**, 266408 (2006).

[75] V. M. Turkowski and J. K. Freericks, "Nonequilibrium dynamical mean-field theory of strongly correlated electrons," in *Strongly Correlated Systems, Coherence and Entanglement* (WORLD SCIENTIFIC, 2007) pp. 187–210.

[76] M. Eckstein and M. Kollar, "Nonthermal steady states after an interaction quench in the falicov-kimball model," Physical Review Letters **100**, 120404 (2008).

[77] U. Brandt and C. Mielsch, "Thermodynamics and correlation functions of the falicov-kimball model in large dimensions," Zeitschrift für Physik B Condensed Matter **75**, 365–370 (1989).

[78] P. G. J. van Dongen and D. Vollhardt, "Exact mean-field hamiltonian for fermionic lattice models in high dimensions," Physical Review Letters **65**, 1663–1666 (1990).

[79] P. G. J. van Dongen, "Exact mean-field theory of the extended simplified hubbard model," Physical Review B **45**, 2267–2281 (1992).

[80] V. Turkowski and J. K. Freericks, "Nonequilibrium sum rules for the retarded self-energy of strongly correlated electrons," Physical Review B **77**, 205102 (2008).

[81] M. Eckstein and M. Kollar, "Theory of time-resolved optical spectroscopy on correlated electron systems," Physical Review B **78**, 205119 (2008).

[82] M. Eckstein and M. Kollar, "Measuring correlated electron dynamics with time-resolved photoemission spectroscopy," Physical Review B **78**, 245113 (2008).

[83] P. Werner, T. Oka, and A. J. Millis, "Diagrammatic monte carlo simulation of nonequilibrium systems," Physical Review B **79**, 035320 (2009).

[84] M. Schiró, "Real-time dynamics in quantum impurity models with diagrammatic monte carlo," Physical Review B **81**, 085126 (2010).

[85] The main author explained via email that their method could potentially be used to simulate entangled initial states at finite temperature.

[86] D. Zgid, E. Gull, and G. K.-L. Chan, "Truncated configuration interaction expansions as solvers for correlated quantum impurity models and dynamical mean-field theory," Physical Review B **86**, 165128 (2012).

[87] M Schüler, D. Golež, Y. Murakami, N. Bittner, A. Herrmann, H. U. R. Strand, P. Werner, and M. Eckstein, "NESSi: The non-equilibrium systems simulation package," Computer Physics Communications **257**, 107484 (2020).

[88] D. Vollhardt, "Dynamical mean-field theory for correlated electrons," Annalen der Physik **524**, 1–19 (2011).

[89] P. Coleman, *Introduction to many-body physics* (Cambridge University Press, 2015).

[90] It may help the reader as a mnemonic to note that the greater and right-mixing component have the same order of operators in the expectation value. The only difference is the position of the time argument of the annihilation operator on the contour. A similar observation can be made for the lesser and left-mixing component.

[91] G. Stefanucci and R. van Leeuwen, *Nonequilibrium Many-Body Theory of Quantum Systems* (Cambridge University Press, 2009).

[92] H. Bruus and K. Flensberg, *Many-Body Quantum Theory in Condensed Matter Physics: An Introduction* (Oxford University Press, 2004).

[93] H. Haug and A.-P. Jauho, *Quantum Kinetics in Transport and Optics of Semiconductors* (Springer Berlin Heidelberg, 2008).

[94] L. V. Keldysh, "Diagram technique for nonequilibrium processes," Sov. Phys. JETP **20**, 1018–1026 (1965).

[95] R. N. Silver, D. S. Sivia, and J. E. Gubernatis, "Maximum-entropy method for analytic continuation of quantum monte carlo data," Physical Review B **41**, 2380–2389 (1990).

[96] M. Rumetshofer, D. Bauernfeind, and W. von der Linden, "Bayesian parametric analytic continuation of green's functions," Physical Review B **100**, 075137 (2019).

[97] R. N. Bracewell and R. N. Bracewell, *The Fourier transform and its applications*, Vol. 31999 (McGraw-Hill New York, 1986).

[98] S. R. White and I. Affleck, "Spectral function for the S=1 heisenberg antiferromagetic chain," Physical Review B **77**, 134437 (2008).

[99] T. Barthel, U. Schollwöck, and S. R. White, "Spectral functions in one-dimensional quantum systems at finite temperature using the density matrix renormalization group," Physical Review B **79**, 245101 (2009).

[100] H. Krishna-murthy, J. Wilkins, and K. Wilson, "Renormalization-group approach to the anderson model of dilute magnetic alloys. i. static properties for the symmetric case," Physical Review B **21**, 1003–1043 (1980).

[101] H. Krishna-murthy, J. Wilkins, and K. Wilson, "Renormalization-group approach to the anderson model of dilute magnetic alloys. II. static properties for the asymmetric case," Physical Review B **21**, 1044–1083 (1980).

[102] M. Eckstein and P. Werner, "Photoinduced states in a mott insulator," Physical Review Letters **110**, 126401 (2013).

[103] N. E. Bickers, "Review of techniques in the large-nexpansion for dilute magnetic alloys," Reviews of Modern Physics **59**, 845–939 (1987).

[104] E. Müller-Hartmann, "Self-consistent perturbation theory of the anderson model: Ground state properties," Zeitschrift für Physik B Condensed Matter **57**, 281–287 (1984).

[105] A. Holzner, A. Weichselbaum, I. P. McCulloch, U. Schollwöck, and J. von Delft, "Chebyshev matrix product state approach for spectral functions," Physical Review B **83**, 195115 (2011).

[106] N.-O. Linden, M. Zingl, C. Hubig, O. Parcollet, and U. Schollwöck, "Imaginary-time matrix product state impurity solver in a real material calculation: Spin-orbit coupling in Sr2RuO4," Physical Review B **101**, 041101 (2020).

[107] M. Fishman, S. R. White, and E. M. Stoudenmire, "The itensor software library for tensor network calculations," (2020), arXiv:2007.14822.

[108] "Erwin Schrödinger," `https://commons.wikimedia.org/wiki/File:Erwin_Schr%C3%B6dinger_(1933).jpg`, accessed: 2021-01-12.

[109] M. P. Zaletel, R. S. K. Mong, C. Karrasch, J. E. Moore, and F. Pollmann, "Time-evolving a matrix product state with long-ranged interactions," Physical Review B **91**, 165112 (2015).

[110] D. Bauernfeind, *Fork Tensor Product States: Efficient Multi-Orbital Impurity Solver for Dynamical Mean Field Theory*, Ph.D. thesis, Technische Universität Graz (2018).

[111] This data is not present in the referenced publication and was sent to us by Martin Eckstein and Marcus Kollar.

[112] D. Thain, T. Tannenbaum, and M. Livny, "Distributed computing in practice: the condor experience," Concurrency and Computation: Practice and Experience **17**, 323–356 (2005).

[113] F. Maislinger and H. G. Evertz, "Impact ionization and multiple photon absorptions in the two-dimensionalphotoexcited hubbard model," arXiv preprint arXiv:2007.16201 (2020).

[114] D. M. Kennes, C. Karrasch, and A. J. Millis, "Loschmidt-amplitude wave function spectroscopy and the physics of dynamically driven phase transitions," Physical Review B **101**, 081106(R) (2020).

[115] T. E. Oliphant, *A guide to NumPy*, Vol. 1 (Trelgol Publishing USA, 2006).

[116] S. van der Walt, S. C. Colbert, and G. Varoquaux, "The NumPy array: A structure for efficient numerical computation," Computing in Science & Engineering **13**, 22–30 (2011).

[117] E. Jones, T. Oliphant, P. Peterson, *et al.*, "SciPy: Open source scientific tools for Python," (2001–), from which we employed the routine *expm_multiply* for the time evolution operator.

[118] N. E. Bickers, D. J. Scalapino, and S. R. White, "Conserving approximations for strongly correlated electron systems: Bethe-

salpeter equation and dynamics for the two-dimensional hubbard model," Physical Review Letters **62**, 961–964 (1989).

[119] R. D. Schaller and V. I. Klimov, "High efficiency carrier multiplication in PbSe nanocrystals: Implications for solar energy conversion," Physical Review Letters **92**, 186601 (2004).

[120] R. J. Ellingson, M. C. Beard, J. C. Johnson, P. Yu, O. I. Micic, A. J. Nozik, A. Shabaev, and A. L. Efros, "Highly efficient multiple exciton generation in colloidal PbSe and PbS quantum dots," Nano Letters **5**, 865–871 (2005).

[121] O. E. Semonin, J. M. Luther, S. Choi, H.-Y. Chen, J. Gao, A. J. Nozik, and M. C. Beard, "Peak external photocurrent quantum efficiency exceeding 100% via MEG in a quantum dot solar cell," Science **334**, 1530–1533 (2011).

[122] J. M. Pietryga, Y.-S. Park, J. Lim, A. F. Fidler, W. K. Bae, S. Brovelli, and V. I. Klimov, "Spectroscopic and device aspects of nanocrystal quantum dots," Chemical Reviews **116**, 10513–10622 (2016).

[123] E. Assmann, P. Blaha, R. Laskowski, K. Held, S. Okamoto, and G. Sangiovanni, "Oxide heterostructures for efficient solar cells," Physical Review Letters **110**, 078701 (2013).

[124] E. Manousakis, "Optimizing the role of impact ionization in conventional insulators," Scientific Reports **9**, 1–8 (2019).

[125] A. Manzi, Y. Tong, J. Feucht, E.-P. Yao, L. Polavarapu, A. S. Urban, and J. Feldmann, "Resonantly enhanced multiple exciton generation through below-band-gap multi-photon absorption in perovskite nanocrystals," Nature Communications **9**, 1–6 (2018).

[126] H. I. Wang, M. Bonn, and E. Cánovas, "Boosting biexciton collection efficiency at quantum dot–oxide interfaces by hole localization at the quantum dot shell," The Journal of Physical Chemistry Letters **8**, 2654–2658 (2017).

[127] H. Goodwin, T. C. Jellicoe, N. J. L. K. Davis, and M. L. Böhm, "Multiple exciton generation in quantum dot-based solar cells," Nanophotonics **7**, 111–126 (2018).

[128] J. Holleman, M. M. Bishop, C. Garcia, J. S. R. Vellore Winfred, S. Lee, H. N. Lee, C. Beekman, E. Manousakis, and S. A. McGill, "Evidence for impact ionization in vanadium dioxide," Physical Review B **94**, 155129 (2016).

[129] A. Franceschetti, J. M. An, and A. Zunger, "Impact ionization can explain carrier multiplication in PbSe quantum dots," Nano Letters **6**, 2191–2195 (2006).

[130] H. Wang, E. R. McNellis, S. Kinge, M. Bonn, and E. Cánovas, "Tuning electron transfer rates through molecular bridges in quantum dot sensitized oxides," Nano Letters **13**, 5311–5315 (2013).

[131] D. G. Sahota, R. Liang, M. Dion, P. Fournier, H. A. Dabkowska, G. M. Luke, and J. S.

Dodge, “Many-body recombination in photoexcited insulating cuprates,” Physical Review Research **1**, 033214 (2019).

[132] M. Wolf, R. Brendel, J. H. Werner, and H. J. Queisser, “Solar cell efficiency and carrier multiplication in si1-xGex alloys,” Journal of Applied Physics **83**, 4213–4221 (1998).

[133] A. P. Kirk and M. V. Fischetti, “Fundamental limitations of hot-carrier solar cells,” Physical Review B **86**, 165206 (2012).

[134] J. E. Coulter, E. Manousakis, and A. Gali, “Optoelectronic excitations and photovoltaic effect in strongly correlated materials,” Physical Review B **90**, 165142 (2014).

[135] A. Takahashi, H. Itoh, and M. Aihara, “Photoinduced insulator-metal transition in one-dimensional mott insulators,” Physical Review B **77**, 205105 (2008).

[136] M. Eckstein and P. Werner, “Thermalization of a pump-excited mott insulator,” Physical Review B **84**, 035122 (2011).

[137] A. H. Al-Mohy and N. J. Higham, “Computing the action of the matrix exponential, with an application to exponential integrators,” SIAM Journal on Scientific Computing **33**, 488–511 (2011).

[138] G. S. He, L.-S. Tan, Q. Zheng, and P. N. Prasad, “Multiphoton absorbing materials: molecular designs, characterizations, and applications,” Chemical Reviews **108**, 1245–1330 (2008).

[139] W. R. Zipfel, R. M. Williams, and W. W. Webb, “Nonlinear magic: multiphoton microscopy in the biosciences,” Nature Biotechnology **21**, 1369–1377 (2003).

[140] F. Helmchen and W. Denk, “Deep tissue two-photon microscopy,” Nature Methods **2**, 932–940 (2005).

[141] H.-B. Sun and S. Kawata, “Two-photon photopolymerization and 3d lithographic microfabrication,” in *NMR 3D Analysis Photopolymerization* (Springer Berlin Heidelberg, 2006) pp. 169–273.

[142] L. Li and J. T. Fourkas, “Multiphoton polymerization,” Materials Today **10**, 30–37 (2007).

[143] Y.-L. Zhang, Q.-D. Chen, H. Xia, and H.-B. Sun, “Designable 3d nanofabrication by femtosecond laser direct writing,” Nano Today **5**, 435–448 (2010).

[144] B.-U. Sohn, M. Kang, J. W. Choi, A. M. Agarwal, K. Richardson, and D. T. H. Tan, “Observation of very high order multi-photon absorption in GeSbS chalcogenide glass,” APL Photonics **4**, 036102 (2019).

[145] M. Albota, “Design of organic molecules with large two-photon absorption cross sections,” Science **281**, 1653–1656 (1998).

[146] G. P. Banfi, V. Degiorgio, M. Ghigliazza, H. M. Tan, and A. Tomaselli, “Two-photon absorption in semiconductor nanocrystals,” Physical Review B **50**, 5699–5702 (1994).

[147] Y. Wang, X. Li, X. Zhao, L. Xiao, H. Zeng, and H. Sun, "Nonlinear absorption and low-threshold multiphoton pumped stimulated emission from all-inorganic perovskite nanocrystals," Nano Letters **16**, 448–453 (2015).

[148] Y. Xu, Q. Chen, C. Zhang, R. Wang, H. Wu, X. Zhang, G. Xing, W. W. Yu, X. Wang, Y. Zhang, and M. Xiao, "Two-photon-pumped perovskite semiconductor nanocrystal lasers," Journal of the American Chemical Society **138**, 3761–3768 (2016).

[149] T. Ogasawara, M. Ashida, N. Motoyama, H. Eisaki, S. Uchida, Y. Tokura, H. Ghosh, A. Shukla, S. Mazumdar, and M. Kuwata-Gonokami, "Ultrafast optical nonlinearity in the quasi-one-dimensional mott insulator Sr2CuO3," Physical Review Letters **85**, 2204–2207 (2000).

[150] M. Ashida, Y. Taguchi, Y. Tokura, R. T. Clay, S. Mazumdar, Y. P. Svirko, and M. Kuwata-Gonokami, "Dimensionality dependence of optical nonlinearity and relaxation dynamics in cuprates," Europhysics Letters (EPL) **58**, 455–461 (2002).

[151] S. Carusotto, G. Fornaca, and E. Polacco, "Two-photon absorption and coherence," Physical Review **157**, 1207–1213 (1967).

[152] M. Srednicki, "Chaos and quantum thermalization," Physical Review E **50**, 888–901 (1994).

[153] J. M. Deutsch, "Eigenstate thermalization hypothesis," Reports on Progress in Physics **81**, 082001 (2018).

[154] K. Shinjo and T. Tohyama, "Photoinduced absorptions inside the mott gap in the two-dimensional extended hubbard model," Physical Review B **96**, 195141 (2017).

[155] J. Okamoto, "Time-dependent spectral properties of a photoexcited one-dimensional ionic hubbard model: an exact diagonalization study," New Journal of Physics **21**, 123040 (2019).

[156] S. Ishihara, "Photoinduced ultrafast phenomena in correlated electron magnets," Journal of the Physical Society of Japan **88**, 072001 (2019).

[157] C. Shao, T. Tohyama, H.-G. Luo, and H. Lu, "Analysis of time-resolved single-particle spectrum on the one-dimensional extended hubbard model," Physical Review B **101**, 045128 (2020).

[158] N. Maeshima and K. Yonemitsu, "Photoinduced metallic properties of one-dimensional strongly correlated electron systems," Journal of the Physical Society of Japan **74**, 2671–2674 (2005).

[159] H. Lu, C. Shao, J. Bonča, D. Manske, and T. Tohyama, "Photoinduced in-gap excitations in the one-dimensional extended hubbard model," Physical Review B **91**, 245117 (2015).

[160] K. Yonemitsu and K. Nasu, “Theory of photoinduced phase transitions in itinerant electron systems,” Physics Reports **465**, 1–60 (2008).

[161] S. Iwai, M. Ono, A. Maeda, H. Matsuzaki, H. Kishida, H. Okamoto, and Y. Tokura, “Ultrafast optical switching to a metallic state by photoinduced mott transition in a halogen-bridged nickel-chain compound,” Physical Review Letters **91**, 057401 (2003).

[162] H. Okamoto, H. Matsuzaki, T. Wakabayashi, Y. Takahashi, and T. Hasegawa, “Photoinduced metallic state mediated by spin-charge separation in a one-dimensional organic mott insulator,” Physical Review Letters **98**, 037401 (2007).

[163] L. Perfetti, P. A. Loukakos, M. Lisowski, U. Bovensiepen, M. Wolf, H. Berger, S. Biermann, and A. Georges, “Femtosecond dynamics of electronic states in the mott insulator 1t-TaS2 by time resolved photoelectron spectroscopy,” New Journal of Physics **10**, 053019 (2008).

[164] H. Okamoto, T. Miyagoe, K. Kobayashi, H. Uemura, H. Nishioka, H. Matsuzaki, A. Sawa, and Y. Tokura, “Ultrafast charge dynamics in photoexcited NdCuO4 and La2CuO4 cuprate compounds investigated by femtosecond absorption spectroscopy,” Physical Review B **82**, 060513(R) (2010).

[165] H. Matsuzaki, H. Nishioka, H. Uemura, A. Sawa, S. Sota, T. Tohyama, and H. Okamoto, “Ultrafast charge and lattice dynamics in one-dimensional mott insulator of CuO-chain compound Ca2CuO3 investigated by femtosecond absorption spectroscopy,” Physical Review B **91**, 081114(R) (2015).

[166] H. Matsuzaki, M.-A. Ohkura, Y. Ishige, Y. Nogami, and H. Okamoto, “Photoinduced switching to metallic states in the two-dimensional organic mott insulator dimethylphenazine-tetrafluorotetracyanoquinodimethane with anisotropic molecular stacks,” Physical Review B **91**, 245140 (2015).

[167] C. Rylands and N. Andrei, “Loschmidt amplitude and work distribution in quenches of the sine-gordon model,” Physical Review B **99**, 085133 (2019).

[168] F. Maislinger, “Photoinduced dynamics of the finite size 2d hubbard model,” Presentation at the 14th Vicom workshop, Krumbach, Austria (2018).

[169] The analysis of eigenstate spectra via the Loschmidt amplitude was independently developed for the present study.

[170] A. Silva, “Statistics of the work done on a quantum critical system by quenching a control parameter,” Physical Review Letters **101**, 120603 (2008).

[171] J. M. Deutsch, “Quantum statistical mechanics in a closed system,” Physical Review A **43**, 2046–2049 (1991).

[172] We used Marsaglia's method[254], sampling in the occupation number basis. Because the transformation to the eigenbasis is unitary, the states are also drawn uniformly from the hypersphere of normed states in the eigenbasis.

[173] V. Eisler and F. Maislinger, "Hydrodynamical phase transition for domain-wall melting in the XY chain," Physical Review B **98**, 161117 (2018).

[174] V. Eisler and F. Maislinger, "Front dynamics in the XY chain after local excitations," SciPost Physics **8**, 37 (2020).

[175] C. L. Cleveland and R. Medina A., "Obtaining a heisenberg hamiltonian from the hubbard model," American Journal of Physics **44**, 44–46 (1976).

[176] John B Parkinson and Damian JJ Farnell, *An introduction to quantum spin systems*, Vol. 816 (Springer, 2010).

[177] V. Zauner, M. Ganahl, H. G. Evertz, and T. Nishino, "Time evolution within a comoving window: scaling of signal fronts and magnetization plateaus after a local quench in quantum spin chains," Journal of Physics: Condensed Matter **27**, 425602 (2015).

[178] V. Eisler, F. Maislinger, and H. G. Evertz, "Universal front propagation in the quantum ising chain with domain-wall initial states," SciPost Physics **1**, 014 (2016).

[179] S. Sachdev, *Quantum Phase Transitions, Second Edition* (Cambridge University Press, 2011).

[180] A. Polkovnikov, K. Sengupta, A. Silva, and M. Vengalattore, "Colloquium: Nonequilibrium dynamics of closed interacting quantum systems," Reviews of Modern Physics **83**, 863–883 (2011).

[181] M. Heyl, A. Polkovnikov, and S. Kehrein, "Dynamical quantum phase transitions in the transverse-field ising model," Physical Review Letters **110**, 135704 (2013).

[182] M. Heyl, "Dynamical quantum phase transitions: a review," Reports on Progress in Physics **81**, 054001 (2018).

[183] P. Jurcevic, H. Shen, P. Hauke, C. Maier, T. Brydges, C. Hempel, B. P. Lanyon, M. Heyl, R. Blatt, and C. F. Roos, "Direct observation of dynamical quantum phase transitions in an interacting many-body system," Physical Review Letters **119**, 080501 (2017).

[184] M. Schiró and M. Fabrizio, "Time-dependent mean field theory for quench dynamics in correlated electron systems," Physical Review Letters **105**, 076401 (2010).

[185] B. Sciolla and G. Biroli, "Quantum quenches and off-equilibrium dynamical transition in the infinite-dimensional bose-hubbard model," Physical Review Letters **105**, 220401 (2010).

[186] J. P. Garrahan and I. Lesanovsky, "Thermodynamics of quantum jump trajectories," Physical Review Letters **104**, 160601 (2010).

[187] S. Diehl, A. Tomadin, A. Micheli, R. Fazio, and P. Zoller, "Dynamical phase transitions and instabilities in open atomic many-body systems," Physical Review Letters **105**, 015702 (2010).

[188] J. C. Halimeh and V. Zauner-Stauber, "Dynamical phase diagram of quantum spin chains with long-range interactions," Physical Review B **96**, 134427 (2017).

[189] B. Žunkovič, M. Heyl, M. Knap, and A. Silva, "Dynamical quantum phase transitions in spin chains with long-range interactions: Merging different concepts of nonequilibrium criticality," Physical Review Letters **120**, 130601 (2018).

[190] T. Prosen and I. Pižorn, "Quantum phase transition in a far-from-equilibrium steady state of anXYSpin chain," Physical Review Letters **101**, 105701 (2008).

[191] T. Prosen and B. Žunkovič, "Exact solution of markovian master equations for quadratic fermi systems: thermal baths, open XY spin chains and non-equilibrium phase transition," New Journal of Physics **12**, 025016 (2010).

[192] See Supplemental Material for details.

[193] See Supplemental Material for details.

[194] N. Iorgov, "Form factors of the finite quantumXY-chain," Journal of Physics A: Mathematical and Theoretical **44**, 335005 (2011).

[195] N. Iorgov and O. Lisovyy, "Finite-lattice form factors in free-fermion models," Journal of Statistical Mechanics: Theory and Experiment **2011**, P04011 (2011).

[196] See Supplemental Material for details.

[197] See Supplemental Material for details.

[198] S. Sachdev and A. P. Young, "Low temperature relaxational dynamics of the ising chain in a transverse field," Physical Review Letters **78**, 2220–2223 (1997).

[199] T. Antal, P. L. Krapivsky, and A. Rákos, "Logarithmic current fluctuations in nonequilibrium quantum spin chains," Physical Review E **78**, 061115 (2008).

[200] H. Rieger and F. Iglói, "Semiclassical theory for quantum quenches in finite transverse ising chains," Physical Review B **84**, 165117 (2011).

[201] M. Kormos, C. P. Moca, and Zaránd, **98**, 032105 (2018).

[202] V. Eisler and Z. Rácz, "Full counting statistics in a propagating quantum front and random matrix spectra," Physical Review Letters **110**, 060602 (2013).

[203] J. Viti, J.-M. Stéphan, J. Dubail, and M. Haque, "Inhomogeneous quenches in a free fermionic chain: Exact results," EPL (Europhysics Letters) **115**, 40011 (2016).

[204] N. Allegra, J. Dubail, J.-M. Stéphan, and J. Viti, "Inhomogeneous field theory in-

side the arctic circle," Journal of Statistical Mechanics: Theory and Experiment **2016**, 053108 (2016).

[205] G. Perfetto and A. Gambassi, "Ballistic front dynamics after joining two semi-infinite quantum ising chains," Physical Review E **96**, 012138 (2017).

[206] M. Kormos, "Inhomogeneous quenches in the transverse field ising chain: scaling and front dynamics," SciPost Physics **3**, 020 (2017).

[207] See Supplemental Material for details.

[208] C. A. Tracy and H. Widom, "Level-spacing distributions and the airy kernel," Communications in Mathematical Physics **159**, 151–174 (1994).

[209] M. Fagotti, "Higher-order generalized hydrodynamics in one dimension: The noninteracting test," Physical Review B **96**, 220302 (2017).

[210] G. Vidal, J. I. Latorre, E. Rico, and A. Kitaev, "Entanglement in quantum critical phenomena," Physical Review Letters **90**, 227902 (2003).

[211] I. Peschel and V. Eisler, "Reduced density matrices and entanglement entropy in free lattice models," Journal of Physics A: Mathematical and Theoretical **42**, 504003 (2009).

[212] M. Fagotti and F. H. L. Essler, "Reduced density matrix after a quantum quench," Physical Review B **87**, 245107 (2013).

[213] P. Caputa and M. M. Rams, "Quantum dimensions from local operator excitations in the ising model," Journal of Physics A: Mathematical and Theoretical **50**, 055002 (2017).

[214] O. E. Lanford and D. W. Robinson, "Mean entropy of states in quantum-statistical mechanics," Journal of Mathematical Physics **9**, 1120–1125 (1968).

[215] A. Wehrl, "General properties of entropy," Reviews of Modern Physics **50**, 221–260 (1978).

[216] See Supplemental Material for details.

[217] F. Franchini, *An Introduction to Integrable Techniques for One-Dimensional Quantum Systems* (Springer International Publishing, 2017).

[218] V. Eisler and Maislinger F., Unpublished.

[219] B. Bertini, M. Collura, J. De Nardis, and M. Fagotti, "Transport in out-of-EquilibriumXXZChains: Exact profiles of charges and currents," Physical Review Letters **117**, 207201 (2016).

[220] O. A. Castro-Alvaredo, B. Doyon, and T. Yoshimura, "Emergent hydrodynamics in integrable quantum systems out of equilibrium," Physical Review X **6**, 041065 (2016).

[221] L. Piroli, J. De Nardis, M. Collura, B. Bertini, and M. Fagotti, "Transport in out-of-equilibrium XXZ chains: Nonballistic behavior and correlation functions," Physical Review B **96**, 115124 (2017).

[222] M. Collura, A. De Luca, and J. Viti, "Analytic solution of the domain-wall nonequilibrium stationary state," Physical Review B **97**, 081111 (2018).

[223] M. Nozaki, T. Numasawa, and T. Takayanagi, “Quantum entanglement of local operators in conformal field theories,” Physical Review Letters **112**, 111602 (2014).

[224] L. Vidmar and M. Rigol, “Generalized gibbs ensemble in integrable lattice models,” Journal of Statistical Mechanics: Theory and Experiment **2016**, 064007 (2016).

[225] R. Vasseur and J. E. Moore, “Nonequilibrium quantum dynamics and transport: from integrability to many-body localization,” Journal of Statistical Mechanics: Theory and Experiment **2016**, 064010 (2016).

[226] T. Antal, Z. Rácz, A. Rákos, and G. M. Schütz, “Transport in theXXchain at zero temperature: Emergence of flat magnetization profiles,” Physical Review E **59**, 4912–4918 (1999).

[227] D. Karevski, “Scaling behaviour of the relaxation in quantum chains,” The European Physical Journal B - Condensed Matter **27**, 147–152 (2002).

[228] T. Platini and D. Karevski, “Scaling and front dynamics in ising quantum chains,” The European Physical Journal B **48**, 225–231 (2005).

[229] J. L. Lancaster, “Nonequilibrium current-carrying steady states in the anisotropicXYspin chain,” Physical Review E **93**, 052136 (2016).

[230] D. Gobert, C. Kollath, U. Schollwöck, and G. Schütz, “Real-time dynamics in spin-12chains with adaptive time-dependent density matrix renormalization group,” Physical Review E **71**, 036102 (2005).

[231] S. Jesenko and M. Žnidarič, “Finite-temperature magnetization transport of the one-dimensional anisotropic heisenberg model,” Physical Review B **84**, 174438 (2011).

[232] T. Sabetta and G. Misguich, “Nonequilibrium steady states in the quantum XXZ spin chain,” Physical Review B **88**, 245114 (2013).

[233] M. Gruber and V. Eisler, “Magnetization and entanglement after a geometric quench in the XXZ chain,” Physical Review B **99**, 174403 (2019).

[234] M. Ljubotina, M. Žnidarič, and T. Prosen, “Spin diffusion from an inhomogeneous quench in an integrable system,” Nature Communications **8**, 1–6 (2017).

[235] M. Ljubotina, M. Žnidarič, and T. Prosen, “A class of states supporting diffusive spin dynamics in the isotropic heisenberg model,” Journal of Physics A: Mathematical and Theoretical **50**, 475002 (2017).

[236] J.-M. Stéphan, “Return probability after a quench from a domain wall initial state in the spin-1/2 XXZ chain,” Journal of Statistical Mechanics: Theory and Experiment **2017**, 103108 (2017).

[237] G. Misguich, K. Mallick, and P. L. Krapivsky, “Dynamics of the spin- 12 heisenberg chain initialized in a domain-wall state,” Physical Review B **96**, 195151 (2017).

[238] G. Misguich, N. Pavloff, and V. Pasquier, "Domain wall problem in the quantum XXZ chain and semiclassical behavior close to the isotropic point," SciPost Physics **7**, 025 (2019).

[239] O. Gamayun, Y. Miao, and E. Ilievski, "Domain-wall dynamics in the landau-lifshitz magnet and the classical-quantum correspondence for spin transport," Physical Review B **99**, 140301 (2019).

[240] O. A. Castro-Alvaredo, C. De Fazio, B. Doyon, and I. M. Szécsényi, "Entanglement content of quasiparticle excitations," Physical Review Letters **121**, 170602 (2018).

[241] O. A. Castro-Alvaredo, C. De Fazio, B. Doyon, and I. M. Szécsényi, "Entanglement content of quantum particle excitations. part i. free field theory," Journal of High Energy Physics **2018**, 39 (2018).

[242] N. Iorgov, V. Shadura, and Y. Tykhyy, "Spin operator matrix elements in the quantum ising chain: fermion approach," Journal of Statistical Mechanics: Theory and Experiment **2011**, P02028 (2011).

[243] U. Divakaran, F. Iglói, and H. Rieger, "Non-equilibrium quantum dynamics after local quenches," Journal of Statistical Mechanics: Theory and Experiment **2011**, P10027 (2011).

[244] V. Hunyadi, Z. Rácz, and L. Sasvári, "Dynamic scaling of fronts in the quantumXXchain," Physical Review E **69**, 066103 (2004).

[245] V. B. Bulchandani and C. Karrasch, "Subdiffusive front scaling in interacting integrable models," Physical Review B **99**, 121410 (2019).

[246] J.-M. Stéphan, "Free fermions at the edge of interacting systems," SciPost Physics **6**, 057 (2019).

[247] V. Eisler, F. Iglói, and I. Peschel, "Entanglement in spin chains with gradients," Journal of Statistical Mechanics: Theory and Experiment **2009**, P02011 (2009).

[248] V. Eisler and I. Peschel, "Surface and bulk entanglement in free-fermion chains," Journal of Statistical Mechanics: Theory and Experiment **2014**, P04005 (2014).

[249] V. Alba and F. Heidrich-Meisner, "Entanglement spreading after a geometric quench in quantum spin chains," Physical Review B **90**, 075144 (2014).

[250] V. Eisler and D. Bauernfeind, "Front dynamics and entanglement in the XXZ chain with a gradient," Physical Review B **96**, 174301 (2017).

[251] J. Dubail, J.-M. Stéphan, J. Viti, and P. Calabrese, "Conformal field theory for inhomogeneous one-dimensional quantum systems: the example of non-interacting fermi gases," SciPost Physics **2**, 002 (2017).

[252] I. Peschel, "On the entanglement entropy for an XY spin chain," Journal of Statistical

Mechanics: Theory and Experiment **2004**, P12005 (2004).

[253] A. R. Its, B.-Q. Jin, and V. E. Korepin, "Entanglement in theXYspin chain," Journal of Physics A: Mathematical and General **38**, 2975–2990 (2005).

[254] G. Marsaglia, "Choosing a point from the surface of a sphere," The Annals of Mathematical Statistics **43**, 645–646 (1972).